Light-Matter Interactions of Two-Dimensional Materials and the Coupled Nanostructures

by

Shengxi Huang

B.S., Tsinghua University (2011)

M.S., Massachusetts Institute of Technology (2013)

Submitted to the Department of Electrical Engineering and Computer Science

in partial fulfilment of the requirements for the degree of

Doctor of Philosophy in Electrical Engineering and Computer Science

at the

MASSACHUSETTS INSTITUTE OF TECHNOLOGY

June 2017

Author ……
Department of Electrical Engineering and Computer Science
May 17, 2017

Certified by ……
Mildred Dresselhaus
Institute Professor, Professor of Electrical Engineering, Professor of Physics
Thesis Supervisor

Certified by ……
Jing Kong
Professor of Electrical Engineering and Computer Science
Thesis Supervisor

Accepted by ……...
Leslie A. Kolodziejski
Professor of Electrical Engineering and Computer Science
Chair, Department Committee on Graduate Theses

Light-Matter Interactions of Two-Dimensional Materials and the Coupled Nanostructures

by

Shengxi Huang

Submitted to the Department of Electrical Engineering and Computer Science

on May 17, 2017, in partial fulfillment of the

requirements for the degree of

Doctor of Philosophy in Electrical Engineering and Computer Science

Abstract

Two-dimensional (2D) materials have gained increasing attention due to their unique and extraordinary electrical and optoelectronic properties. These properties can be largely attributed to the fundamental light-matter interactions. This thesis project uses spectroscopy techniques and focuses on the study of the light-matter interaction in 2D materials, as well as their coupling with other nanostructures, which are essential in achieving useful optoeletronic applications with 2D materials.

First, the fundamental properties of 2D materials were investigated using spectroscopy. Photoluminescence (PL) spectroscopies of MoS_2 and its related structures were studied, showing that the interaction between MoS_2 layers and other dielectrics can strongly affect their PL emissions, exciton and trion properties. Moreover, combining Raman spectroscopy and X-ray photoelectron spectroscopy, the effects of substrates and defects for MoS_2 have been revealed.

Next, interlayer vibrational properties of 2D materials are studied utilizing low-frequency Raman spectroscopy. Twisted bilayer MoS_2 and few-layer black phosphorus were chosen to demonstrate the interlayer coupling from the perspective of interlayer breathing and shear Raman modes. These exemplary studies offer a great tool to investigate the interlayer coupling, thickness, and stacking configurations of 2D materials using low-frequency Raman spectroscopy.

The anisotropic light-matter interactions of 2D materials were also examined. Using polarization dependent Raman and optical absorption spectroscopies, together with first-principles density functional theory analysis and group theory, the anisotropy of electron-photon and electron-phonon interactions can be revealed. This method can experimentally exhibit the anisotropy of electron-phonon interactions in 2D materials, and can be generalized to other layered materials with in-plane anisotropy.

The interactions of 2D materials with other materials systems were also investigated using optical spectroscopies. The interactions of 2D materials and selected organic molecules were revealed using graphene-enhanced Raman spectroscopy. The interaction

between 2D materials and plasmonic nanocavities were found to exhibit an interesting enhancement phenomenon for the optical response of 2D materials.

Overall, the studies presented in this thesis work show broad opportunities for using spectroscopic tools to study light-matter interactions of 2D materials, as well as the combined system of 2D materials and other nanostructures. This work is significant fundamentally, and also offers useful guidelines for practical applications of 2D materials in electronics and optoelectronics.

Thesis Supervisor: Mildred Dresselhaus
Title: Institute Professor, Professor of Electrical Engineering, Professor of Physics

Thesis Supervisor: Jing Kong
Title: Professor of Electrical Engineering and Computer Science

I would like to dedicate this thesis to my late advisor, Prof. Mildred Dresselhaus. Prof. Jing Kong has signed this thesis on behalf of Prof. Dresselhaus, who recently passed away. I would also like to thank Prof. Kong for acting this capacity.

Acknowledgements

I would like to dedicate this thesis to my advisor, Prof. Mildred Dresselhaus. It has been a great privilege and great pleasure to be able to work with her during the past four years. She has impacted me in many ways, research, attitudes towards work and life, and many others. Millie vividly showed me what is enthusiasm for science: she truly enjoyed coming to work and discussing with people, and she really worked until the last moment, which well reflected her spirit and legendary. She will be dearly, dearly missed.

I would also like to give my sincere thanks to Prof. Jing Kong. She has helped me tremendously regarding research, career advice, etc. I also learned a very important thing from her: be kind and be grateful.

I would like to thank my other committee members, Prof. Tomas Palacios and Prof. Pablo Jarillo-Herrero, for their great advice and inputs on my thesis work.

Many thanks to my collaborators, Prof. Vincent Meunier, Prof. Riichiro Saito, Prof. Marija Drndic, Dr. David Geohegan, Dr. Alex Puretzky, Dr. Liangbo Liang, Dr. An-Ping Li, Dr. Stephen Doorn, Dr. Han Htoon, Prof. Jianfang Wang, Prof. Bilge Yildiz. I am very grateful for their support to make my works complete.

Many thanks to all my experiment buddies, Xi Ling, Yan Chen, Yuxuan Lin, Tian Ming, Lin Zhou, Mingda Li, for a lot of wonderful time together working, brainstorming, eating, and having fun, as well as many other labmates and friends.

Many thanks to Guolong, for always reminding me what is important in life, and for always being there to help and support tremendously, especially when my ACL was broken and during the recovery from surgery.

Last but not the least, many thanks to my parents. They have offered me what a child can hope for the best. They always remind me that never let external factors restrict what I can achieve. I also feel extremely lucky that we still speak the same language after I have gone thus far.

Contents

List of Tables

List of Figures

Chapter 1
Introduction

2D materials (Figure 1-1) have the layered structure, and are typically atomically thin. This extremely small thickness endows 2D materials with many unusual and important properties. For example, some 2D materials have very stable excitons due to the reduced dimension, which makes them advantageous in photonic applications. Many 2D materials can be used to build flexible devices due to their ultra flexibility and stretchability. They are also suitable for sensing devices due to their super large surface-to-volume ratio. Optical spectroscopic techniques are effective ways to characterize 2D materials, such as Raman, photoluminescence and optical absorption spectroscopies. For example, 2D materials typically have large Raman cross section, producing strong Raman signal and making Raman a sensitive probe for the material properties. In this introduction section, we introduce several common and newly-emerged 2D materials, as well as the basic optical spectroscopic techniques that can be used to characterize 2D materials.

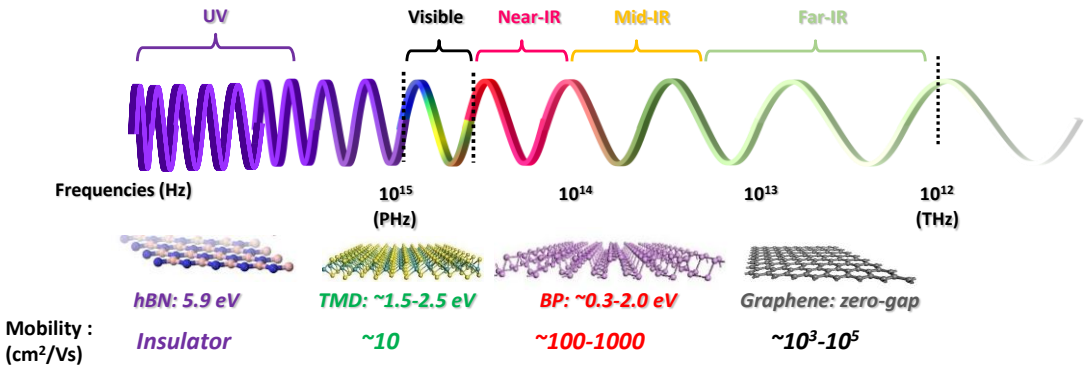

Figure 1-1. Various 2D materials with the corresponding frequency ranges and mobility, including graphene, black phosphorus (BP), transition metal dichalcogenide (TMD) and hBN (hexagonal boron nitride). Figure from (*1*).

1.1 Two-Dimensional materials

1.1.1 Graphene

Graphene is a layer of crystalline graphite, and it is the basic building block of sp^2 carbon materials. Below the basic optical, electrical and spectroscopic properties of graphene are introduced. (*2*)

1.1.1.1 Optical Properties of Graphene

It is widely established that graphene has numerous fascinating properties. (*3–8*) Though considered as a semi-metal, graphene has unique electromagnetic/plasmonic effects compared to conventional noble metals. (*9, 10*) First, its plasma frequency in the long-wavelength limit is expressed as (*11–14*)

$$\omega_{p,G} = \sqrt{\frac{8E_F\sigma_{uni}q}{\hbar\varepsilon}}$$

in which E_F is the Fermi energy of graphene, σ_{uni} is the universal optical conductivity of graphene and is independent of any material parameters: $\sigma_{uni} = \pi e^2/(2h)$, (*15, 16*) q is the unit charge, and ε is the permittivity. Notice that the expression of plasma frequency for graphene is very different from the plasma frequency for metals which is (*17*)

$$\omega_{p,M} = \sqrt{\frac{2\pi n e^2 q}{\varepsilon m}}$$

in which n is the carrier density, and m is the carrier effective mass. We can see that $\omega_{p,G} \propto E_F^{1/2} \propto n^{1/4}$, and $\omega_{p,M} \propto n^{1/2}$. Such a difference in the plasma frequencies between graphene and metals is due to the Dirac fermions in graphene, rather than ordinary Schrödinger fermions in normal metals. The plasma frequency of graphene is in the terahertz range, which is 10^3 times lower than ω_p in metals, and which can be tuned through gating or doping, (*10, 18, 19*) or by fabricating graphene ribbons with micron widths (see Figure 1-2), where ω_p is in the terahertz range. Here ω_p differs with the ribbon widths and with the Fermi energy E_F, as shown in Figure 1-2. Second, single-layer graphene has a linear dispersion relation and a uniform 2.293% light absorption across a

wide frequency range, (*10*, *20–22*) resulting from its Dirac-cone band structure and linear energy-momentum relation E(k), as seen in Figure 1-3. Many works have studied the surface plasmonic properties of graphene or graphene ribbons, with different experimental techniques including optical measurements, electron energy loss spectroscopy, angle-resolved photoemission spectroscopy, and surface tunneling spectroscopy, (*18*, *19*, *23–25*) as further discussed in the cited references.

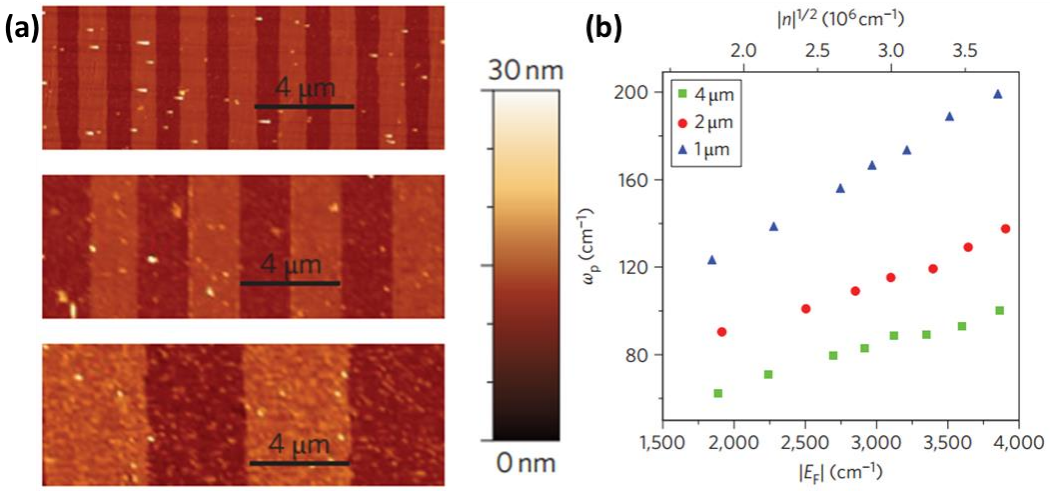

Figure 1-2. Control of the graphene plasmon resonance frequency by electrical gating and microribbon widths. (a) AFM (atomic force microscopy) images of graphene microribbons with widths of 1 μm, 2 μm, and 4 μm. Color bar of the height is shown on the right. (b) Fermi energy (E_F) dependence of the graphene plasmon frequency ω_p (top axis gives related dependence on charge density $|n|^{1/2}$) of three different graphene ribbons widths. Figure adapted from (*19*).

1.1.1.2 Electrical Properties of Graphene

One of the greatest advantages of studying graphene is that its transport and optical properties can be sensitively and controllably tuned by doping. The Fermi level can easily be shifted by either introducing electrons (n-doping) or holes (p-doping). Numerous ways of establishing a desired doping level have been investigated, for instance by chemical doping, (*26*, *27*) electrochemical doping, (*28–31*) electrostatically by top or back gating, (*32–34*) and by the direct introduction of heteroatoms into the lattice. (*35*)

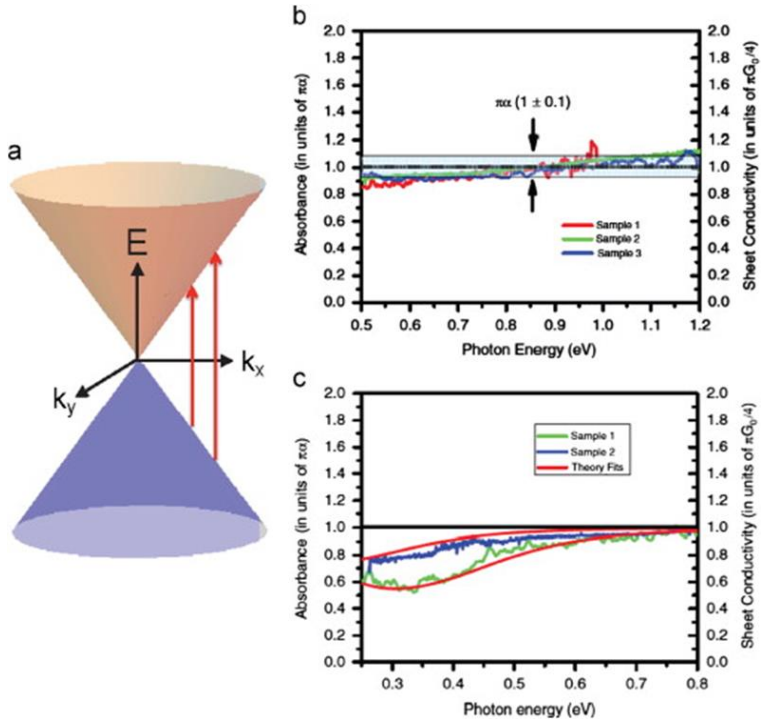

Figure 1-3. Universal light absorbance and optical conductivity of graphene. (a) Schematic of Dirac cone and interband optical transitions in graphene. (b) Optical absorbance (left axis) and optical sheet conductivity (right axis) of three graphene samples. The spectral range is from 0.5 eV to 1.2 eV. The black horizontal line shows the universal absorbance value of 2.293% per layer, with the variation within 10%. (c) The optical absorbance of graphene Sample 1 and Sample 2 over a smaller spectral range from 0.25 eV to 0.8 eV. Figure from (*21*, *22*).

One of the most studied and widely used techniques is to introduce the charge by top or back gating. (*32*–*34*) This technique is appealing due to its similarity to present use in gating field-effect transistors, which allows the knowledge and know-how learned from standard microelectronics to be used more widely in graphene electronics. However, one drawback of this approach is the extremely high gating potential (~100 V) that is required, because present gate dielectrics have a relatively large thickness which restricts the gate capacitance value. For example, bias voltages as high as 80 V had to be used to achieve a carrier density of ~ 5×10^{12} cm^{-2}, (*34*) and such a high bias voltage could cause charge

trapping from the substrate, thereby altering the properties of both the substrate and graphene.

Electrochemical doping, on the other hand, is significantly more efficient, insofar voltages as small as 1.5 V are sufficient to reach charge carrier concentrations of 5×10^{13} cm^{-2}. Higher doping levels can also be achieved by using a combination of a protecting layer and a liquid electrolyte (*36*) or using ferroelectric polymers. (*37*) Electrochemical doping is thus especially appealing when higher doping levels are desired, and these high doping levels are achieved by the electrical double layer (EDL) formed at the interface between the electrolyte solution and the graphene surface. The ions in the liquid are attracted by graphene, which is charged by opposite sign. These ions migrate to the surface, thus forming a very thin layer, which performs as a capacitor with an extremely high capacitance value. Therefore, effective control of carrier densities in the graphene can be implemented through electrochemistry, which furthermore provides a fast response by electrochemical doping.

1.1.1.3 Spectroscopic Properties of Graphene

Spectroelectrochemical studies are most commonly carried out by using Raman spectroscopy because this technique is readily available and does not normally perturb the material under investigation, thereby allowing repeated and systematic measurements. The commonly studied features in the Raman spectra of graphene are the G, D, and G′ bands (the G′ band is also called the 2D band), see Figure 1-4. The shape of the electronic bands can be probed by varying the laser excitation energy, which shifts the peak position of the D and G′ bands and thus provides additional important information. Figure 1-5 shows the scattering processes that generate these vibrational bands or features. (*33*) From Figure 1-5, we can see that G band comes from a first-order one-phonon scattering process, while other bands come from second-order scattering processes. The D band is a symmetry breaking band, which thus requires the presence of defects in the sample, although boundaries (edges) of the sample also produce D band intensity. Since the D band is not allowed by the crystal symmetry of the graphene lattice, the D band is commonly used to evaluate the quality of a particular graphene sample. The G and G′ bands are present in all sp^2 carbon and graphene-related materials and are symmetry allowed. The intensity, frequency, and

linewidth of these bands are dependent on several factors, such as strain and doping, the number of graphene layers, and the laser excitation energy. For example, the shape of the G′ band of graphene is related to the number of graphene layers and how the layers are stacked with respect to one another. As shown in Figure 1-6, (*33*) the shape of the G′ band is dramatically different from single layer to four layers and to bulk HOPG (highly oriented pyrolytic graphite). The G′ band is generated from the second-order two-phonon intervalley scattering (Figure 1-5), and the G′ band can be fitted with multiple Lorentzian lineshapes, depending on the structure of the sample.

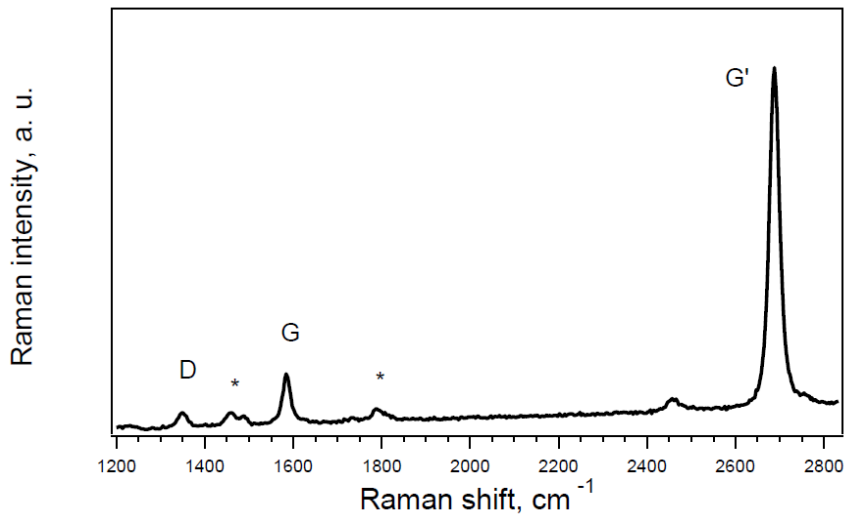

Figure 1-4. Raman spectrum of graphene at 0 V, excited by a 2.33 eV laser radiation, in an electrochemical environment. The asterisks (*) indicate Raman bands of the electrolyte. From (*31*).

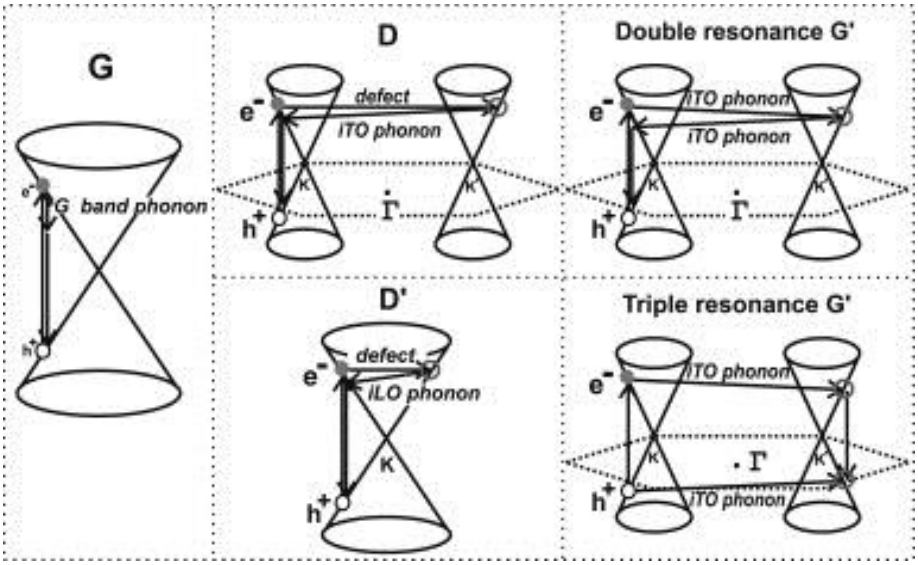

Figure 1-5. The Raman scattering processes of G, D, D′, and G′ bands of graphene. Figure is from (*33*).

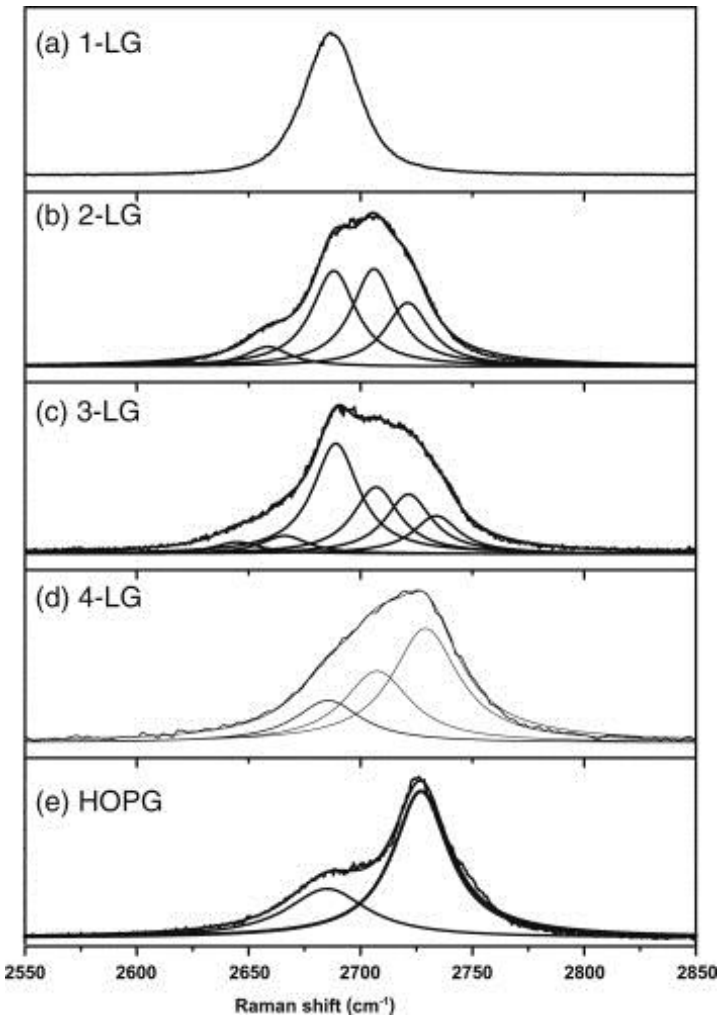

Figure 1-6. Raman spectra of the G′ band of graphene with different numbers of layers. The excitation laser wavelength is 514 nm. Figure is from (*33*).

The doping of graphene results in changes in all Raman features. Using spectroelectrochemistry to accurately control and to shift the Fermi level, it has, for example, been found that the intensity of the D peak decreases with increasing doping, (*38*) as seen in Figure 1-7. Such an effect was attributed to the fact that the strength of the electron scattering is doping dependent, such that the total scattering rate of the photoexcited electrons and holes increases with doping. It is consequently important to know the doping level of the graphene when estimating the amount and type of defects from the intensity of the D peak.

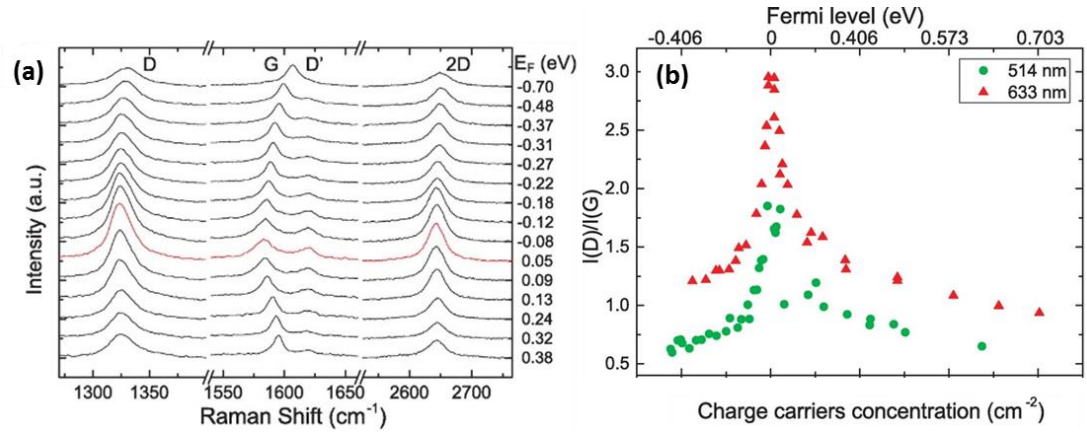

Figure 1-7. The change of D band with electrochemical doping. (a) Raman spectra of defective graphene at different Fermi energies (E_F), measured under 633 nm laser excitation. (b) The normalized intensity of the D band as a function of Fermi level, or charge carrier concentration at 514 nm and 633 nm laser excitations. Figure is adapted from (*38*).

The G band in Figure 1-4 is observed to be due to the optical phonon of graphene, which occurs at a high frequency of ~ 1580 cm^{-1} because the carbon atoms are so light, being atomic number 6 in the periodic table. From a many-body point of view, the origin of the G band can be explained as that of an electron that is excited from the valence band into a conduction band by absorbing a phonon. An electron-hole pair is thus created. When the electron and the hole then recombine, a phonon is emitted, which has a slightly shifted frequency and a lifetime connected to its bandwidth. The energy of the phonon and of the charge carriers will thus be renormalized by the various interactions. Since the band structure of graphene is conical with a linear E(k) relation (see Figure 1-3(a)), and thereby symmetric for electrons and holes with respect to the Dirac point, the frequency shift of the G band upon doping can be expected to be equal for positive and negative doping. However, the C-C bond strength is also changed somewhat when the graphene is doped. (*34*) Positive (negative) charge doping removes (adds) electrons from (to) antibonding orbitals which increases (decreases) the bond strength. This phenomenon has an opposite effect on positive doping relative to negative doping. Both the renormalization and the bond strength change lead to an upshift of the phonon frequency for positive doping.(*28*,

31) For negative doping, on the other hand, the two effects work against each other. (*28*, *31*)

The G′ or 2D band in Figure 1-4 is also sensitive to doping, although to a lesser extent than the G band. Doping induces changes in the frequency of the G′ band due to changes in the C-C bond strength, the electron-phonon coupling, and electron-electron interactions. The frequency of the G′ band increases for positive doping, whereas it first increases for negative doping followed by a relatively large decrease at higher negative potentials. It has been found both experimentally (*31*) and theoretically, (*39*) that the G band frequency shifts by ~ 0.5 times as much as the G′ band per volt in the range from 0 to 1 V. Strain can also influence the frequency of the G and G′ band. The two effects can be disentangled from one another by correlating the peak positions in the Raman spectra. (*31*, *40*)

1.1.2 Transition-Metal Dichalcogenide

Transition metal dichalcogenide (TMD) is a group of materials consisting of about 40 members. Depending on the specific material, the properties of TMD can vary much. There are also different phases (structures) for one material, including 2H, 3R, 1T and 1T'. Some typical transition metal dichalcogenides include molybdenum disulfide (MoS_2), tungsten disulphide (WS_2), tungsten diselenide (WSe_2).

Monolayer MoS_2, composed of three layers of atoms where Mo atoms are sandwiched between two layers of S atoms, has attracted much attention of researchers because of its direct bandgap electronic structure and unique excitonic properties in its 2H phase. Monolayer 2H MoS_2 is predicted to have broad applications in photonic devices, (*41–44*) including light-emitting devices, (*45*) photodetectors, (*46*, *47*) solar cells, (*48*) etc, mainly due to its strong photoluminescence (PL) emission, (*42*, *49–53*) light absorption, (*42*, *51*) photocurrent (*41*, *54*) and valleytronics. (*55–57*) For these optoelectronic applications, the photoluminescence (PL) emission of MoS_2 plays an important role.

The optical properties can be very sensitive to the number of layers. For instance, the PL intensity of MoS_2 drops dramatically going from a single-layer to few-layers, (*42*, *49*, *52*) due to the electronic structure changing from a direct to indirect bandgap. (*49*, *52*, *58–61*) Such a change underscores the importance of interlayer coupling in MoS_2, which is

sensitive to the layer-layer relative stacking. The attractiveness of bilayer compared to monolayer MoS_2 for optical and electronic applications, has been illustrated by the development of a MOSFET device where the optimal balance between carrier mobility and on/off ratio was achieved for bilayer systems, (*62*) as well as its unique spin and valley properties which are different from monolayer MoS_2. (*61*, *63*, *64*) However, as previously reported in studies using PL spectroscopy, (*52*, *65*, *66*) the properties of bilayer MoS_2 are sensitive to stacking, due to the high variability in possible interlayer coupling. This stacking sensitivity is expected to strongly affect the development of MoS_2-based electronics.

1.1.3 Black Phosphorus

Black phosphorus (BP) has witnessed its renaissance in 2014. (*1*, *67*) Since then, it has been the focus of research in various fields, including electronics, optoelectronics, thermoelectrics, etc. As can be seen in Figure 1-8, the number of publications related to BP increased very quickly during the recent three years when BP is considered as a two-dimensional (2D) materials for properties and applications study (Figure 1-8). There are several reasons for this tremendous popularity of BP. One reason is that it triggers the study of 2D materials with in-plane anisotropy, including GaTe, SnSe, $ReSe_2$, ReS_2 etc. (*68*–*71*) Another reason is that BP has a bandgap of 0.3 - 2 eV from bulk to monolayer (*72*, *73*) and with a much higher mobility than transition metal dichalcogenides (TMDs), (*42*, *52*, *53*, *74*, *75*) which fills the gap between TMD (about 1.5-2 eV) and graphene (below 0.2 eV), (*3*) and therefore potentially have important applications in mid-IR photonic devices, as well as in high-performance field-effect transistors with an ideal trade-off for carrier mobility and current on/off ratio.

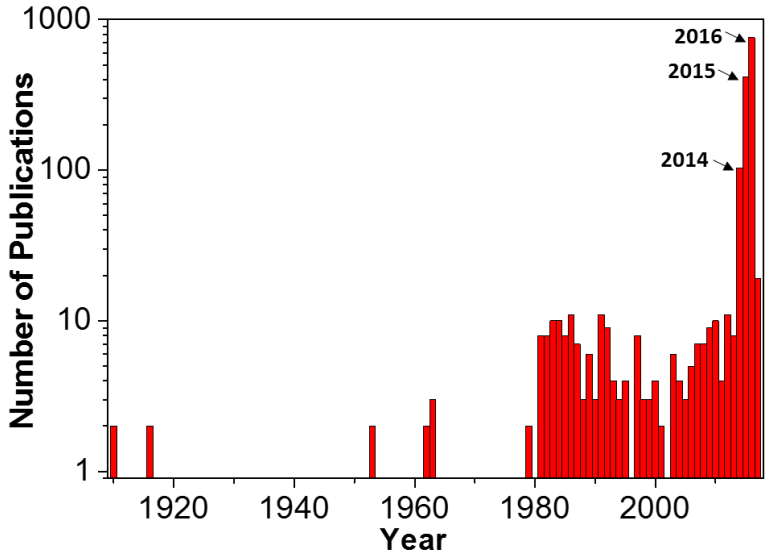

Figure 1-8. Number of publications on black phosphorus changes with year. Source: Web of Science; Date: Jan. 19, 2017.

Despite the excellent properties of BP, there are currently some challenges in realizing high-performance BP-based devices. One challenge is the easy degradation of BP. It has been shown that BP surface is subject to oxygen and water vapor in air within minutes, and therefore forms PO_x on surface, which tremendously decreases the mobility and roughens the surface. One solution to this is passivation of the surface using polymer or Al_2O_3 capping layers, which can effectively preserve the properties of BP for at least weeks. (*76*, *77*) Another challenge is the synthesis of BP. Currently, the synthesis of BP is mostly through chemical vapor transport (CVT), and produces crystals only in bulk forms. (*78*, *79*) The chemical vapor deposition (CVD) synthesis can potentially produce few-layer or monolayer BP, but the technique is still under development. (*80*) Moreover, the fabrication techniques of BP devices require further development of the processes suitable for BP, such as sculpturing them into nanoribbon. (*81*)

As a leading anisotropic 2D material, many studies has been focused on the properties of BP using multiple tools. For example, Liang et al. used STM to characterize the band gap and edge state of BP; (*73*) Das et al. used TEM to study the anisotropic sculpting of BP. (*81*) Among various characterization methods, (*73*, *81–85*) optical method is simple,

non-destructive, fast, and ubiquitous among many other 2D materials. Here, we mainly introduce the fundamental physics and principles underneath the optical characterization, and the optical spectroscopies of BP including Raman, photoluminescence, and optical absorption spectroscopies.

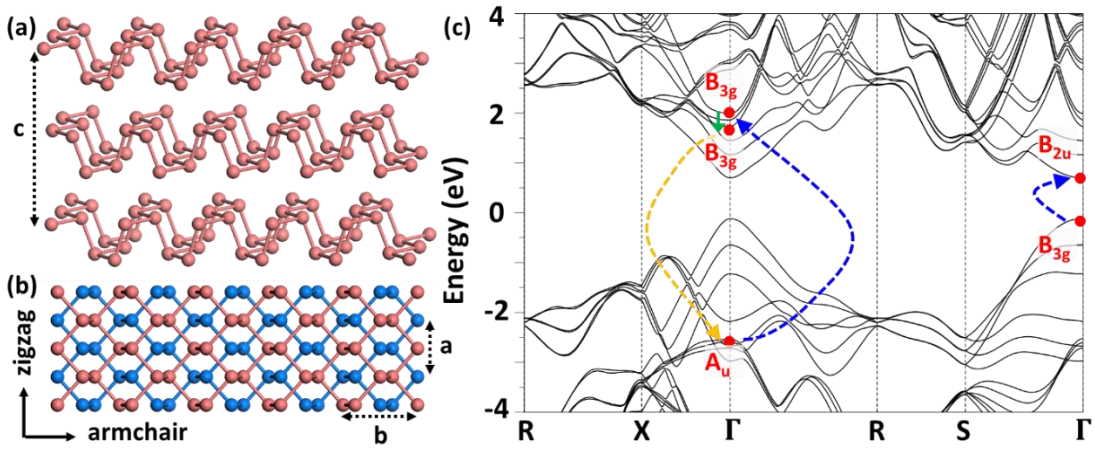

Figure 1-9. (a) Side view of a three-layer of BP; (b) top view of (a), the adjacent layers are labeled with different colors, and the lattice constants a, b, c are labeled in (a-b); (c) the electronic band structure of BP calculated by DFT. Three transitions are shown by the arrows.

Bulk BP has the symmetry with space group *cmce* (No. 64) and point group D_{2h}^{18} (mmm), which is orthorhombic structure. (*1*, *86*, *87*) Each layer of BP has the puckered layer of phosphorus atoms. The crystal structure of BP is shown in Figure 1-9(a-b), which shows the perspective view and the top view, respectively. In the top view, different layers of BP are shown with different colors. It can be seen that from the top view in Figure 1-9(b), each layer of BP shows hexagonal structure, and therefore there are two in-plane directions defined as zigzag and armchair directions, as seen in Figure 1-9(b). In fact, each layer of BP consists atoms from two sub-layers as can be seen from the perspective view in Figure 1-9(a), different from the case in graphene. The adjacent two layers are shifted along the zigzag direction for half a lattice constant, as seen in Figure 1-9(b). The crystal unit cell of bulk BP is orthorhombic with two layers and 8 atoms (lattice constants a=~3.3 Å, c=~10.5

Å and b=~4.4 Å, as shown in Figure 1-9(a-b)). The symmetries of *N-layer* (*N*L) BP films (where *N* is the number of layers) are slightly different from those of bulk BP: odd *NL* BP belongs to space group *Pmna* (No. 53) and point group D_{2h}^{7} (mmm); even *N*L BP belongs to space group *Pmca* (No. 57) and point group D_{2h}^{11} (mmm). Although *N*L systems belong to different space groups from the bulk BP, all of them share the same point group D_{2h}(mmm) which has 3 rotation axes, 3 mirror planes and inversion symmetry. (*88*) The symmetry properties of the BP family are distinguished by the translational symmetry indicated by the superscript of the space group label, i.e. D_{2h}^{7} for odd number of layer BP, D_{2h}^{11} for even number of layer BP, and D_{2h}^{18} for bulk BP. From monolayer to bulk, BP has direct bandgap at Γ point from around 2.0 eV to 0.3 eV. The band structure of a trilayer BP is shown in Figure 1-9(c). As can be seen, a direct bandgap of around 1.0 eV exists at Γ point.

Since the focus of this thesis work is optical properties, we introduce the basic optical transitions here. As shown in Figure 1-9(c), the blue dotted curves show the processes of optical absorption, in which an electron from the lower energy band absorbs a photon and be excited to a higher energy band. The dotted curve connecting two energy bands (B_{3g} and B_{2u} bands on the right) at the Γ point is the band-edge transition, in which the electron from the highest valence band is excited to the lowest conduction band. Other optical absorption connecting two bands lower (higher) than the highest (lowest) valence (conduction) band can occur, and an example is shown in the Figure 1-9(c) connecting the A_u and B_{3g} states labeled. The optical absorption typically involves electrons and photons, and therefore it is an electron-photon interaction. Another electron-photon interaction is photon emission, in which an electron from a higher level undergoes a radiative decay and be relaxed to a lower level, and the energy difference is emitted as the form of a photon. This process is shown in the orange curve in Figure 1-9(c). In both optical absorption and emission, the process has higher probability to occur in two energy levels with higher joint density of states according to the Fermi's golden rule.(*89*) Besides the electron-photon interaction, another common process is electron-phonon interaction, in which electron emits (absorbs) a phonon and be excited (relaxed) to a higher (lower) energy level, as seen in the green arrow in Figure 1-9(c). The energy of the phonon can be probed by Raman scattering, which

consists of two electron-photon and one electron-phonon interactions, as shown in Figure 1-9(c) connecting three energy states at Γ point: two B_{3g} states and one A_u state. In a typical Raman process, a photon from external excitation source (typically laser) enters the material, and the electron from a lower state (in the case shown in Figure 1-9(c), A_u state) absorbs the photon and be excited to a higher energy state (the higher B_{3g} state in Figure 1-9(c)), which is an electron-photon interaction. Then the electron emits a phonon and is relaxed to the lower B_{3g} state, which is an electron-phonon interaction. Finally, the electron from the lower B_{3g} state emits a photon and is relaxed to the initial A_u state, which is also an electron-photon interaction. The emitted photon energy can be detected by the Raman spectrometer. The phonon energy is the energy difference between the two B_{3g} states, and therefore can be obtained by calculating the difference between the incident and emitted photon energies. In the experiment of BP with few-layer, since the Raman excitation laser is usually in the visible range, the optical transitions not only consists band-edge transitions, but also the higher level transitions are usually involved. (*68*, *87*, *90*)

1.1.4 Gallium Telluride

Two-dimensional (2D) materials constitute a large family with various members from the ones with high in-plane symmetry, such as graphene, to those with low in-plane symmetry, such as black phosphorus (BP), gallium telluride (GaTe), tin selenide (SnSe) and rhenium disulfide (ReS_2). (*1*, *71*, *91–93*) These materials show diverse optical and electrical properties depending on their unique structures. (*94–99*) In particular, low-symmetry 2D materials show significant in-plane anisotropy in their electrical, optical and thermal properties. For example, compared to the D_{6h} symmetry of graphene, the reduced symmetry (D_{2h}) of BP has been reported to result in the mobility, (*100*) photoemission,(*96*) and thermoelectric ZT factor (*101*, *102*) being larger along the armchair direction than along the zigzag direction. In our recent research, (*87*) we used spectroscopic techniques to reveal the anisotropic light-matter interactions in BP, including electron-photon and electron-phonon interactions, which indicates that it is crucial to understand the detailed anisotropy before applying the low-symmetry layered material to practical applications. (*94*, *98*, *100*, *103*, *104*)

As one of the important members among low-symmetry layered materials, GaTe has gained increasing attention in recent years. (*68*, *105–115*) With a direct bandgap of ~1.7 eV for thicknesses ranging from few-layer to bulk, GaTe has demonstrated extremely high photoresponsivity (10^4 A/W) and a short response time (6 ms) in photodetectors, (*107*) and promising potentials in various other photonic applications such as solar cells, imaging arrays, radiation detectors, nonlinear optics, (*109*, *114*, *116*) as well as in thermoelectric devices. (*117*, *118*) Although the in-plane anisotropic performance of those properties has been observed, (*91*, *111*, *119*) the reason behind, as well as a convenient spectroscopic identification of the crystalline orientation, is still under exploration.

1.1.5 Molybdenum Diltelluride

$MoTe_2$ has recently attracted enormous interests due to its novel physical properties (*120*) and promising applications in electronics, optoelectronics, photovoltaics, valleytronics and spintronics, etc.[4-7] $MoTe_2$ can crystallize in four different phases: 2H phase (hexagonal structure), 1T' phase (monoclinic structure), T_d phase (orthorhombic structure) and 1T (octahedral structure).[8-11] Since the energy difference between semiconducting phase 2H and semimetallic phase 1T' $MoTe_2$ is small compared with other transition metal dichalcogenides (TMDs),[12] $MoTe_2$ with various phases can be directly synthesized by tuning growth parameters (precursors, temperature, cooling rate etc.).[8,10,11] Laser patterning[4] and strain engineering[13] techniques have been suggested as ways to realize semiconducting-semimetallic phase transition of $MoTe_2$. While the studies of other TMDs mainly focus on the semiconducting phase, the semimetallic phases of $MoTe_2$ (1T' and T_d) have attracted much attention and possess potential applications in quantum computing.[1-3,5] 1T' $MoTe_2$ has been observed to transfer to T_d $MoTe_2$ through temperature-induced phase transition when cooling down below 240 K.[2] The low-temperature phase T_d $MoTe_2$ is a type-II Weyl semimetal, which exhibits novel quantum properties such as topological surface state Fermi arcs, chiral anomaly-induced negative magnetoresistance, etc.[2] Moreover, pressure-driven superconductivity[3] and large magnetoresistance[1] were observed in 1T' $MoTe_2$. Besides these remarkable properties, the low-symmetry crystal structure may lead to several anisotropic properties in 1T' $MoTe_2$.

1.2 Spectroscopy Techniques

1.2.1 Raman Spectroscopy

Compared to other characterization tools, Raman spectroscopy provides a quick, convenient, nondestructive and noninvasive method for characterizing the 2D materials with high selectively for the interior layers. (*121–124*) Measurements can be made at room temperature and at ambient pressure without complicated sample preparation processes. Figure 1-10 shows the typical Raman spectra of MoS_2 and BP. Raman scattering involves the inelastic scattering of the incident light in a material, where the energy of the scattered light either decreases by exciting an elementary excitation of the solid material (i.e. a phonon) or increases by absorbing a phonon. Raman spectra give the intensity of the scattered light as a function of the energy shift from the incident light (Raman shift). The typical accuracy of measurements of Raman spectra is 1 cm^{-1} (~0.1 meV) which is sufficient for measuring the interlayer interaction (several meV) of TMDs. Raman spectroscopy has been widely used and has become a standard characterization technique for TMDs, graphene and other atomic layer materials. (*122*)

There are several advantages of using Raman spectroscopy for the characterization of low dimensional materials, including 2D TMDs. (*125*, *126*) One reason is that the electronic density of states (DOS) has a so-called van Hove singularity, (*122*) which leads to a strong Raman feature when the photon energy is matched to the van Hove singularity of the DOS for each layer. This special case is known as resonance Raman scattering. If we have many laser sources available for an experiment and if we measure the Raman intensity as a function of laser energy (that is called a Raman excitation profile), we can see this resonance Raman effect clearly by probing the van Hove singularity. (*127*) By using resonance Raman spectroscopy, we can thus obtain not only phonon frequency information for each material but also electronic energy band information which is sensitive to the strain in the materials. (*128*) In addition, by changing the laser excitation energy, we can selectively distinguish each layer of

different layered materials, as they have different characteristic resonant conditions, thereby gaining deeper understanding of the physical principles that are involved.

The second advantage is that more specific selection rules predicted from the group theory applicable to the particular optical transition can be applied to many TMD layered materials with lower symmetry compared to graphene. In this way, differences in symmetry distinguish the spectral features of a particular TMD layer from another. Furthermore, by focusing the laser light in a confocal optical microscope, we can measure a high spatially resolved Raman signal (about one micron). By scanning focused laser light on the TMDs, we can get Raman imaging maps (*129, 130*) which could provide detailed information about the characteristic defects of the particular crystal structure over a relatively large area in comparison to high-resolution transmission electron microscope studies. Therefore, added information may often be efficiently obtained by using multiple techniques on an individual grown sample or on a specially grown group of samples, specially designed to study a particular effect.

In addition, in the optical transitions involved in the Raman process, the optical dipole selection rule restricts the possible electronic transitions and the possible Raman-active phonon modes, which could be sensitive to the number of atomic layers and to the laser polarization direction. (*68, 87*) In this thesis, some examples of 2D materials will be shown, in which we demonstrate how to analyze the Raman spectra combined with theory, and with other complementary experimental probes, as appropriate.

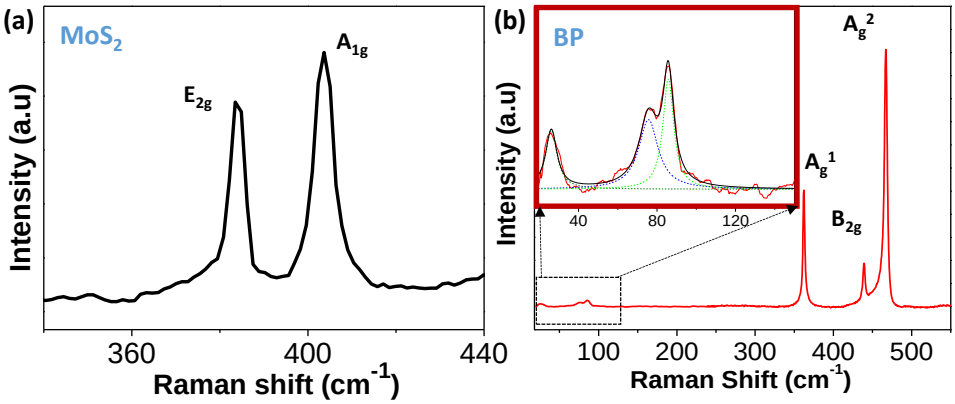

Figure 1-10. Raman spectrum of (a) MoS_2 and (b) BP. Inset of BP is the zoom-in of low-frequency range of BP Raman spectrum. The symmetry assignments of the Raman modes are also labelled.

1.2.2 Photoluminescence Spectroscopy

Photoluminescence (PL) describes the radiative emission of materials after excitation of light. Many of the 2D materials, including TMD, BP, GaTe, has strong PL emission, and the peak position of PL spectrum is at the exciton emission energy, which equals the difference of direct bandgap and exciton binding energy. Therefore, PL can be an important way to characterize the material properties of light emission and excitons/doped excitons.

In a typical PL spectrum of monolayer MoS_2, for example, three peaks are observable: the A peak, A^- peak, and B peak, representing the MoS_2 excitons, trions, (*131*) and excitons due to spin-orbit splitting in the valence band, (*132*) respectively. These peaks are located at around 1.90 eV, 1.86 eV and 2.05 eV, (*42*, *131*) respectively. Compared to bulk materials, monolayer MoS_2, as well as in other transition metal dichalcogenides (TMDs), has more stable excitons, whose binding energy is as high as ~0.9 eV, (*59*, *133*) because of the strong Coulomb interaction between the electrons and holes due to the quantum confinement effect. (*42*, *59*, *134*) Under a high carrier density, an exciton can be bound to an electron easily to form a trion. Trions provide an important means to study many-body interactions, (*131*) but they are rarely observed in conventional semiconductors because of their unstable existence. (*135*, *136*) However, trions in monolayer MoS_2 can exist stably

with a binding energy of about 20 meV. (*131*, *137*, *138*) It has been reported that trions can be controlled by optical, (*131*) electronic (*131*, *139*) or chemical (*140*) methods, including intensity change and energy shift. Trions are affected by factors such as electron density, Coulomb interaction and energy band structure, and these factors can be effectively applied to atomic-thin MoS_2 and other TMDs, making them important materials for tunable photonic devices.

1.2.3 Optical Absorption Spectroscopy

Optical absorption spectroscopy also describes the material characters to interact with light, and is directly related to electron-photon interaction in the materials. Optical absorption in the visible to UV range with large spot size can be achieved using UV-visible spectrometer. However, for exfoliated 2D materials, the flake size is typically much smaller than the beam size. In this case, microscope with focused white light is required to achieve the absorption spectroscopy.

In the example of measuring the optical absorption spectra of exfoliated BP and GaTe, (*68*, *87*) the absorption spectra were measured using a home-built micro-absorption setup based on a combination of inverted and upright microscopes that were used to focus the incident white light beam onto a BP flake and to collect the transmitted light. The white light was generated using a laser driven light source with fiber optic coupled output (25 μm diameter fiber). A reduced image of the output fiber face on the upper surface of the quartz substrate (spot size ~1.5 μm) was formed using two microscope objectives (a 5x-collimating objective, NA (numeric aperture) =0.1 and a 100x-long working distance objective, NA=0.8 in the inverted microscope). The transmitted light was collected by a 50x-objective (NA=0.5) in the upright microscope and analyzed by a spectrometer equipped with a CCD camera. The absorbance (A) was calculated simply as $A=\ln(I_0/I)$ where I_0 and I are the light intensities transmitted through the quartz substrate nearby a BP flake location and through a BP flake, respectively.

1.2.4 Anisotropic Optical Spectroscopy

Since many 2D materials have in-plane anisotropy, it is important to do anisotropic spectroscopy to determine the material properties along different crystal orientations. Such a method can also be used to identify the crystal orientation of 2D materials non-destructively and in-situ, which possesses tremendous advantages compared to the classical transmission electron microscopy (TEM).

To measure polarized spectroscopy, the incident light can be linearly polarized using a linear polarizer, and the scattered/transmitted/reflected light can be filtered with polarization selector. Depending on the material symmetries and the specific properties, such as Raman tensor, the spectroscopic signals can vary. Moreover, due to the valleytronics of TMD materials, (*141*) circularly-polarized light can also be used to selectively excite excitons in certain valleys, and this method is important to study valley and spin-related optoelectronic properties of 2D materials.

Chapter 2 Photoluminescence and Raman Spectroscopies of 2D Materials

In this chapter, the basic photoluminescence and Raman spectroscopies of 2D materials, mainly MoS_2, are introduced. In particular, we focus on PL of twisted bilayer MoS_2 due to its interesting properties and important implication for stacked 2D materials. We also present the effect of substrates and defects on MoS_2.

2.1 PL of Twisted bilayer MoS_2

To develop a good photonic device based on MoS_2, the tunability of the optical features of the material is important. Currently, the PL emission of MoS_2 can be tuned in several ways, such as chemical doping, (*53*, *138*, *140*) electrical doping, (*139*) changing temperature, (*142*, *143*) strain engineering, (*144*) alloying, (*145*) etc. Here, considering the transformation of the direct to indirect band gap from monolayer to bilayer MoS_2, the interlayer coupling between the two MoS_2 layers should play an important role in the change of the band structure, and consequently, the change of the PL emission. This argument implies that twisted bilayer MoS_2 is a promising system for tuning the PL emission. While the monolayer MoS_2 has been intensively studied, (*41*, *42*, *44–46*, *48*, *131*) the optical properties of bilayer MoS_2 lack detailed exploration. F. Crowne et al. (*132*) found that the energy of the bilayer MoS_2 A^- peak is blue shifted compared to that of the corresponding monolayer. However, the detailed relation of the A^- peak profile and the bilayer configurations has not yet been explored in the MoS_2 system, even though extensive

investigations have been carried out on the twisted bilayer graphene system, (*146–152*) where it has been found that different twisted patterns render different optical and electrical properties due to the change of the energy band structure with different interlayer couplings. In this work, (*52*) the PL profiles in different bilayer MoS_2 configurations were studied using monolayer MoS_2 grown by chemical vapor deposition (CVD). By selectively positioning one layer of MoS_2 onto another layer, we found that by tuning the bilayer twisted angle, the PL emission can also be tuned. Different twisted angles result in different PL emission energies and intensities, and furthermore the relative intensities and energies of the A^- and A peaks. With a systematic study of the relation between the PL emission and the twisted angles, we found that the interlayer coupling plays an important role in changing the interlayer distance and the electronic properties of the twisted bilayer MoS_2. This study leads to an enhancement of the understanding the bilayer energy band structure and interlayer coupling of MoS_2.

To construct the bilayer MoS_2 with different twisted-angles, the sample preparation has two important issues that need to be considered: how to stack the bilayer MoS_2 together, without any interlayer residue, and how to determine the twisted angle (θ) between the two layers. For the first issue, a dry-transfer process was developed and is depicted in Figure 2-1(a). The process starts with CVD MoS_2 flakes on a SiO_2/Si substrate. The chip was cut into two pieces as the bottom and the top MoS_2 layers. The chip with the top layer was spin coated with diluted 4.5% poly(methyl methacrylate) (PMMA) to protect the monolayer MoS_2 flakes. Then potassium hydroxide (KOH) solution was used to etch the SiO_2/Si substrate. The PMMA-MoS_2 film was then put upside-down on a poly dimethyl-siloxane (PDMS) elastomer attached to a glass slide. After baking the composite at 130 ℃, the glass slide was placed under the microscope with the MoS_2 layers at the bottom. The bottom MoS_2 flakes on the SiO_2/Si chip were placed under the glass slide, and the two layers of MoS_2 could be stacked together with various twisted angles. The glass slide was lowered to contact the bottom layer and then carefully raised to remove PDMS. The PMMA was removed by annealing the bottom layer chip in an Ar atmosphere in 400 ℃ for 3 hours. In this dry-transfer process, PMMA was not introduced between the two layers. Thus, the

coupling between the two MoS_2 layers is strong and without interference from a foreign substance.

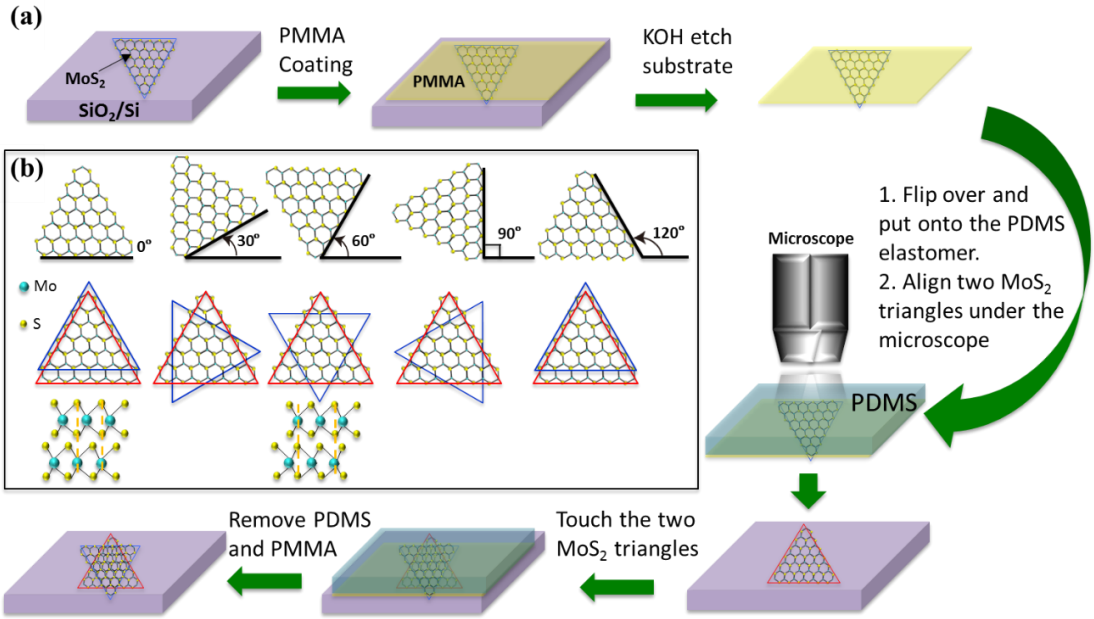

Figure 2-1. (a) The transfer process for the MoS_2 bilayer. (b) Bilayer MoS_2 configurations of $\theta = 0^o$, 30^o, 60^o, 90^o, and 120^o. The 120^o configuration is identical to 0^o. Red and blue triangles indicate the bottom and top MoS_2 layers, respectively. All triangle flakes in the figure are S-terminated zigzag edges. In the real samples, if the triangle edges of the top and bottom flakes are different (one layer is S-terminated and the other is Mo-terminated), then 60^o should be added to the twisted angle value. Side views of 0^o and 60^o bilayers are shown below the corresponding top views.

For the second issue, i.e., determining the twisted angle, an easy method providing a direct observation of the twisted angle was used. In this work, the twisted angle is defined as the angle that the bottom flake rotates counter-clockwise to match the orientation of the top flake. Under this definition, natural bilayer MoS_2 has a 60^o twisted angle. This definition takes into consideration the PL difference between the top and bottom layers. This is valid because the top layer was transferred onto the as-grown bottom layer, and the mechanical and chemical environmental change might result in a slight change in the PL

properties. Figure 2-1(b) illustrates the bilayer configurations with θ = 0º, 30º, 60º, 90º, and 120º. Due to the periodic character of the twist, the 120º configuration is identical to θ = 0º . The side-views of the natural θ = 60º and θ = 0º bilayers of MoS_2 are also displayed under the corresponding top views. When θ = 60º, the top layer Mo (S) atoms align vertically with the bottom layer S (Mo) atoms. In the real samples, the initial value of the twisted angle was determined by observing the alignment of the two triangles. Then the edge profiles (Mo- or S-terminated zigzag) of the bottom and top triangles were determined using the result described by A. van der Zande et al.,(*153*) and the twisted angle values had 60º added to them, if the top and bottom layers had different edge profiles. The accuracy of the determined twisted angle is within 2º.

The characterization results of a bilayer MoS_2 prepared using the dry-transfer method are shown in Figure 2-2. The optical image in Figure 2-2(a) shows that the two MoS_2 monolayers were stacked successfully with a twisted angle of 51.5º. (The top and bottom layers are marked by the blue and red triangles, respectively.) The monolayer and bilayer regions can be readily distinguished under an optical microscope. The top layer has been well-preserved because the transferred MoS_2 appears clear and uniform. Figure 2-2(b) is the atomic force microscope (AFM) image and its height profiles of the corresponding regions are marked by the green, red, and blue lines, displayed in Figure 2-2(c). The height profiles show that the step height of the SiO_2/Si surface and the bottom CVD MoS_2 is about 2.1 nm, and that of the bottom and top layer MoS_2 is about 0.9 nm, which is close to the thickness of monolayer MoS_2. The height profiles verify that the interlayer region is PMMA-free. From Figure 2-2(d), it is clear that the Raman intensity is high in the bilayer region and approximately one half in intensity in the bottom layer (monolayer) region. The frequency difference between the E_{2g} and A_{1g} Raman modes is 21 cm^{-1} in the monolayer region and 22 cm^{-1} in the bilayer region. This frequency difference of the monolayer region suggests a good quality of the CVD MoS_2, and the top layer and the bilayer frequency difference values indicate a good preservation of the MoS_2 quality during the transfer process.(*154–157*) In addition, a Raman peak at around 464 cm^{-1} was observed on the bilayer regions, indicating the good interlayer coupling in our bilayer MoS_2 sample.(*158*) In contrast to the intensities of the E_{2g} and A_{1g} Raman modes, the PL intensity is low in the

bilayer region compared to that of the monolayer region, as shown in Figure 2-2(e). Raman and PL mapping of the whole region further confirms the observation, as shown in Figure 2-2(f) and (g). Mapping of the integrated intensity of the E_{2g} and A_{1g} peaks is shown in Figure 2-2(f) where it is found that the bilayer region is much brighter than the monolayer regions. In Figure 2-2(g), however, mapping of the integrated intensity of the PL peaks shows that the bilayer region is much darker than the monolayer regions: the A and A^- peak intensities on the bilayer region are only 23% and 6% of those on the bottom layer region, respectively. In addition, the relative intensity of the A^- and A peaks varies in the bilayer and bottom monolayer regions, which is 0.67 on the bilayer and 2.56 on the bottom layer regions. From the bottom layer to the bilayer region, the A, A^- and B peak energies are blue shifted by 13.8 meV, 3 meV and 43.4 meV, respectively.

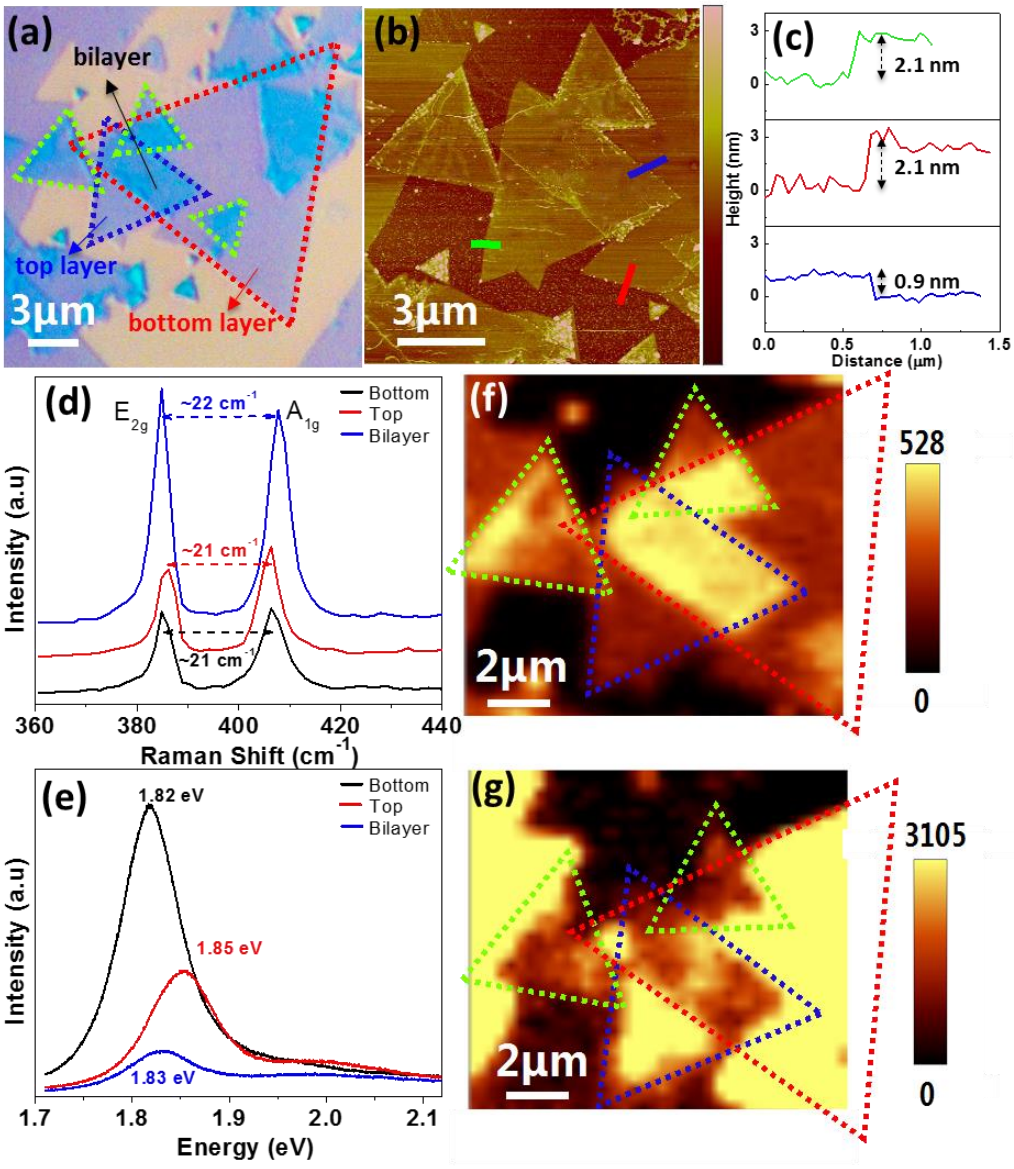

Figure 2-2. A twisted bilayer MoS_2 flake without PMMA between the two layers. The twisted angle is $\theta = 51.5^{o}$. (a) Optical microscope image of the bilayer MoS_2. Dashed triangles outline the MoS_2 flakes. The red triangle is the bottom layer and the smaller blue triangle is the top layer. Green triangles also indicate top layer flakes, but they are not selected here to study the optical properties. The regions of the bottom monolayer, top monolayer and bilayer are marked with arrows. (b) AFM image of the twisted bilayer MoS_2. Color bar: 18 nm. (c) Height vs. distance profiles of the green, red, blue lines in (b), respectively. (d) Raman spectra and (e) PL spectra of bottom, top layer and bilayer regions.

In (d), for convenience, the notations E_{2g} and A_{1g} are kept in twisted bilayer MoS_2, even though the symmetry is different from D_{3h} for monolayer MoS_2. (f) Mapping of the Raman integrated intensity (E_{2g} and A_{1g} peaks). (g) Mapping of the PL integrated intensity. Intensity color bars are shown at the right of (f) and (g).

Furthermore, we found that the variation of the PL from bilayer MoS_2 depends on the twisted angle. Figure 2-3 presents PL (Figure 2-3(a)) and Raman (Figure 2-3(b)) spectra for three bilayer regions with different twisted angles: θ=17.7º, 51.5º, 84.7º. It is apparent that their Raman spectra are similar: bilayer regions have about twice the Raman intensities of the monolayer regions. However, the PL spectra of the three bilayers are much different. This indicates that the bilayer PL profile varies with different bilayer twisted angles. In this work, a total of about 40 bilayer flakes with different twisted angles were measured to study the relation between the PL emission and bilayer twisted angles.

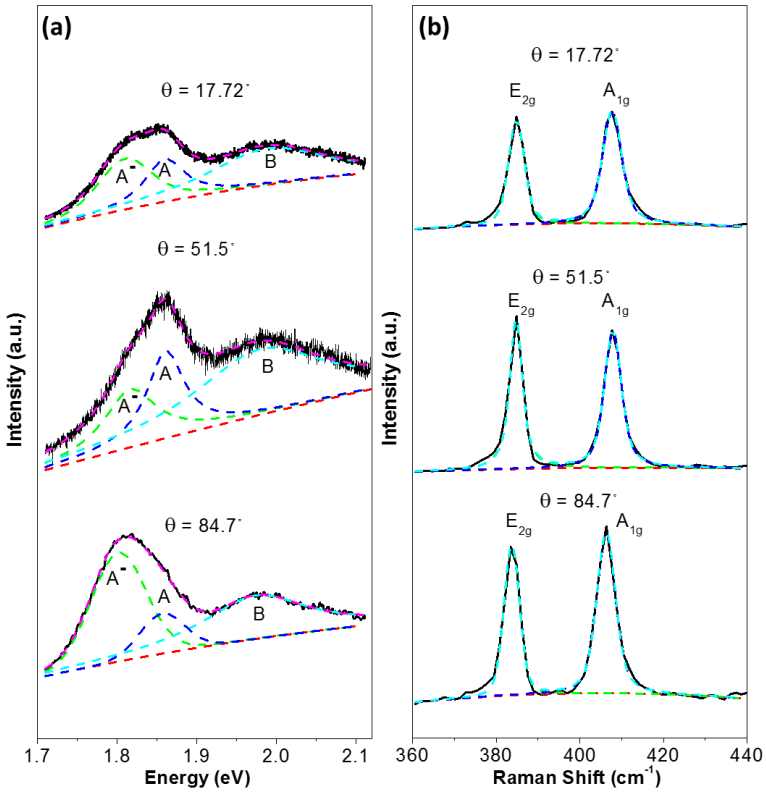

Figure 2-3. (a) PL spectra and (b) Raman spectra of the MoS_2 bilayer regions with $\theta =$ 17.7º, 51.5º, and 84.7º, respectively. All spectra are normalized by the average of the A_{1g} peak intensities on the bottom and top monolayers.

First, the intensity relations of the A and A^- peaks for different twisted angles were studied. In Figure 2-4(a), the intensity ratio of the A^- and A peaks in the bilayer region is normalized by the value for the bottom layer region, i.e., $R = \left(\frac{I_{A^-,BL}}{I_{A,BL}}\right) / \left(\frac{I_{A^-,BotL}}{I_{A,BotL}}\right)$. Here $I_{A,BL}, I_{A^-,BL}, I_{A,BotL}, I_{A^-,BotL}$ mean the PL intensities of the A exciton and A^- trion on the bilayer region, and the A exciton and A^- trion on the bottom layer region, respectively. This intensity ratio R eliminates the influence of the variation of the A and A^- peak ratio in the monolayer introduced from the CVD growth process itself. As shown in Figure 2-4(a), the ratio R exhibits an oscillatory behavior as a function of the twisted angle. The curve for the ratio R vs. θ is approximately symmetric with respect to the twisted angle of 60º, which is consistent with the symmetric nature of the D_{3h} crystal structure of monolayer MoS_2. The slight departure of the symmetry mainly results from the variations in the CVD MoS_2 material itself in different regions on the SiO_2/Si substrate, or from the noise that may be related to defects introduced by the transfer process, which results in slight changes of the MoS_2 structure quality. The maximum intensity ratio peaks appear at $\theta \approx$ 0º, 60º and 120º (=0º), and minima exist in the vicinities of 30º and 90º. Such an angle dependence of the intensity ratio suggests that the interlayer couplings for $\theta =$ 30º and 90º may be distinctly different from the interlayer couplings at $\theta =$ 0º and 60º, as confirmed by our first-principles density functional theory (DFT) calculations (Figure 2-5). The calculated bilayer separation relative to the 60° separation d-d_{60} is shown as a function of the twisted angle in Figure 2-5(c). Compared to the 60° configuration, the interlayer separation is increased by 0.35 Å at θ = 30° and 90°, while it is not significantly changed at θ = 0°. Hence, the interlayer coupling reaches the maximum at θ = 0° and 60°, and the minimum at θ = 30° and 90°. The smaller distances yield the largest van der Waals cohesion and it

follows that the 0° and 60° bilayer MoS_2 have the lowest ground-state total energies and are the most stable.

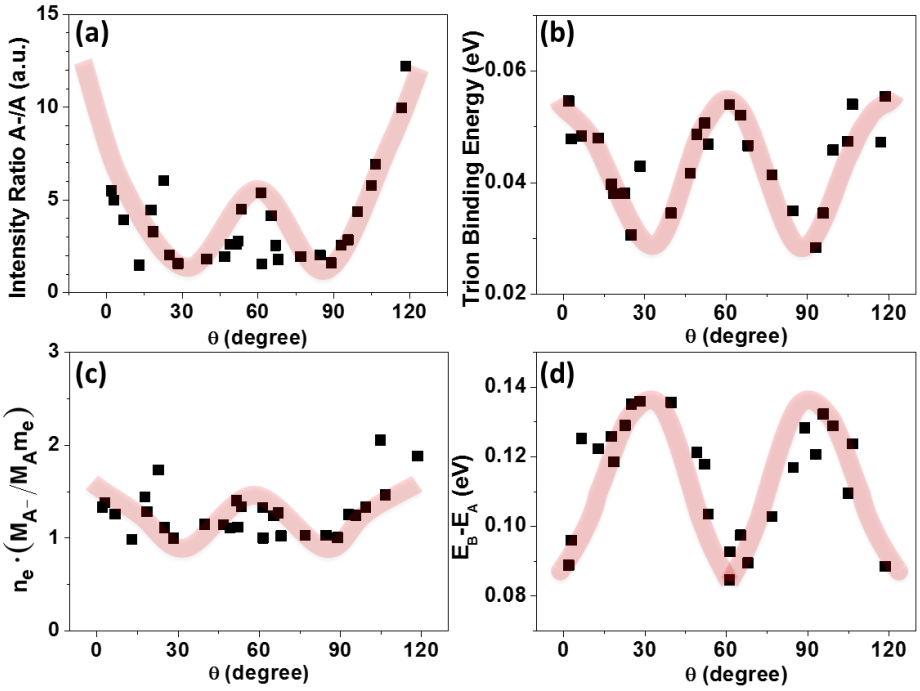

Figure 2-4. Twisted angle dependence of the: (a) A^- trion to A exciton PL intensity ratio, (b) trion binding energy ε_{A^-}, (c) $n_e \cdot \frac{M_{A^-}}{M_A m_e}$ normalized by the value at $\theta = 30^o$, (d) PL peak energy difference between the B and A excitons. The black solid squares are experimental data points and the pink solid lines show the changing trend of each parameter.

In order to support the hypothesis that the interlayer coupling contributes to the PL spectra with different twisted angles, a control sample of bilayer MoS_2 with PMMA sandwiched between the layers was prepared using the wet-transfer method. In this sample preparation method, PMMA was spin coated on the top MoS_2 layer, and its SiO_2/Si substrate was etched by KOH to isolate the top MoS_2 layer. The bottom MoS_2 chip was also spin coated with PMMA and was used to fish out the top MoS_2 film from water.

PMMA on the bottom layer was used to prevent the peeling and degradation of the MoS_2 layer in water. (*159*) Thus the top MoS_2 layer was placed on the bottom layer with PMMA in between. The PMMA in between was hard to thoroughly clean by the following annealing process, which was used to clean the PMMA on the top of the bilayer MoS_2. For a bilayer of MoS_2 with PMMA between the top and bottom MoS_2 layers, the Raman intensity of the bilayer region is almost twice as high as that of the monolayer region. Similarly, for the PL, it is observed that the bilayer PL intensity is about twice stronger than that for the monolayer. Moreover, a slight peak splitting is also found in the bilayer PL spectra. Compared to the PMMA-free bilayer, the one with PMMA in between has similar Raman spectra but different PL spectra. The control experiment indicates that the interlayer coupling plays a more important role in the PL emission of the twisted bilayer MoS_2 than for the Raman spectra. More specifically, the interlayer separation is large in the presence of PMMA between the two layers, resulting in a small or even negligible interlayer coupling. Therefore, the bilayer PL spectrum is roughly the sum of the two monolayer PL spectra. In the case of the PMMA-free twisted bilayer, the interlayer coupling is strong, resulting in a similar behavior to that found in natural bilayer MoS_2. This is also an indication that the p_z orbitals of the S atom extend far beyond the MoS_2 monolayer and play major roles in the energy band structure. The p_z orbitals of the top and bottom layers mix, which leads to a rearrangement of the electronic band structure and a corresponding change in the PL spectra. (*49*, *59*)

From the PL spectra of twisted bilayer MoS_2 without PMMA in between, some important features of the energy band structures and interlayer couplings are revealed. Compared to monolayer MoS_2, the twisted bilayer MoS_2 has only approximately one fifth to one eighth the PL intensity, possibly due to the charge transfer between the two layers, or to the change from a direct to an indirect bandgap semiconductor as the number of layers increases. (*49*) While the charge transfer effect may not be strong in the homojunction, the direct to indirect bandgap change could be the main cause for the low PL intensity in bilayer MoS_2. (*65*) Our DFT calculations also confirm that the twisted bilayer MoS_2 has indirect bandgap, which varies with twisted angles (Figure 2-5(b) and (d)). Among the bilayer MoS_2 samples, distinct PL spectra were observed for different twisted angles. Besides the

change in A^-/A intensity ratio shown in Figure 2-3(a), we also observed the change in trion binding energy with twisted angles. For the undoped and ungated twisted bilayer MoS_2 sample without PMMA, the binding energy of the trions can be identified with the PL emission energy difference between the A and A^- peaks. (*131*, *138*, *139*) This energy difference changes with the bilayer twisted angle as well, as shown in Figure 2-4(b): it is a maximum at $\theta = 0^o$, 60^o and 120^o, and a minimum around 30^o and 90^o. The curve in Figure 2-4(b) shows oscillatory and periodic features with a ~60^o period, consistent with the symmetry of the D_{3h} crystal structure of monolayer MoS_2. At $\theta = 60^o$, the trion binding energy is 47 ± 3 meV, and at $\theta = 30^o$ and 90^o, the trion binding energy reaches the minimum of approximately 28 ± 2 meV.

The changes of A^- and A PL peaks shown in Figure 2-4(a,b) suggest the change in interlayer coupling of bilayer MoS_2 with different twisted angles. In the steady state, the A^-/A intensity ratio displayed in Figure 2-4(a) can be expressed as

$$\frac{I_{A^-}}{I_A} = \frac{\Gamma_{A^-} N_{A^-}}{\Gamma_A N_A} \qquad \text{Eq. 2-1}$$

where N_A and N_{A^-} are the exciton and trion concentrations, respectively; Γ_A and Γ_{A^-} represent the radiative recombination rates of the exciton and trion, respectively. The radiative recombinations occur mainly at the ***K*** point of the Brillouin zone. These recombination rates have been measured and calculated by J. Ross et al. (*139*) and S. Mouri et al. (*140*) for the monolayer system. According to the mass action law, (*139*) the ratio of the A^- and A concentrations can be expressed as

$$\frac{N_{A^-}}{N_A} = \frac{\pi \hbar^2 n_e M_{A^-}}{4 M_A m_e k_B T} \exp\left(\frac{\varepsilon_{A^-}}{k_B T}\right) \qquad \text{Eq. 2-2}$$

where $n_e, \varepsilon_{A^-}, m_e$ are excess electron concentration, trion binding energy, and electron effective mass at the ***K*** point of the Brillouin zone, respectively; M_A, M_{A^-} are the effective masses of the exciton and the trion. For excitons and trions, we have $M_A = m_e + m_h$ and $M_{A^-} = 2m_e + m_h$ in which m_h is the hole effective mass at the ***K*** point. The conduction band minimum (CBM) at the ***K*** point is mostly composed of d_{z^2} orbitals from the Mo atoms which are sandwiched between two layers of S atoms, and valence band maximum

(VBM) at the ***K*** point is mostly composed of $d_{x^2-y^2}$ and d_{xy} orbitals of the Mo atoms, and all these orbitals are not significantly affected by the interlayer coupling.(*49*, *59*, *60*) It follows that the band edge at the ***K*** point is not sensitive to the interlayer coupling and thus not sensitive to the twisted angle. Further evidence of this effect is provided by our DFT calculations, as shown in Figure 2-5(b) and (d). Since the radiative recombination rates Γ_A and Γ_{A^-} takes place mainly at the ***K*** point, we can assume that Γ_A and Γ_{A^-} for the twisted bilayer MoS_2 do not change much with the twisted angle. Using Eq. 2-1, Eq. 2-2 and the above analysis on recombination rates, we can write

$$\frac{I_{A^-}}{I_A} \propto n_e \cdot \frac{M_{A^-}}{M_A m_e} \cdot \exp\left(\frac{\varepsilon_{A^-}}{k_B T}\right) \qquad \text{Eq. 2-3}$$

This equation indicates that the variations in the A^-/A intensity ratio shown in Figure 2-4(a) could in priniciple have three distinct contributions: differences in (1) excess carrier concentration n_e, (2) effective mass ratio $\frac{M_{A^-}}{M_A m_e}$, and/or (3) trion binding energy ε_{A^-} in bilayer MoS_2 with different twisted angles. Plugging the data of $\frac{I_{A^-}}{I_A}$ from Figure 2-4(a) and ε_{A^-} from Figure 2-4(b) into Eq. 2-3, we obtained an experimental measure of changes in $n_e \cdot \frac{M_{A^-}}{M_A m_e}$ with different twisted angles, as shown in Figure 2-4(c). Here, $n_e \cdot \frac{M_{A^-}}{M_A m_e}$ is normalized by its value at $\theta = 30^o$. It shows oscillatory features with small amplitudes as a function of the twisted angle, reaching the maximum (about 1.38) at $\theta = 0^o$ and 60^o, and the minimum (about 1) at $\theta = 30^o$ and 90^o. To quantitatively reveal the contribution of each factor in Eq. 2-3 to the change of the A^-/A intensity ratio with the twisted angle, we extracted the amplitude of the change in $\frac{I_{A^-}}{I_A}$, $\exp\left(\frac{\varepsilon_{A^-}}{k_B T}\right)$ and $\frac{n_e M_{A^-}}{M_A m_e}$ from 30^o to 60^o. Our analysis indicates that $\frac{I_{A^-}}{I_A}$ increases from 1 to 3.43, $\exp\left(\frac{\varepsilon_{A^-}}{k_B T}\right)$ increases from 1 to 2.58, and $n_e \cdot \frac{M_{A^-}}{M_A m_e}$ increases from 1 to 1.33. Clearly, $\exp\left(\frac{\varepsilon_{A^-}}{k_B T}\right)$ is the major contribution term to the variation of $\frac{I_{A^-}}{I_A}$ with the twisted angle, while both the excess charge (n_e) and effective mass ratio $\frac{M_{A^-}}{M_A m_e}$ have only more modest contributions to the A^-/A intensity ratio. It is worth mentioning that some other factors, such as transitional shift of the bilayer at certain twisted

angles, defects or residues introduced during the sample preparation, PL measurement and fitting uncertainties, might have random contributions to the change of the measured PL features with the twisted angle.

To further discuss the $n_e \cdot \frac{M_{A^-}}{M_A m_e}$ contribution to the A^-/A intensity ratio, we investigated the effective masses by DFT calculations. It shows that m_e and m_h are insensitive to either the twisted angle or the separation distance. It follows that the term of interest $\frac{M_{A^-}}{M_A m_e}$ shows little variation when the twisted angle is changed, shown as blue empty triangles in Figure 2-5(e). It remains in the [0.93,1] range for all considered twisted angles (normalized by its value at $\theta = 30^o$). This is consistent with the observed insensitivity of the energy band at the *K* point to the interlayer coupling. (*49*) Therefore, we can attribute most of the change in the term $n_e \cdot \frac{M_{A^-}}{M_A m_e}$ (Figure 2-4(c)) to the change in excess electron concentration n_e. In Figure 2-5(e), we plotted the intensity ratio $\frac{I_{A^-}}{I_A}$, $\exp\left(\frac{\varepsilon_{A^-}}{k_B T}\right)$, excess electron concentration n_e (from Figure 2-4(c)) and DFT-calculated mass ratio $\frac{M_{A^-}}{M_A m_e}$ at $\theta = 0^o$, 30^o, 60^o and 90^o. It further suggests that besides the major contribution from the trion binding energy, the excess electron concentration n_e is another possible contribution to the change of the A^-/A intensity ratio. Actually, the presence of the A^- peak indicates the presence of an excess carrier concentration of MoS_2. (*131*) Previous works have shown that the PL of MoS_2, especially for monolayer or bilayer, is sensitive to the surrounding medium. (*140*) The doping effect from the SiO_2/Si substrate is usually considered as a major source of excess charge. (*160*, *161*) The excess electrons from the SiO_2/Si substrate might transfer to the twisted bilayer MoS_2 differently, depending on the MoS_2 interlayer coupling. Our DFT calculations in Figure 2-5(c) show that the interlayer distance of MoS_2 at $\theta = 0^o$ and 60^o reaches the minimum of 6.03 Å. This value is 0.35 Å less than the maximum distance at $\theta = 30^o$ and 90^o. Therefore, at $\theta = 0^o$ and 60^o, the interlayer coupling is the strongest with a minimum interlayer distance, so excess electron charges from the SiO_2/Si substrate can more readily transfer into the bilayer MoS_2 films. It follows that the excess electron concentration n_e could reach the maximum at $\theta =$

0º, 60º and 120º. Conversely, at $\theta = 30^{o}$ and 90º, since the interlayer coupling is the weakest with a maximum interlayer separation, the excess charges from the SiO_2/Si substrate could reach a minimum.

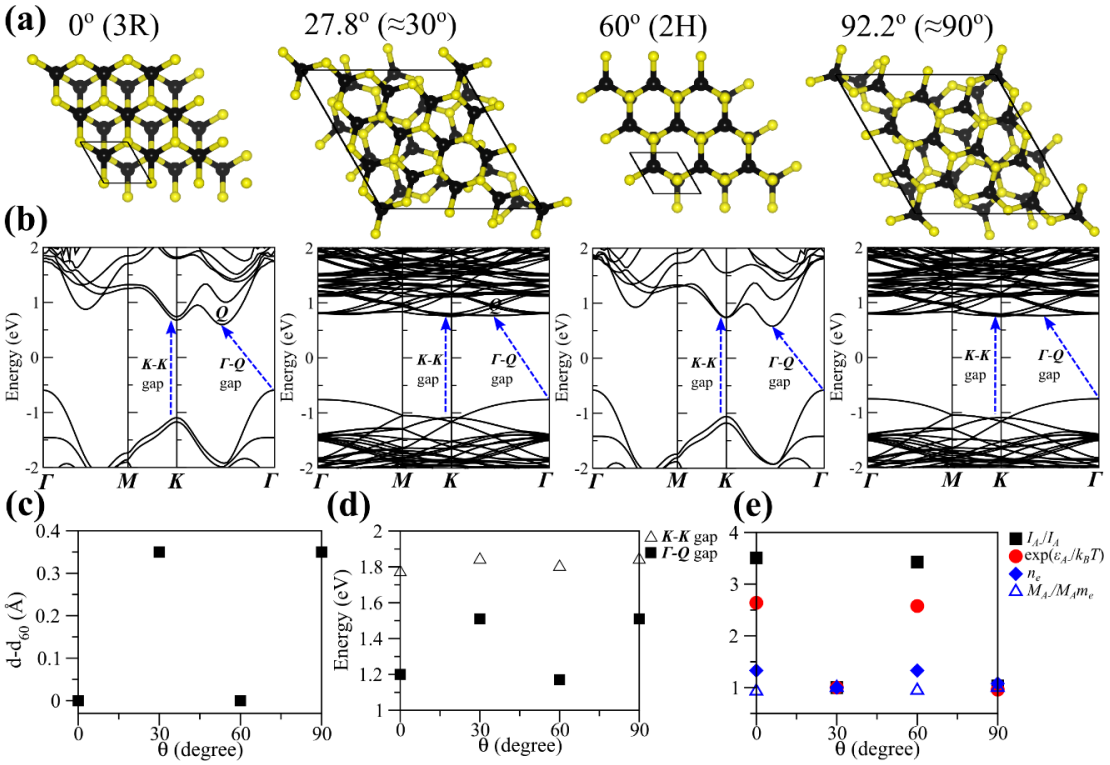

Figure 2-5. (a) Atomic structures of bilayer MoS_2 systems with different twisted angles considered in DFT calculations. Black (yellow) balls correspond to Mo (S) atoms. The black solid line shows the unit cell of an angle and the size of the unit cell varies strongly with the angle. 0° and 60° bilayer systems correspond to the natural crystal forms 3R and 2H with the primitive unit cells, respectively. The unit cells of exact 30° and 90° are extremely large, and thus 27.8° and 92.2° are chosen instead to approximate them. (b) DFT band structures corresponding to systems shown in (a). Both indirect gap between the band extreme Γ and Q and direct gap at K are highlighted by blue dash arrows. (c) The calculated interlayer separation relative to the 60° separation d-d_{60} as a function of twisted angle. (d) Calculated angle dependence of the indirect Γ-Q gap and direct K-K gap. (e) The angle dependence of the experimental intensity ratio $\frac{I_{A-}}{I_A}$, $\exp\left(\frac{\varepsilon_{A-}}{k_B T}\right)$, excess electron

concentration n_e and DFT-calculated mass ratio $\frac{M_{A^-}}{M_A m_e}$ at $\theta = 0^o, 30^o, 60^o, 90^o$. All the data shown in (e) are normalized by their values at $\theta = 30^o$.

One should note that the changing trends of the trion binding energy and the excess electron concentration are the same with the twisted angle. The trion binding energy is the energy required for the removal of one electron from the trion. At $\theta = 0^o$ and 60^o, the excess electron concentration reaches the maximum, making the electron removal (or trion ionization) difficult, and therefore the trion binding energy is largest. At $\theta = 30^o$ and 90^o, the minimum excess electron concentration makes it easier for the electron removal, and hence the binding energy is the minimum. Therefore, the excess electron concentration, n_e, is positively correlated with binding energy, ε_{A^-}, which has also been proved by the change of trion binding energy with Fermi level shift in a previous study. (*131*) The observation that both trion binding energy and the excess electron density reaches the their maxima at $\theta = 60^o$ is also consistent with the fact that the natural $\theta = 60^o$ configuration is the most stable and has the minimum free energy. (*162*) A similar case occurs with the configuration when $\theta = 0^o$, which is also a natural crystal form of MoS_2. Moreover, the change of trion binding energy demonstrates a relation of trion binding energy and interlayer coupling. Monolayer MoS_2, which has no interlayer coupling, shows a trion binding energy of about 18 meV. (*131*) Our results show that at $\theta = 30^o$ and 90^o, where the interlayer coupling is the weakest, the trion binding energy is around 30 meV, and when the interlayer coupling increases, the trion binding energy increases, and reaches the maximum value of about 47 meV at $\theta = 0^o$ and 60^o, where the interlayer coupling is the strongest.

In addition to the angle dependence of the trion intensity and binding energy (Figure 2-4(a,b)), the PL peak energy difference between the B and A excitons E_B-E_A exhibits similar but opposite periodic and oscillatory features with changes in twisted angle, as shown in Figure 2-4(d). Here E_A and E_B are the PL peak energies of the A and B excitons, respectively. At $\theta = 0^o$ and 60^o, where the interlayer coupling is the strongest, E_B-E_A reaches the minimum around 80 meV; at $\theta = 30^o$ and 90^o, where the interlayer coupling is

the weakest, it reaches the maximum of about 140 meV. For monolayer MoS_2, which has no interlayer coupling, E_B-E_A is around 150 meV. Clearly, E_B-E_A is anti-correlated to the interlayer coupling. The PL peak energy difference of the A and B excitons gives information on the valence band splitting

$$E_B - E_A = \Delta - (\varepsilon_B - \varepsilon_A)$$

where Δ is the valence band splitting at the $\boldsymbol{K}$ point, and $\varepsilon_A, \varepsilon_B$ are the binding energies of the A and B excitons. Δ is entirely due to spin-orbit coupling (SOC) for the monolayer MoS_2 and (mostly) due to the interlayer coupling for the bilayer and bulk. (*163*, *164*) A previous theoretical study found that Δ in MoS_2 increases with the number of the layers, (*163*) while another study predicted that the A exciton binding energy ε_A decreases with the number of the layers. (*165*) However, these studies are focused on MoS_2 in its most stable configuration 2H (i.e., $\theta = 60^o$), and the angle tuning effect is not considered. Nevertheless, these studies allow us to infer that Δ, ε_A and ε_B are probably sensitive to the interlayer coupling and thus to the twisted angle. Unfortunately, a quantitative analysis of the exact angle dependence of Δ, ε_A and ε_B is currently practically impossible, since calculations of these quantities for different twisted angles require the concurrent inclusion of SOC, many-electron (*166*) and excitonic effects, etc. At 0º and 60º for which the unit cells have 6 atoms, such calculations are presently possible. (*164*) But at 30º and 90º for which the unit cells constructed contain 78 atom (actually at angles 27.8 º and 92.2º, respectively, and the unit cells for exactly 30º and 90º are even larger), the computational cost grows exponentially, rendering the calculations essentially impossible at the present time. Therefore, a detailed investigation of the angle dependence of Δ, ε_A and ε_B is out of the scope of this work, since we are here mainly focused on the properties of trions. Nevertheless, the observed trend of E_B-E_A in Figure 2-4(d) with the twisted angle is very interesting and might provide another way to study the interlayer coupling of few-layer MoS_2, which could motivate further experimental and theoretical studies.

In conclusion, the PL emission of twisted bilayer MoS_2 is investigated systematically in the present work. The results of the PL emission under various bilayer configurations reveal that the concentration of trions and excitons, and their binding energies change with

the twisted angle between the two MoS_2 layers. Both the A^-/A PL intensity ratio and the trion binding energy show periodic and oscillatory features with the change of the twisted angle, both of which reach their maxima at a twisted angle of 0º (where the two layers are aligned) or 60º (where the two layers have the opposite angular orientations), and reach their minima at 30º or 90º. Combining our experimental observations and DFT calculations, we reveal that at a twisted angle of 0º or 60º, the interlayer coupling is maximized mainly due to the minimized interlayer separation, and the change of the A^-/A PL intensity ratio is mainly attributed to the change of trion binding energy with the twisted angle. In addition, the twisted angle dependence of E_B-E_A is investigated, which is the opposite to that of the A^-/A PL intensity ratio and the trion binding energy. These results are useful for the study of the interlayer coupling of few-layer MoS_2, and therefore provide guidelines for the practical design and application of optoelectronic devices based on MoS_2.

2.2 Substrate Effect of MoS_2: Raman, PL and Photoelectron Spectroscopies

As a material with an extra-large surface-to-bulk ratio, single layer MoS_2 is highly conducive to forming defects. (*167*) The defects in MoS_2 play an essential role in tuning the properties of single layer MoS_2 in various ways, and so, affect the performance of devices based on MoS_2. They can, for example, enhance the electrochemical activity, (*168*, *169*) and tune the electronic, (*170*) magnetic (*171*) and optical (*172*) properties of MoS_2. For example, in electrochemical applications, recent experiments and theories (*168*, *169*, *173*) show that S-vacancies in the basal plane of MoS_2 can activate the catalytic reactivity of MoS_2. By introducing S-vacancies and suitable strains in single layer MoS_2, Li *et al.* (*169*) achieved the highest activity so far for the hydrogen evolution reaction (HER). In terms of electronic properties, on the other hand, defects in MoS_2 prepared using CVD method, such as vacancies, dislocations and grain boundaries reduce the electronic mobility in MoS_2 by several magnitudes compared to exfoliated MoS_2 from single-crystal bulk. (*170*) Regarding optical properties, Tongay *et al.* (*172*) experimentally demonstrated that

S-vacancies induce new PL peaks and enhance the PL intensities. In magnetics, Han *et al*. (*171*) reported ferromagnetic effects resulting from vacancies in MoS_2.

Although the role of MoS_2 defects in altering the properties has been widely recognized, there are still open questions at a deeper and mechanistic level for connecting the presence and type of defects to electronic, optical and catalytic characteristics. For example, only S-vacancies were considered in activating the MoS_2 basal plane to enable the HER, while other types of defects, such as Mo-vacancies, have not been studied in detail. (*168, 169*) Moreover, CVD MoS_2 shows n-type electronic conductivity. (*174*) Qiu *et al*. (*175*) and Ugeda *et al*. (*176*) believed that this phenomenon is caused by the S-vacancies and by the resulting defect donor states in MoS_2. However, Komsa *et al*. (*177*) found through first principles calculations that, the S-vacancies form acceptor states rather than donor states in the MoS_2 energy bands. Therefore the n-type conductivity in CVD MoS_2 remains elusive despite the fact that S-vacancies are the most common defects in MoS_2 prepared by the CVD process. Recently, Yu *et al*. (*178*) proposed that the donor states in polycrystalline MoS_2 stem from defect complexes made of a dislocation and two S-vacancies.

To understand the role of defects in MoS_2 functionality, in this work, we systematically assessed the impact of defects on the electronic structure of single layer (SL) MoS_2 model system on several different substrates. The single layer MoS_2 used in our study was prepared through CVD synthesis. (*179*) The substrate layer beneath the MoS_2 layer were Au, single layer (SL) boron nitride (BN)/Au, SL graphene (SLG)/Au and CeO_2/Au. Methods commonly used to create defects in MoS_2 in literature included vacuum thermal annealing, (*172*, *175*, *180*) electron irradiation, (*167*, *170*) plasma treatment, (*168*) Se insertion, (*181*) and ion irradiation. (*172*, *182–188*) In this work, we introduce defects in SL-MoS_2 by both thermal annealing in vacuum and Ar^+ ion irradiation. (*189*) While both ways to create defects have been used in previous works, here we reveal the electronic structure induced by defects formed in those ways. The presence of defects in MoS_2 was confirmed by X-ray photoelectron spectroscopy (XPS), as well as Raman and photoluminescence (PL) spectroscopies. Both XPS and scanning tunneling microscopy/spectroscopy (STM/STS) showed that the defects in the MoS_2 can change the

electronic energy levels in MoS_2 and introduce defect states in the bandgap. Raman and PL spectroscopies can be sensitive and convenient tools to probe the defects in MoS_2. The presence of defect states within the bandgap was observed using STS, which is likely to be associated with defects including S-vacancies and Mo-vacancies and match well with our molecular dynamics (MD) and density functional theory (DFT) simulations. In addition, the reduction in the oxide substrate (CeO_2) during annealing was also found to change the band alignment between MoS_2 and the substrate, showing that thermal annealing can also alter the electronic energy levels of MoS_2 by choosing the suitable substrates. We also demonstrated that the introduction of defects by ion irradiation can effectively enhance the HER activity. Our work, therefore, provides a detailed electronic structure description of defected MoS_2 on various substrates, and demonstrated that introducing defects can be an effective method to tune the functionality of 2D materials.

Single layer MoS_2 forms a hexagonal lattice structure from the top view, and has three sub-layers of atoms, one layer of Mo atoms sandwiched between two layers of S atoms (Figure 2-6(a)). (*42*, *52*) Figure 2-6(a) also shows the structures studied in this work, and the processes of thermal annealing and ion sputtering. First, we look at the impact of thermal annealing on the electronic structure of single layer MoS_2 on various substrates. XPS measurements were performed on the MoS_2 samples on different substrates after transfer and after annealing at 300 ℃ and 450 ℃ under 10^{-10} mbar base pressure. Peaks of all the elements can be easily observed and are labeled, including Mo 3p, Au 4d, C 1s, Mo 3d, S 2p and Au 4f. We mainly study the Mo $3d_{5/2}$ peak position relative to the Au $4f_{7/2}$ peak. A change in this relative position is indicative to charge transfer between MoS_2 and Au (Figure 2-6(b)). We define ΔE as the binding energy difference between the Au $4f_{7/2}$ and Mo $3d_{5/2}$ electrons (labeled in Figure 2-6(b-c)), and thus, ΔE is a measure of the energy level shifts in MoS_2.

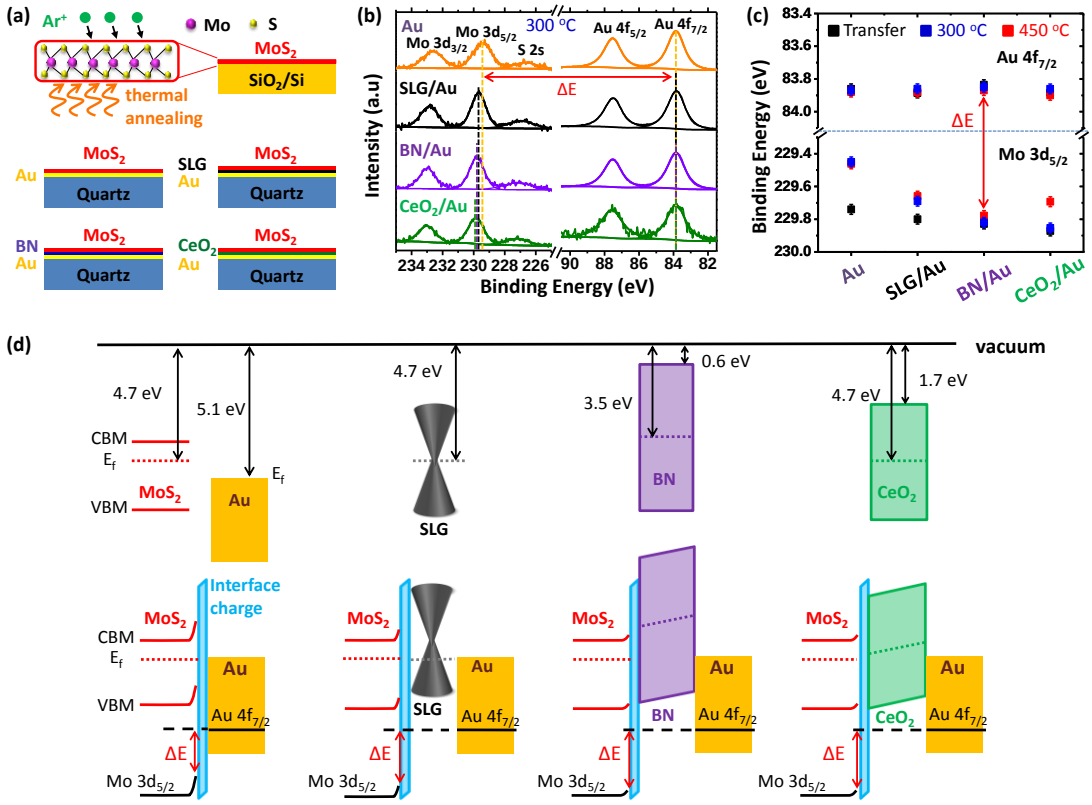

Figure 2-6. Illustration of MoS_2 on various substrates and XPS characterization. (a) Four structures studied in this work: MoS_2/Au, MoS_2/SLG/Au, MoS_2/BN/Au and MoS_2/CeO_2/Au. All the structures are supported by mica or quartz substrates. The MoS_2 single layers in all these structures are transferred from CVD grown MoS_2 on Si/SiO_2 substrate. Vacuum thermal annealing or Ar^+ irradiation is used to treat the samples to either enhance the contact with substrates or produce defects. (b) XPS traces of the Mo 3d and Au 4f peaks of MoS_2 on the four substrates: Au, SLG/Au, BN/Au and CeO_2/Au. All samples are measured after vacuum annealing at 300 ℃ under 10^{-9} mbar. The dashed vertical lines illustrate the binding energies of Mo $3d_{5/2}$ and Au $4f_{7/2}$ electrons. (c) Binding energies of the Mo $3d_{5/2}$ and Au $4f_{7/2}$ for the four samples after transfer and vacuum annealing at 300 ℃ and 450 ℃. The red arrow illustrates ΔE. (d) Illustration of the energy band alignment for the four samples. The upper four graphs show the materials before contact, and the lower four show the samples after good contact between MoS_2 and the substrates, and the band bending effects are shown. Here valence band maximum (VBM), conduction band minimum (CBM) of MoS_2, Fermi levels (E_f) of MoS_2 and Au are labeled.

For MoS_2 transferred on to different substrates, the Au $4f_{7/2}$ has almost no variation in binding energy (Figure 2-6(b-c)). In contrast, Mo $3d_{5/2}$ has different binding energies depending on the substrate, as seen in Figure 2-6(c). The Mo $3d_{5/2}$ peak is at 229.74 eV for MoS_2/Au after transfer (prior to annealing), but shifted to higher binding energies by 0.06, 0.08 and 0.13 eV for MoS_2/SLG/Au, MoS_2/BN/Au and MoS_2/CeO_2/Au, respectively, as shown with black squares in Figure 2-6(c). The different binding energy of Mo $3d_{5/2}$ electrons is attributed to the different band alignments between MoS_2 and the substrates. The mechanism of this phenomenon is illustrated in Figure 2-6(d). Au has an electron affinity of 5.1 eV, larger than MoS_2 (4.7 eV). (*190–192*) Therefore, when MoS_2 is in contact with Au, electron transfer between the two materials occurs to maintain equilibrium of electron chemical potential. Since Au is a metal and has an abundance of electrons, the Fermi level of the semiconducting MoS_2 decreases to align with the Fermi level of Au. This induces upward band bending of MoS_2 near the contact plane with Au (Figure 2-6(d)), and decreases the binding energy of the Mo $3d_{5/2}$ state. The blue parallelogram shows the interface charge (*193*) which contributes a potential drop between MoS_2 and Au in Figure 2-6(d). When there is a layer of graphene inserted between MoS_2 and Au, graphene is in direct contact with Au and can become p-doped due to the smaller electron affinity of graphene than Au. The graphene layer also contributes to the potential drop, thus the band bending in MoS_2 is weaker than for the case only with Au substrate. Since the energy states for the bound electrons (Mo $3d_{5/2}$ electrons) in MoS_2 follow the same trend as in the conduction and valence bands, the binding energy of Mo $3d_{5/2}$ electrons on the MoS_2 surface increases with the insertion of the graphene layer, resulting in a larger ΔE in MoS_2/SLG/Au compared to MoS_2/Au. hBN and CeO_2 substrates are insulators and thus contribute to more potential drop, resulting in even weaker band bending in MoS_2. Therefore, the Mo $3d_{5/2}$ binding energy at the MoS_2 surface is further increased. These results importantly indicate that SLG, BN and CeO_2 can be effective media to partially screen interface charge, which is ubiquitous at the interface of MoS_2 and many metals. (*193*) Therefore, these substrates can facilitate the applications of electronic devices based on MoS_2.

Annealing at 300 ℃ in vacuum increases the variation of ΔE (Figure 2-6(b-c)) among the different substrates. As can be seen by data (blue squares) in Figure 2-6(c), the binding energy of Au $4f_{7/2}$ remains the same after thermal annealing. Upon annealing at 300 ℃ and compared to the as-transferred states, Mo $3d_{5/2}$ shifts to even lower binding energies on MoS_2/Au and MoS_2/SLG/Au, while the Mo $3d_{5/2}$ remains almost unchanged on MoS_2/BN/Au and MoS_2/CeO_2/Au. The removal of water or gas residues between MoS_2 and the substrates and a better contact between MoS_2 and the substrates (*194*) after annealing at 300 ℃ is a likely reason for these changes. Hence the charge transfer process between MoS_2 and Au or between MoS_2 and SLG/Au was facilitated by thermal annealing, resulting in a larger band bending, larger energy shifts in the Mo $3d_{5/2}$ peaks and smaller ΔE values. The difference between ΔE for MoS_2/Au and MoS_2/CeO_2/Au is 0.4 eV, close to the work function difference between Au and MoS_2. This is consistent with the band bending explanation shown in Figure 2-6(d).

Next, we show further evidence to the charge transfer between MoS_2 and different substrates based on the Raman and PL spectra measured after annealing at 300 ℃. All spectra are normalized by the intensity of the A_1' mode. Note that the notations E' and A_1' are for single layer MoS_2 with D_{3h} symmetry, and they become E_{2g} and A_{1g}, respectively, for bulk MoS_2 that has D_{6h} symmetry. (*195*) Clearly, the A_1' peak is red shifted after transfer, and all substrates induce peak widening compared to the as-grown sample. Since A_1' is sensitive to doping, (*196*) it is reasonable to infer that the substrates introduce p-type doping to MoS_2, which is also consistent with our XPS results and with the literature. (*161*) The E' peaks also widen and redshift after transfer, which indicates the strain introduced during the transfer process. (*75*, *197*) The as-grown sample show strong and narrow PL peak at around 1.85 eV. The suppression of the PL peaks of MoS_2 on Au and SLG/Au substrates is due to the metallic nature of the substrates, and the subsequent charge transfer that occurs between MoS_2 and the substrate and the PL quenching effect. We can still observe a very weak PL peak for MoS_2/SLG/Au, which suggests the charge-transfer effect in MoS_2/SLG/Au is not as strong as in MoS_2/Au. This is in line with our XPS results in Figure 2-6(b-c) that the binding energy of Mo $3d_{5/2}$ is slightly higher for MoS_2/SLG/Au than for MoS_2/Au. The PL peaks for MoS_2/BN/Au and MoS_2/CeO_2/Au are still strong,

indicating the insulating nature of these two substrates, again consistent with the findings from XPS in Figure 2-6(b-c). However, the PL peaks are widened compared to as-synthesized MoS_2, which is likely due to the transfer process.

The effect of annealing to a higher temperature, 450 ℃ is also shown in Figure 2-6(b-c). For MoS_2 on Au, SLG/Au and BN/Au, the Mo $3d_{5/2}$ binding energy does not show much difference between 300 ℃ and 450 ℃. However, the CeO_2/Au substrate induces a remarkable decrease of ΔE by about 0.18 eV after annealing at 450 ℃. Figure 2-7(a) also confirms that Au $4f_{7/2}$ binding energy is not affected by either the thermal annealing or by the reduction of CeO_2. In fact, as observed in Figure 2-7(a), the binding energy of Mo $3d_{5/2}$ remains at about 229.88 eV for an as-prepared sample, as well as after 200 ℃ and 300 ℃ thermal annealing. After 450 ℃ annealing, the binding energy of Mo 3d decreases to about 229.7 eV. It is important to recall here that CeO_2 is a red-ox active material, and loses oxygen upon annealing in reducing conditions; (*198*, *199*) i.e. annealing in ultra high vacuum as in this experiment. 450 ℃ is high enough temperature to enable oxygen mobility, and therefore enable reduction of CeO_2 to a reduced, oxygen-deficient state. It is clear in the X-ray photoelectron spectra of Ce 3d electrons in Figure 2-7(b), that the Ce^{3+} peaks at binding energies of 886 eV and 904 eV are enhanced after 450 ℃ annealing, confirming that Ce^{4+} in CeO_2 is partially reduced to Ce^{3+} by 450 ℃ thermal annealing. This is consistent with previous reports that CeO_2 reduces in a low effective oxygen pressure environment. (*200–202*) Reduced CeO_{2-x} is a mixed ionic electronic conductor, electronic conduction ocurring through hopping of localized Ce 4f electrons from Ce^{3+} to Ce^{3+} site. (*203*) Because of electronic conductivity of reduced CeO_{2-x}, a smaller potential drop takes place in the CeO_2 layer of the MoS_2/CeO_2/Au structure, and therefore a stronger band-bending in MoS_2. Consequently, a smaller binding energy of Mo $3d_{5/2}$ and a smaller ΔE prevails, as shown in Figure 2-7(c).

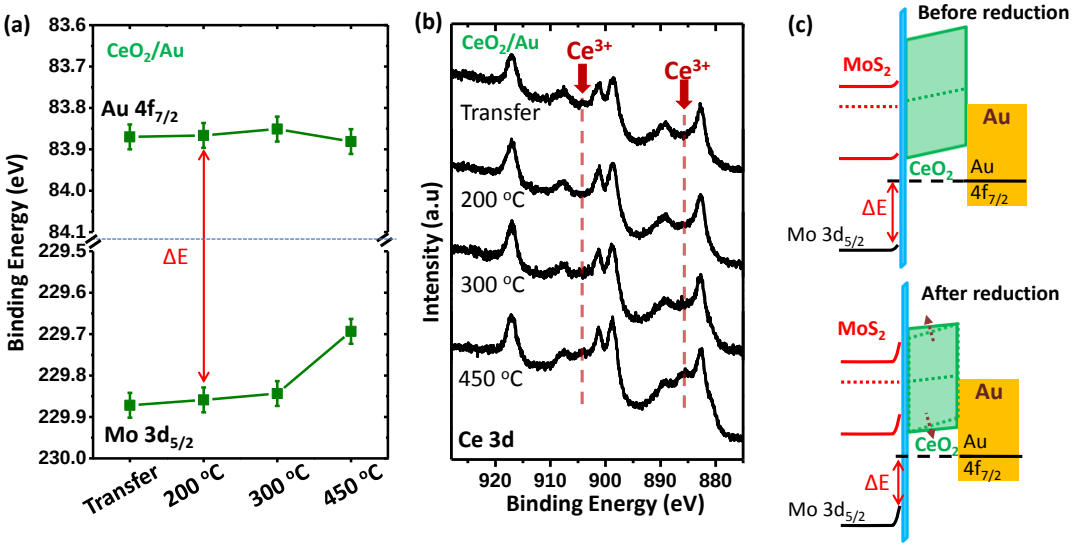

Figure 2-7. Shift of the Mo $3d_{5/2}$ binding energy, and Ce^{4+} reduction to Ce^{3+} during annealing. (a) The binding energies of the Mo $3d_{5/2}$ and Au $4f_{7/2}$ electrons for the $MoS_2/CeO_2/Au$ sample after transfer, and after annealing at 200 ℃, 300 ℃ and 450 ℃. (b) The Ce 3d X-ray photoelectron spectra of $MoS_2/CeO_2/Au$ samples after each annealing step. The dashed red lines indicate the appearance of Ce^{3+} peaks after 450 ℃ annealing. (c) Illustration of energy band alignment for the $MoS_2/CeO_2/Au$ sample. The upper graph shows the bands before the Ce^{4+} reduction, and the lower one shows the bands after the Ce^{4+} reduction.

For thermal annealing, no defects in MoS_2 are introduced. Upon annealing in UHV to 450 ℃, our XPS results showed that the Mo 3d peak shapes did not change (Figure 2-8(a)). The XPS peak intensity ratio of Mo and S peaks does not change after 450 ℃ annealing. These mean MoS_2 remained stable and without detectable formation of defects. This is consistent with Raman results presented later in the paper (Figure 2-8(b-c)). However, thermal annealing changed the coupling between MoS_2 and the substrate by improving contact between MoS_2 and the substrate (*194*) in MoS_2/Au, $MoS_2/SLG/Au$ and $MoS_2/BN/Au$, or by introducing defects into the reducible substrate CeO_2 in $MoS_2/CeO_2/Au$. Both effects significantly change the band alignment between MoS_2 and

the substrate, and potentially have a great impact on the device performance, since many electronic and optoelectronic devices depends on the energy levels and band alignment of MoS_2. (*194*)

2.3 Effect of Defects on MoS_2: Optical and Electron Spectroscopies

Ion irradiation is another way to create defects and defect induced electronic states in 2D materials. For this purpose, we introduced defects into single layer MoS_2 by low energy Ar^+ sputtering, and studied the change of binding energy, peak shape, and optical properties for MoS_2 on Au substrates. As shown in Figure 2-8(a), the Mo $3d_{5/2}$ binding energy decreases by 0.8 eV and Au $4f_{7/2}$ peaks remain unchanged after sputtering with 0.5 keV Ar^+ ion beam for 1 min. In contrast to this significant energy shift between 450 ℃ annealing and sputtering, no change in ΔE was detectable between 300 ℃ and 450 ℃ annealing. Further annealing the sputtered samples at 450 ℃ does not change the band alignment either. However, the defects introduced by ion irradiation did significantly alter the band alignment between MoS_2 and Au.

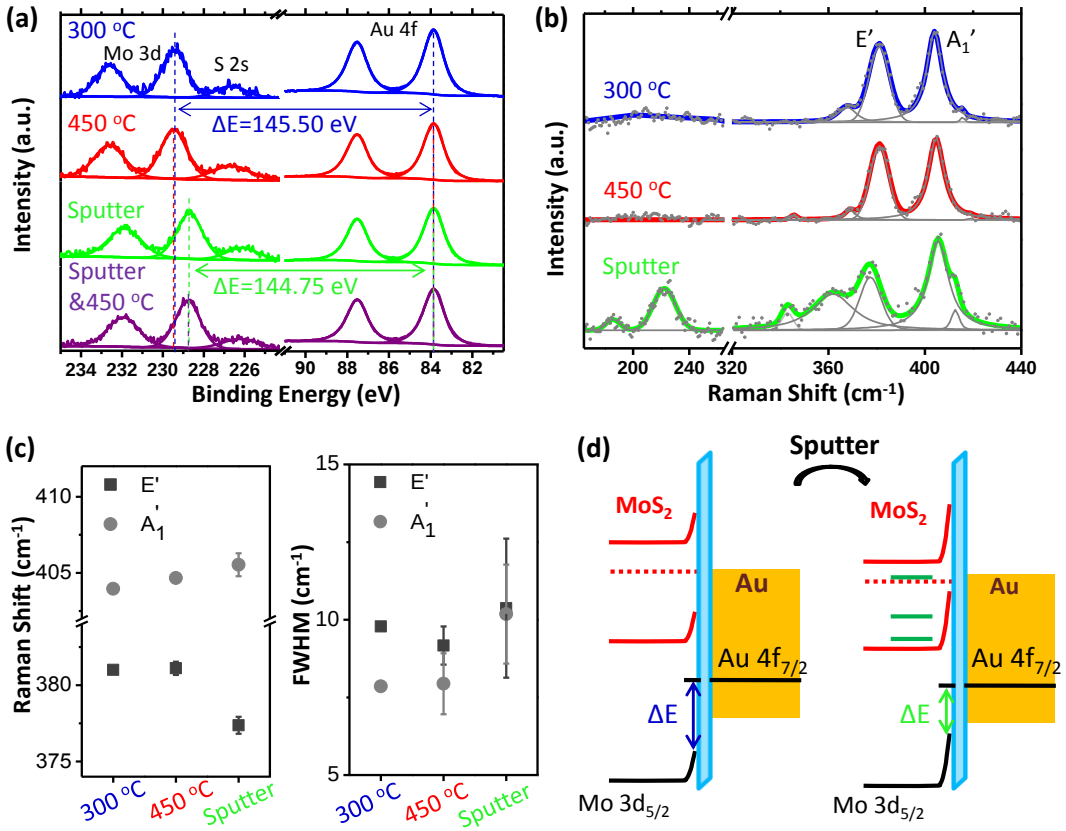

Figure 2-8. XPS and Raman characterization of samples before and after introducing defects by Ar^+ sputtering for MoS_2 on Au substrate. (a) X-ray photoelectron spectra of the Mo 3d, S 2s and Au 4f electrons in the MoS_2/Au sample after annealing at 300 ℃ and 450 ℃ in UHV, sputtering, and sputtering with subsequent annealing at 450 ℃. ΔE for the upper two and the lower two plots are shown. (b) Raman spectra of the MoS_2/Au sample after annealing at 300 ℃ and 450 ℃ in UHV, and after sputtering. The MoS_2 Raman peaks E' and A_1' are labeled. All spectra are normalized by the corresponding A_1' peaks. The measured data are shown as dots. Fitted individual peaks and overall spectra are shown as grey and colored curves, respectively. (c) Raman shift and FWHM of E' and A_1' peaks for the MoS_2/Au sample after annealing at 300 ℃ and 450 ℃, and after sputtering. (d) Illustration of energy band alignment for the MoS_2/Au sample. The left graph shows the bands before sputtering, and the right one shows the bands after sputtering. The introduction of defect states in the band gap is shown on the right.

To provide more quantitative information about the defects in MoS_2 after sputtering, we performed Raman and PL spectra measurements on the MoS_2/Au samples before and after sputtering. Figure 2-8(b) shows the Raman spectra of MoS_2/Au after 300 ℃ and 450 ℃ annealing, and sputtering. The E' and A_1' modes of MoS_2 are easily observed, and all spectra are normalized by A_1' modes. As can be seen, Raman spectra do not show considerable differences for 300 ℃ and 450 ℃ annealing, but after sputtering, E'/A_1'modes are red/blue shifted, and both are widened (Figure 2-8(c)). There is a shoulder (at around 362 cm^{-1}) on the left of E' mode and one (at around 415 cm^{-1}) to the right of A_1' mode, which are assigned as defect modes. (*186*) Both peaks are significantly enhanced after sputtering, another feature confirming the introduction of defects with sputtering. At about 220 cm^{-1}, there is an LA mode which also indicates the existence of defects for MoS_2, and this mode becomes considerable after sputtering. (*186*) The corresponding PL peaks show that after sputtering, PL peaks totally disappear. PL in MoS_2 is generated due to the radiative decay of excitons which binds electrons and holes near the edges of conduction and valence bands. (*52*, *204*) The reduction of the PL peak intensities indicates that the electronic structure changed due to a large defect density, and the population of the defect states increase the non-radiative decay channel of excitons.

The evolution of Raman peaks with thermal annealing and sputtering is summarized in Figure 2-9(c). There is an obvious red shift in E' peak and blue shift in A_1' peak after sputtering. Both peaks are widened as well, and the variation for the peaks also increases after sputtering. As reported before, (*186*) defects in MoS_2 can cause the frequency shifts and widenings in E' and A_1' peaks observed here. From the Raman signatures, we can also deduce inter-defect distances to be 1.60±0.03 nm (defect density 7.46±0.42 $\times 10^{12}$ cm^{-2}) after sputtering. (*186*) Thus our Raman measurement manifests itself as a sensitive and non-destructive approach to probe the defects in MoS_2, which is in good agreement with the XPS measurements. The introduction of defect states in MoS_2 is illustrated with green levels within the gap in Figure 2-8(d). The reason for the change of band alignment between MoS_2 and Au as observed in XPS measurement (Figure 2-8(a)) is likely due to the creation of defect states within the band gap of MoS_2, which rise the Fermi energy of MoS_2, leading

to larger difference of work function between MoS_2 and Au. Hence, a larger band bending effect and a smaller ΔE (Figure 2-8(d)) were observed. More detailed information of defect-related states in the gap will be discussed in STM/STS section later.

Besides MoS_2/Au, we also observed similar Raman and PL changes on other samples after sputtering. For example, for the Raman and PL spectra of MoS_2/BN/Au sample after 300 ℃ and 450 ℃ annealing, and after sputtering, similar defect-related Raman modes (the 362 cm^{-1} mode and the LA mode at 220 cm^{-1}) appear after sputtering, E' and A_1' peaks widen after sputtering, and they red and blue shifts, respectively, all indicating the introduction of defects. The PL peak for MoS_2/BN/Au disappears after sputtering, indicating the introduction of in-gap defect states and the change of energy band structure.

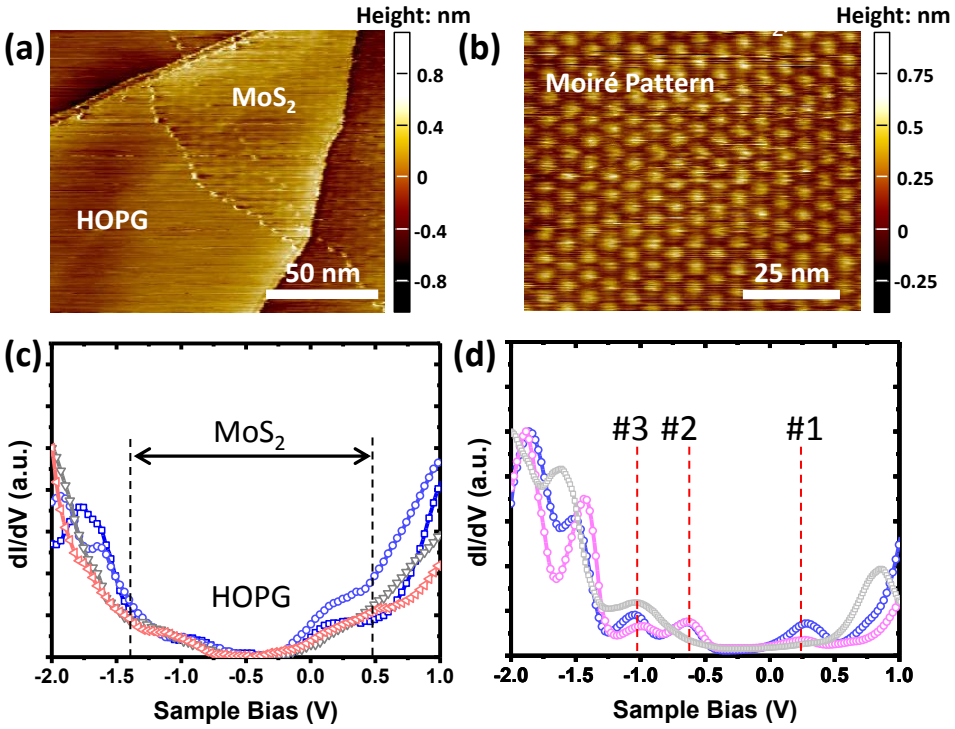

Figure 2-9. STM image and dI/dV on MoS_2 with and without defects on HOPG substrate. (a) STM constant current image of MoS_2 on HOPG, and the Moiré pattern between MoS_2 and HOPG hexagonal lattices can be observed. Imaging conditions: 50 pA, -1.5 V sample bias. (b) Zoom-in on the MoS_2 zone in the STM image in (a). (c) dI/dV spectrum on the MoS_2 on HOPG prior to ion irradiation. A lock-in preamplifier is used with 30 mV at 1 kHz frequency. The Dirac cone of graphite and the MoS_2 band gap can be observed. The

four dI/dV curves were measured at different locations on the sample. (d) dI/dV spectrum of MoS_2 on HOPG after being ion irradiated with 500 eV Ar^+. Three clear defect states can be observed. The curves were measured at different locations on the sample.

As shown above, the XPS and Raman spectroscopy indicate formation of defect states within the bandgap of MoS_2, leading band bending and a stronger charge transfer between MoS_2 and Au substrate. To provide more direct information on the electronic structure of ion irradiated MoS_2, we performed scanning tunneling microscopy (STM) and tunneling spectroscopy (dI/dV spectroscopy) on single layer MoS_2 in its as-transferred state and after introducing defects by Ar^+ sputtering. We transferred pristine MoS_2 onto HOPG substrates using a water-assisted method, leaving a clean and residue-free surface of MoS_2. The boundary between HOPG substrate and single layer MoS_2 can be seen clearly in Figure 2-9(a), with the Moiré pattern of MoS_2 and HOPG lattices in MoS_2/HOPG region shown in Figure 2-9(b). The presence of the Moiré pattern indicates a coherent interface between MoS_2 and HOPG substrate. The dI/dV spectra, representing the Density of States (DoS), on MoS_2 on HOPG prior to irradiation is in Figure 2-9(c). dI/dV shows both the Dirac cone of graphite, and the edges of the conduction band and valence band of MoS_2. The HOPG substrate contributes to the dI/dV spectra, and hence it was difficult to precisely quantify the MoS_2 bandgap. Based on the slope change in the spectra, we approximate the bandgap to be 1.9 eV, a slightly smaller value than other works reported for pristine monolayer MoS_2, which may be due to the strain in our sample. (*205–208*) The MoS_2 layers were sputtered with 500 eV Ar^+ ions for 1 min in the STM chamber, same procedure as the other samples presented in Figure 2-8. Sputtering led to poor image resolution and therefore it was not possible to obtain tunneling spectra precisely on atomic defects. We collected spectra on various locations to obtain a general result on the defected surface. The dI/dV spectra shown in Figure 2-9(d) are representative spectra that show defect states after ion irradiation. Three new peaks in the bandgap located approximately 0.3 eV (#1), 1.2 eV (#2) and 1.6 eV (#3) below the conduction band minimum can be observed (Figure 2-9(d)). Previous work has reported the STS of bulk MoS_2 which shows in-gap defect states as well. (*209*) Since the defect density in our sample is large, as quantified from Raman to be close

to 10^{12} cm^{-2}, we may see defect states from several defect types and configurations in the dI/dV spectra. These results qualitatively indicate the existence of different types of defects located at different positions. This is a reasonable outcome given the nature of ion irradiation induced defects. As will be shown by theoretical calculations later, the peaks closer to valence band (#2, #3) are likely related to the Mo-vacancies, and the one closer to the conduction band (#1) may arise from double S-vacancies. (*169*)

To identify the likely type of defects upon irradiation of MoS_2, and to associate those defects with the electronic states shown in Figure 2-9(d), MD simulations and first principles calculations, respectively, were carried out. In MD simulations, Ar^+ ion with incident energy of 500 eV was initially placed at 20 Å above the freestanding single layer MoS_2 sheet, and the incident direction is perpendicular to the MoS_2 sheet (Figure 2-10(a)). The most likely defect configurations upon ion irradiation in MoS_2 were found as single S-vacancy (V_s), single Mo-vacancy (V_{Mo}), double S-vacancy (V_{2s}), S replaced by Mo (Mo_S), Mo replaced by S (S_{Mo}), Mo and three S-vacancy (V_{Mo3s}), and Mo and six S vacancy (V_{Mo6s}) (Figure 2-10(a)). Figure 2-10(b) presents the DoS as a function of energy for single layer MoS_2 without defects, and the DoS with V_s, V_{Mo}, V_{2s} (the three most probable defects) as determined by DFT calculations. From Figure 2-10(b), S-vacancies introduce defect states within the energy gap close to the bottom of the conduction band and near the center of the gap, while the less probable Mo-vacancy is more likely to introduce defect states closer to the top of the valence band, consistent with previous reports.(*170*) Comparing the electronic structure of defected MoS_2 probed by dI/dV (Figure 2-9(d)) with the MD and DFT results, we infer that the electronic structure changes resulting from Ar^+ sputtering observed in both XPS and dI/dV are dominated by S-vacancies (both single and double S-vacancies) and single Mo-vacancy.

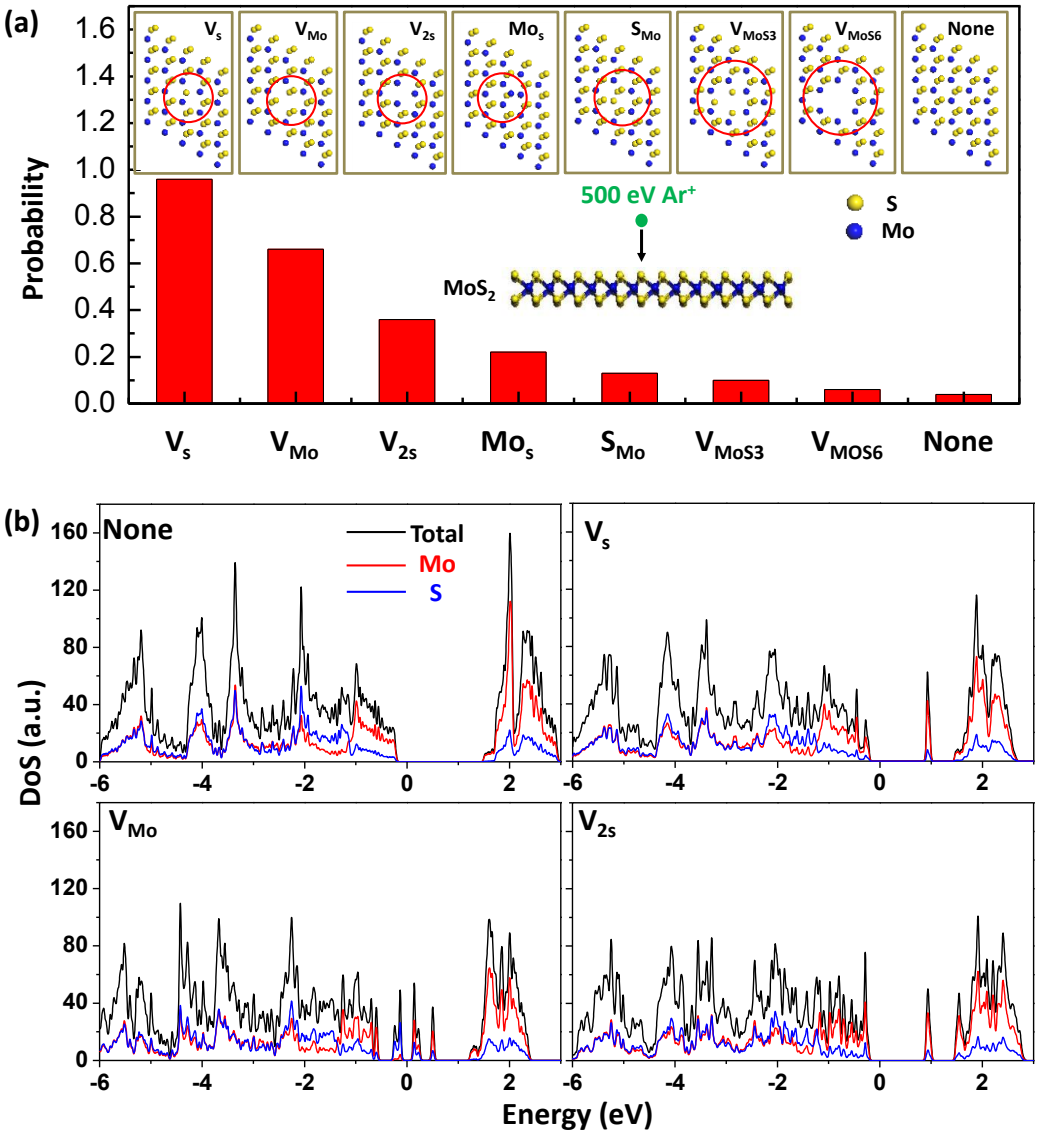

Figure 2-10. Possible defect structures that can be introduced by sputtering and the local electronic structure changes caused by these defects. (a) The probability density for different defect structures to form after 500 eV Ar^+ sputtering, as found from MD simulations. (b) The total density of states (DoS) and the contributions from the Mo and S states in MoS_2 with no defects, and with three types of defects, V_s, V_{2s} and V_{Mo}.

It is worth noting that we cannot rule out the contribution from other defect configurations, such as Mo_S, S_{Mo}, etc, however presence is expected to be less than the

three major defects examined in Figure 2-10(b). Some of these defects states have signatures in DOS as V_s, V_{2s} and V_{Mo}. In previous works, thermal annealing at 500 ℃ is considered to mainly cause S-vacancies in MoS_2. (*172*) Here we report that with ion sputtering introduces other types of defects because of atom sputtering and mixing effects. Hence ion sputtering provides a potential way to tune the defect states of MoS_2 and other 2D materials, beyond thermal annealing and thermodynamic defect equilibria. Furthermore, as expected, our MD simulation results demonstrate the possibility of forming different defect configurations by varying the ion energy for 200, 500, and 2000 eV Ar+ ion sputtering. By selecting the appropriate ion sputtering conditions, it is possible to tune the properties and performance of 2D functional materials.

Finally, as one demonstration of tuning the functionality of MoS_2 through defect engineering, we test the HER activity of as-synthesized MoS_2 single layer and the ones with defects introduced by ion sputtering. We use an inert substrate, glassy carbon, for this experiment. As shown in Figure 2-11(a), the pristine MoS_2 transferred on glassy carbon shows strong E' and A_1' Raman peaks with no defect peaks at 362 or 220 cm^{-1}. After 500 eV Ar^+ ions sputtering MoS_2 for 2 min, the sample shows distinct defect peaks, and the intensities of E' and A_1' peaks are decreased, consistent with Figure 2-8(b). The HER reaction kinetics is faster, with a higher current density on MoS_2 that was ion sputtered (Figure 2-11(b)). This result clearly demonstrates the enhancement of HER activity after introduction of defects, and is consistent with recent works which activated the inert basal plane of MoS_2 for HER activity by Ar^+ plasma. (*169*, *210*) Results indicate a good potential for the application of defect engineering of MoS_2 and other TMD materials.

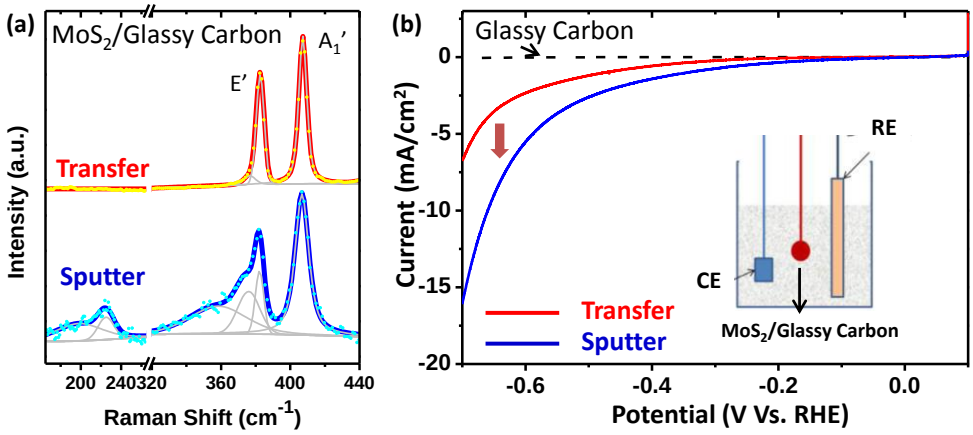

Figure 2-11. Raman characterization and HER measurement of MoS_2 on glassy carbon. (a) Raman spectra of the sample without sputtering (top spectrum), and after 2 min 0.5 keV Ar^+ sputtering (bottom spectrum). The dots are measured data, and the solid curves are fitted peaks and spectra. The peaks at around 220 cm^{-1} and 362 cm^{-1} indicate defects. The spectra are normalized by the corresponding A_1' modes. (b) Linear sweep voltammetry curves for glassy carbon substrate, and for MoS_2 on glassy carbon before and after sputtering with Ar^+ ions. The inset figure shows the HER measurement set up.

As a summary of Sections 2.2 and 2.3, we performed a systematic study of the effects of substrate and defects on single layer MoS_2 electronic structure using XPS, Raman and PL spectroscopies. Thermal annealing in UHV considerably improved the contact between MoS_2 and substrate, facilitating charge transfer between MoS_2 and metallic substrates like Au and SLG/Au, and causing energy band bending in MoS_2. In addition, and importantly, reduction of the CeO_2 substrate upon annealing significantly affects the energy band alignment of MoS_2 and CeO_2/Au substrate, because the reduction introduces electronic conductivity into this susbtrate. Defects introduced by ion sputtering influenced the electronic structure of MoS_2 and band alignment of MoS_2/Au heterostructure. The local defect states within the band gap were identified by STM and dI/dV speactra. The MD and DFT simulations indicate that these defect states are likely to be single and double S vacancies, and single Mo vacancies. In addition, we demonstrated that the introduction of

defects by ion sputtering enhances HER activity of single layer MoS_2. Tunability of defect types and concentrations in MoS_2 by ion sputtering at different energies provides a possibility to engineer the properties of MoS_2 as well as other 2D materials. This work demonstrates an effective set of spectroscopic methods, supported by atomistic and electronic calculations, to probe the band bending, charge transfer and defect states in MoS_2, which are sensitive to substrate, thermal annealing and ion sputtering. Our results show the importance and potential of defect engineering in tuning the functionality of MoS_2 and other TMD materials in electronics, optoelectronics and electrochemistry.

Chapter 3 Interlayer Raman Modes for Layered Materials

In 2D materials, there are typically two types of Raman modes, intralayer Raman mode, and interlayer Raman mode. For intralayer Raman modes, the vibration is within the plane, and the vibrational restoring force is the valence bonds between each atoms. For interlayer Raman modes, the whole layer of the material vibrates as a unit compared to the adjacent layers, and the vibrational restoring force is the van der Waals coupling between each layer. Due to the much weaker van der Waals coupling compared to valence bonds, the interlayer Raman modes typically has much lower frequency than the intralayer Raman modes, therefore requiring a special Raman spectrometer to detect them. Moreover, there interlayer Raman modes are very sensitive to interlayer coupling strength, manifesting themselves as a sensitive probe for interlayer coupling strength of artificially stacked 2D materials, or the exact number of layers for few-layer 2D materials.

3.1 Interlayer Raman of Twisted Bilayer MoS_2

Raman spectroscopy is a widely used technique to characterize nanomaterials, due to its convenience, non-destructiveness and sensitivity to materials change, including strain, temperature, doping and defects. The Raman spectrum of MoS_2 in the high-frequency (HF) region (E_{2g} around 385 cm^{-1} and A_{1g} around 405 cm^{-1}) has been extensively studied. (*154*, *211–214*) The low-frequency (LF) range (< 50 cm^{-1}), where the interlayer in-plane shear and out-of-plane breathing modes (Figure 3-1), originating from the relative vibrations between layers, has recently begun to attract increasing attention, because these modes are

more sensitive to both the interlayer coupling and number of layers. (*215*, *216*) LF modes can also effectively probe the thickness-dependent interlayer coupling in other two-dimensional (2D) material systems, such as few-layer graphene and black phosphorus. (*86*, *125*, *217–219*) In addition to their capability to determine thickness, the interlayer shear and breathing modes have been used to uncover the relationship between interface coupling and stacking pattern in twisted multilayer graphene. (*220–222*) The LF modes show a unique fingerprint for the two most stable stacking configurations (i.e., 2H and 3R) in chemical vapor deposition (CVD) grown bilayers and trilayers of $MoSe_2$ and WSe_2. In contrast to the HF modes which are almost unaffected by stacking, this LF sensitivity enables a clear determination of layer stacking. (*223–225*) However, most of the previous studies were limited to a few high-symmetry stacking patterns at 0º or 60º. (*215*, *223*) Therefore, except for a recent experimental study mainly on $MoSe_2/MoS_2$ heterobilayers, (*226*) a systematic LF Raman study on transition metal dichalcogenides (TMDs) to reveal the evolution of interlayer stacking and coupling within the full range of twisting angles is still needed.

Here, we report an integrated experimental/theoretical investigation of the interlayer shear and breathing modes of twisted bilayer MoS_2 from 0º to 60º. (*75*) The Raman measurements reveal that these modes change notably with twisting, suggesting their sensitivity to interlayer stacking and coupling. Our first-principles density functional theory (DFT) calculations provide a detailed microscopic picture of how the interlayer stacking and coupling evolve with twisting. We find that when the twisting angle is near 0º or 60º, the frequencies and intensities of the shear and breathing modes strongly vary, showing a frequency shift of up to 8 cm^{-1} and an intensity change by as much as a factor of 4.8. This behavior is due to the mixture of multiple high-symmetry stackings near 0º or 60º, leading to significant changes in the stacking and interfacial coupling upon twisting. In contrast, for twisting angles between 20º and 40º where the stacking is found to yield mismatched lattices without any highly ordered domains, the shear mode cannot be observed, since its effects are expected at very low frequency (below 10 cm^{-1}). Here we use the concept of mismatched lattices wherever the resulting bilayer structure does not show any evident patches of high-symmetry stacking. The appearance of very low

frequency spectral features for twisting angles between 20º and 40º is due to the fact that in-plane layer-layer shear vibrations lead to virtually no restoring forces associated with the mismatched stacking (i.e., very weak interlayer shear coupling). The out-of-plane breathing mode shows small variations with different twisting angles, as the mismatched stacking leads to an almost constant interlayer breathing mode coupling. For some flakes, we observe the appearance of multiple breathing modes. This observation indicates the presence of a non-uniform interlayer coupling across the interface, probably caused by either multiple high-symmetry stacking patches or mechanical transfer-induced localized strains, defects or wrinkles. This signature is particularly important for the characterization of samples used in a number of optoelectronic applications, which require highly-uniform materials.

In contrast to the LF interlayer Raman modes, the HF modes are found to be much less sensitive to interlayer stacking and coupling: the maximum variation in frequency is found to be about 1 cm^{-1}. It follows that LF Raman modes are required to probe the interlayer stacking and coupling of twisted bilayer MoS_2, and they are best suited to reveal the interfacial qualities, such as the degree of non-uniformity. These results can be extended to other 2D materials and their heterostructures. With the growing interest in the mechanical stamping of monolayers to create a variety of van der Waals (vdW) homostructures and heterostructures for diverse electronic and optical applications, (*227–230*) LF Raman spectroscopy can be critical for understanding and characterizing the interfacial properties of layered materials.

We used the dry transfer method to stack two CVD monolayers together to prepare twisted bilayer MoS_2 samples (Figure 3-1(a)). This method is simple and effective, and allows preparation of samples with controllable twisting angles. In addition, this stacking method does not introduce any contaminating substances between the two layers. These properties ensure a robust and reproducible interlayer coupling. (*52*) The inset to Figure 3-1(b) shows an illustrative optical microscope image of twisted bilayer MoS_2 after dry transfer on a SiO_2/Si substrate. The bilayer area can be readily distinguished. Optical microscopy can detect the twisting angle θ but not the detailed stacking pattern and interfacial coupling strength. In contrast, and as will be shown here, LF Raman

spectroscopy is a particularly well-suited technique to determine these properties. Figure 3-1(b) shows a typical Raman spectrum in the frequency range of 15 ~ 490 cm^{-1} for a bilayer MoS_2 with θ=46°. In the HF range, the characteristic first-order E_{2g} and A_{1g} modes, (*154*) second-order 2LA(M) mode and first-order A_{1g}^2 mode (*158*) of MoS_2 can be seen. Note that strictly speaking, the symmetry assignments here are valid only for the bulk 2H stacking, while the symmetry assignments of a bilayer system can be changed with the stacking and twisting. But for simplicity and consistency, the notations of E_{2g} and A_{1g} are used for all twisted bilayer systems.

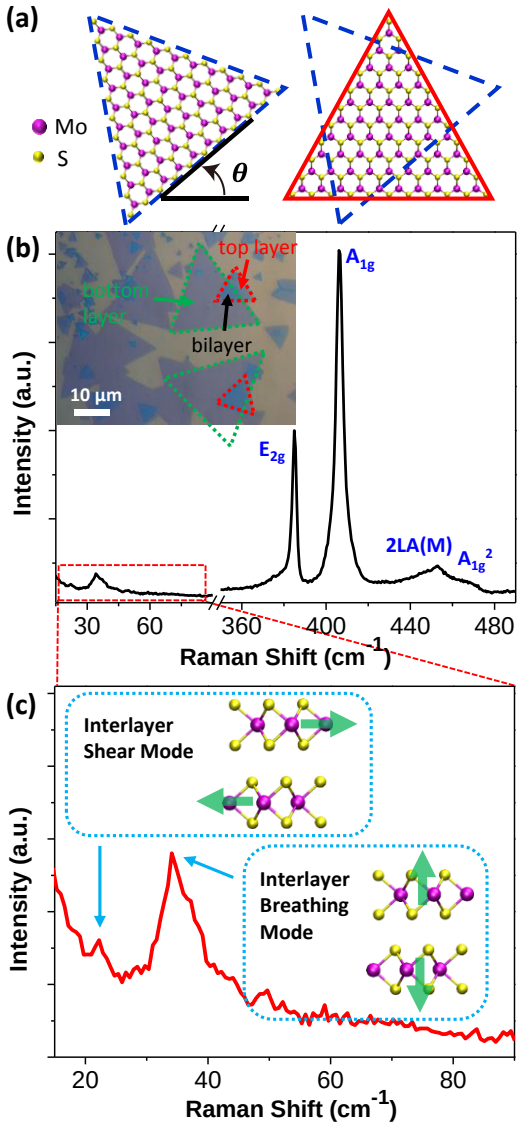

Figure 3-1. (a) Scheme of the angular twisting in bilayer MoS_2. The left and right plots show the separated top layer and bottom layer, respectively. Purple (yellow) spheres denote Mo (S) atoms. (b-c) Raman spectrum of twisted bilayer MoS_2 at θ=46º. See (a) for definition of θ. (b) Full spectrum showing E_{2g}, A_{1g}, 2LA(M) and A_{1g}^2 modes of MoS_2. Inset: optical microscope image of a dry-transferred twisted bilayer sample. The green (red) triangles show the outlines of some bottom (top) layer MoS_2 triangles, and one bilayer region is labeled. The LF (low-frequency) range is marked with a red dashed rectangle and is enlarged in (c), including interlayer shear and breathing modes. Their vibrational motions are shown in the insets to (c). Green arrows indicate the vibrational directions of each layer.

Distinctive Raman signals are also present in the LF range (<50 cm^{-1}). Zooming into this range (Figure 3-1(c)), there are two peaks corresponding to the interlayer shear and breathing modes.(*215, 216*) As shown in the insets to Figure 3-1(c), the LF interlayer modes describe the layer-layer vibrations with each layer moving as a whole unit, and hence their frequencies are solely determined by the weak interlayer restoring forces and thus are typically below 100 cm^{-1}. (*86*) They are categorized into two types: the in-plane shear mode and the out-of-plane breathing mode. (*231*) On the other hand, the HF modes involve vibrations from intralayer chemical bonds, and thus the strong restoring forces are dominated by strong intralayer chemical bonds instead of the weak interlayer coupling. Due to the high sensitivity to the interface, the shear and breathing modes can be effectively used to probe the interlayer stacking and coupling.

Because of the D_{3h} symmetry of monolayer MoS_2, the properties of twisted bilayer MoS_2 show a variation period of 60º. (*52, 65, 66*) The shear and breathing modes of MoS_2 bilayer with θ between 0º and 60º are shown in Figure 3-2(a), together with the data from monolayer MoS_2 and exfoliated bilayer (2H stacked) MoS_2 presented for comparison. The interlayer shear and breathing modes are absent for monolayer MoS_2, further confirming that they originate from interlayer vibrations. For bilayer samples, the naturally 2H stacked (exfoliated sample) MoS_2 shows a sharp shear mode at 22.9 cm^{-1} and a broad breathing mode at 38.1 cm^{-1}, consistent with previous works. (*215*, *216*) Compared to exfoliated samples, experimentally stacked bilayers generally show shear modes with lower

intensities and breathing modes with higher intensities, and both of these frequencies are down shifted. Different twisting angles also show different characteristics for the shear and breathing modes. The shear mode is typically of lower intensity than that of the breathing mode, and is even absent for certain twisting angles. Similar phenomenon of the disappearance of the interlayer shear mode has also been observed in other bilayer TMD materials. (*226*) The frequency of the LF interlayer breathing mode also changes as a function of θ, shown in Figure 3-2(a). In contrast to the LF interlayer Raman modes, the HF intralayer E_{2g} and A_{1g} Raman modes in Figure 3-2(b) show a much smaller dependence of their frequency and intensity as a function of θ, indicating that the HF modes are not as effective as the LF modes in detecting changes in stacking configurations.

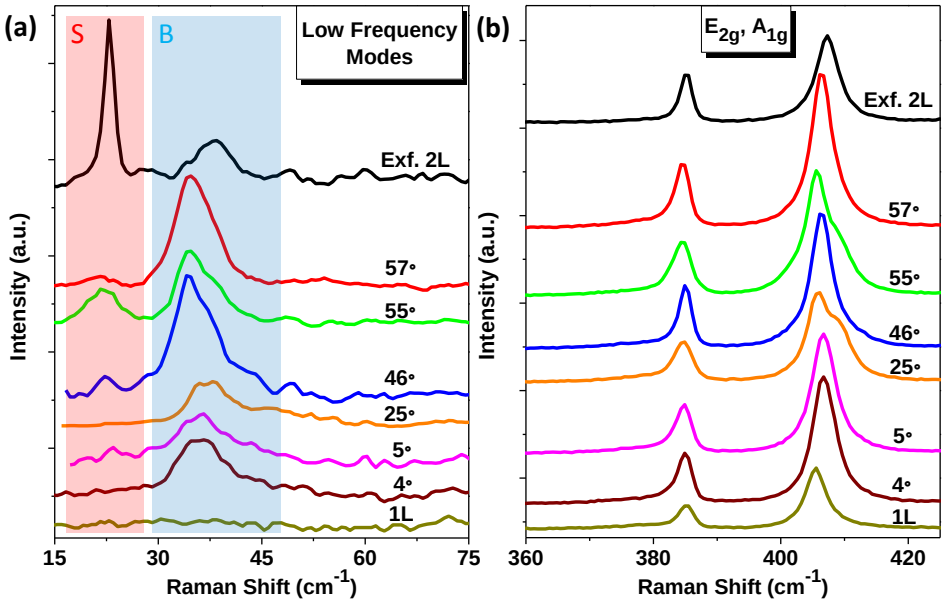

Figure 3-2. Raman spectra of twisted bilayer MoS_2 with different twisting angles selected from 0º to 60º, and of monolayer (1L) and exfoliated bilayer MoS_2 (Exf. 2L): (a) the LF range including interlayer shear and breathing modes, and (b) the HF (high-frequency) range including E_{2g} and A_{1g} modes. In (a) the red rectangle and letter "S" label the interlayer shear modes, and the blue rectangle and letter "B" label the interlayer breathing modes.

We carefully studied the dependence of the shear and breathing modes on the twisting angles of bilayer MoS_2, and we extracted information for each Raman peak as a function of θ. The θ values are grouped into five ranges: 0º-10º, 10º-20º, 20º-40º, 40º-50º and 50º-60º. In each θ range, the results for the statistical mean value and maximum variation for the peak information are shown in Figure 3-3. Figure 3-3(a-b) show the intensity dependence of each peak on each θ range. For both modes, when θ is close to 0º and 60º, the intensities show large variations, as indicated by the large bar heights. When θ approaches 30º, the shear mode disappears, and the breathing mode intensities show only a weak dependence on θ, compared to the cases where θ is close to 0º or 60º. Hence the breathing mode has a smaller bar height in the [20º, 40º] range. The disappearance of the shear mode in the available frequency window between 20º and 40º is due to its extremely low frequencies (< 10 cm^{-1}), as will be discussed below. For all the twisting angles, there is an intensity change of about a factor of 3.8 for the breathing mode, and of about 4.8 times for the shear mode. The frequencies of the shear and breathing modes for different θ are shown in Figure 3-3(c) and (d), respectively. The shear mode clearly disappears when θ is between 20º and 40º, while it shows up as θ approaches 0º or 60º. Similar to the intensity, the shear mode frequency near 0º or 60º varies significantly with θ (up to ~ 8 cm^{-1}). For the breathing mode, the frequency remains around 37 cm^{-1} when θ is between 20º and 40º, but varies by as much as 6.7 cm^{-1} when θ approaches 0º or 60º. Overall, both the intensities and frequencies of the shear and breathing modes show strong variations when θ is close to 0º or 60º, and they show considerably weaker variations when θ is between 20º and 40º, as is clearly shown in Figure 3-3 by the bar heights. For comparison purposes we marked the parameters for exfoliated (naturally 2H stacked) bilayer MoS_2 with dashed lines in Figure 3-3. Compared to most twisted bilayer samples, the exfoliated sample shows a higher shear mode intensity, a lower breathing mode intensity, and relatively larger frequencies for both the shear and breathing modes. Such intensity and frequency differences can be attributed to the strong interlayer coupling of the naturally 2H stacking, as will be explained below.

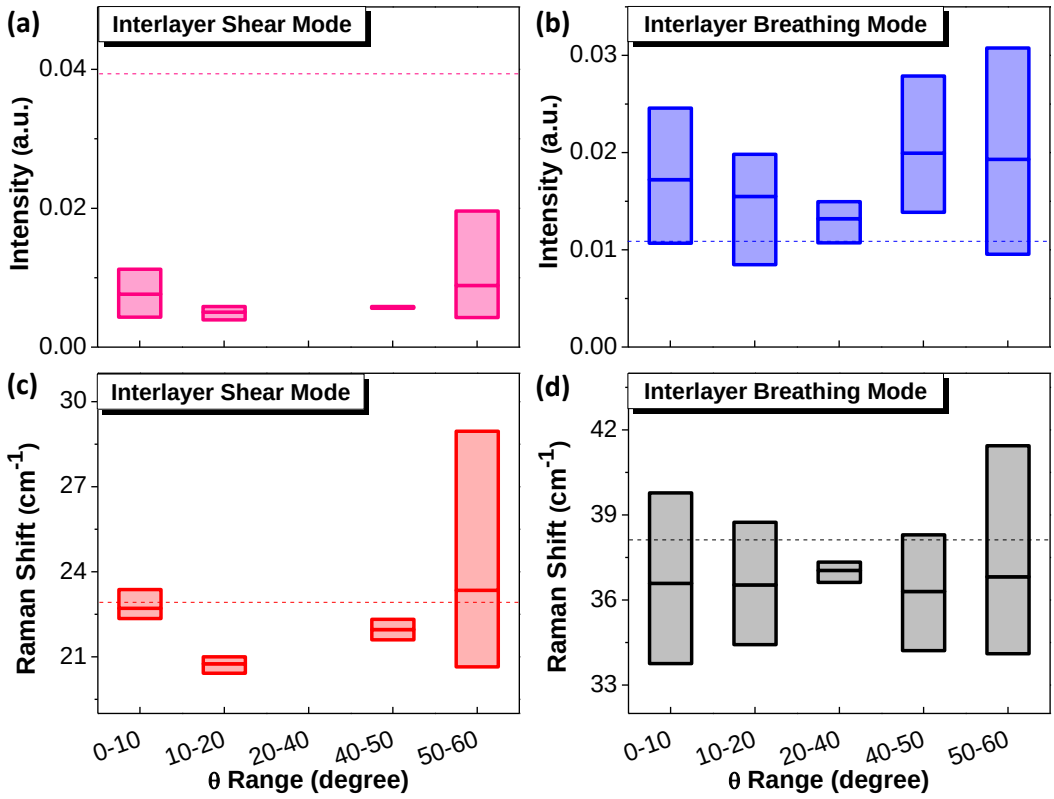

Figure 3-3. Twisting angle θ dependence of the LF interlayer Raman modes. θ dependence of the intensities of (a) shear modes located around 23 cm^{-1} and (b) breathing modes located around 37 cm^{-1}. θ dependence of the frequencies of (c) shear modes and (d) breathing modes. The θ values are categorized into five ranges. The heights of the data bars show the variation range of the data points in each θ range, and the horizontal line in the middle of each bar shows the mean value in the θ range. The values measured for exfoliated bilayer MoS_2 are labeled as the horizontal dashed lines in (a-d) for comparison.

It is interesting to note that some twisted flakes, such as for θ = 55º in Figure 3-2(a) and θ = 3º, 13º, 59º, etc., have asymmetric breathing modes, suggesting the possibility of overlapping of multiple modes. These multiple peaks also exist in the corresponding anti-Stokes spectra. For bilayer MoS_2 with a uniform interface, there should be only one breathing mode. The presence of multiple breathing modes could arise from a non-uniform interface across which the interlayer distance and coupling vary significantly. For θ near

0º or 60º, different high-symmetry stacking patches co-exist (Figure 3-4), which could lead to multiple breathing mode peaks, since each stacking patch contributes a different breathing mode, which will be discussed in detail below. In contrast, for θ near 30º where the stacking does not show any obvious high-symmetry patches, the presence of multiple peaks could be caused by localized strains, defects or wrinkles, introduced during the dry transfer procedure (such effects could be possible for θ near 0º or 60º as well). (*65*) In short, LF Raman spectroscopy could provide a sensitive tool to detect the presence of non-uniform interface. It is well established that strains can affect the Raman spectrum of MoS_2. (*156*, *232*, *233*) In particular, LF interlayer Raman modes are very sensitive to the interlayer distance and coupling. Local strains introduced during the transfer process could lead to local variations of interlayer distance and coupling. Subsequently, multiple LF Raman peaks with different frequencies can appear. However, it is difficult to conclude that such phenomena are only due to strains instead of other localized effects. Strains on mono- or few-layer MoS_2 lead to a notable frequency shift of the high-frequency E_{2g} peak: $\Delta\omega/\epsilon$ is up to -2 cm^{-1} per % of uniaxial tensile strain and 3 cm^{-1} for a 0.2% biaxial compressive strain, respectively. For the high-frequency A_{1g} peak, there is almost no frequency shift for the uniaxial strain, and the frequency shift can be about 2 cm^{-1} for a 0.2% biaxial compressive strain. (*156*, *232*, *233*) However, our measurements covering the whole θ range [0º, 60º] show that the variations of the E_{2g} and A_{1g} frequencies are within ~1 cm^{-1} (will be discussed below), indicating that strains are not significant in the samples. Therefore, we expect that strains, though present, are not a dominating factor.

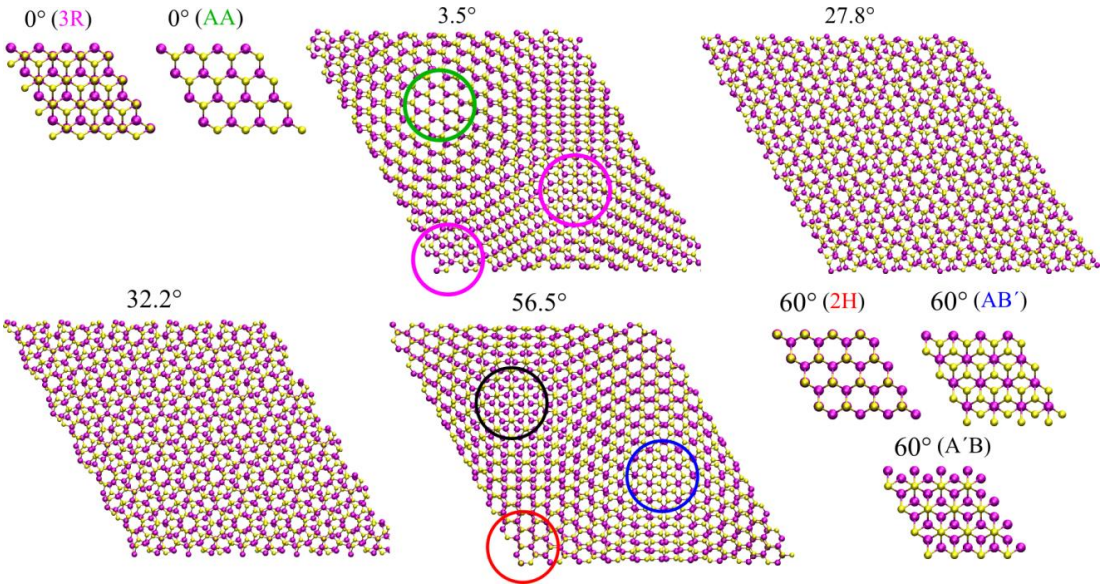

Figure 3-4. Atomic structures of commensurate bilayer MoS_2 at various twisting angles. Purple (yellow) spheres denote Mo (S) atoms. At θ = 0º, there are two high-symmetry stacking patterns 3R and AA. When the system deviates from 0º slightly (e.g., 3.5º), both the 3R and AA stacking patches are still present, as highlighted by the purple and green circles, respectively. The boundary stackings between these high-symmetry patches serve as the transition to other stacking arragements. The patch sizes continuously decrease as θ deviates increasingly from 0º, and eventually the stacking becomes completely mismatched near 30º (e.g., 27.8º). At 60º, there are three high-symmetry stacking patterns, 2H, AB′ and A′B. When the system deviates slightly from 60º (e.g., 56.5º), 2H, AB′ and A′B stacking patches are still present, as highlighted by the red, blue and black circles, respectively. The patch sizes continuously decrease with θ deviating more from 60º, and eventually the stacking becomes completely mismatched near 30º (e.g., 32.2º).

In addition to the LF shear and breathing modes, we also summarize how HF intralayer Raman modes (E_{2g}, A_{1g}, 2LA(M) and $A_{1g}{}^2$) change upon twisting. The frequencies of HF modes barely change. For instance, the A_{1g} mode is red shifted from 0º (or 60º) to 30º, but the frequency change is only around 1 cm^{-1}. For some flakes, the A_{1g} peak splits, and multiple peaks can be observed in the LF range as well, suggesting that the A_{1g} splitting and the multiple LF modes share the same origin, namely, the presence of a non-uniform

interface. The number of flakes featuring multiple LF interlayer modes is more than twice that of flakes with A_{1g} splitting, clearly indicating that the LF modes are more sensitive to interfacial environment than the HF modes. The variation of the E_{2g} frequency is also within about 1 cm^{-1}. The 2LA(M) mode around 452 cm^{-1} shown in Figure 3-1(b) is a second-order Raman mode involving two longitudinal acoustic (LA) phonons at the M point of the Brillouin zone. (*158*) Moreover, the A_{1g}^2 mode in bilayer MoS_2, (*158*, *215*) located around 466 cm^{-1}, corresponds to the Raman inactive B_{2g} mode in bulk MoS_2, which becomes Raman active in few-layer MoS_2 due to symmetry breaking. For 2LA(M) and A_{1g}^2 modes, the dependence of their frequencies on θ is also weak. In short, the HF Raman modes are less effective than the LF ones to probe the interface. Finally, we note that for all of these HF intralayer Raman modes, relatively strong variations also occur when θ is close to 0º or 60º. This phenomenon is consistent with the experimental results for the LF modes, suggesting that the variation of interlayer coupling near 0º or 60º is the strongest and most complex.

To understand the experimental data in more detail, we first examined the atomic structures of twisted bilayer MoS_2 to reveal the microscopic picture of the stacking evolution with twisting. Unlike bilayer graphene that has two high-symmetry stacking patterns AB (i.e., Bernal) and AA, bilayer MoS_2 has five high-symmetry stacking patterns due to its two different elements, as shown in Figure 3-4. (*66*, *223*, *234*, *235*) At $\theta = 0º$, there are two stacking patterns interchangeable by translation: 3R and AA. For 3R, Mo is over S and the other Mo and S are over the center of the hexagons; for AA, Mo is over Mo and S is over S. At $\theta = 60º$, there are three stacking configurations that are interchangeable by translation: 2H, AB′ and A′B. For 2H, Mo is over S and S is over Mo; for AB′, Mo is over Mo and all S are over the center of the hexagons; for A′B, S is over S and all Mo are over the center of the hexagons. Note that 2H at 60º (also denoted as AA′) is the most stable configuration, and 3R at 0º (also denoted as AB) is the second most stable. These two stackings are present in natural and CVD-grown bilayer systems. (*65*, *223*) In the mechanically stacked samples, all five stacking patterns are possible and some of them coexist for the same twisting angle. In Figure 3-4, at 3.5º where the system slightly deviates from 0º, both 3R and AA stacking patches appear. The patch sizes where the AA and 3R

configurations are seen continuously decrease as θ deviates more from 0º, and eventually the stacking becomes completely mismatched at 27.8º (more angles 1.8º, 7.3º, 13.2º and 21.8º are studied). (*75*) On the other hand, at 56.5º where the system slightly deviates from 60º, the 2H, AB′ and A′B stacking patches all appear (Figure 3-4). Similar to the 0º case, the patch size continuously decreases as the deviation of θ from 60º increases, and eventually the stacking becomes completely mismatched at 32.2º. We also considered non-commensurate finite-size bilayer MoS_2. Similar to Figure 3-4, when the system only slightly deviates from 0º or 60º, high-symmetry stacking configurations appear in roughly circular shapes. Their size continuously decreases, as θ deviates more from 0º or 60º. When $\theta > 10º$ and $\theta < 50º$, the high-symmetry stacking patches disappear, and the overall stacking becomes increasingly mismatched and does not display any high-symmetry domains.

DFT calculations were also carried out on various commensurate bilayer MoS_2 structures. We first examined the five high-symmetry stackings at 0º and 60º. As shown in Figure 3-5(a-b), 2H stacking is the most stable and all energies will be expressed relative to its energy. 3R stacking shares a very similar interlayer separation and total energy (less stable by only 0.3 meV/atom).[45] Thus, the frequency of the shear mode is only weakly modified. The breathing mode is also mildly downshifted by 3 cm^{-1} from 2H to 3R (Figure 3-5(c)). Compared to 2H stacking, the interlayer distance of AB′ stacking slightly increases by 0.04 Å and the AB′ configuration becomes less stable by 4.2 meV/atom. Moving from 2H to AB′, the shear and breathing modes are slightly downshifted by 3.8 cm^{-1} and 6.8 cm^{-1}, respectively. On the other hand, the interlayer distance of A′B (or AA) stacking is significantly increased by 0.68 (or 0.71) Å and these stacking configurations become much less stable by 11.5 (or 12.1) meV/atom, compared to 2H stacking.(*66*, *234*, *235*) This leads to dramatic frequency changes from 2H to A′B (or AA) stacking: the shear mode is down shifted by as much as 17.6 (or 22.0) cm^{-1} and the breathing mode by 7.4 (or 10.8) cm^{-1}. In stark contrast, the frequencies of the HF intralayer E_{2g} and A_{1g} modes are almost unchanged for all five high-symmetry stackings, where the maximum frequency variation is within 1-2 cm^{-1} (Figure 3-5(d)). These results clearly demonstrate that in-plane rotation and translation can induce different high-symmetry stackings for bilayer MoS_2 with

considerable changes of the interlayer distance and coupling. Such changes significantly modify LF Raman modes while HF modes are essentially unaffected.

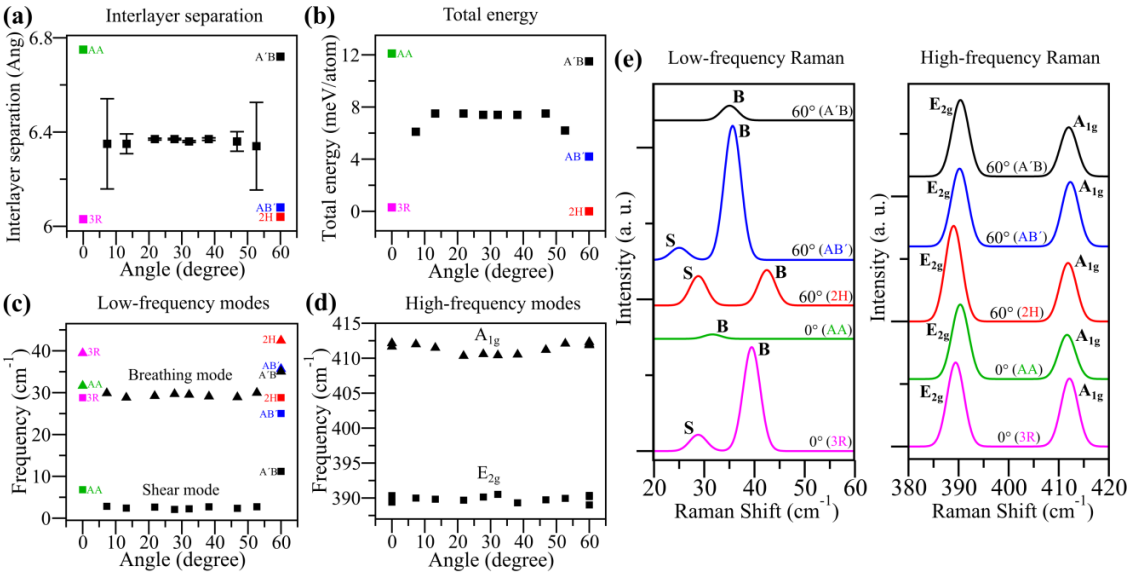

Figure 3-5. DFT calculations for twisting angles θ from 0º to 60º. (a) Average interlayer separation between the two Mo layers. The bars show the minimal and maximal local layer separations at an angle. (b) Total energy versus θ. The energy of 60º (2H stacking) bilayer is set as zero. (c) The θ dependence of the frequencies of LF shear mode (squares) and breathing mode (triangles). (d) The θ dependence of the frequencies of HF E_{2g} (squares) and A_{1g} (triangles) modes. In (a-d), both stackings 3R and AA are included at 0º (hence two data points at 0º), and all three stackings 2H, AB′ and A′B are included at 60º (hence three data points at 60º). In (a-c), these data points are differentiated by colors and labels, while in (d) they almost overlap. (e) Simulated Raman spectra of the five high-symmetry stackings at 0º and 60º. From (c-e), the LF Raman modes clearly show much larger frequency and intensity changes versus the stacking and twisting angle, compared to the HF Raman modes.

In addition to shifts in frequencies, the intensity dependence of the LF Raman modes on stacking is also very noticeable, as shown in the simulated Raman spectra in Figure 3-5(e). In contrast, the intensities of HF modes have a much weaker dependence on

stacking. This result can be understood by the fact that Raman intensity of a phonon mode is positively correlated with the change of the system's electric polarizability by the corresponding phonon vibration. (*225, 236*) For the HF modes corresponding to intralayer vibrations, the change of the polarizability (i.e., Raman intensity) is primarily contributed by the vibrations of intralayer chemical bonds. Hence, a change of layer-layer stacking results in a relatively small intensity change. In contrast, for the LF modes corresponding to layer-layer vibrations, the change of the polarizability is solely due to layer-layer vibrations. Thus, the change of layer-layer stacking can lead to a relatively dramatic intensity change, as seen in Figure 3-5(e). Interestingly, in going from the 2H to 3R stackings in bilayer MoS_2, the intensity of the shear mode decreases while the intensity of the breathing mode increases (this effect was also experimentally observed in bilayer WSe_2), (*223*) and a similar intensity trend occurs for the 2H to AB′ transition. The 3R and AB′ stackings share similar interlayer coupling strength with 2H stacking, so their intensity changes are largely due to the altered atomic arrangements and different electronic environments for each atom. For A′B or AA stacking, on the other hand, as the interlayer distance is much larger (close to decoupling of the two layers), the layer-layer vibrations lead to a much smaller polarizability change, and hence the shear mode has almost zero intensity and the breathing mode has considerably weaker intensity.

Turning to θ near 0º or 60º, the stacking yields a pattern composed of a mixture of multiple high-symmetry domains. For 52.7º, bilayer MoS_2 has 2H, AB′ and A′B stacking patches, which have quite different interlayer separations from one another. Consequently, notable variations in the local interlayer distance (about 0.37 Å in Figure 3-5(a)) are expected. A similar variation of the local interlayer distance is found in the 7.3º sample since it has 3R and AA stacking patches with very different interlayer separations.(*65*) When the system deviates slightly from the natural 2H stacking at 60º, AB′ and A′B stacking patches appear. The shear mode intensity is considerably decreased for both AB′ and A′B stackings but the breathing mode intensity increases significantly for AB′ stacking (Figure 3-5(e)). Hence, compared to exfoliated 2H bilayer, generally for θ near 60º, the shear mode becomes weaker while the breathing mode is enhanced, largely due to the appearance of twisting-related AB′ and A′B stackings (such as at 57º and 55º in Figure 3-2

and more twisting angles shown in (*75*)). For the bilayer system near 0º, 3R and AA stacking patterns appear. Both exhibit weakened shear modes while 3R stacking has an enhanced breathing mode, compared to 2H stacking (Figure 3-5(e)). Hence, relative to the exfoliated 2H bilayer, generally for θ near 0º, the shear mode is weak while the breathing mode can be enhanced owing to the presence of 3R stacking (such as the 4º and 5º in Figure 3-2). This analysis can explain why, for $\theta < 10^{o}$ or $\theta > 50^{o}$, the average intensity of the shear mode is lower while that of the breathing mode is higher, compared to the exfoliated bilayer (Figure 3-3(a,b)). Regarding the frequencies, since all other stacking configurations have weaker interlayer coupling than the 2H stacking, the average frequencies of the shear and breathing modes are generally lower compared to the exfoliated bilayer (Figure 3-3(c,d)). Besides, for $\theta < 10^{o}$ or $\theta > 50^{o}$, the co-existing high-symmetry stacking patches can lead to very different frequencies and intensities for the shear and breathing modes (Figure 3-5(e)). Twisting one bilayer compared to another can change both the weight of each stacking patch and the boundary stacking between the patches in the overall stacking pattern, and such changes will in turn, modify their relative contributions to the Raman scattering. Therefore the frequency and intensity variations of the shear and breathing modes can be large at different θ near 0º or 60º, as indicated by long bar heights in Figure 3-3 (frequency variation up to 8 cm^{-1} and intensity variation by 4.8 times).

The situation is different for θ in the [20º, 40º] range, where the stacking is such that it does not present any sizeable domains similar to those with high-symmetry stackings (Figure 3-4). It follows that neither rotation nor translation within this angular range change the coupling. This is confirmed by DFT calculations which show that the interlayer distance remains ~6.36 Å with essentially no variation (Figure 3-5(a)) and the total energy varies negligibly (Figure 3-5(b)). Hence, the interlayer coupling is nearly constant, and consequently the frequency and intensity variations of the breathing mode in the [20º, 40º] range are insignificant (short bar heights in Figure 3-3). Furthermore, compared to 2H stacking, the interlayer distance near 30º increases by 0.32 Å and the structure is energetically less stable by ~7.4 meV/atom, suggesting much weaker interlayer coupling. Thus, the breathing mode frequency is lower than that of the exfoliated 2H bilayer, as shown in Figure 3-3(d). Note that the shear mode cannot be observed in [20º, 40º], since it

has a calculated frequency as low as ~2 cm^{-1} (Figure 3-5(c)). This frequency is buried in the strong Rayleigh line and therefore beyond the detection limit available to Raman measurements. Such stark contrast between the shear and breathing modes originates from the mismatched stacking. The absence of local high-symmetry domains makes the stacking features essentially insensitive to the in-plane shear motion, leading to very small overall restoring force. In contrast, the out-of-plane breathing motion changes the interlayer distance and coupling, and always leads to a finite overall restoring force. (*222*, *226*) To provide further evidence for these conclusions, we introduced artificial in-plane and out-of-plane relative shifts by 0.5 Å to the bilayer systems for various stackings and angles. Compared to 2H stacking where the in-plane shift gives energy difference of 3.62 meV/atom, the in-plane shift results in almost no energy difference for 21.8º, 27.8º, 32.2º and 38.2º (only ~0.05 meV/atom), confirming the very low restoring force from the in-plane shear motion for these mismatched stacking arrangements. However, the out-of-plane shifts lead to comparable magnitudes of energy differences for different stackings and angles. Clearly, the shear mode is overall more sensitive to twisting and it might provide a good indicator of the degree of stacking mismatch, while the breathing mode is present for all twisting angles and thus serves as a practical indicator of the interlayer coupling for mechanically stacked systems.

Finally, for θ in the [10º, 20º] or [40º, 50º] ranges, the predicted local stacking arrangements lie between the high-symmetry stacking mixture near 0º or 60º and the mismatched stacking near 30º, and it follows that the θ dependence of the shear and breathing modes is intermediate (Figure 3-3). Note that there is a seemingly appreciable discrepancy between the measured (Figure 3-3(c)) and calculated (Figure 3-5(c)) values of the shear mode in the [10º, 20º] or [40º, 50º] ranges, where the measured frequencies are around 21-22 cm^{-1} while the calculated ones are around 2-3 cm^{-1}. At these angles, an ideal interface has largely mismatched stacking arrangements without high-symmetry stacking patches, and our calculations suggest that little restoring force can come from the in-plane shear motion (thus frequency 2-3 cm^{-1}). However, the presence of various non-ideal effects (such as local strains, wrinkles or defects) can in actuality induce shorter interlayer distance locally, and thus the shear mode with relatively stronger restoring force and higher

frequencies can appear (like frequency 21-22 cm^{-1}). If a sample has little or no non-ideal effects, the shear mode should disappear. In fact, only less than half of the samples in the [10º, 20º] or [40º, 50º] ranges show the shear mode experimentally. This suggests that localized strains, wrinkles or defects are probably present in these samples to cause the measured 21-22 cm^{-1} modes, while the majority of the samples are free of these non-ideal effects and thus the shear mode has too low a frequency to be observable as the theory predicts.

To quantify the strengths of interlayer shear and breathing coupling, we estimated their force constants based on the widely used linear chain model. (*215–217*, *237*) The force constant of the shear mode (K_s) was found to vary from 2.30×10^{19} to 4.51×10^{19} N/m^3 in the range of $\theta < 20^o$ and $\theta > 40^o$, where the shear mode is observable. This gives a variance of 0.2×10^{19} N/m^3 and a relative deviation of ~7.2%. Note that the shear mode disappears in the [20º, 40º] range due to its extremely low frequency (only ~ 2 cm^{-1} according to DFT calculations). Hence, in [20º, 40º], K_s is estimated to be about 0.02×10^{19} N/m^3, and thus the relative deviation in the whole range [0º, 60º] is very large (up to more than 90%). However, the force constant of the breathing mode (K_b) ranges from 6.26×10^{19} to 9.52×10^{19} N/m^3 in [0º, 60º], giving a variance of 0.43×10^{19} N/m^3 and relative deviation of 5.9%, much smaller than the variation of K_s. The strengths of the interlayer coupling are generally two orders of magnitude smaller than those of the intralayer vibrations (the force constants of E_{2g} and A_{1g} modes are 1.88×10^{21} and 3.46×10^{21} N/m^3, respectively). (*216*)

In conclusion, we have systematically investigated the interlayer stacking and coupling in twisted bilayer MoS_2 using a combination of LF Raman spectroscopy and first-principles DFT calculations. Our results show that in-plane rotation and translation can induce five different high-symmetry stacking patterns at 0º (3R and AA) and 60º (2H, AB′ and A′B) with substantially different interlayer distances and coupling strengths. Consequently, the frequencies and intensities of the LF interlayer shear and breathing modes change dramatically with stacking. Upon twisting away from 0º and 60º, the stacking becomes a mixture of these high-symmetry stacking patterns, and thus twisting leads to significant changes in stacking and coupling, as reflected by notable frequency and intensity variations of the shear and breathing modes (frequency variation by 8 cm^{-1} and intensity variation by

4.8 times). On the other hand, when θ is within [20º, 40º], the coupling is nearly constant since the stacking pattern shows highly mismatched lattices with no local high-symmetry domains. This explains why the breathing mode shows small variations in such θ range. Interestingly, the shear mode disappears near 30º, as the in-plane shear motion leads to almost no restoring force from the mismatched stacking and its frequency is close to zero. Moreover, a non-uniform interface with variable interlayer coupling can be formed due to the co-existence of multiple high-symmetry stacking patches, or mechanical stamping induced localized strains, defects, or wrinkles. Such non-uniformity can be properly captured by LF Raman spectroscopy (i.e., multiple breathing modes). This work paves the way towards a deeper understanding of interfacial properties of 2D homostructures and heterostructures, and proves that LF Raman spectroscopy offers effective and quick characterization of layered materials.

3.2 Few-layer Black Phosphorus

Phonons play an important role in the diverse properties of materials, (*238*) and they have been intensively studied in vdW layered materials, such as graphene and TMDs. (*239–246*) Raman spectroscopy is a particularly powerful and non-destructive tool to investigate phonons and their coupling to electrons, and it has been successfully applied to vdW layered materials. (*34*, *154*, *247–249*) Due to the lattice dynamics of vdW layered materials, the phonon modes can be classified as high-frequency (HF) intralayer modes and low-frequency (LF) interlayer modes. (*238*) Intralayer modes involve vibrations from the intralayer chemical bonds (Figure 3-6(c)), and the associated frequencies reflect the strength of those bonds. In contrast, the interlayer modes correspond to layer-layer vibrations with each layer vibrating as a whole unit (Figure 3-6(b)), and hence their frequencies are determined by the interlayer vdW restoring forces. The weak nature of vdW interactions typically renders the frequencies of interlayer modes much lower than those of intralayer modes, usually below 100 cm^{-1}. Depending on the vibrational direction, LF interlayer modes are categorized into two types: the in-plane shear modes and the out-of-plane breathing modes (Figure 3-6(b)). Due to their greater sensitivity, the LF interlayer modes have been shown to be very important in studying the interlayer coupling and for identifying the thickness for few-layer graphite and TMDs. (*215*, *216*, *250*)

The HF intralayer Raman modes in bulk BP crystals were studied in the 1980's (*251*) and recently similar HF modes have been reported in thin film BP. (*100*, *252–254*) Normally, three characteristic HF Raman modes (A_g^1, B_{2g} and A_g^2) can be observed under the typical back-scattering configuration, corresponding to the out-of-plane vibration (~365 cm^{-1}), in-plane vibrations along the zigzag (~440 cm^{-1}) and armchair (~470 cm^{-1}) directions, respectively (Figure 3-6(c)). Moreover, it is found that their dependence on the laser polarization can be used to determine the crystalline orientation of BP.(*252*, *254*) However, the frequencies of HF intralayer modes are found to exhibit almost no dependence on film thickness. (*251–254*) Clearly, the study of the LF interlayer phonon modes in few-layer BP (Figure 3-6(b)) is needed to reveal more information on the interlayer coupling and thickness. LF phonons have been studied in bulk BP using inelastic neutron scattering in the1980's. (*255*, *256*) However, to the best of our knowledge, there has been no experimental work on the observation of LF interlayer modes in few-layer BP and only two theoretical works published recently. (*257*, *258*) The measurement of LF (<100 cm^{-1}) Raman modes is challenging since these modes are usually blocked by the notch filters used to reject the excitation laser light, and it requires a Raman system with a LF rejection filter or a triple-grating Raman system. In this work, we successfully observed the LF interlayer breathing Raman modes in few-layer BP for the first time. (*86*) These breathing modes are assigned to A_g symmetry and can be also used for crystalline orientation determination according to an experimental laser polarization dependence analysis and first-principles density functional theory (DFT) calculations. The thickness dependence study indicates that the breathing modes in few-layer BP are strongly thickness-dependent, and thus could be used as an important and effective indicator of the number of layers. In addition, based on our temperature dependence study, the breathing modes show much smaller anharmonic shifts compared to those observed for HF modes.

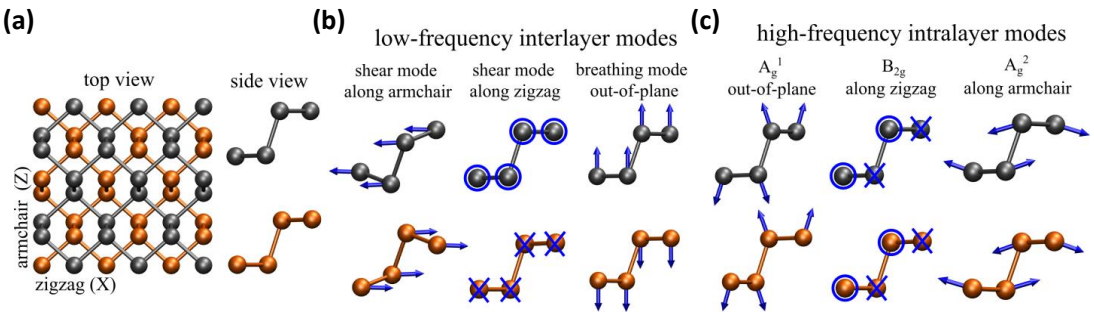

Figure 3-6. (a) Top and side views of BP with puckered layers. The top and bottom layers are differentiated using black and gold colors. (b) Vibrations of LF interlayer modes: two in-plane shear modes and one out-of-plane breathing mode. (c) Vibrations of HF intralayer modes: three characteristic Raman modes A_g^1, B_{2g} and A_g^2. The circle and cross indicate vibrations coming out of the plane of the page and going into it, respectively.

According to symmetry analysis, (*259*, *260*) the bulk BP crystal belongs to the space group *Cmce* (No. 64) and point group D_{2h}^{18} (mmm).(*251*) Note that the space group is labeled as *Cmca* (No. 64) in the old convention of the International Tables of Crystallography. As shown in Figure 3-6(a), the crystal unit cell of bulk BP is orthorhombic with two layers and 8 atoms (a=~3.3 Å, b=~10.5 Å and b=~4.4 Å). The primitive unit cell is half of the crystal unit cell and contains 4 atoms, and hence there are 12 normal phonon modes at the Γ point:

$$\Gamma_{bulk} = 2A_g + B_{1g} + B_{2g} + 2B_{3g} + A_u + 2B_{1u} + 2B_{2u} + B_{3u}, \qquad \text{Eq. 3-1}$$

where A_g, B_{1g}, B_{2g}, B_{3g} modes are Raman-active, B_{1u}, B_{2u}, B_{3u} modes are infrared-active, and A_u mode is optically inactive. (*251*, *252*, *261*) According to the classical Placzek approximation, (*236*) the Raman intensity of a phonon mode is proportional to $|e_i \cdot \tilde{R} \cdot e_s^T|^2$, where e_i and e_s are the electric polarization vectors of the incident and scattered lights respectively, and $\tilde{R}$ is the Raman tensor of the phonon mode. Only when $|e_i \cdot \tilde{R} \cdot e_s^T|^2$ is not zero, can the phonon mode be observed by Raman spectroscopy. As a common practice in the literature, (*251*, *252*, *260*) we denote the in-plane zigzag direction as the X axis, the out-of-plane direction as the Y axis, and in-plane armchair direction as the Z axis. The calculated Raman tensors $\tilde{R}$ of Raman-active modes A_g, B_{1g}, B_{2g} and B_{3g} are

$$\tilde{R}(A_g)=\begin{pmatrix} a & \cdot & \cdot \\ \cdot & b & \cdot \\ \cdot & \cdot & c \end{pmatrix}, \qquad \tilde{R}(B_{1g})=\begin{pmatrix} \cdot & d & \cdot \\ d & \cdot & \cdot \\ \cdot & \cdot & \cdot \end{pmatrix},$$

$$\tilde{R}(B_{2g})=\begin{pmatrix} \cdot & \cdot & e \\ \cdot & \cdot & \cdot \\ e & \cdot & \cdot \end{pmatrix}, \qquad \tilde{R}(B_{3g})=\begin{pmatrix} \cdot & \cdot & \cdot \\ \cdot & \cdot & f \\ \cdot & f & \cdot \end{pmatrix}, \qquad \text{Eq. 3-2}$$

where *a*-*f* are major terms while other terms (denoted by "·") are either zero or negligible due to symmetry. (*252*, *262*, *263*) In the typical experimental back-scattering configuration, the electric polarization vectors e_i and e_s are in-plane (the X-Z plane), and thus only A_g and B_{2g} modes can be observed according to the Raman tensors, although B_{1g} and B_{3g} are Raman-active. (*215*, *252–254*) The symmetries of *N-layer* (*N*L) BP films (where *N* is the number of layers) are slightly different from those of bulk BP: odd *NL* BP belongs to space group *Pmna* (No. 53) and point group D_{2h}^{7} (mmm); even *N*L BP belongs to space group *Pmca* (No. 57) and point group D_{2h}^{11} (mmm). Although *N*L systems belong to different space groups from the bulk BP, all of them share the same point group D_{2h} (mmm). Consequently, the symmetry classification of Raman modes and the forms of their Raman tensors remain unchanged for any thickness (Eq. 3-1 and Eq. 3-2), consistent with previous theoretical works. (*258*, *263*, *264*)

In *N*L BP, there are *N*−1 interlayer shear modes vibrating along the zigzag direction, *N*−1 interlayer shear modes along the armchair direction, and *N*−1 interlayer breathing modes along the out-of-plane direction, similar to 2D graphene and TMDs. (*250*, *257*) The difference is that the shear modes vibrating along zigzag and armchair directions are non-degenerate in BP due to its in-plane anisotropy. For perfect (defect-free and free-standing) BP films, the shear modes are either Raman-active (B_{1g} or B_{3g}) or infrared-active (B_{1u} or B_{3u}). Similarly, the breathing modes are either Raman-active (A_g) or infrared-active (B_{2u}). (*258*) As discussed in Eq. 3-2, in the back-scattering configuration, only A_g and B_{2g} modes can be detected by Raman spectroscopy. Consequently, among the LF interlayer modes, only the Raman-active breathing modes with A_g symmetry can be observed in the Raman spectra. Furthermore, the number of breathing modes with Raman-active A_g symmetry is *N*/2 for even *N*L and (*N*-1)/2 for odd *N*L (see Table 3-1). (*258*) For monolayer BP (or phosphorene), the interlayer breathing modes do not exist. Bulk BP has a breathing mode

(around 87 cm^{-1}), (*255–257*, *261*) but its calculated Raman tensor $\tilde{R}$ is zero, indicating that it cannot be detected. Therefore, in short, the breathing modes can only be observed in few-layer BP, not in single-layer and bulk BP. In addition, according to the inelastic neutron scattering measurements on bulk BP, (*255–257*, *261*) the two shear modes (vibrating along armchair and zigzag directions respectively) have frequencies around 19 and 52 cm^{-1}, while the frequency is ~87 cm^{-1} for the breathing mode. From our calculations and previous theoretical works, (*257*, *258*) in few-layer BP, the frequencies of all shear modes are no larger than their bulk values (thus $\leq$ 52 cm^{-1}); similarly the frequencies of all breathing modes are no larger than their bulk values (thus $\leq$ 87 cm^{-1}). These results suggest that LF peaks observed above 52 cm^{-1} likely originate from the breathing modes.

The experimental Raman measurements were carried out on few-layer BP flakes (Figure 3-7). The BP flakes deposited on a glass substrate were mechanically exfoliated from the bulk and coated with a parylene (~100 nm) or PMMA film (~300 nm) immediately to avoid degradation. From the optical contrast of the flakes, the bluish flakes are determined as few-layer BP, while the reddish and whitish flakes are thicker ones. (*100*, *265*, *266*) The corresponding Raman spectrum on the few-layer BP (the blue area labeled in Figure 3-7(a)) is shown in Figure 3-7(b). The three well-known HF A_g^1, B_{2g} and A_g^2 peaks of BP are located at 362.3 cm^{-1}, 439.2 cm^{-1}, and 467.1 cm^{-1}, respectively. More interestingly, another three peaks with relatively weaker intensities are observed in the LF region. As shown in the zoom-in spectrum in the inset of Figure 3-7(b), the frequencies of these three peaks are determined by peak fitting as 26.2 cm^{-1}, 75.6 cm^{-1} and 85.6 cm^{-1}, respectively. According to our theoretical analysis, they are expected to be LF interlayer breathing modes (labeled as "B modes") belonging to Raman-active A_g symmetry. In addition, only when $N \geq 6$, can there be no less than three B modes with A_g symmetry. Therefore, we conclude that the number of layers of the measured few-layer BP flake in Figure 3-7(a) is at least 6. The calculated Raman spectrum of 6L BP is shown in Figure 3-7(c). Besides the A_g^1, B_{2g} and A_g^2 modes in the HF region, three B modes appear in the LF region with their frequencies located around 31.9 cm^{-1}, 55.1 cm^{-1} and 78.6 cm^{-1} (inset in Figure 3-7(c)), confirming our interpretation of the experimental observations. To provide further experimental evidence that the three LF Raman peaks in Figure 3-7(b) are

B modes with A_g symmetry, we performed laser polarization dependence measurements of all Raman modes, as shown in the following.

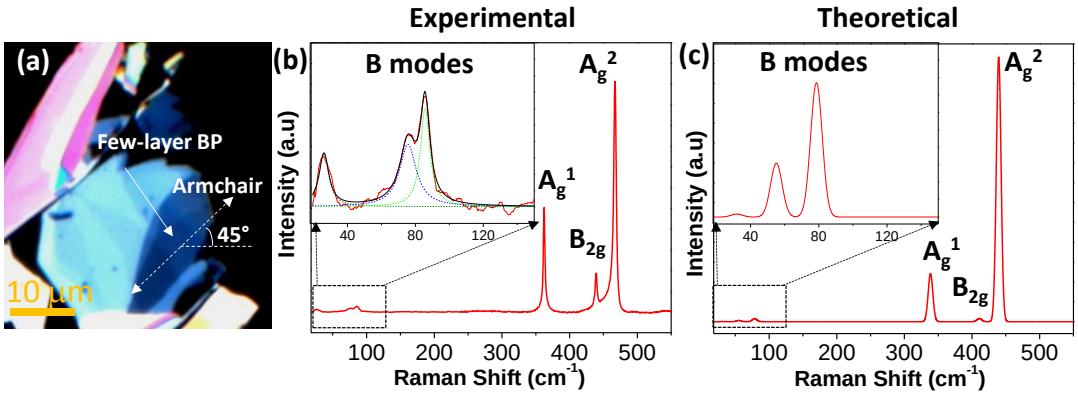

Figure 3-7. (a) A typical optical image of exfoliated BP flakes on a glass substrate coated with parylene, including few-layer BP (the blue area). The armchair direction is labeled, determined by the polarization dependence study. (b) Experimental Raman spectrum of few-layer BP corresponding to the flake in (a). Inset: the zoom-in spectrum from 20 to 150 cm^{-1}. (c) Calculated Raman spectrum of 6L BP in the experimental back-scattering geometry. Inset: the zoom-in spectrum in the same LF region as (b). Three interlayer breathing modes (B modes) with Raman-active A_g symmetry are predicted in the LF range. In (c), the HF A_g^1 and A_g^2 peaks are reduced by ~50 times for the comparison purpose.

Due to the in-plane anisotropic structure of the BP thin film, its Raman modes show significant polarization dependence, which can be used to identify the crystalline orientation of the sample. (*252*, *254*) Two methods were reported to study the polarization dependence. One is by rotating the sample while fixing the polarization of the incident and scattered light; (*252*) the other is by changing the polarization of the incident and scattered light while fixing the sample. (*254*) Here we employed the first method. As discussed above, the Raman intensity is $I \propto |e_i \cdot \tilde{R} \cdot e_s^T|^2$. In the experimental back-scattering geometry, the electric polarization vectors e_i and e_s of the incident and scattered lights are in-plane (the X-Z plane: X (Z) axis is defined as sample initial zigzag (armchair) direction before rotating the sample). By setting the polarization angle of the incident (scattered) light as θ

(γ) with respect to X-axis, we have $I \propto \left|(cos\theta, 0, sin\theta) \quad \tilde{R} \quad \begin{pmatrix} cos\gamma \\ 0 \\ sin\gamma \end{pmatrix}\right|^2$. In our case, θ and γ are fixed, and the sample is rotated in the X-Z plane by φ with respect to X axis. The Raman intensity then becomes:

$$I \propto \left|(\cos(\theta-\varphi), 0, \sin(\theta-\varphi)) \quad \tilde{R} \quad \begin{pmatrix} \cos(\gamma-\varphi) \\ 0 \\ \sin(\gamma-\varphi) \end{pmatrix}\right|^2$$

In our experiment, we used the parallel polarization configuration, so that $\gamma = \theta$ always. For an A_g mode, its Raman tensor is $\tilde{R} = \begin{pmatrix} a & \cdot & \cdot \\ \cdot & b & \cdot \\ \cdot & \cdot & c \end{pmatrix}$, thus

$$I_{A_g} \propto a^2 \left|1 + (\frac{c}{a} - 1) sin^2(\varphi - \theta)\right|^2 \qquad \text{Eq. 3-3}$$

Since θ is fixed, the intensity of an A_g mode depends on both the sample rotation angle φ and the ratio *c*/*a*. For a B_{2g} mode, the Raman tensor $\tilde{R} = \begin{pmatrix} \cdot & \cdot & e \\ \cdot & \cdot & \cdot \\ e & \cdot & \cdot \end{pmatrix}$, thus

$$I_{B_{2g}} \propto e^2 sin^2 2(\varphi - \theta) \qquad \text{Eq. 3-4}$$

which only depends on the rotation angle φ, since θ is fixed. According to our calculations and a previous experimental work for few-layer BP, (*252*) *c* (tensor component related to the armchair direction) is expected to be larger than *a* (tensor component related to the zigzag direction) in Eq. 3-3, hence *c*/*a* > 1. Therefore, the minimum intensity angle of an A_g mode is $\varphi = \theta$ or $\theta + 180°$ (the sample zigzag direction is now rotated to the polarization direction of incident light); the maximum intensity angle of an A_g mode is $\varphi = \theta + 90°$ or $\theta + 270°$ (the sample armchair direction is now rotated to the polarization direction of incident light). The minimum intensity angle of a B_{2g} mode is $\varphi = \theta$ or $\theta + 90°$ or $\theta + 180°$ or $\theta + 270°$ (the sample's armchair or zigzag direction is now rotated to be aligned with the polarization direction of incident light); its maximum intensity angle is $\varphi = \theta + 45°$ or $\theta + 135°$ or $\theta + 225°$ or $\theta + 315°$. Hence, by rotating the sample under a parallel polarization configuration, the intensity variation period is always 180° for an A_g mode, while it is 90° for a B_{2g} mode. In addition, when the sample armchair (zigzag)

direction is along the polarization direction of incident light, an A_g mode shows the maximum (minimum) intensity, while a B_{2g} mode is forbidden. (*252*) These simple results can be used as effective indicators of the crystalline orientation. Note that the above theoretical analysis is based on real Raman tensor elements, while strictly speaking they should be complex. (*252*, *267*) This leads to no change for the polarization dependence of a B_{2g} mode, but a phase difference between complex Raman tensor elements *a* and *c* is introduced and certain values of the phase difference can result in two maximum intensity peaks for an A_g mode. (*252, 267*) One peak corresponds to the sample armchair direction and the other corresponds to the sample zigzag direction. The main effect of the phase difference is to induce a minimum intensity peak between the armchair and zigzag directions. (*252, 267*) By varying the phase difference, the overall polarization dependence profile of an A_g mode will be changed. (*252*, *267*) Nevertheless, for any value of the phase difference, we found that the intensities and angles of the maximum and secondary maximum intensity peaks do not change (intensities always $|c|^2$ and $|a|^2$, while angles always corresponding to armchair and zigzag directions). Therefore, the angle of the maximum intensity peak of an A_g mode always corresponds to the same crystalline orientation, independent of the phase difference. Hence the most important result from the polarization dependence holds even the Raman tensor elements are complex. Moreover, as discussed below in Figure 3-8 for our BP sample, the phase difference is assumed in such value that no secondary maximum intensity peak appears for any A_g mode (where the minimum intensity peak actually appears), and thus the effect of the complex Raman tensor and phase difference is insignificant in our work.

Figure 3-8(a) shows a series of Raman spectra of few-layer BP in the LF region at different sample rotation angles. With the sample rotated from 0° to 180°, the intensities of the three LF modes vary periodically, and reach maximum and minimum values around 45° and 135°, respectively. It should be mentioned that we could not differentiate the LF modes from the background noise for the rotation from 105° to 165° because the associated peaks are too weak at these polarization values. These results clearly establish the importance of considering the sample orientation relative to the polarization of the incident light when studying the LF modes of BP. The polar plots of the fitted peak intensities of

both the LF and HF modes as a function of the rotation angle are shown in Figure 3-8(b-g). The three LF modes (Figure 3-8(b-d)) and HF A_g^1 and A_g^2 modes (Figure 3-8(e) and (g)) share very similar polarization dependence: all of them have the same intensity variation period of 180° with two intensity maxima around 45° or 225°. However, the HF B_{2g} mode shows the intensity variation period of 90° with four intensity maxima around 0°, 90°, 180°, 270° (Figure 3-8(f)). These are consistent with our theoretical predictions discussed above. The polarization dependence measurement further confirms that the three LF modes share the same symmetry as the HF A_g^1 and A_g^2 modes (i.e., A_g symmetry). These three LF modes are thus assigned to interlayer breathing modes that have A_g symmetry, since shear modes (belonging to B_{1g} or B_{3g} symmetry)(*258*) have different polarization dependence from the A_g modes. Note that although LF breathing (B) modes and HF A_g modes share very similar polarization dependence in Figure 3-8(b-g), there are still minor differences. At the minimum intensity rotation angles (~135° or 315°), one notes that the LF B mode (26.2 cm^{-1}) and HF A_g^1 and A_g^2 modes show relatively strong intensities, while the LF B modes (75.6 cm^{-1} and 85.6 cm^{-1}) are barely present. This can be explained by different values of the *c*/*a* ratio in the Raman tensors of B and A_g modes despite the existence of an identical symmetry (see Eq. 3-3).

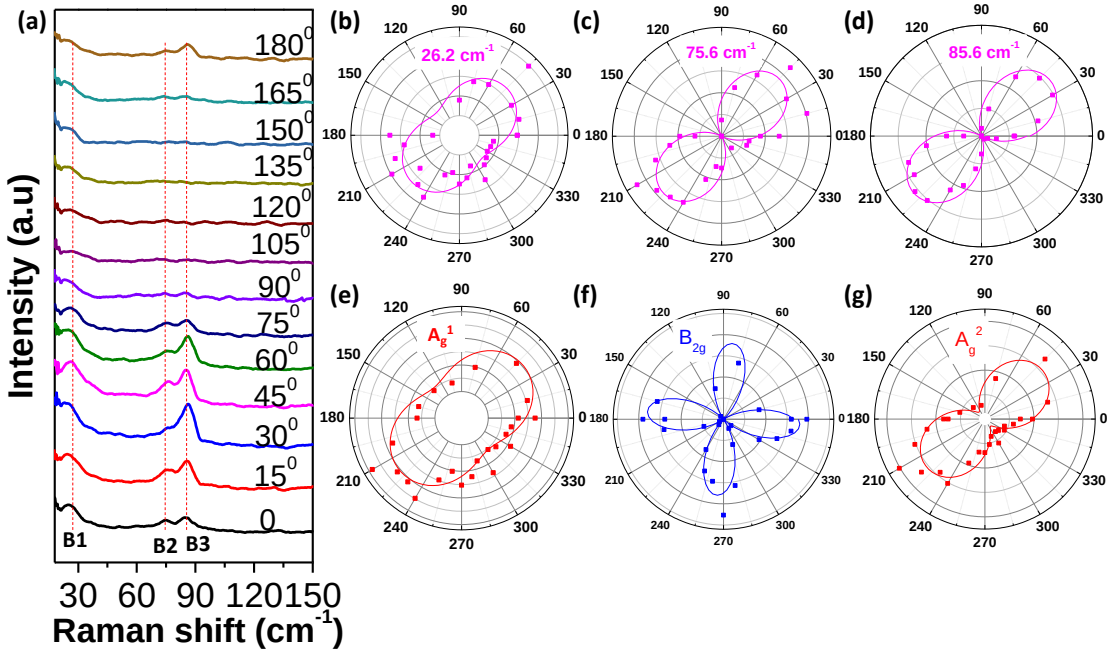

Figure 3-8. (a) Raman spectra of few-layer BP in the LF range at different sample rotation angles. (b-d) The profiles of the intensities of the LF interlayer breathing modes at different rotation angles. (b): 26.2 cm^{-1}; (c) 75.6 cm^{-1}; (d) 85.6 cm^{-1}. (e-f) The profiles of the intensities of the HF intralayer modes at different rotation angles. (e): A_g^1; (f) B_{2g}; (d) A_g^2. The sample was rotated clockwise from 0° to 360°.

In addition, the polarization dependence study further indicates that the armchair direction of the sample is oriented about the 45° direction shown in Figure 3-7(a), since the maximum intensity angles of B and A_g modes correspond to the sample armchair direction. It is important to point out that our combined experimental/theoretical analysis is based on the assumption that the ratio $c/a > 1$, which is consistent with a previous experimental work.[45] In the present work, for few-layer BP under the 632.8 nm laser excitation wavelength, it is expected that $c/a > 1$. However, increase in BP thickness (to very thick sample) and change in laser wavelength (towards Raman resonance) could modify the c/a ratio and possibly to values smaller than 1, as reported by some authors recently. (*252*, *267*) If $c/a < 1$, for an A_g mode, the intensity variation period is still 180°, but the maximum intensity angle corresponds to the zigzag direction instead of armchair direction. Regardless of the c/a ratio larger or smaller than 1, it is certain that the intensity angle extrema are corresponding to the armchair or zigzag direction. (*252*, *267*)

As suggested by the polarization dependence, the intensities of the Raman modes of BP are strongly related to the crystalline orientations relative to the polarization of the incident light. Therefore, when studying the thickness dependence of the Raman modes, it is important to set the flakes along the same crystalline orientation. Therefore, for every flake chosen for a thickness dependence study, we collected the Raman spectra of the flakes at different orientations and determined the armchair direction of the flakes. The B modes of the different flakes are all collected with the laser polarization along the armchair direction, at which intensities reach the maximum. The optical images and the corresponding Raman spectra of the flakes on 300 nm SiO_2/Si substrates with PMMA coating are shown in Figure 3-9. Since the BP sample is polymer coated immediately after exfoliation to avoid degradation, it becomes very difficult to directly measure the

thicknesses of the flakes using, for example, atomic force microscope (AFM). But from the optical contrast of the flakes, their relative thicknesses can be determined to order from the thinnest flake to thickest one marked as 1 and 5, respectively (Figure 3-9(a)). On flake 1, we did not observe any LF peak at any polarization direction (Figure 3-9(b)). In addition, the Raman intensities of the HF modes on flake 1 are very weak. These results indicate that flake 1 is likely a monolayer (recall that monolayer cannot have LF interlayer modes). (*96*, *253*, *268*) For the few-layer BP in Figure 3-9(b), from flake 2 to flake 3, a LF B mode appears and the Raman peak splits into two from flake 4 to flake 5. However, for very thick multilayer (ML) flake and bulk samples, the LF B mode is not observed (Figure 3-9(b)). The absence of LF modes in bulk BP is consistent with the theoretical analysis outlined above. For very thick ML flakes that are bulk-like, the intensities of LF modes are too low to be detected. Only in the few-layer samples (flakes 2-5 in Figure 3-9(b)), LF modes show observable intensities. Such a tendency is consistent with other vdW layered materials such as TMDs, where bulk-inactive vibrational modes become Raman-active and observable in few-layer but they are non-detectable in very thick samples.[41,](*269*, *270*) In addition, we also show the dependence of FWHM (Figure 3-9(d)) and intensity (Figure 3-9(e)) of the B modes. The decrease of the FWHM with the increase of the thickness indicates that the lifetime of the B mode phonons is longer in the thicker flakes, similar to TMDs. (*271*) In Figure 3-9(e), the intensity of the higher-frequency B mode generally increases with the thickness from flake 2 to 5.

Table 3-1. Calculated frequencies (in cm^{-1}) of breathing modes for 2L to 8L BP using the DFT PBE+optB88 method. In *N*L BP, there are $N-1$ breathing modes either Raman-active (A_g, highlighted in red) or infrared-active (B_{2u}, in black). The number of breathing modes with Raman-active A_g symmetry is $N/2$ for even N, and $(N-1)/2$ for odd N. The breathing modes are labeled as B*n*. The breathing mode of bulk BP is also shown but it cannot be detected.

Layer	B1	B2	B3	B4	B5	B6	B7
2	62.7						
3	52.0	70.5					
4	36.2	63.1	75.6				
5	33.7	53.4	69.5	76.2			
6	31.9	42.1	55.1	71.0	78.6		
7	28.2	35.7	51.7	65.2	74.5	80.4	
8	24.8	31.0	47.8	60.9	71.4	77.6	83.2
bulk							86.1

To understand the thickness dependence of B modes, we calculated the frequencies of B modes of 2L to 8L BP using DFT PBE+optB88 method (Table 3-1). This method gives the bulk B mode's frequency 86.1 cm^{-1}, very close to the experimental value (87 cm^{-1}). (*255–257*, *261*) Other DFT functionals have also been used for comparison. In each column of Table 3-1, the frequency of the B mode monotonically decreases with increasing thickness, consistent with previous theoretical works on BP (*257*, *258*) and experimental reports on TMDs,[40,41] as this constitutes a general trend for vdW layered materials. Furthermore, the highest-frequency B mode of any thickness in Table 3-1 is the bulk-like B mode, where each adjacent layer is vibrating in opposite directions. With increasing thickness, it blue shifts and approaches the bulk limit of 87 cm^{-1}, very similar to that observed for the higher-frequency B mode (the black points in Figure 3-9(c)). It follows that the observed higher-frequency mode in a BP flake should correspond to the flake's highest-frequency B mode (i.e., bulk-like B mode). As for the lower-frequency B mode (the red points in Figure 3-9(c)), it probably corresponds to the second-highest B mode of the flake. Note that only these two B modes can be unambiguously observed for BP flakes 2-5. The other Raman-active B modes predicted in Table 3-1 are too difficult to be detected experimentally possibly due to their weak intensities or too low frequencies. Similarly, only two B modes can be observed in few-layer TMDs as well.[42] Since the highest-frequency B mode is not Raman-active (B_{2u}) for odd *N*, the BP flakes 2-5 showing bulk-like B modes might be all even *N*L. Another possibility is that the polymer capping or the

supporting substrates or defects in the material may break the symmetry to induce Raman-activation of the bulk-like B modes in odd *N*L BP. A definite conclusion cannot be drawn because direct measurements of the flakes' thickness cannot be performed in this experiment since it requires protection capping of the unstable BP with a polymer. Nevertheless, we showed in Figure 3-9(c) that the frequency changes of LF B modes with the thickness can exceed 10 cm^{-1}, while the frequency variations of HF A_g^1, B_{2g} and A_g^2 modes are much smaller, around 2 cm^{-1}. (*251–254*, *268*) Consequently, the LF modes could offer an effective approach to determine the thickness and probe the interlayer vdW coupling of BP after the corresponding calibration measurements. We expect that the present work can stimulate further experimental efforts to identify the thickness and probe the LF modes, thus establishing more conclusive relationships between them.

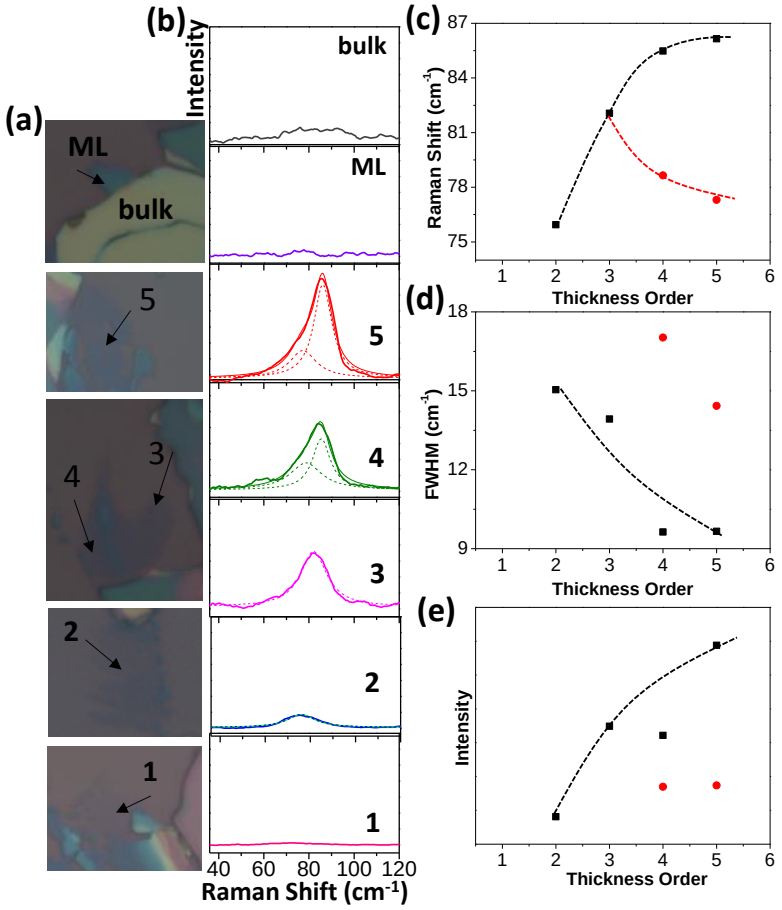

Figure 3-9. (a) Optical images of BP flakes with different thicknesses. The thickness increases with the flake from bottom to top. (b) Raman spectra collected on the flakes

corresponding to (a) in the LF range. The dash lines are the Lorentzian peak fittings. (c-e) Raman shift (c), FWHM (d) and intensities (e) of the breathing modes as a function of the thickness. The black (red) points correspond to the higher-frequency (lower-frequency) breathing mode.

The temperature dependence of Raman spectra is important for understanding the fine structure and properties of the material, probing phonons and their interactions with other particles, which in turn has a large impact on the electronic and thermoelectric device performances. The temperature dependence of the B, A_g^1, B_{2g} and A_g^2 modes of the BP flake in Figure 3-7 is measured under 632 nm laser excitation from -150 to 30 ºC (Figure 3-10). The data are fitted linearly using the equation: (*272*) $\omega = \omega_0 + \chi T$ (red lines in Figure 3-10), where ω_0 is the frequency at T=0 ºC and χ is the first-order temperature coefficient, which defines the slope of the dependence. It can be clearly seen that the different modes have different temperature dependence. In particular, the B mode shows a very weak temperature dependence, which has almost no frequency change in the examined temperature range (Figure 3-10(a)) with $\omega_B = 87.4 - 1.8 \times 10^{-4} T$ for -150 ºC < T < 30 ºC. This suggests a very weak anharmonic property of the B mode in few-layer BP. (*272*, *273*) However, anharmonic phonon effects occur for the HF modes according to the stronger temperature dependence (Figure 3-10(b-d)), where $\omega_{\mathrm{Ag1}} = 361 - 0.0073T$ for A_g^1, $\omega_{\mathrm{B2g}} = 438 - 0.013T$ for B_{2g} and $\omega_{\mathrm{Ag2}} = 465 - 0.012T$ for A_g^2, all for -150 ºC < T < 30 ºC. Furthermore, the first-order temperature coefficient is larger for the in-plane vibrational modes (B_{2g} and A_g^2) than for the out-of-plane vibrational mode (A_g^1). This is consistent with the results obtained for bulk BP. (*262*) The temperature coefficients of the in-plane Raman modes of few-layer BP (-0.013 cm^{-1}/K for B_{2g} mode and -0.012 cm^{-1}/K for A_g^2 mode) are similar to some other layered materials, such as graphene (-0.015 cm^{-1}/K for G band) (*273*, *274*) and MoS_2 (-0.013 cm^{-1}/K for E_{2g} mode). (*275*, *276*)

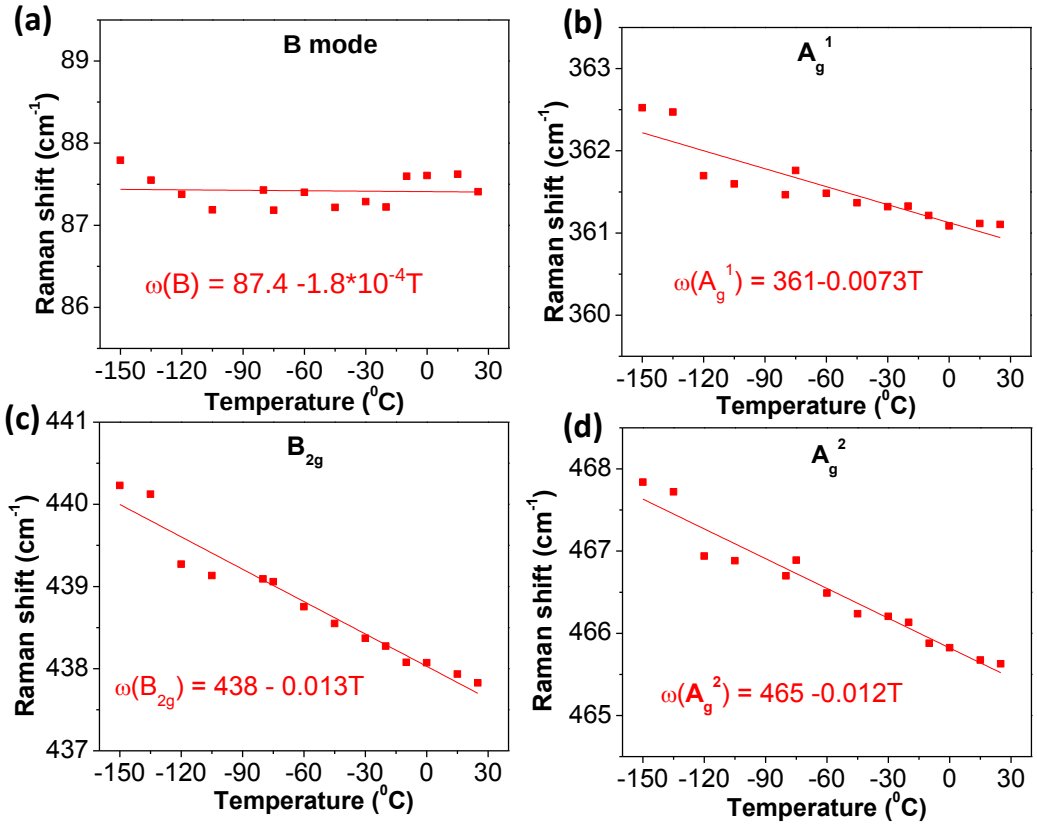

Figure 3-10. Temperature dependence of the frequencies of breathing mode (a), A_g^1 (b), B_{2g} (c) and A_g^2 (d) modes. The red lines are the corresponding fitting lines.

In Figure 3-10, we linearly fitted the data and considered the first-order temperature coefficient χ, which has two components leading to the Raman frequency shift. The temperature dependence of the Raman frequency can be rewritten as $\omega = \omega_0 + \chi_T \Delta T + \chi_V \Delta V = \omega_0 + (\frac{\partial \omega}{\partial T})_V \Delta T + (\frac{\partial \omega}{\partial V})_T \Delta V$, where the first term $(\frac{\partial \omega}{\partial T})_V \Delta T$ is the "self-energy" shift, which is the pure temperature effect, and the second term $(\frac{\partial \omega}{\partial V})_T \Delta V$ is due to the crystal thermal expansion. (*272*, *273*) For the out-of-plane B mode of few-layer BP, which is solely due to interlayer coupling, the contribution to the Raman shift from the second term $(\frac{\partial \omega}{\partial V})_T \Delta V$ depends on the thermal expansion along the out-of-plane direction. Since the interlayer distance does not change appreciably with temperature, the thermal

expansion along the out-of-plane direction can be ignored. (*277*, *278*) Therefore, the contribution from the crystal thermal expansion can be ignored for the B mode, as confirmed by our calculations. Thus, the weak anharmonic behavior of the B mode in the temperature range -150 to 30 ºC in Figure 3-10(a) suggests that the contribution from the first term ($(\frac{\partial \omega}{\partial T})_V \Delta T$) should be near zero as well, indicating the weak phonon coupling for the B mode. For the HF out-of-plane intralayer mode A_g^1, the contribution from the in-plane thermal expansion is also negligible. The anharmonic behavior of A_g^1 mode in Figure 3-10(b) is hence largely due to the "self-energy shift" (i.e., the anharmonic phonon coupling). While for the HF in-plane intralayer modes B_{2g} and A_g^2, the contribution from the in-plane thermal expansion is significant, since tensile stress can be induced in the BP plane and the sequential softening of the P-P bonds occurs with increasing temperature. The anharmonic phonon effect for B_{2g} and A_g^2 in Figure 3-10(c-d) is thus mainly due to the decrease of the force constants by the thermal expansion.

In conclusion, the determination of the thickness and crystalline orientation are two crucial aspects for advancing studies of few-layer BP. Raman spectroscopy is expected to provide considerable insight on both aspects due to the non-destructive and convenient characterization. The identification of the crystalline orientation has been successfully achieved using the polarization dependence of the HF intralayer Raman modes (*252*, *254*). However, these modes fail to provide information on BP's thickness. In this work, for the first time, the LF interlayer breathing modes are observed in few-layer BP and show promising potential for identifying both the crystalline orientation and the thickness, as well as probing the interlayer vdW coupling. The breathing modes are assigned to the same symmetry as the HF A_g modes, so they share similar laser polarization dependence. By rotating the few-layer sample under a parallel polarization configuration using the 632.8 nm laser excitation wavelength, they all show the same intensity variation period of 180° with the strongest intensities occurring when the sample armchair direction is along the polarization direction of the light. The crucial difference is that the LF breathing modes are found to be much more sensitive to the thickness and interlayer interactions, compared to HF Raman modes. Furthermore, the temperature dependence study shows that in the temperature range -150 to 30 ºC, the breathing mode has very small anharmonicity, while

the HF modes show large anharmonic shifts, suggesting different phonon-phonon coupling behaviors among LF and HF modes. Overall, these experimental/theoretical results on BP phonons, especially the low-frequency phonons, should be very helpful for future studies of the electronic and thermal properties of BP thin films.

Chapter 4
Anisotropic Light-Matter Interaction

In 2D materials, there is a very interesting class that has in-plane anisotropy, which means the material properties differ along different in-plane directions. Many newly-emerged 2D materials have in-plane anisotropy, including BP, GaTe, 1T'-$MoTe_2$, $ReSe_2$. It is important to develop characterization techniques to determine the crystal orientation of these in-plane anisotropic 2D materials, as well as to understand their anisotropic light-matter interactions. In this section, such a non-destructive characterization technique is developed, and we will introduce the examples of three materials, BP, GaTe and 1T'-$MoTe_2$.

4.1 Black Phosphorus

In contrast to graphene (*3*) and some transition metal dichalcogenides (*44*), numerous properties of BP (*1*) and other low-symmetry 2D materials (*107*, *279*, *280*) show strong dependence on the in-plane crystalline orientation, such as electrical mobility,(*100*) photoluminescence emission, (*96*) photoresponsivity (*281*) and thermoelectric performance. (*282*) These properties are strongly associated with the behaviors of electrons, phonons and other quasiparticles which can be probed by light-matter interaction using spectroscopy techniques, including optical absorption and Raman scattering. (*100*, *251*, *252*, *267*, *283–286*) Here, we show, both experimentally and theoretically, how the electron-photon and electron-phonon interaction anisotropies in BP can be related to material thickness, as well as photon and phonon energies. (*87*)

The structure of a multi-layer BP is shown in Figure 4-1(a). The *x*, *y*, *z* coordinates, adopted from the conventional notation for BP, are also labeled, where the *x*- and *z*- axes

correspond to the armchair and zigzag directions of the BP layer plane, respectively. (*287*) High-resolution transmission electron microscopy (HRTEM) images and the diffraction patterns of selected areas are used to directly identify the armchair and zigzag directions. As shown in Figure 4-1(b), the atomically resolved HRTEM image indicates that the distance between every other phosphorus atom along the armchair (zigzag) direction is 0.45 nm (0.33 nm), consistent with the lattice parameters from our calculations and reported before. (*251, 284*) To study the anisotropic electron-phonon and electron-photon interactions, polarized Raman spectra measurements and the corresponding TEM characterization were carried out on the same flake. The zigzag direction obtained from the TEM characterization is defined as the 0º angle, from where we start to rotate the sample up to 180º. Raman spectra under different rotation angles were collected under the parallel configuration (i.e., the polarization of Raman scattered light parallel to that of the incident light), shown in Figure 4-1(e,f) (633 nm laser excitation). Three typical Raman modes, A_g^1, B_{2g} and A_g^2 are observed around 361, 438, 466 cm^{-1}, respectively, (*100, 251*) for both flakes with different thicknesses as identified from their optical contrast. The intensity of the A_g modes changes with the variation period of 180º, but the maximum intensity occurs at different polarization angles for the two flakes: either along armchair (the flake in Figure 4-1(c)) or zigzag direction (the flake in Figure 4-1(d)). These combined TEM/Raman measurements unambiguously prove that the maximum Raman intensity of A_g modes can switch direction from armchair to zigzag depending on flake thickness. Furthermore, B_{2g} behave similarly for the two flakes, with an intensity variation period of 90º, and minimum intensity corresponding to the armchair- and zigzag-polarized laser (insets in Figure 4-1(e,f)).

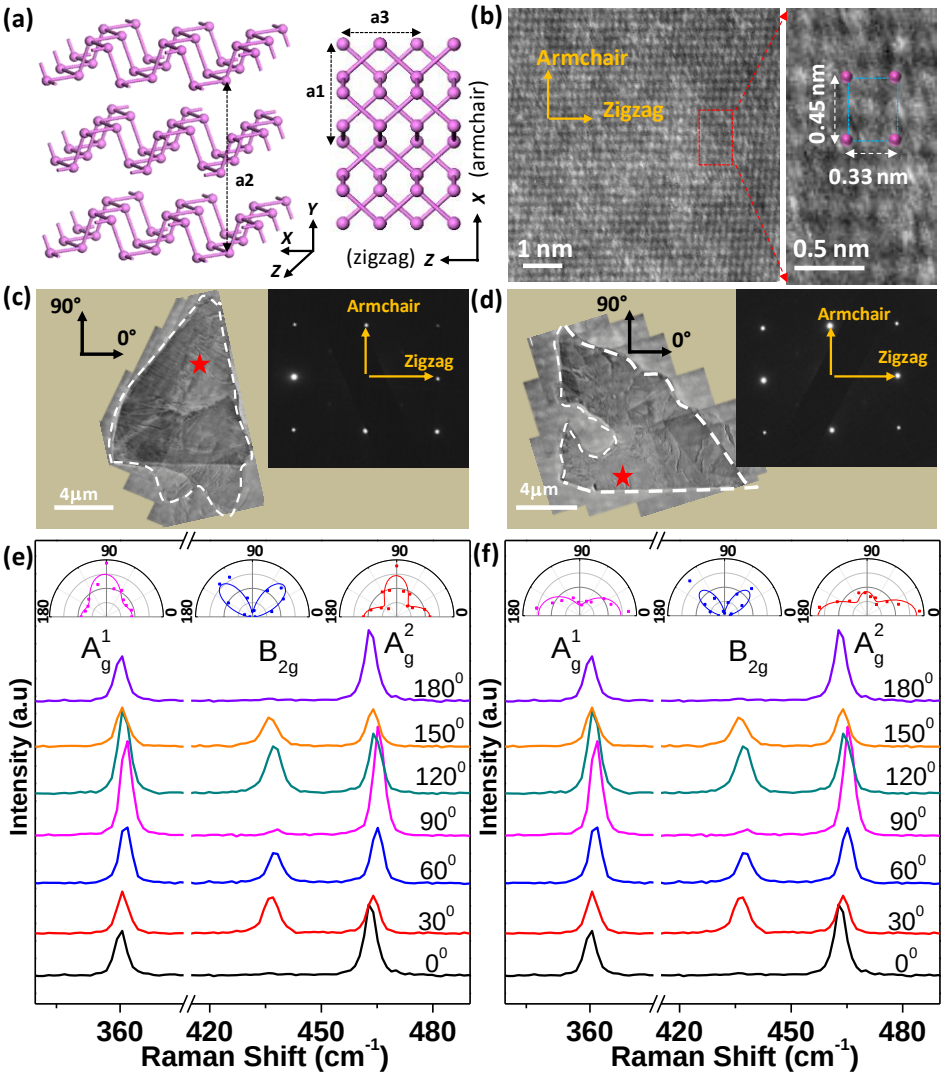

Figure 4-1. TEM characterization and anisotropic Raman scattering of BP. (a) Geometrical structure of multi-layer black phosphorous. (b) Typical HRTEM image of BP. (c)-(d) TEM images of two BP flakes of different thickness and the corresponding diffraction patterns. The red stars label the position where the Raman spectra are collected. (e)-(f) The corresponding polarized Raman spectra of BP flakes in (c) and (d), respectively. 0º corresponds to the configuration with the incident laser polarization along the zigzag direction. Insets on top of (e) and (f) show the corresponding polar plots of the polarization dependent Raman intensity for the two BP flakes. The symbols are the experimental values

and the lines are least-squares fittings. The excitation wavelengths for (e) and (f) are both 633 nm (E_L = 1.96 eV).

To understand the dependence of anisotropic Raman scattering on both the excitation wavelength and flake thickness, we studied 13 BP flakes with different thicknesses using three laser excitation wavelengths (532, 633 and 785 nm). The 13 BP flakes have the same crystalline orientation, because they are mechanically exfoliated from the same bulk BP single crystal and are physically connected to each other. For all the 13 flakes under all of the excitation wavelengths, B_{2g} modes show the same intensity anisotropy. However, the flakes differ regarding A_g^1 and A_g^2: the main axes (the directions for the maximum intensities) can be along either armchair or zigzag direction, strongly depending on the flake thickness and excitation wavelength.

Table 4-1. Four typical categories of the BP flakes with the anisotropic Raman scattering under different incident laser wavelengths. The blue and green arrows indicate the main axes of the polar plots. The data for the 5 nm flake under 785 nm laser excitation is not included in the table because of the weak Raman signal.

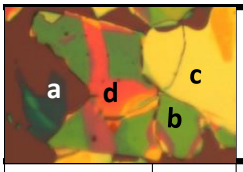		a (~5 nm)	b (~20 nm)	c (~40 nm)	d (~200 nm)
532 nm excitation	A_g^1	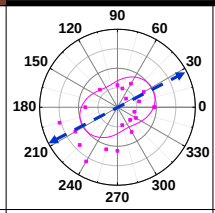	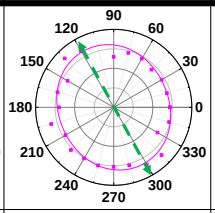	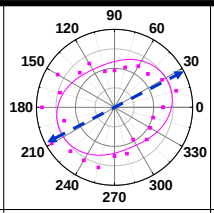	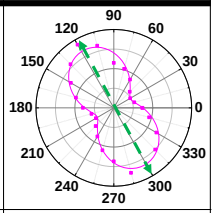
	A_g^2	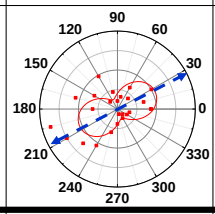	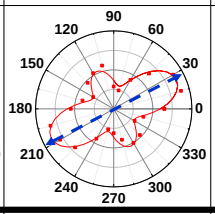	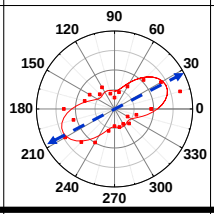	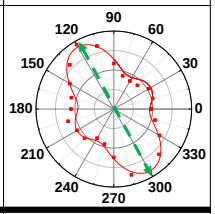
633 nm excitation	A_g^1	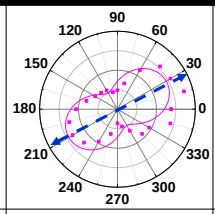	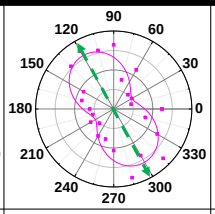	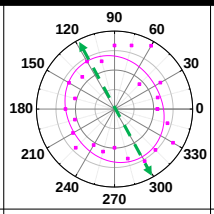	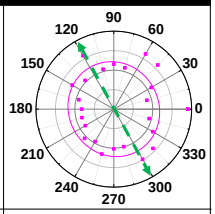
	A_g^2	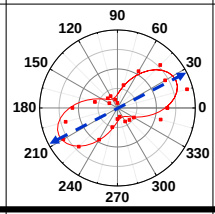	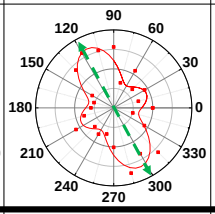	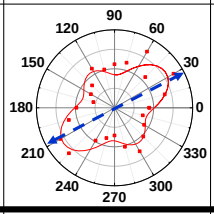	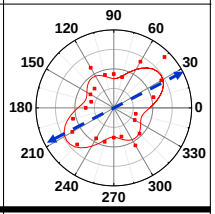
785 nm excitation	A_g^1	----	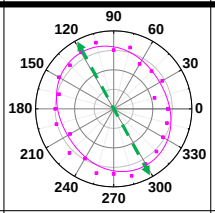	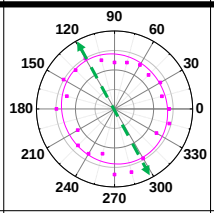	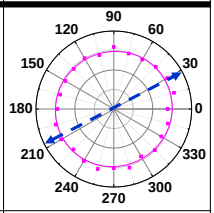
	A_g^2	----	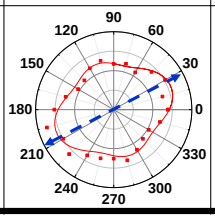	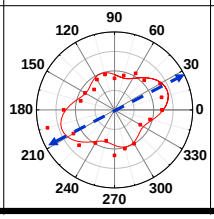	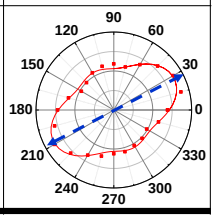

According to the direction of the main axis of the polar plot, Table 4-1 shows polar plots of the Raman intensities of A_g modes for four typical flakes (a, b, c, and d) with thicknesses of around 5, 20, 40, and 200 nm, respectively. Here, 0º is an arbitrary angle corresponding to the sample configuration at the start of the rotation. First, we observed that with the same excitation wavelength, the direction of the main axis of the polar plot changes between armchair and zigzag when the flake thickness increases. Taking the 532 nm excitation data (E_L=2.33 eV) as an example, for the 5 nm flake, both A_g^1 and A_g^2 show the maximum intensity at 30º and 210º. When the flake thickness increases to 20 and 40 nm, the polarization dependence of A_g^1 becomes very weak, while A_g^2 still shows a polarization dependence consistent with results found for the 5 nm flake. For the 20 nm flake, the polarization dependence shows remarkable secondary maxima for A_g^2 at 120º and 300º, which are due to the large phase difference between the complex Raman tensor elements *a* and *c* (discussed in detail later). (*267*) With the thickness of BP flakes increasing to 200 nm, the main axes of the polar plots for both A_g^1 and A_g^2 are at 120º and 300º, perpendicular to those for the 5 nm flake. We also observe a strong dependence of the main axis direction on the laser excitation wavelength. As shown in Table 4-1, for the same flake, the main axes of the polar plots for 532, 633, and 785 nm excitations (E_L=2.33, 1.96, and 1.58 eV) can rotate by 90º, and be along either 30º or 120º. These results conclusively demonstrate that the main axes of A_g modes can switch between armchair and zigzag directions depending on the flake thickness and excitation wavelength, which is of significance since it should settle the existing debate in the literature about whether the A_g main axis is along armchair or zigzag. (*96*, *252*, *267*, *284*) Our systematic study suggests that all of previous works (*96*, *252*, *267*, *284*) are correct but correspond to the presence of multiple independent variables such as different sample thicknesses and excitation wavelengths. Therefore, our results establish that caution is required when Raman spectroscopy is employed for BP crystalline orientation determination. An alternative approach (i.e., angle-resolved optical absorption technique) which is both reliable and simple will be discussed below.

The anisotropic interference effect could contribute to the thickness dependence of anisotropic Raman scattering, but is not the only contributing factor as it cannot explain

the laser energy dependence. (*286*) To reveal the origin of the observed dependence of the anisotropy of the Raman scattering, we carried out in-depth analyses using density functional theory (DFT) and quantum perturbation theory. The Raman scattering process involves the electron-photon and electron-phonon interactions. (*122*) The E_L-dependent Raman intensity for a ν phonon mode can be written as:

$$I_\nu(E_L) = \left| \sum_{i,m,m'} \frac{\langle f|H_{\mathrm{op}}|m'\rangle\langle m'|H_{\mathrm{ep}}^{\nu}|m\rangle\langle m|H_{\mathrm{op}}|i\rangle}{(E_L - \Delta E_{mi})(E_L - \hbar\omega_\nu - \Delta E_{m'i})} \right|^2 \qquad \text{Eq. 4-1}$$

where $\langle f| = \langle i|$, E_L is the laser photon energy, $\Delta E_{mi} = E_m - E_i - \mathrm{i}\gamma$, E_i, E_m, and $E_{m'}$ are the energy of the initial electronic state i and intermediate states m and m', respectively, and γ is the broadening factor. $\langle m|H_{\mathrm{op}}|i\rangle$ and $\langle f|H_{\mathrm{op}}|m'\rangle$ correspond to optical absorption and emission processes, which are related to the electron-photon interaction only, while $\langle m'|H_{\mathrm{ep}}^{\nu}|m\rangle$ is the electron-phonon interaction. From Fermi's Golden Rule, the optical absorption coefficient α obeys:

$$\alpha(E_L) \propto \sum_{m,i} |\langle m|H_{\mathrm{op}}|i\rangle|^2 \delta(E_m - E_i - E_L) \qquad \text{Eq. 4-2}$$

When the electron-photon interaction Hamiltonian H_{op} is treated within the dipole approximation, the electron-photon matrix element $\langle m|H_{\mathrm{op}}|i\rangle$ responsible for an optical transition between states i and m is given by

$$\langle m|H_{\mathrm{op}}|i\rangle \propto \mathrm{P} \cdot \mathrm{D}_{mi} \qquad \text{Eq. 4-3}$$

where **P** is the polarization vector of the incoming light, and the dipole vector $\mathbf{D}_{mi}$ is defined as $\mathbf{D}_{mi} = \langle m|\nabla|i\rangle$. (*288*) In order to obtain a non-vanishing $\langle m|H_{\mathrm{op}}|i\rangle$, $\mathbf{D}_{mi}$ should have a non-zero component parallel to the light polarization vector **P**. Therefore, the selection rule for the optical transition determines which two energy bands are involved in the electron transition for a given incident excitation energy with a specific light polarization, resulting in a different value of $\langle m|H_{\mathrm{op}}|i\rangle$, and in turn, different α for different incident light polarizations and different excitation photon energies.

Figure 4-2(a) shows the calculated optical absorption coefficient α for monolayer,

bilayer, trilayer, 10-layer and bulk BP under armchair- and zigzag-polarized light excitations. The calculated absorption of zigzag-polarized light (black line) starts from around 3.0 eV, while for armchair-polarized light (red line), the absorption starts at a much lower photon energy (i.e., starting at the optical gap). In addition, the calculations indicate that BP absorbs more visible light polarized along the armchair than along the zigzag direction. Moreover, from monolayer to bulk BP, the calculated α does not change significantly with the thickness for the same light polarization (Figure 4-2(a)), indicating that the absorbance ($A = \alpha l$) should increase with thickness (l). We further measured the absorption spectra of the BP flakes with different thicknesses using a micro-absorption setup. The unpolarized light absorbance A indeed increases with the BP thickness l. The absorbance changes when the incident light polarization is modified. Figure 4-2(b,c) show the typical absorbance spectra with both armchair- and zigzag-polarized incident light for a thin (~9 nm) and a thick (~225 nm) flakes, and the corresponding polar plots of the absorbance at 1.96 eV versus the laser polarization are shown in the insets. Similar characteristics of anisotropic absorbance were observed at 2.33 and 1.58 eV. Note that we can directly identify armchair and zigzag directions of the BP crystals through the anisotropic optical absorption, because as indicated by our calculations and previous works, (*72*, *267*, *285*) the absorption along the armchair direction should be larger than that along the zigzag one in the visible spectral range for all flake thicknesses, due to the fact that the imaginary part of refractive index of BP (i.e., the extinction coefficient) in the armchair direction is notably larger than in the zigzag direction. (*289*) The simple anisotropic optical absorption involves only electron-photon interaction and hence provides a reliable alternative for crystalline orientation identification, while Raman scattering involves both electron-photon and electron-phonon interactions and thus is much more complex. For example, A_g^2 Raman intensities of two flakes in Figure 4-2 exhibit opposite anisotropies, due to the more complicated anisotropy of the electron-phonon interaction.

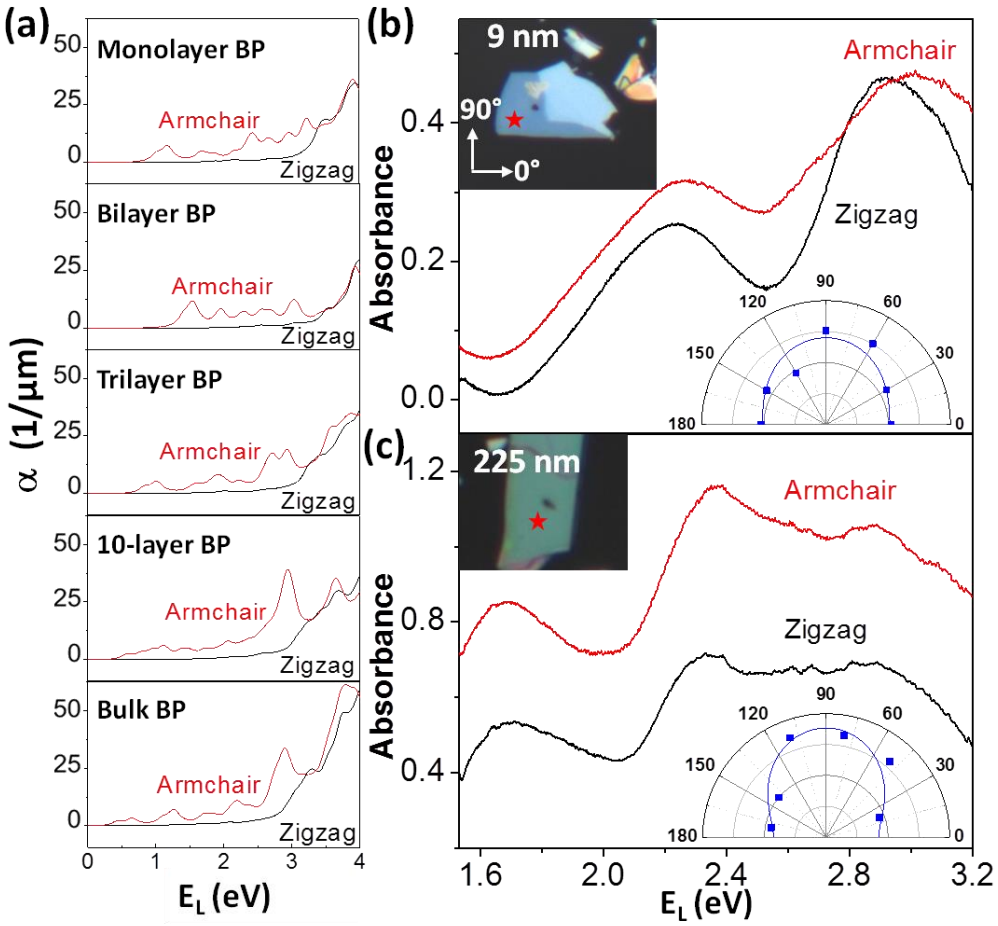

Figure 4-2. Anisotropic absorption of BP flakes with different thicknesses. (a) Calculated absorption coefficient $\boldsymbol{\alpha}$ as a function of laser energy for monolayer, bilayer, trilayer, 10-layer and bulk BP. (b)-(c) Typical absorbance spectra of a thin (b) and a thick (c) BP flake with incident light polarization along the armchair and zigzag directions. Insets: optical images and corresponding polar plots of the absorbance at 633 nm (E_L = 1.96 eV) vs. the sample rotation angle in a plane normal to the flake. The symbols are the experimental values and the lines are least-squares fittings. The red stars in the insets label the sample measurement positions. 0^o and 90^o corresponds to the zigzag and armchair directions, respectively.

To analyze the anisotropy of electron-phonon interaction, first, the energy band structure of monolayer, bilayer, trilayer and bulk BP, as well as the symmetry assignments for all bands at the Γ point were calculated. For different BP thicknesses, the band structures, as well as the symmetry assignments for each band, are different. Figure 4-3(a) shows the calculated band structure of a trilayer BP. In particular, four energy bands with symmetries B_{2u}, B_{3g} and A_u are labeled. Figure 4-3(b,c) show two typical examples of the optical absorption for trilayer BP with $E_L = 0.82$ eV and $E_L = 4.33$ eV, respectively. For $E_L = 0.82$ eV, the electron transition occurs between the energy bands $B_{3g} \rightarrow B_{2u}$. The anisotropic absorption for this case shows that the maximum (minimum) absorption occurs when the laser polarization is along armchair (zigzag) due to the symmetry, shown in Figure 4-3(b), while for $E_L = 4.33$ eV, the $A_u \rightarrow B_{3g}$ transition occurs with the reverse anisotropic absorption due to the different symmetry, shown in Figure 4-3(c). Other than the transitions shown in Figure 4-3(b,c), $B_{1u} \rightarrow A_g$ transition with E_L= 2.00 eV and $A_g \rightarrow B_{3u}$ transition with E_L= 5.86 eV contribute to the maximum absorption along armchair and zigzag directions, respectively, consistent with the results shown in Figure 4-2(a) that the absorption along armchair is preferable than zigzag in the visible spectral range. In Raman scattering, H_{ep}^{v} selects the symmetry of $|m\rangle$ and $|m'\rangle$, which should have the same and different symmetries for A_g and B_{2g} modes, respectively, and the shape of the polar plot of the Raman intensity should be the product of the two anisotropic electron-photon interaction processes, if we assume that the electron-phonon interaction H_{ep}^{v} has no polarization dependence. Under this assumption, the anisotropic Raman intensities of A_g modes would always show a variation period of 180° with the main axis along armchair direction with laser excitation in the visible spectral range (i.e., the same as for the anisotropic absorption). The symmetry combination of the initial, intermediate and final states allowed by the selection rule are listed in Table 4-2 and Table 4-3. Obviously, this conflicts with our experimental observation that the anisotropy of A_g modes is more complicated than the anisotropy of optical absorption, and is intricately dependent on the thickness, excitation wavelength and phonon energy. Therefore, our angle-resolved spectroscopy measurements successfully revealed the anisotropic electron-phonon

interaction in BP.

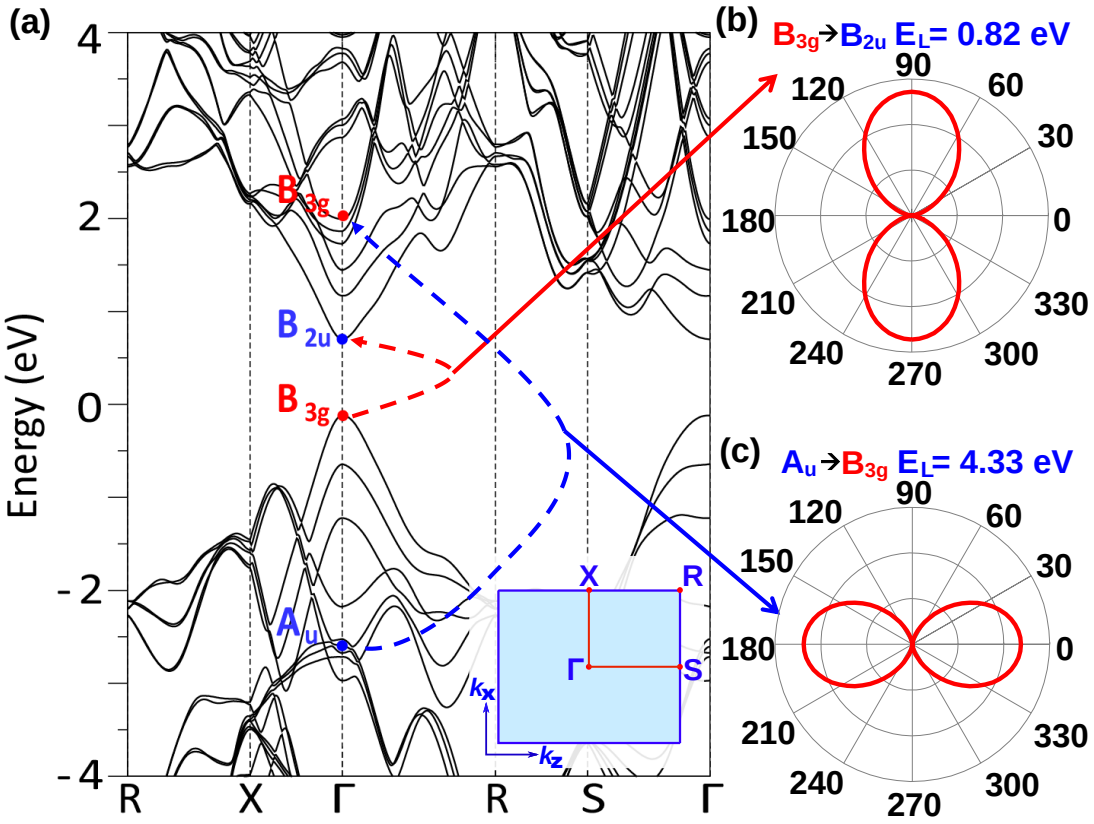

Figure 4-3. Optical selection rules in black phosphorus and the calculated anisotropic absorption. (a) Calculated electronic band structure $E(k)$ of trilayer BP. B_{3g} bands are indicated by red labels while B_{2u} and A_u bands are indicated by blue labels at the Γ point. Inset: 2D Brillouin zone of trilayer BP. (b)-(c) Calculated polarization dependence of the optical transition probability from B_{3g} to B_{2u} (b) and from A_u to B_{3g} (c) as indicated in (a). 0^o (90^o) corresponds to the zigzag (armchair) direction of BP.

As electron-phonon interaction is a governing parameter for electrical, thermal, thermoelectric and superconductive properties in materials,(*3*, *290–292*) our findings provide rich information for the study of anisotropic 2D materials. For instance, the weaker polarization dependence of A_g^1 compared to A_g^2 indicates that the out-of-plane vibrations (A_g^1) couple less anisotropically with in-plane electronic states compared to the in-plane

vibrations (A_g^2).(*290*, *292*, *293*) In addition, the selectivity of the Raman anisotropy to the flake thickness and laser energy (Table 4-1) indicates that the electrons couple strongest to A_g phonons in either armchair or zigzag direction, depending on the symmetries of the involved electronic states (Figure 4-3(a)). Therefore, our combined angle-resolved Raman and optical absorption measurements facilitate the understanding of the electron-phonon interaction in anisotropic 2D materials.

Table 4-2. Selection rules for intermediate states *m* and *m'* for a given initial state $|i\rangle$ and for polarization vector *xx* or *zz* which both correspond to the A_g phonon excitation. These selection rules correspond to the following product of matrix elements: $\langle f|H_{op}|m'\rangle\langle m'|H_{ep}(A_g)|m\rangle\langle m|H_{op}|i\rangle$ with $\langle f| = \langle i|$.

xx		***zz***	
$\|i\rangle$	$\|m\rangle = \|m'\rangle$	$\|i\rangle$	$\|m\rangle = \|m'\rangle$
A_g	B_{1u}	A_g	B_{3u}
B_{1g}	A_u	B_{1g}	B_{2u}
B_{2g}	B_{3u}	B_{2g}	B_{1u}
B_{3g}	B_{2u}	B_{3g}	A_u
A_u	B_{1g}	A_u	B_{3g}
B_{1u}	A_g	B_{1u}	B_{2g}
B_{2u}	B_{3g}	B_{2u}	B_{1g}
B_{3u}	B_{2g}	B_{3u}	A_g

Table 4-3. Selection rules for intermediate states *m* and *m'* for a given initial state $|i\rangle$ and polarization vector *xz* or *zx* which both correspond to the B_{2g} phonon excitation. These selection rules correspond to the following product of matrix elements: $\langle f|H_{op}|m'\rangle\langle m'|H_{ep}(B_{2g})|m\rangle\langle m|H_{op}|i\rangle$, with $\langle f| = \langle i|$.

xz			zx		
$\|i\rangle$	$\|m\rangle$	$\|m'\rangle$	$\|i\rangle$	$\|m\rangle$	$\|m'\rangle$
A_g	B_{1u}	B_{3u}	A_g	B_{3u}	B_{1u}
B_{1g}	A_u	B_{2u}	B_{1g}	B_{2u}	A_u
B_{2g}	B_{3u}	B_{1u}	B_{2g}	B_{1u}	B_{3u}
B_{3g}	B_{2u}	A_u	B_{3g}	A_u	B_{2u}
A_u	B_{1g}	B_{3g}	A_u	B_{3g}	B_{1g}
B_{1u}	A_g	B_{2g}	B_{1u}	B_{2g}	A_g
B_{2u}	B_{3g}	B_{1g}	B_{2u}	B_{1g}	B_{3g}
B_{3u}	B_{2g}	A_g	B_{3u}	A_g	B_{2g}

The anisotropic Raman scattering can also be numerically understood from a semi-classical perspective. Since the Raman tensor is related to the derivative of the complex dielectric tensor with respect to the phonon vibration (the imaginary part of the dielectric tensor corresponds to optical absorption), the Raman tensor of an A_g mode, $\tilde{R}(A_g) = \begin{pmatrix} a & \cdot & \cdot \\ \cdot & b & \cdot \\ \cdot & \cdot & c \end{pmatrix}$, is complex. (*267*) The corresponding Raman intensity under the parallel configuration is therefore:

$$I_{A_g}^{\parallel} = \left|(\sin\theta, 0, \cos\theta)\tilde{R}(\sin\theta, 0, \cos\theta)^T\right|^2$$

$$= |a|^2\left[(sin^2\theta + \left|\frac{c}{a}\right| cos\Phi_{ca}cos^2\theta)^2 + \left|\frac{c}{a}\right|^2 sin^2\Phi_{ca}cos^4\theta\right] \qquad \text{Eq. 4-4}$$

where θ is the angle between the laser polarization and zigzag direction; Φ_{ca} is the phase difference between the Raman tensor elements *c* and *a*. The amplitude ratio $|c/a|$ and Φ_{ca} are the indicators of the in-plane anisotropy in BP. From Eq. 4-4, $|c/a| > 1$ or $|c/a| < 1$ determines whether the main axis is along zigzag or armchair direction, and Φ_{ca} is positively correlated with the strength of the secondary maximum on the Raman polarization profile. The $|c/a|$ and Φ_{ca} values, obtained by directly fitting the experimental Raman polar plot with Eq. 4-4, are shown in Figure 4-4(a,b) for both A_g^1 and

A_g^2 with different thicknesses under 633 nm laser excitation. Note that optical interference has proved to considerably affect or enhance Raman intensities for layered materials, such as multilayer graphene, MoS_2, etc. (*294*, *295*) Similar interference effect can also occur in BP. (*286*) More importantly, due to its unique in-plane anisotropy as discussed above (i.e., different refractive indices in the zigzag and armchair directions, and the imaginary part in particular), the interference enhancement effect is also polarization-dependent. To evaluate the importance of this effect, we calculated the interference enhancement factors of the A_g modes along the zigzag and armchair directions (more details about the calculations in Appendix). For the three laser lines we used, the interference enhancement is stronger when the incident polarization is along the zigzag direction, due to the weaker absorption in that direction. The ratio of the enhancement factors between the zigzag and the armchair directions varies significantly with the BP thickness, which in turn can influence the thickness dependence of Raman intensity ratio $|c/a|$ between the zigzag and the armchair directions. In Figure 4-4(c,d), we eliminate the effect of interference on Raman intensity, and thus the $|c/a|$ and Φ_{ca} values shown are intrinsically from the BP flakes. While $|c/a|$ ratios do not show a clear evolution trend in Figure 4-4(a), the $|c/a|$ ratios in Figure 4-4(c) show a roughly increasing trend with increasing thicknesses and are generally smaller than 1, in agreement with results from Ref. (*286*). This suggests that after elimination of interference effect, the maximum intensities of anisotropic Raman are generally along the armchair direction, thus the thickness dependence becoming simpler. Comparing Figure 4-4(b,d), we notice Φ_{ca} also changes after the elimination of interference effect. These phenomena indicate that the interference effect is considerable for the complex thickness dependence of Raman polarization. However, it is not sufficient to explain all experimental observations. In fact, it is not reasonable that A_g^1 and A_g^2 modes can show different Raman anisotropy if interference effect is the dominating contributor. Moreover, $|c/a|$ ratios are still different from flakes with different thicknesses. These results can be attributed to the quantum effect of optical transition selection rule, as we have explained before. The combination of the quantum theory and interference effect can explain all the observations. Φ_{ca} is relatively small for A_g^1 compared to A_g^2 with different thicknesses, which is also reflected in Table 4-1 where the secondary maxima of A_g^1 are not obvious. As discussed above, this may be because the out-of-plane vibration A_g^1 is relatively insensitive to in-

plane anisotropy. In contrast, Φ_{ca} is relatively large for A_g^2, because of its in-plane vibration.

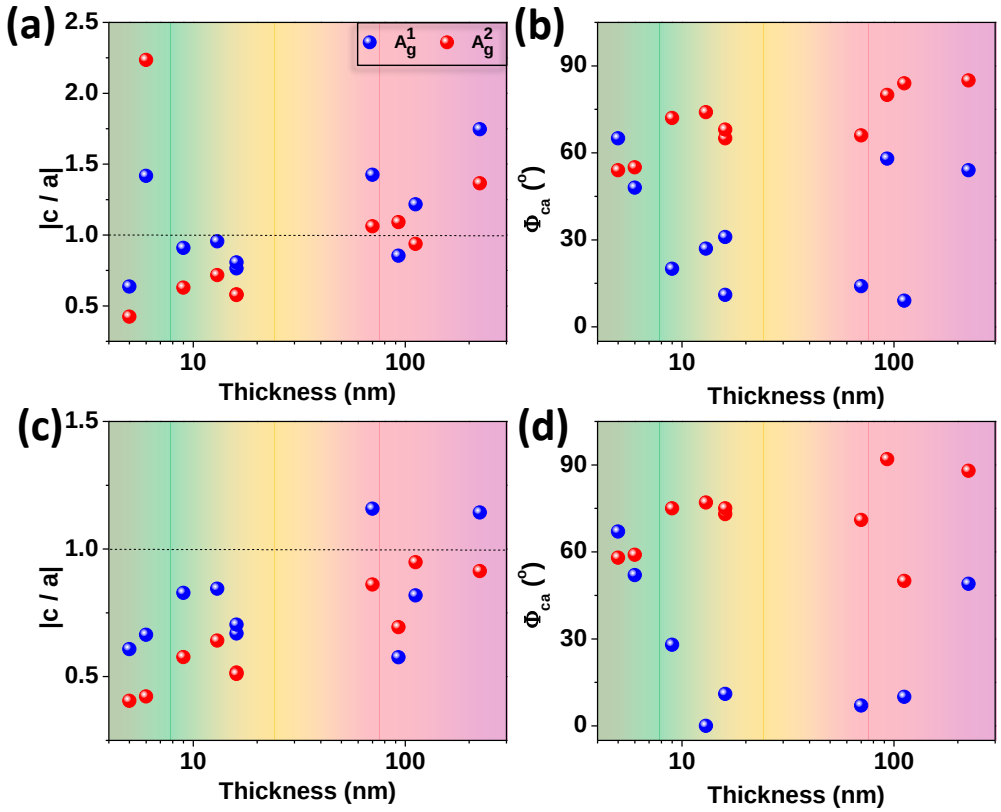

Figure 4-4. $|c/a|$ (a,c) and Φ_{ca} (b,d) as a function of the thickness of BP flakes. The data are from the anisotropic Raman spectra of BP with different thicknesses under 633 nm (E_L=1.96 eV) laser excitation wavelength. (a-b) and (c-d) are the results before and after the elimination of interference effect, respectively. Data in blue and red are for the A_g^1 and A_g^2 modes, respectively. The horizontal dashed line in (a,c) indicates $|c/a|$=1. (a-d) are divided horizontally with color shades corresponding to the thicknesses in Table 4-1: dark green, green, yellow and pink correspond to thicknesses of approximately 5, 20, 40 and 200 nm, respectively.

In conclusion, we have uncovered the origins of the anisotropic light-matter interactions in BP, including the electron-photon and electron-phonon interactions. The

process and selection rule we revealed in BP is applicable to any other anisotropic materials such as GaTe and SnSe. Therefore, our work offers key insights into the light-matter interactions in anisotropic layered materials, thereby paving a coherent route for advancing the study of their anisotropic electrical, thermal and thermoelectric properties.

4.2 Gallium Telluride

In this work, we report the in-plane optical anisotropy in the low-symmetry layered material GaTe, including its anisotropic optical absorption, optical extinction and Raman scattering, which reveal anisotropic light-matter interactions. (*68*) We found that a GaTe multilayer shows a weak anisotropy of optical absorption and extinction in the visible spectral range, but Raman intensity shows a strong dependence on crystalline orientation. These experimental observations can be explained by first-principles calculations and group theory analyses. Moreover, due to the thickness dependence of the energy band structure and the symmetry of each energy level, the anisotropies of the Raman intensity show an intricate dependence on flake thickness, photon and phonon energies, which can be explained by group theory and optical transition selection rules. This work provides important guidelines for the design of optoelectronic and thermoelectric devices made of GaTe, and presents a general methodology for the study of optical anisotropy in layered materials with in-plane anisotropy.

Bulk GaTe is a layered material with monoclinic structure as shown in Figure 4-5(a-b), which consists of 6 Ga and 6 Te atoms in the primitive unit cell. The adjacent GaTe layers are stacked to each other in the ***z***-direction by van der Waals forces. Bulk GaTe has C_{2h}^3 (*C2/m*) symmetry, (*107*, *296*, *297*) which has a two-fold rotational axis C_2 (***y***-axis) and a mirror plane σ_h (***x***-***z*** plane). The inset in Figure 4-5(a) illustrates the Brillouin zone with several high-symmetry points ***Γ***, ***M***, ***Z***, ***M'***, ***P*** and ***N***. According to our density functional theory (DFT) calculations, a direct bandgap is located at the ***Z*** point ($E_g = 1.65$ eV) and slightly larger bandgaps can be seen at the ***P*** or ***M*** point ($E_g = 1.80$ eV), which is consistent with the previous works. (*111*, *298*) Both the highest valence band and the lowest conduction band are almost flat along the ***M***−***Z***−***M'***−***P***−***M*** line of the Brillouin zone and optical transitions for energies close to the bandgap are expected to occur along this line.

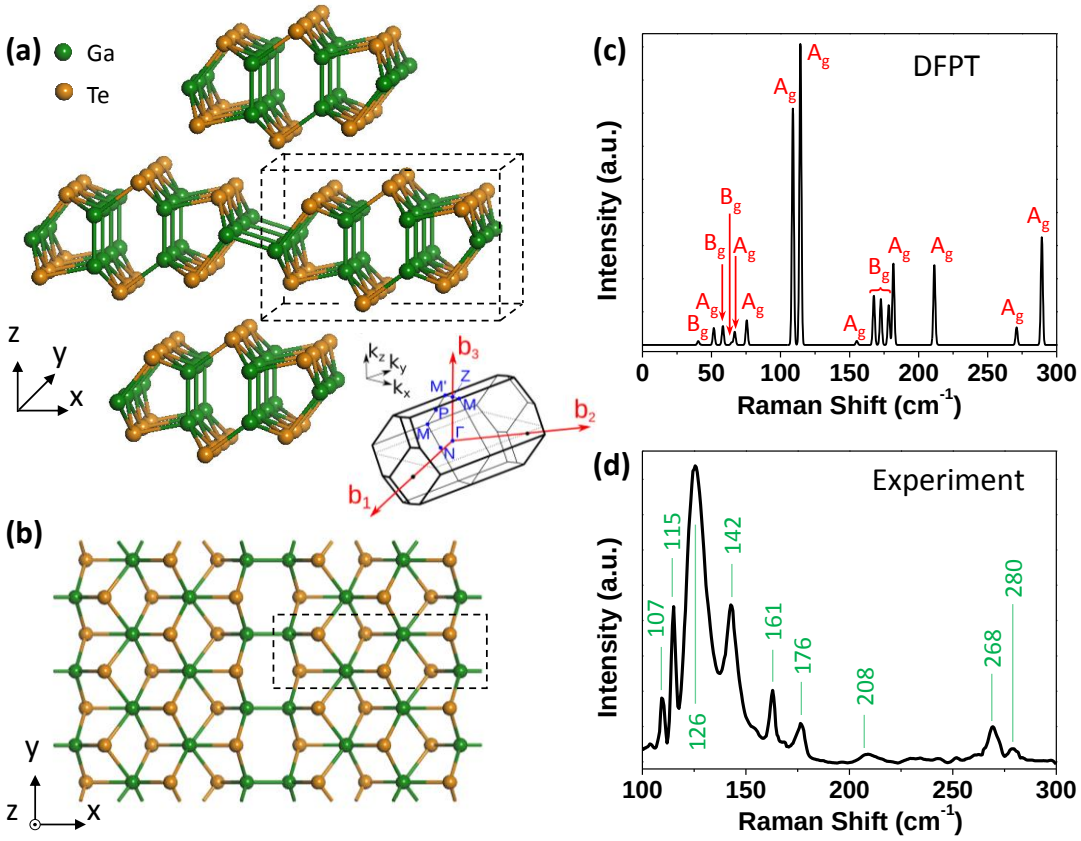

Figure 4-5. Crystal structure and Raman spectra of layered GaTe. (a) Front view for the crystal structure of bulk GaTe. (b) Top view for monolayer GaTe. The black dashed boxes in (a) and (b) correspond to the same group of atoms. Inset of (a): Brillouin zone for the primitive unit cell of bulk GaTe. (c) Calculated non-resonant Raman spectrum of bulk GaTe by DFPT methods. The symmetry of each mode is labeled. (d) Experimental Raman spectrum of a 125 nm thick GaTe flake at room temperature and under vacuum (10^{-5} mbar). The measurement was performed with 532 nm laser excitation. The peak frequencies are shown in units of cm^{-1}.

The non-resonant Raman spectrum obtained from the density functional perturbation theory (DFPT) calculations is shown in Figure 4-5(c). According to group theory and the calculated phonon dispersion relation, GaTe has 36 phonon modes in total, 18 of which are Raman-active: 12 A_g modes and 6 B_g modes. Most of the calculated Raman peaks were also observed in our experiments, as seen in Figure 4-5(d) for a Raman spectrum on a

multilayer GaTe flake measured in vacuum. The Raman modes that were not observed in experiments have either weak intensity or low frequency (< 100 cm^{-1}), which is out of the detection range of conventional Raman spectrometers.

To study the in-plane anisotropic optical properties, we carried out angle-resolved polarized Raman measurements. In Figure 4-6, the optical image (Figure 4-6(a)) of a GaTe flake on a TEM (transmission electron microscopy) grid is shown together with the corresponding TEM diffraction pattern (inset of Figure 4-6(a)) and the polarized Raman spectra (Figure 4-6(b)) with different polarization angles under parallel configuration. Eight Raman modes can be readily observed experimentally: 107, 115, 126, 142, 161, 208, 268 and 280 cm^{-1}. From the electron diffraction pattern, the 0° axis corresponds to the ***x***-axis of the crystalline orientation shown in Figure 4-5(a-b). According to the DFPT calculations, five Raman modes are A_g modes (107, 115, 208, 268, 280 cm^{-1}), one is B_g mode (161 cm^{-1}), and two are double-resonant modes (126, 142 cm^{-1}). These double-resonant modes (*299*, *300*) are created by two phonons of ~60 cm^{-1} and ~70 cm^{-1}, respectively, showing their broad features with Raman intensities proportional to the excitation laser power. The shape of the phonon dispersion is flat and the phonon density of states is large around 60 - 70 cm^{-1}, which is in good agreement with our observation that the Raman modes at 126 and 142 cm^{-1} are strong. (*299*) Moreover, double-resonant modes generally have a weak anisotropy and exhibit broad features because many different combinations for two phonons are possible to contribute to Raman intensity (not necessarily just the $\boldsymbol{\Gamma}$ point phonons).

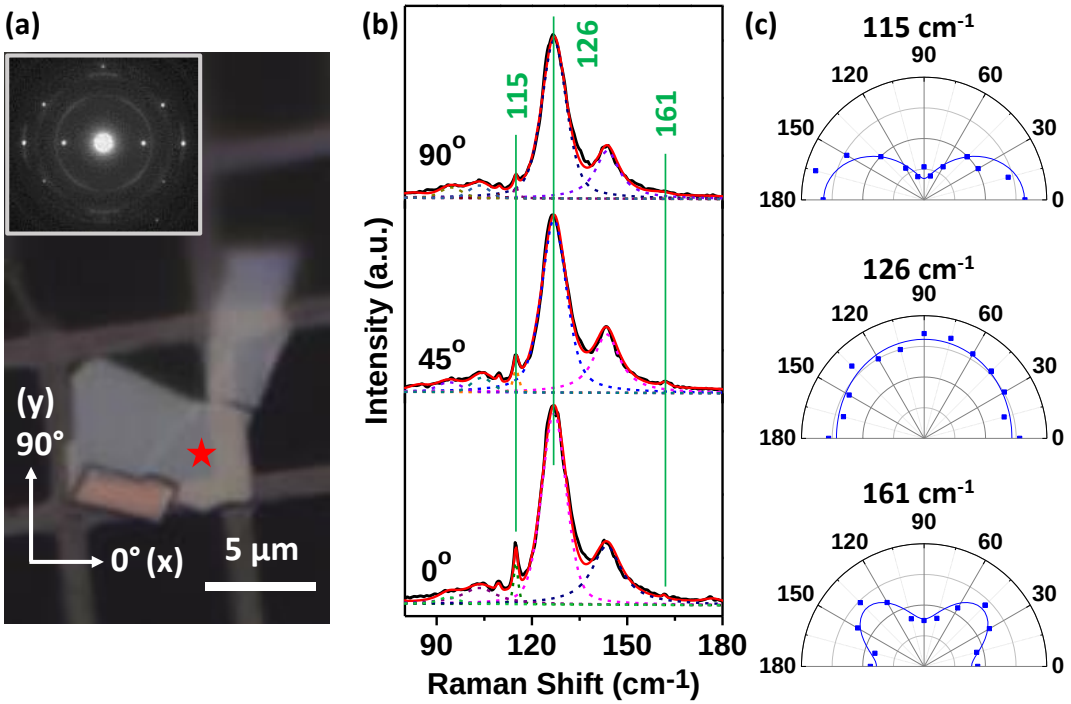

Figure 4-6. Polarized Raman spectra and diffraction pattern of a GaTe flake on a TEM grid. (a) The optical image of the GaTe flake on the TEM grid. 0° (90°) corresponds to *x*- (*y*-) axis of the GaTe crystal. The star indicates where the measurement was performed. Inset: The corresponding electron diffraction pattern. (b) Polarized Raman spectra of GaTe with polarization angles 0°, 45° and 90°. (c) The Raman intensity vs. polarization angle for three typical types of Raman modes: A_g mode (115 cm^{-1}), double-resonant mode (126 cm^{-1}) and B_g mode (161 cm^{-1}); these three modes are also marked in (b). The squares are experimental values and the curves are numerical fittings. The Raman shift values are labeled above each panel. The excitation wavelength in (b-c) is 633 nm.

The polar plots of the angle-resolved polarized Raman intensity are summarized in Figure 4-6(c) for three typical Raman modes: A_g (115 cm^{-1}), double-resonant (126 cm^{-1}) and B_g (161 cm^{-1}) modes, which are also marked in Figure 4-6(b). It can be seen that Raman-active modes show a variety of degrees of anisotropy: under 633 nm laser excitation, the double-resonant modes at 126 and 142 cm^{-1} exhibit weak anisotropy, while the modes at 107, 115, 208, 268 and 280 cm^{-1} show relatively stronger anisotropy with a

period of 180° and with maximum intensities along the ***x***-axis.(*301*) This anisotropy supports the interpretation of the five modes with the same A_g symmetry. On the other hand, the mode around 161 cm^{-1} shows a four-fold anisotropy with a period of 90°, and the maximum (minimum) intensities along 45° and 135° (along the crystal axes ***x*** and ***y***). This further confirms the different symmetry (B_g) of the 161 cm^{-1} mode(*301*) compared to the five other modes with A_g symmetry. It can be seen that the crystalline orientation directly probed by TEM (inset of Figure 4-6(a)) is well matched with the polarized Raman profiles (Figure 4-6(c)). These phenomena in GaTe show that polarized Raman spectroscopy can indicate crystalline orientation, and the anisotropy of the Raman intensity is strongly related to phonon symmetry. Similar phenomena have also been reported in other 2D materials with in-plane anisotropy. (*252*, *302*)

Furthermore, the detailed dependences of the in-plane anisotropy of the Raman intensity on different factors: flake thickness, excitation laser wavelength and phonon frequency, were all studied. In Table 4-4, we list the polar plots of the polarized Raman intensities under different excitation wavelengths (532, 633 and 785 nm) and with different flake thicknesses (58 nm and 136 nm) for first-order Raman modes at 107, 115, 161, 208, 268 and 280 cm^{-1}. The flakes used for the Raman measurements in Table 4-4 are mechanically exfoliated from a single-crystal bulk GaTe, and show variations in thicknesses but are physically connected that ensures the same crystalline orientation. In fact, we have measured more than 60 flakes, and found that the Raman profiles are maintained for thicknesses from 51 to 68 nm, in which the 58 nm-thickness is chosen as the representative for this thickness range. Similarly, the Raman profiles for the flake with a thickness of 136 nm also represent the thickness range from 110 to 170 nm. For few-layer flakes (thickness smaller than ~15 nm), the Raman signals are very weak, partly due to the change of the atomic structure and the small light-matter interactions in those GaTe flakes. (*106*, *107*)

Table 4-4. The Raman anisotropy dependence on flake thickness, laser wavelength and phonon frequency. The Raman intensity polar plots of two flakes with typical thicknesses:

58 and 136 nm, are shown here. These two flakes have the same crystalline orientation. The dots are experimental values and the curves are numerical fittings. The laser excitation wavelengths and the Raman frequencies are also labeled. 0° (90°) corresponds to *x*- (*y*-) axis of the GaTe crystal.

Laser / Peak (cm^{-1})	**532 nm**		**633 nm**		**785 nm**	
	Thin (58 nm)	Thick (136 nm)	Thin	Thick	Thin	Thick
107	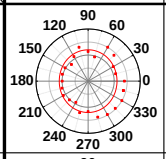	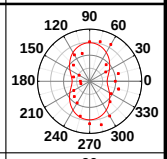	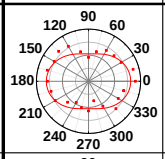	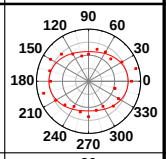	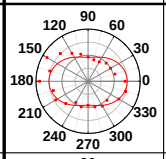	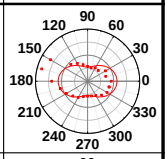
115	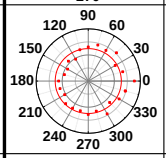	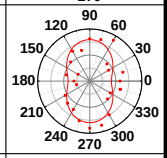	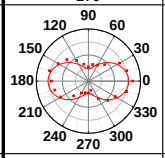	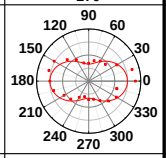	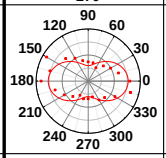	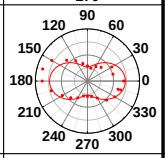
161	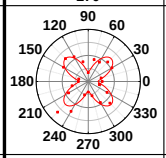	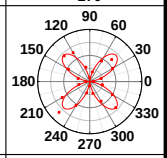	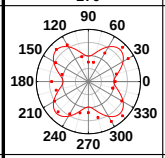	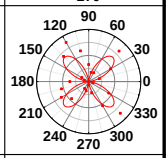	weak	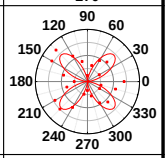
208	weak	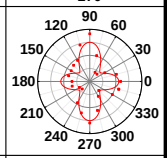	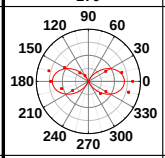	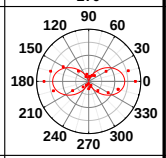	weak	weak
268	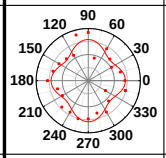	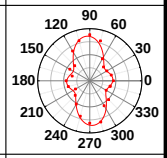	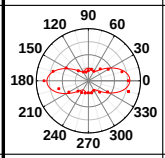	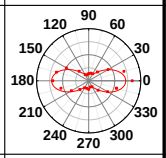	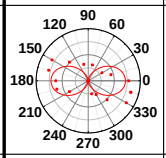	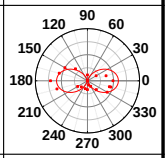
280	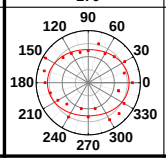	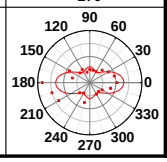	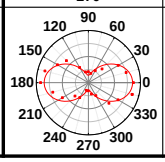	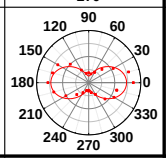	weak	weak

As seen in Table 4-4, the degree of anisotropy for the Raman modes depends not only on phonon mode symmetry, but also on phonon frequency (phonon energy), excitation laser wavelength (photon energy) and flake thickness. It can be seen from Table 4-4 that the major maximum of the Raman intensity is aligned along either 0° or 90° for all the Raman modes except for the 161 cm^{-1} mode, and for all the excitation wavelengths used. This indicates that either 0° or 90° corresponds to the ***x***-axis of the GaTe crystal. The Raman anisotropic profiles are observed to change with laser excitation wavelengths: the major maxima for 532 nm laser excitation are seen to be rotated by 90° from the major maxima for the 633 and 785 nm laser excitation for some Raman modes, such as the 107, 115, 208 and 268 cm^{-1} modes. We also notice that the major maxima of the polarized Raman intensity remain along the same direction (along 0°) for all the A_g modes measured under 633 and 785 nm laser excitations, but can change their directions to be either along 0° or 90° for 532 nm laser. According to the results in Figure 4-6, the major maxima for the Raman polar plots of the A_g modes with 633 nm laser excitation correspond to the ***x***-axis of the crystal. Therefore, in Table 4-4, 0° corresponds to the ***x***-axis of the GaTe crystal. The two groups of flake thicknesses presented here also show differences in the Raman profiles, which indicates the dependence of the anisotropic light-matter interactions on the flake thickness. From Table 4-4, we can see that the thin and thick flakes share the same major maxima direction (either at 0° or at 90°) for different Raman modes and excitation wavelengths. The Raman anisotropy dependence on flake thickness is reflected in the polar plot shape (or the degree of anisotropy): some modes show stronger anisotropy for the thick flakes than the thin flakes (such as 107, 115, 268, 280 cm^{-1} modes under 532 nm laser), but some show similar degrees of anisotropy for both the thin and the thick flakes (such as 107 cm^{-1} mode under 633 nm laser, and 115 cm^{-1} mode under 785 nm laser), and some show stronger anisotropy for the thin flakes than the thick ones (such as 115 cm^{-1} mode under 633 nm laser). This complexity in the degree of anisotropy can be explained by the optical transition selection rules, which will be described below. In addition, it can be seen that for some modes, secondary maxima appear, such as those at 0° for the 208 and 268 cm^{-1} modes, and at 90° for the 280 cm^{-1} mode measured under 532 nm (E_L=2.33 eV) laser

excitation in the thick flakes. This observation is similar to the case of BP, (*87*, *267*, *302*) and suggests that the light absorption, birefringence and phase difference in the Raman tensor elements are relevant for GaTe. (*267*, *302*, *303*) We can also see that the secondary maxima for the thick flakes are more pronounced than those measured for the thin ones for certain modes (268 and 280 cm^{-1} under 532 nm laser). These observations further confirm that the secondary maxima are related to the optical absorption of GaTe and to the birefringence effect, (*87*, *267*, *302*, *303*) since the thicker flakes have larger absorption and the absorption coefficient of GaTe at 2.33 eV (532 nm) is larger than that at 1.96 eV (633 nm) and at 1.58 eV (785 nm). These effects will be explained below. The results presented in Table 4-4 provide a strong indication of the anisotropic Raman intensity in GaTe and its intricate dependence on phonon energy, photon energy and flake thickness, which offers useful guidelines for the applications of GaTe.

Besides Raman scattering, we further studied the optical absorption and optical extinction of GaTe flakes. The extinction is calculated as $\ln(I_0/I)$, where I and I_0 are the light intensities transmitted through the quartz substrate on and off a GaTe flake, respectively. Since the origin of the extinction is optical absorption in GaTe, it is important to measure the anisotropy of optical extinction. Here we measured the extinction spectra in the wavelength range from 450 nm to 790 nm. The extinction for non-polarized light increases with increasing flake thicknesses. For very thin GaTe flakes, such as the 6 nm-thick flake, almost no optical extinction is observed. The extinction of GaTe for polarized light was further investigated on the flakes on a quartz substrate shown in Figure 4-7(a). In order to determine the crystalline orientation of the flakes, we used the results of polarized Raman measurements on them, which indicated the 0° and 90° orientations in Figure 4-7(a) correspond to ***x***- and ***y***-axes, respectively.

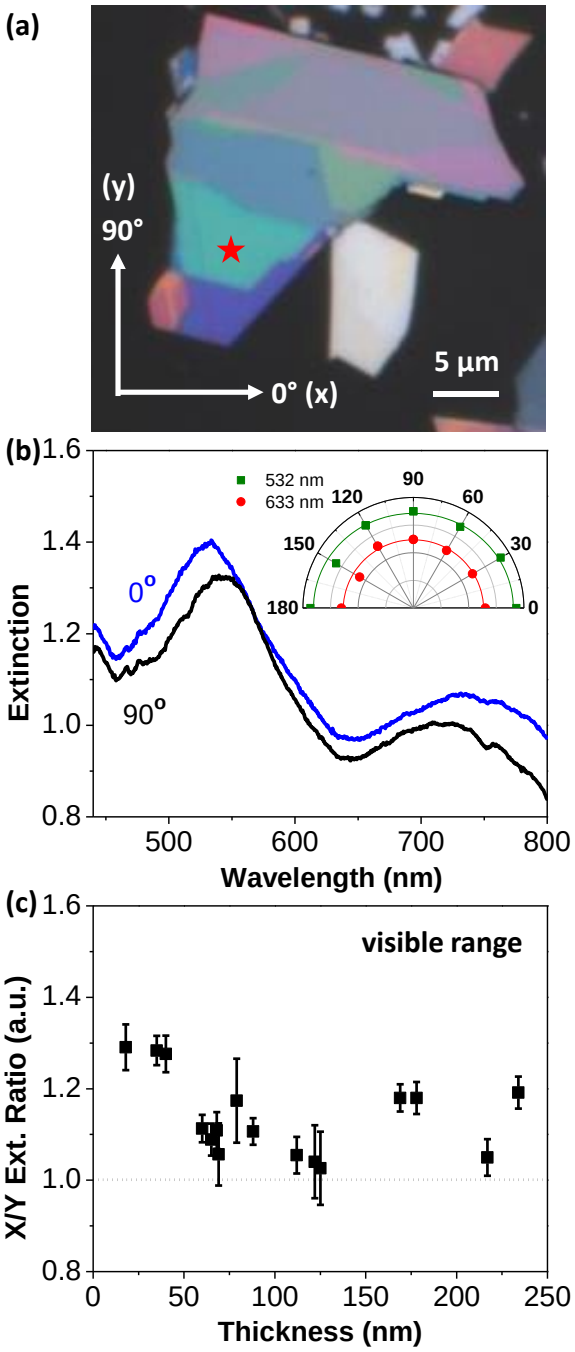

Figure 4-7. Experimental optical extinction of GaTe. (a) The optical microscope image of GaTe flakes on a quartz substrate. (b) Polarized optical extinction spectra measured with incident light polarized at 0° and 90° on the flake labeled with a star in (a). The flake thickness is 112 nm. The inset of (b) shows the extinction at wavelengths 532 and 633 nm with different polarization angles. The polarization angles correspond to the angular

coordinates in (a). 0° and 90° correspond to *x* and *y* axes of the GaTe crystal, respectively. (c) Thickness dependence of the extinction ratio of *x*- and *y*- polarized light. The optical extinction is integrated in the visible spectral range from 450 to 790 nm. The dashed horizontal line indicates that the ratio equals 1.0 (isotropic).

The optical extinction spectra on the 112 nm-thick flake (labeled with a star in Figure 4-7(a)) for ***x***- and ***y***-polarized incident light are shown in Figure 4-7(b). It can be seen that the extinction for ***y***-polarization is slightly smaller than for ***x***-polarization, indicating that the optical extinction in multilayer GaTe shows weak anisotropy, despite the in-plane low symmetry and structural anisotropy of GaTe. The inset in Figure 4-7(b) shows a polar plot for the extinction of the 112 nm-thick flake at wavelengths of 532 and 633 nm (E_L=2.33, 1.96 eV, respectively) at different polarization angles, which also indicates the weak in-plane anisotropy of the optical extinction in the GaTe flake. More polarized extinction profiles for the other flakes connected (see Figure 4-7(a)) indicate weak extinction anisotropy, and slightly stronger optical extinction for the ***x***-polarized light than for the ***y***-polarized light as well. Such weak anisotropy in the optical extinction of GaTe is consistent with the previous work on bulk samples.(*91*) Figure 4-7(c) shows the thickness dependence of the ratio of the integrated extinctions in the visible range (450 to 790 nm) along the ***x***- and ***y***-directions, which indicates extinction anisotropy. It can be observed that the ratio is small for all the measured thicknesses (below 1.3), suggesting the weak anisotropy of the optical extinction in GaTe. In thin flakes (thickness smaller than ~40 nm), the extinction ratio is relatively large and can reach ~1.3. The ratio drops as thickness increases and becomes close to 1.0 (isotropic) for the thickness range 50~130 nm. For even thicker flakes (> 160 nm), there is a rise of the extinction ratio and this rise is probably due to interference effect of light multi-reflected at the boundaries of quartz substrate and GaTe flake, which can play a role when the thickness of the flake is comparable to or larger than the wavelength of light but is negligible for thin flakes. The extinction ratios at the individual wavelengths 532, 633 and 785 nm show the similar thickness evolution as in Figure 4-7(c). Some other anisotropic 2D materials, such as BP, (*87*, *285*) show stronger anisotropy in optical extinction than GaTe. The ratio of the integrated extinction of BP in the visible

range can be 1.6 for a 225 nm-thick flake and 1.5 for a 9 nm-thick flake. (*87*) The relative weak extinction anisotropy of GaTe is advantageous for its practical application in optoelectronic devices, in the sense that the device performance is not sensitive to the polarization angle of the incident light and thus does not require a strict crystalline orientation determination for general use. However, the flake thickness and the substrate should be considered in the design of optoelectronic devices based on GaTe.

In order to explain the observed anisotropies of Raman scattering and optical extinction for GaTe, we carried out a calculation of the electron-photon interactions. Briefly, the optical absorption spectra can be obtained by calculating absorption coefficient α. According to Fermi's Golden Rule, α is proportional to the electron-photon matrix element, $\langle m|H_{\mathrm{op}}|i\rangle$, (*288*) which describes the optical transition from the state i to m, and the matrix element is given by the inner product of the dipole vector $\langle m|\nabla|i\rangle$ and the light polarization vector. When the polarization of the incident light changes, this inner product gives the polarization dependence of α. On the other hand, when the state m or i changes by changing the flake thickness or the laser excitation wavelength, the matrix element $\langle m|H_{\mathrm{op}}|i\rangle$ and its polarization dependence change correspondingly. This result is known as the optical transition selection rules, and can be explained by group theory. In the case of monoclinic bulk GaTe, the high symmetry points $\boldsymbol{\Gamma}$, $\boldsymbol{Z}$ and $\boldsymbol{P}$ in the Brillouin zone belong to the C_{2h}^3 (*C2/m*) space group. The symmetry of the eigenfunction for each energy band at the $\boldsymbol{Z}$ and $\boldsymbol{P}$ points was determined by first-principles calculation. The $\boldsymbol{Z}$ and $\boldsymbol{P}$ points have the largest probability for optical transitions, and Figure 4-8(a) shows the selection rules of the optical transitions near the Fermi energy. The transitions between the A_g state and the B_u state and between the A_u state and the B_g state occur by $\boldsymbol{x}$-polarized light, while the transitions between the A_g state and the A_u state and between the B_g state and the B_u state occur by $\boldsymbol{y}$-polarized light. The main contribution near the gap energy ($\lambda > 600$ nm) comes from $\boldsymbol{x}$-polarized light, and as the photon energy increases, the $\boldsymbol{y}$-polarized light is partially absorbed and the optical absorption/extinction anisotropy becomes weaker. This is due to the involvement of more energy bands in the absorption which contribute to different anisotropies as the photon energy increases. In line with the experimental results, the calculation also yields larger absorption for $\boldsymbol{x}$- than for $\boldsymbol{y}$-polarized light for the photon

energy near the bandgap.

With these selection rules of optical transitions and group theory, we can explain the intricate Raman polarization dependence presented in Table 4-4. The Raman intensity can be obtained by incorporating two electron-photon matrix elements with one electron-phonon matrix element using Eq. 4-1. Same as the case in BP, if we neglect the polarization dependence of the electron-phonon matrix element $\langle m'|H_{\mathrm{ep}}^{v}|m\rangle$, the polarization dependence of the Raman intensity can be described by the product of two electron-photon matrix elements, $\langle f|H_{\mathrm{op}}|m'\rangle$ and $\langle m|H_{\mathrm{op}}|i\rangle$. We show the detailed selection rules for the A_g and B_g Raman modes, and an example of the transition corresponding to the A_g and B_g modes at the ***Z*** or ***P*** point in Figure 4-8(b-c). For the A_g mode, the m and m' states have the same symmetry, and the two electron-photon interaction matrix elements in Eq. 4-1 have the same polarization dependence that gives a 180° period in the polarization dependence; while for the B_g mode, the m and m' states have different symmetries, and the two matrix elements have the opposite polarization dependences, resulting in the 90° period of the B_g polarization profile, which is consistent with the experimental results shown in Table 4-4. Using the above analyses, we can explain the phenomena of major maximum axis flipping shown in Table 4-4: for Raman modes under 532 nm laser excitation, the major axis can flip between 0° and 90°, while 633 and 785 nm lasers do not induce such flipping of major axes. This is because 532 nm (2.33 eV) can excite the electrons to several energy bands with different symmetries, making a complicated polarization profile. Moreover, at low laser excitation energy, the Raman modes are mostly ***x***-polarized, while at higher laser excitation energy, the Raman modes polarized along the ***y***-axis exist (Figure 4-8(a)), which is in a good agreement with the experimental observations in Table 4-4. The differences in the degree of anisotropy for different flake thicknesses (Table 4-4) are due to the change in the energy band structures with flake thickness. Besides, it is observed in Table 4-4 that under 532 nm laser, the 280 cm^{-1} Raman mode has ***x***-polarization, different from the other A_g modes with ***y***-polarization. This is because the electronic states involved in the Raman process are related to the phonon energy. Therefore, it is possible that under 532 nm laser and for the 280 cm^{-1} phonon, ***x***-polarized electron-photon interactions dominate, while for the other A_g modes with

different phonon energies, the electron-photon interactions with ***y***-polarization are dominant.

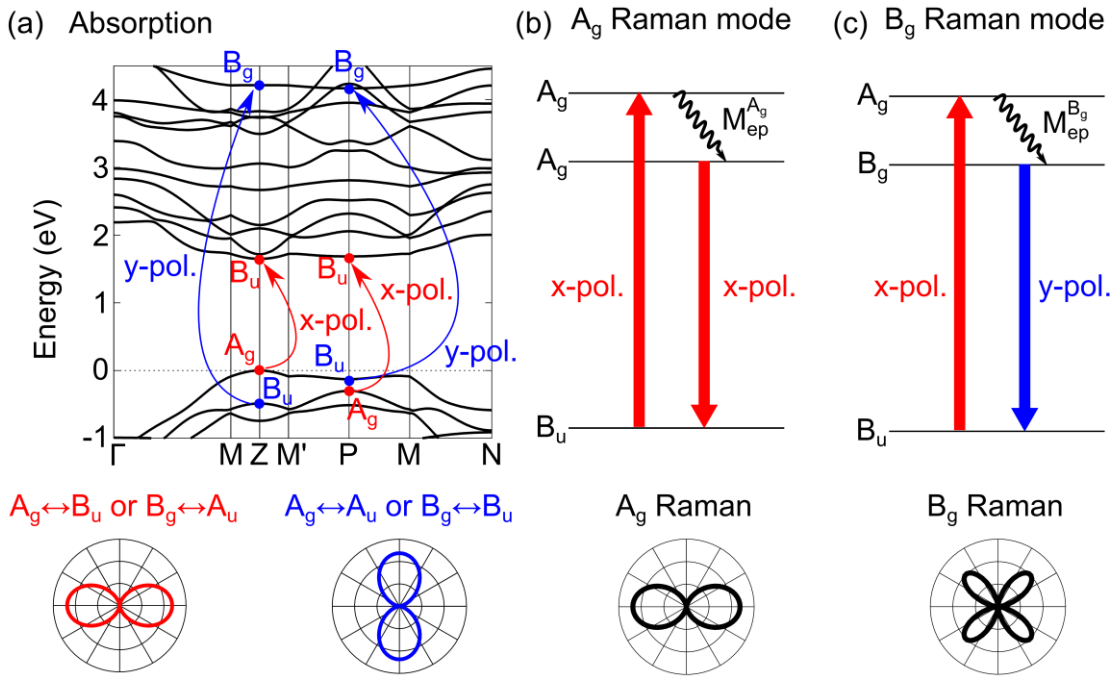

Figure 4-8. Optical transition selection rules in bulk GaTe. (a) Selection rules of optical transition near the Fermi energy at the *P* and *Z* points in the Brillouin zone, and the anisotropic optical absorption corresponding to the transitions activated by *x*-polarized (red arrow and curve) and *y*-polarized (blue arrow and curve) light. (b-c) One of the expected transitions for Raman scattering and polarization shape for the A_g (b) and B_g (c) modes at the *Z* or *P* point. M_{ep}^{Ag} (M_{ep}^{Bg}) indicates the electron-phonon interaction emitting an A_g (B_g) phonon. Red and blue arrows indicate the transition activated by *x*- and *y*-polarized light, respectively. In (a-c), the horizontal (vertical) axes in the polar plots correspond to *x*- (*y*-) axis.

Our optical transition selection rules using quantum mechanical model and group theory are essential for the analysis of the Raman anisotropy in GaTe. If we adopt the classical theory of the Raman tensor for the polarization dependence of the Raman intensity, the phonon modes with the same symmetry would have the same polarization dependence

under the same excitation wavelength. (*304*) However, as can be observed from Table 4-4, under 532 nm laser excitation, the maximum intensity for the A_g mode at 280 cm^{-1} is along the ***y***-axis, while the other A_g modes at 107, 115, 208, 268 cm^{-1} are polarized towards the ***x***-axis, which suggests the necessity of using quantum theory for the Raman intensity (Eq. 4-1) for understanding the polarization dependence. (*304*) Since we notice that there is small discrepancy of anisotropy between theory and experiment, it is expected that the anisotropy of the electron-phonon interaction contributes to the anisotropy of the Raman intensity, which will be part of the future work. This method of characterizing the optical anisotropy of GaTe can be generalized to other 2D materials with in-plane anisotropy, which should be significant for designing thermoelectric, electronic and photonic devices.

In addition, it is demonstrated through calculation that the interference effect can affect the anisotropies in the optical absorption and extinction, but is not as important for the Raman anisotropy. (*294*, *302*, *305*, *306*) For the optical absorption, the calculation involving the interference effect reduces the intrinsic absorption anisotropy, which is obtained solely by the electron-photon matrix elements. It suggests that the interference effect plays an important role in the optical absorption and extinction in GaTe, which is consistent with the experimental results. However, the experimentally observed anisotropy of the Raman intensity cannot be mainly attributed to the interference effect, but is mostly due to the anisotropy of light-matter interactions.

Based on the theory we developed, it is expected that intricate in-plane anisotropy occurs in many low-symmetry 2D materials. Indeed, it has been reported that Raman spectroscopy shows polarization dependence on the crystalline orientation for various low-symmetry 2D materials, such as in BP, GaTe, $ReSe_2$, ReS_2, SnSe, etc. (*304*) The dependence is related to the symmetry of the material. For example, the major axis of Raman intensity polar plot is along either the zigzag or armchair directions for the A_g modes in BP with D_{2h} symmetry, while in $ReSe_2$ and ReS_2 which have $P\bar{1}$ symmetry, the major axis can be along different lattice directions. (*307*, *308*) Furthermore, due to the complexity of Raman process, such a polarization dependence can vary with factors such as excitation laser wavelength, flake thickness, phonon frequency, etc. (*87*, *267*) The anisotropy of optical absorption and extinction can also be observed in some anisotropic

2D materials, but the degree of anisotropy depends on the actual electronic energy bands of the material and may not be directly connected to the structural anisotropy of the material. For example, BP with higher structural symmetry D_{2h}, shows stronger anisotropy of the optical absorption in the visible range than GaTe, which has relatively lower structural symmetry C_{2h}. (*87*) By the same token, the mobility anisotropy may not be directly related to the structural anisotropy, but is more closely related to the energy band diagram. (*100*) More studies on the anisotropic optical and electronic properties of other in-plane anisotropic 2D materials are necessary for the future applications of such materials, to provide more guidance on particular choices of materials to use for particular applications.

In summary, we performed an experiment/theory integrated investigation of the anisotropic optical extinction and Raman scattering in GaTe, which reveals insights into the role of anisotropy in light-matter interactions. The anisotropy of optical extinction is generally weak in the visible spectral range for multilayer GaTe, despite the in-plane structural anisotropy for GaTe. However, the anisotropy of the Raman intensity is strong and sensitively depends on excitation laser energy, phonon energy and GaTe thickness. This intricate dependence of the Raman scattering anisotropy on these different parameters stems from optical transition selection rules, as dictated by group theory. This work underscores the importance of understanding the anisotropic light-matter interactions in GaTe as well as other layered materials with low symmetry and in-plane anisotropy. This work also provides useful guidelines for the exploration of applications in electronic, optoelectronic and thermoelectric devices based on GaTe.

4.3 1T' Molybdenum Ditelluride

The crystal 1T' $MoTe_2$ can be readily degraded in the air and the characterization for the specified structure is not straightforward. To investigate the relationship between anisotropic properties and crystal structure of 1T' $MoTe_2$, a sensitive, reliable and non-destructive method to determine the crystal orientation is highly desirable.

Besides anisotropy, the thickness of 1T' $MoTe_2$ also strongly affects its properties. In contrast to the semi-metal bulk 1T' $MoTe_2$, few-layer 1T' $MoTe_2$ has an energy band gap

opening because of the strong spin-orbit coupling.[1] Monolayer 1T' $MoTe_2$ is predicted as a class of large-gap quantum spin Hall insulators, and can be used as the key material in the topological field effect transistor, which uses topological phase transition to realize fast on/off switching.[5] Moreover, the 1T' $MoTe_2$ samples with odd number of layers have inversion symmetry, while the inversion symmetry is broken for even number of layers.[14] Since monolayer and few-layer 1T' $MoTe_2$ easily degrade in air, direct measurement of the thickness using atomic force microscopy (AFM) is unpractical. Therefore, it is of great importance to develop a non-destructive, convenient method to probe the thickness of 1T' $MoTe_2$.

In this work, we have investigated the polarization dependence of 1T' $MoTe_2$ with various thickness using polarized Raman spectroscopy with different excitation laser wavelengths (532, 633 and 785 nm). (*120*) In particular, we performed transmission electron microscopy (TEM) on 1T' $MoTe_2$ and correlate it with polarized Raman results. The combination of select area electron diffraction (SAED), TEM and high angle annular dark field scanning transmission electron microscopy (HAADF-STEM) imaging and polarized Raman spectroscopy for the flakes of 1T' $MoTe_2$ with different thickness reveals the relationship between crystalline orientation and Raman intensity as a function of excitation laser wavelength, phonon mode and phonon frequency. Moreover, it was found that polarization dependent Raman spectroscopy can also be effective in determining the thickness of 1T' $MoTe_2$. Our work demonstrates that polarized Raman spectroscopy can be used as a powerful and nondestructive method to identify the crystal structure and thickness of 1T' $MoTe_2$ simultaneously, which opens up opportunities for in-situ probing anisotropic properties of 1T' $MoTe_2$.

Bulk 1T' $MoTe_2$ belongs to the space group $P2_1/m$. As illustrated in Figure 4-9(a,b), the monoclinic structure of 1T' $MoTe_2$ consists of a shifted Mo atom from the center of Te octahedron and the Mo atoms form the in-plane Mo-Mo bonds, resulting zigzag Mo chains along the [010] (y)-direction. The in-plane Mo-Mo bonds distort the Te octahedral plane, and form the monoclinic structure.[15] The HAADF-STEM image of the exfoliated 1T' $MoTe_2$ flake (Figure 4-9(c)) confirms the monoclinic structure and high quality of the bulk 1T' $MoTe_2$ crystal and exfoliated 1T' $MoTe_2$ flakes.

The phonon modes of 1T' $MoTe_2$ were investigated using polarized Raman scattering in the parallel configuration (the polarization of the scattered light is parallel with the polarization of incident light). Bulk (monolayer) 1T' $MoTe_2$ have 36 (18) vibrational modes, and 18 (9) of them are Raman active from group theory. There are a total of 12 (6) A_g modes and 6 (3) B_g modes for bulk (monolayer) 1T' $MoTe_2$. The calculated frequencies of the 18 (9) Raman modes are listed in our work.(*120*) The typical polarized Raman spectra of a 1T' $MoTe_2$ (5.7 nm thick) flake under different laser wavelengths (532, 633 and 785 nm) and different polarized angles (0°, 45°, and 90°) are shown in Figure 4-9(d). Here, we define 0° as the [010] (y) crystal orientation, 90° as the [100] (x) orientation. The peak intensity for 1T' $MoTe_2$ reveals strong dependence on excitation laser wavelengths, and varies dramatically with polarization angles, as seen in Figure 4-9(d). The change of the Raman spectra with different polarization angles are due to the in-plane anisotropy of 1T' $MoTe_2$. The number of modes changes with excitation laser wavelengths and polarizations, which is relevant to resonance Raman properties and the symmetry of the wavefunctions, respectively, as discussed below. For the Raman spectra excited by the 532 nm laser, there are 11 Raman peaks observed at 78, 94, 104, 111, 128, 163, 190, 252, 259, 265 and 279 cm^{-1}, among which 94, 104, 111, 190 cm^{-1} modes correspond to the B_g Raman modes and the others correspond to A_g modes. The Raman spectra of the 633 nm laser shows fewer peaks, and the peaks at 190, 252, 279 cm^{-1} did not appear. The number of Raman peak excited by the 785 nm laser is much fewer and only four peaks at 78, 163, 252, 265 cm^{-1} were observed. This is due to the lack of resonance condition with increasing laser wavelength. The weakening electron-photon resonance condition from the 532 nm laser to the 785 nm laser leads to the weaker or even vanishing Raman peaks.

Moreover, the peak frequency and relative intensity also vary with excitation laser wavelengths. For example, for 0° polarization, the intensities of 163 and 78 cm^{-1} modes are similar to those for the 532 nm laser, but the intensity of 163 cm^{-1} mode becomes significantly smaller than that of 78 cm^{-1} modes for 633 and 785 nm laser. Also, it can be observed that peaks under 633 nm laser is a little red-shifted compared to other lasers. In the following, we demonstrate how Raman spectra measured under various laser

excitations can be useful for the practical application of $MoTe_2$ with two major aspects: determining the crystalline orientation and flake thickness.

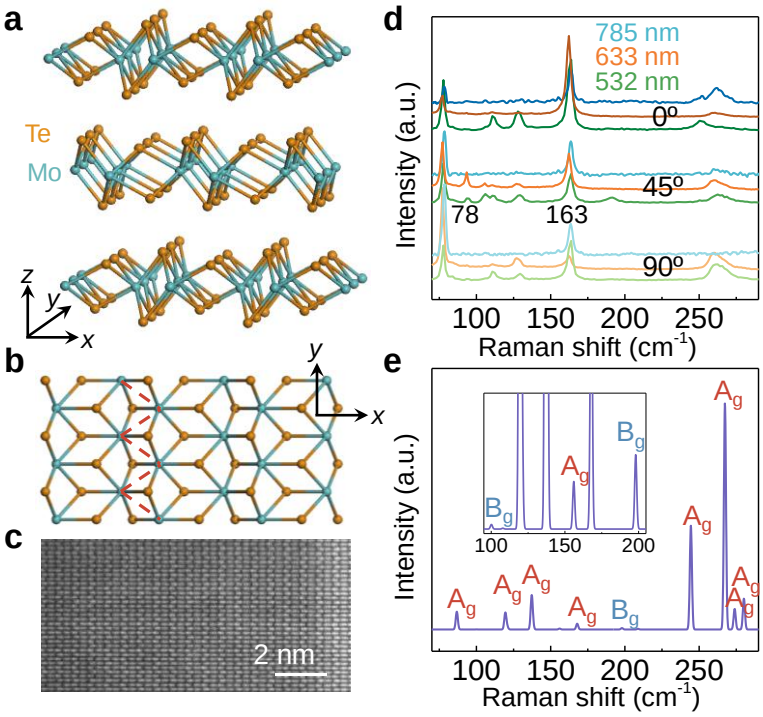

Figure 4-9. (a-b) The crystalline structure of the bulk 1T' $MoTe_2$ from the perspective view (a) and top view (b). The red dashed lines in (b) denote a zigzag Mo chain. (c) HAADF-STEM image from the exfoliated 1T' $MoTe_2$ flake supported on a TEM grid. (d) Typical Raman spectra of a 1T' $MoTe_2$ flake measured under three excitation lasers and three polarization angles. For each polarization angle, the bottom, middle and top spectra are measured under 532, 633 and 785 nm laser excitations, respectively. (e) Calculated nonresonant Raman spectrum of bulk 1T' $MoTe_2$.

To probe the crystal orientation of 1T' $MoTe_2$, and investigate how it relates to anisotropic Raman spectroscopy in 1T' $MoTe_2$, SAED, TEM, HAADF-STEM and polarized Raman spectroscopy were performed on the same 1T' $MoTe_2$ flakes with various thickness. Figure 4-10(a) presents a typical optical microscope image of 1T' $MoTe_2$ flakes protected by TEM grid and PMMA layer. The corresponding SAED pattern of the 1T' $MoTe_2$ flake shows rectangular pattern (Figure 4-10(b)), which can be indexed with the monoclinic structure of the 1T' phase, and used to determine the crystal orientation on this

specific flake. The corresponding HAADF-STEM image in Figure 4-10(c) matches well with the image simulation based on the 1T' $MoTe_2$ structure, shown in the inset of Figure 4-10(c), which unambiguously points out the crystal orientation of the flake and verifies the high-quality of exfoliated flakes.

We measured the polarized Raman spectra and corresponding crystal orientation by TEM on 1T' $MoTe_2$ flake, presented in Figure 4-10(d). It can be observed clearly that the peak intensities change with polarization angles in different ways. 7 Raman modes are observed, among which 5 are of A_g symmetry (78, 128, 161, 259, 265 cm^{-1}) and 2 are of B_g symmetry (94, 104 cm^{-1}) (Figure 4-10(d)). As shown in Figure 4-10(e), the Raman polar plots correspond well to the crystalline orientation determined by TEM. The intensity of the four A_g Raman peaks at 78, 128, 259, 265 cm^{-1} varies with a period of 180º, and the maximum intensity appears at a specific polarization angle along with the [100] crystal axis. In contrast, for the A_g Raman peak around 161 cm^{-1}, the maximum intensity occurs when the polarization angle is along with the [010] crystal axis. We also noticed that for some modes, such as 259 cm^{-1} mode, the minimum Raman intensity is not along 0°, since there is a small secondary maximum near 0°. This phenomenon, also observed in other layered materials with in-plane anisotropy, originates from the optical absorption that induces phase mismatch for the Raman tensor elements along different crystal orientations. For the two B_g Raman peaks at 94, 104 cm^{-1}, the intensity changes in a period of 90º, with a maximum intensity at 45º and minimum at 0º and 90º. It should be noted that for each mode, such relationship between crystal orientation and Raman intensity remains the same for flakes with different thicknesses. Thus, the combined TEM/Raman measurements unambiguously reveal the relationship between Raman signals and crystal orientation. More importantly, this nondestructive, sensitive and fast anisotropic Raman characterization provides a reliable method to obtain the crystal information of 1T' $MoTe_2$ with various thicknesses.

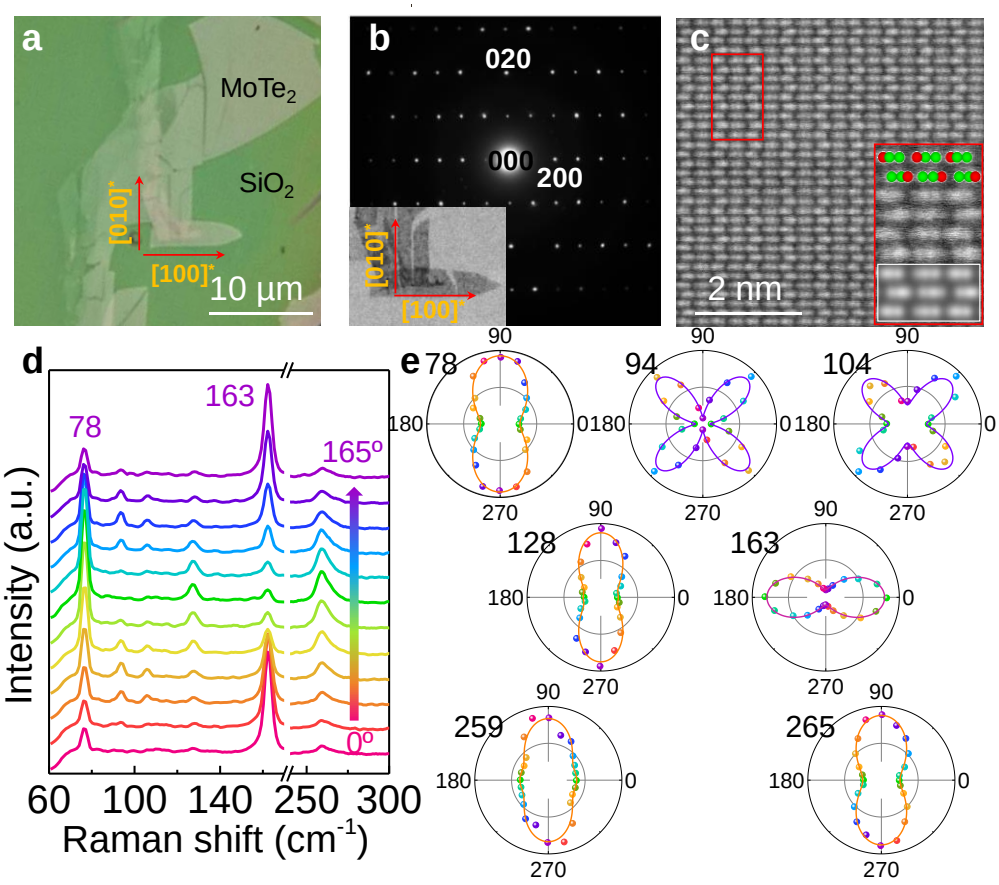

Figure 4-10. (a) Optical microscope image of exfoliated 1T' $MoTe_2$ flakes on TEM grid. The arrows labelled by [100]* and [010]* (superscript * indicates the index in reciprocal space) are determined from SAED pattern in (b). (b) SAED pattern from the area shown in (a). The TEM image is shown in the inset. (c) High resolution HAADF-STEM image from the 1T' $MoTe_2$ flake. The inset with red frame is the magnified image from the red rectangle area. [001] atomic projection of the 1T' is embedded with red and green spheres representing Mo and Te atoms, respectively. The white framed inset shows the simulated image based on 1T' crystal structure, which is consistent with the experimental image. (d) The polarized Raman spectra (633 nm laser excitation) of the same 1T' $MoTe_2$ flake measured with polarization angle from 0° (bottom) to 165° (top) with an interval of 15°. (e) The polar plots of Raman intensity as a function of polarization angles for different Raman modes.

The Raman anisotropy of 1T' $MoTe_2$ flake has remarkable changes under different excitation laser wavelengths. Polarized Raman using three excitation laser wavelengths (532, 633 and 785 nm) were measured on 1T' $MoTe_2$ flakes with various thicknesses on Si/SiO2 substrates. The flakes that are physically connected were selected to ensure the same crystalline orientation. The Raman polar plots of a typical flake of various Raman modes under three laser excitations are summarized in Table 4-5.

The Raman modes show different anisotropy under the same laser excitation wavelengths. For example: 94, 104, 190 cm-1 modes always show 90° period (shown with purple fitted curve in Table 4-5), while all the other modes show 180° period. The reason for such different polar spectra is that, Raman modes have different symmetries: A_g modes show 180° period, and B_g modes show 90° period. Also, for the modes with the same symmetry, the observed anisotropy can be different. For example, for the A_g modes under 532 nm laser, 78, 111, 128, 163, 252 cm-1 modes show that maximum intensities are along 0° (shown with violet fitted curve in Table 4-5), while 259, 265, 279 cm-1 modes have their maximum intensities along 90° (shown with orange fitted curve in Table 4-5).

For the same Raman mode, the Raman anisotropy can change their orientations with changing laser wavelengths. For example, 78 cm^{-1} mode shows the maximum intensity along 0° under 532 nm laser, but along 90° under 633 and 785 nm laser; 128 cm^{-1} mode shows the maximum intensity along 0° under 532 nm laser, but along 90° under 633 nm laser. Some modes change degree of anisotropy with laser wavelengths, and some even become isotropic under certain laser excitations. For example, 163 cm^{-1} shows stronger anisotropy under 633 nm laser than under 532 nm laser, and under 785 nm laser, it shows isotropic Raman intensity. This phenomenon can be attributed to the optical transition selection rule, which will be discussed in detail later. In short, by changing the laser excitation energies, the final or initial electronic states with the different symmetry of the wave functions are selected so as to satisfy the resonance condition. Then the electron-photon matrix elements can have unique polarization dependence even for the same phonon modes that satisfies the group theory. It is noted that the classical theory of Raman tensor cannot explain these phenomena.[19]

Table 4-5. Raman polar plots of a typical flake (5.7 nm thick) of various Raman modes under different incident laser.

mode (cm^{-1})	532 nm	633 nm	785 nm	mode (cm^{-1})	532 nm	633 nm	785 nm
78	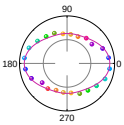	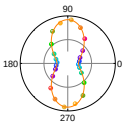	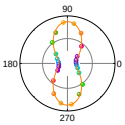	190	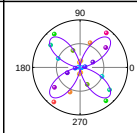		
94	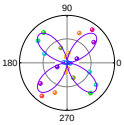	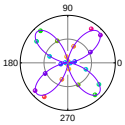		252	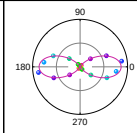		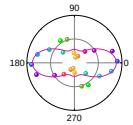
104	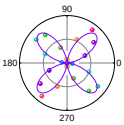	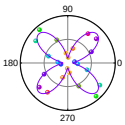		259	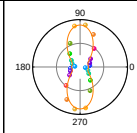	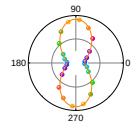	
111	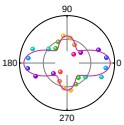	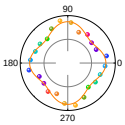		265	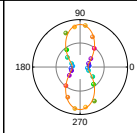	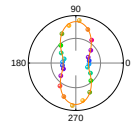	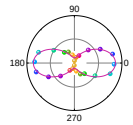
128	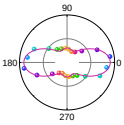	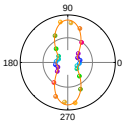		279	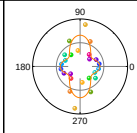		
163	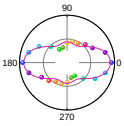	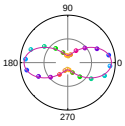	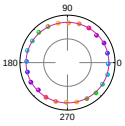				

For flakes with different thicknesses from few-layer to bulk, Raman anisotropy orientations do not change for each mode. As seen in Table 4-5, for the few-layer and bulk flakes, under the same excitation laser wavelengths and for the same Raman modes, the orientations of their Raman intensity polar plots remain the same. This feature can tremendously simplify the method of using polarized Raman to determine crystalline orientation, since the flake thickness does not need to be taken into consideration.

Overall, as seen in Figure 4-10 and Table 4-5, polarized Raman measurement should be a sensitive probe to determine the crystalline orientation of 1T' $MoTe_2$, but some cautions need to be taken on the selection of excitation laser wavelength due to the sensitivity of Raman anisotropy with laser wavelength.

Despite the insensitivity of Raman anisotropy to flake thickness, several Raman features, including peak frequency and intensity ratio, varies with the thickness of 1T' $MoTe_2$ flakes. We have analyzed various features of Raman spectra of 1T' $MoTe_2$ under different laser excitations, and found that the A_g modes at 78 and 259 cm^{-1} as well as the intensity ratio (I(259)/I(252)) can be used for the identification of the thickness of 1T' $MoTe_2$ sample.

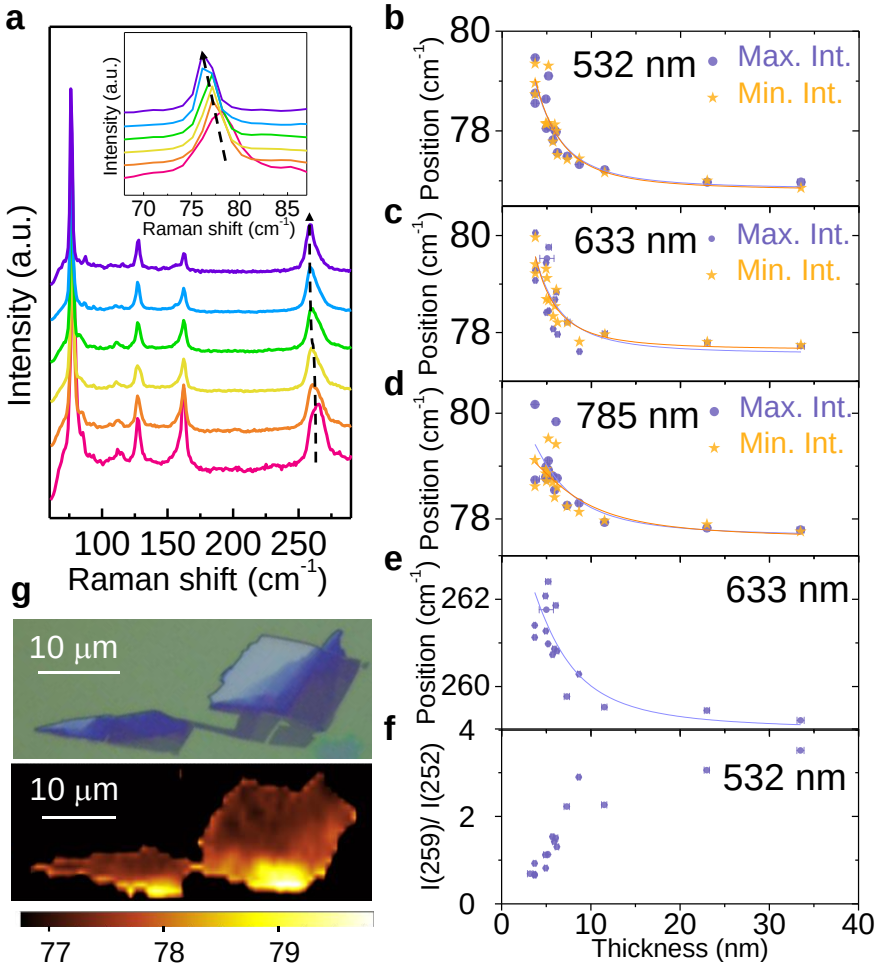

Figure 4-11. (a) Raman spectra of 1T' $MoTe_2$ flakes with different thicknesses. Thickness from bottom to top: 3.6, 5.1, 5.8, 6.3, 8.5, 31 nm. The inset shows the zoom-in of 78 cm^{-1} peak. The spectra were measured under 633 nm laser and along 90° crystal orientation. The spectra intensities are normalized by the corresponding 78 cm^{-1} mode. (b-d) The frequency change of 78 cm^{-1} mode with flake thickness under 532, 633, 785 nm laser, respectively. Max. and Min. Int. denote the polarization angle selected for maximum and minimum

intensities in the polar plot, respectively. (e) The frequency change of 261 cm^{-1} mode with flake thickness measured under 633 nm laser with 90° crystal orientation. (f) The thickness dependence of intensity ratio of 259 and 252 cm^{-1} modes measured under 532 nm laser. Both intensities of (e) and (f) are selected with the polarization for their corresponding maximum intensities, i.e. 90° for 259 cm^{-1} mode and 0° for the 252 cm^{-1} mode. (g) Optical image of the flakes (top) and Raman mapping of the 78 cm^{-1} mode frequency (bottom).

First, the frequencies of 78 and 259 cm^{-1} modes (under 633 nm laser) exhibit a monotonic redshift when the thickness is increased (Figure 4-11(a)). As shown in Figure 4-11(c), for the few-layer flake (thickness 3.7 nm), the 78 cm^{-1} mode under 633 nm has the frequency of nearly 80 cm^{-1}, but as the thickness increases to 33.5 nm, its frequency decreases to ~77.7 cm^{-1}. Similarly, under 532 nm laser, the frequency of 78 cm^{-1} mode changes from 79.5 cm^{-1} to ~76.9 cm^{-1} monotonically when thickness increases from 3.7 to 33.5 nm (Figure 4-11(b)). Similarly, for 785 nm laser, there is a frequency decreases of 78 cm^{-1} mode from 80.2 cm^{-1} to 77.8 (3.7 nm to 33.5 nm thickness) (Figure 4-11(d)). For the 261 cm^{-1} mode with 633 nm laser, the frequency decrease from 262.4 to 259.2 cm^{-1} for thickness increases from 5.2 to 33.5 nm (Figure 4-11(e)). Note that the frequencies measured here are chosen for the polarization with the maximum intensity (or minimum intensity) of the modes to minimize the uncertainty of the measured frequency and the subsequent numerical fitting. One possible reason of such a frequency drop with increased flake thickness is the increase of dielectric screening of the long-range Coulomb interaction for an excitation going from few-layer to multi-layer $MoTe_2$.[19] In particular, the 78 cm^{-1} mode remains high intensity under variable polarization angles, and the frequency is insensitive to polarization. Thus, the frequency-decreases-rule for 78 cm^{-1} mode is a good identification for thickness, even for arbitary polarization angle.

Another method to determine the thickness of flakes is using the intensity ratio of 259 to 252 cm^{-1} modes. We found that the ratio increases with increasing thickness, as shown in Figure 4-11(f). The ratio is as small as 0.7 for the flake thickness of 3.2 nm, but increases monotonically to 3.5 for the 33.5 nm thick flake. The mechanism that I(259)/I(252)

increases with layer thickness is possibly the opposite trend of I(259) measured by x-polarized light and I(252) measured by y-polarized light changing with thickness.

To explain Raman anisotropy, we calculated electronic band structure, optical absorption in the reciprocal space and phonon spectra at the zone-center Γ point of bulk 1T' $MoTe_2$. At the zone-edge X point of the Brillouin zone, there exist several saddle points which will give rise to a Van Hove singularity of electronic joint density of states, or the electron-photon absorption resonance. Indeed, the calculated optical absorption shows that such an electron-photon resonance appears at or near X point for three laser wavelengths (especially for 532 nm) used in the experiment. Thus, for both inter-valley and intra-valley electronic excitations, the assisting phonon should be sought for at or near Γ point.

The polarized Raman modes can be explained using the group theory and optical transition selection rule.[17,18,20] Briefly, of the point group of bulk 1T' $MoTe_2$ is C_{2h}, in which the principal C_2 axis lies in the in-plane y-axis shown in Figure 4-9(a-b). For the linear polarization in the direction of 0° (y direction), the combination of B_g and B_u symmetries, or A_g and A_u symmetries for the initial and photo-excited states are selected (Figure 4-12(a)). Here for simplicity, we explain the case of B_g and B_u symmetries for the combination of initial and photo-excited state. We can also obtain the full list of the combination of initial and photo-excited states with 0° and 90° (x direction) polarized light similar to Table 4-2 and Table 4-3. For the parallel polarization for incident and scattered light in the Raman measurement, A_g phonon modes can be measured, and 180° period in the polar plots are observed (Figure 4-12(b,c)). When the two intermediate states belong either x or y character, B_g phonon modes can be measured, in which we can get 90° period in the polar plots (Figure 4-12(d)). By changing laser excitation wavelength, different intermediate states are selected. This is the reason why different polar plots were observed for different excitation laser wavelengths, shown in Table 4-5.

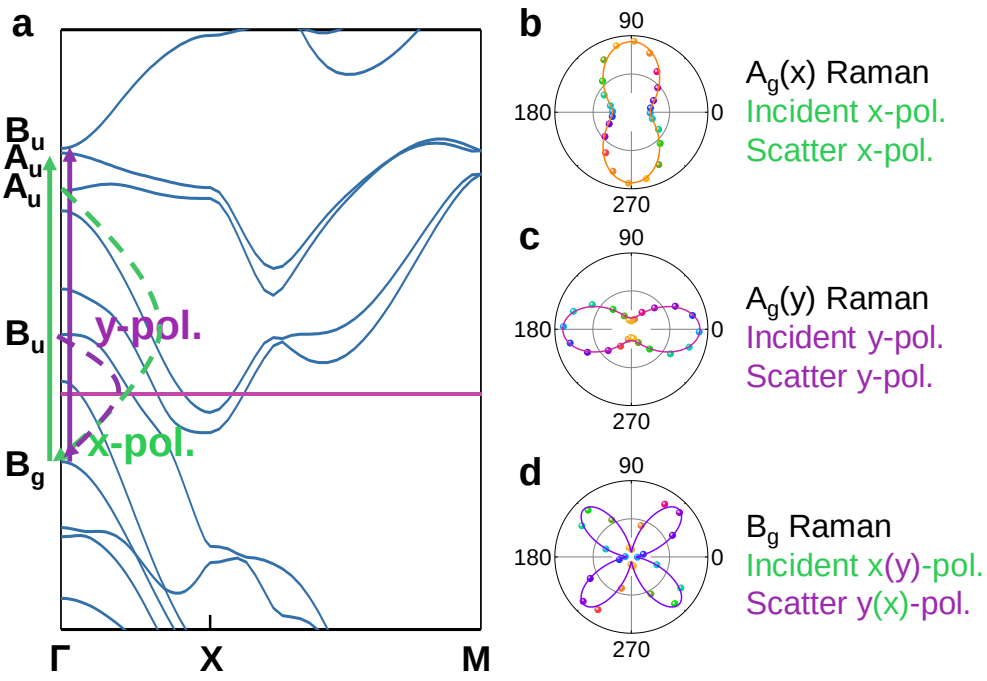

Figure 4-12. Selection rule of optical transition. (a) Energy band diagram of bulk 1T' MoTe2. The symmetry of energy levels at Γ point are shown, and the polarization of incident and scatter light connecting this energy levels are labelled. (b-c) Two types of A_g Raman modes. (d) B_g Raman mode.

In conclusion, we have demonstrated Raman as a non-destructive and convenient way to determine the crystalline orientation and flake thickness of 1T' $MoTe_2$. We also perform TEM analysis on 1T' $MoTe_2$, and successfully correlate it with polarized Raman. We found that the polarized Raman can be effectively used to determine the crystalline orientation of 1T' $MoTe_2$ flake with thicknesses ranging from few-layer to bulk. Due to the sensitivity of Raman anisotropy with laser excitation wavelengths, special attentions should be paid on the laser wavelength used when determining the crystalline orientation. In addition, the thickness of the flakes can be determined using two ways, the frequency of 78 and 259 cm^{-1} modes, and the intensity ratio of 259 and 252 cm^{-1} mode. The former decreases and the latter increases with increased thickness of the flakes. These experimental observations can be well explained using group theory and DFT calculations. Our work provides insight into

the phonon property of the anisotropic material, and paves the way for broad applications of 1T' $MoTe_2$.

4.4 Summary

In this chapter, three 2D materials with in-plane anisotropy, BP, GaTe and 1T' $MoTe_2$, are studied. It has been found that these three materials have different symmetries, but all of them show the intricate Raman anisotropy, and all of these phenomena can be explained using the optical transition selection rule we developed. (*309*) In fact, this selection rule can also be widely applied to many other 2D materials with in-plane anisotropy, therefore offers a new and effective method for the study of emerging 2D materials.

Chapter 5
Interaction of 2D Material with Other Systems

In this chapter, the interaction of 2D materials with other nanostructures are presented, including the interaction of graphene and organic molecules, and the interaction of TMD material with plasmonic nanocavities. These study indicate applications in chemical sensing and photonics, respectively.

5.1 Interaction of 2D Material with Organic Molecules: Graphene-enhanced Raman Scattering

Surface-enhanced Raman scattering (SERS) is an important Raman enhancement technique in the study of the physics and chemistry of materials.(*310–313*) Noble metals with rough surfaces are typically used as SERS substrates. (*314*, *315*) The Raman enhancement processes are mainly due to the interplay between an electromagnetic mechanism (EM) (*316*) and a chemical mechanism (CM). (*317*) In the EM, the electromagnetic field of the incident light is enhanced by a plasmonic mechanism near the "hot spots" on the rough surface of a metal. In the CM, the substrate and the molecules are coupled through both charge transfer and the mixing of molecular orbitals with electronic states. In SERS, the dominant enhancement mechanism is the EM, and it can enhance the Raman signals by as much as 10^{10} times. (*318*) The enhancement factors (EFs) vary with the vibrational modes for both EM and CM, but they have different mechanisms. For EM, the variation of EF depends on the electromagnetic frequency resonance. (*310*, *313*) However, for CM, EF depends on the molecule-substrate interaction, showing a strong

molecular selectivity. Investigating the molecular selectivity of SERS is very important to understand the CM in detail, which until now has been insufficiently explored to effectively provide a complete picture of the overall enhancement mechanisms of SERS. (*310*, *319*, *320*)

Graphene-enhanced Raman scattering (GERS), which uses graphene rather than a rough metal surface as a Raman enhancement surface, is a newly-developed Raman enhancement technique. (*321–323*) GERS is dominated by the CM effect, with associated EF values varying from less than 10 to as high as ~100. (*321*, *324*) While a number of factors responsible for this EF have been successfully explained, such as the number of graphene layers, (*325*) the molecule-graphene distance, (*326*) molecular orientations, (*327*) Fermi level of graphene (*328*) and laser excitation energies, (*324*) the molecular selectivity of graphene-enhanced Raman scattering has not yet been systematically explored.

Compared to SERS, GERS has a relatively lower EF. Although GERS has not demonstrated its detection limit down to the single molecule level up to now, its EF values can still be very useful and large enough in some applications for the detection of a small number of molecules. Thanks to the unique two-dimensional planar structure and the chemical inertness of graphene, GERS presents many advantages, such as the repeatability and stability of the enhanced Raman signal, when compared to conventional SERS. (*324*, *329*, *330*) Previous works have established that the GERS EFs vary with the type of molecules and the phonon modes within the same molecules. (*321*) In particular, some molecules can have GERS enhancement while others do not. Even for the same type of vibrational mode, different molecules can show different GERS EFs. Such a remarkable selectivity of molecules is very important for GERS to be a promising tool in microanalysis, as well as to gain a deep understanding of the CM. To predict which kinds of molecules have strong GERS enhancement, and to provide a more comprehensive understanding of the CM in SERS, a systematic study of molecular selectivity of GERS is necessary.

The molecular selectivity of GERS originates from the different strengths of the interactions between graphene and different molecules. (*317*, *319*) Van der Waals (vdW) forces govern most of the molecule-graphene interactions. In GERS, the different

interaction strengths between the molecules and the graphene substrate contribute different values of GERS EFs. Therefore, the molecular selectivity of the GERS effect can be exploited to determine the coupling strength between graphene and the molecules.

A large Raman cross section of the molecule ensures sufficient Raman scattering efficiency and therefore the observation of clear Raman signals. (*331*) For this reason, we chose molecules with large Raman cross sections to investigate GERS capabilities for molecular selectivity. (*332*) The Raman scattering of different types of molecules on graphene is shown on Figure 5-1. These molecules can be categorized as follows. Category (1) encompasses molecules with similar molecular structures to graphene but different energy levels and includes different phthalocyanine (Pc) derivatives: copper phthalocyanine (CuPc), zinc phthalocyanine (ZnPc) and Copper(II) 1,2,3,4,8,9,10,11,15,16,17,18,22,23,24,25-hexadecafluoro-29H,31H-phthalocyanine (F_{16}CuPc). Category (2) involves molecules with similar energy levels but different molecular structures, such as tetrathienophenazine (TTP), Tris(4-carbazoyl-9-ylphenyl) amine (TCTA), and 2,2',7,7'-tetra(N-phenyl-1-naphthyl-amine)-9,9'-spirobifluorene (sp2-NPB). Finally, category (3) include other molecules of interest, such as 3,5-tris(N-phenylbenzimiazole-2-yl)benzene (TPBi), and bathocuproine (BCP), etc.

We analyzed the enhancement effects of all these molecules on graphene and could highlight two molecular selection rules. First, molecular energy levels play an important role in determining whether or not a significant enhancement effect can be observed. We find that the HOMO and LUMO levels of the molecule need to be in the appropriate energy range with respect to graphene's Fermi level for a given set of laser excitation energies. This rule is supported by the experimental results and theoretical analyses using the third order perturbation theory in the quantum theory of Raman scattering. (*333*) The second selection rule is that the symmetry of the molecule is important in showing a considerable enhancement effect. The molecules which show symmetries closest to that of graphene (D_{6h}) symmetry are more likely to yield a large GERS EF. This molecular symmetry rule, confirmed by Raman measurement results using molecules with different structures, can be theoretically explained by group theory and the charge-transfer effect between the molecules and graphene. Both molecular selection rules for the molecular energy levels

and for the molecular symmetry suggest that a strong GERS EF requires both strong molecule-graphene coupling and effective charge transfer, which are further supported by the UV-visible absorption spectroscopy measurement of molecules before and after contacting graphene surfaces. First-principles density functional theory (DFT) calculations were also carried out to confirm the sensitive dependence of GERS EF on the molecular HOMO/LUMO levels and on the molecule-graphene coupling. The rules of molecular selectivity in a GERS system explored in our work are important for the fundamental study of the CM in GERS and of the graphene-molecule interaction, as well as the potential application of GERS in molecular detection and biological, physical, and chemical process monitoring. (*334–339*)

Selection of the type of molecules is essential in GERS experiments. In previous reports, most of the studied molecules have large Raman cross sections, including protoporphyin IX (PPP), crystal violet (CV), Rhodamine 6G (R6G), and phthalocyanine (Pc) and its derivatives. (*321*) However, many molecules that we tested in the GERS experiments did not show Raman signals because of the low Raman cross section (smaller than 10^{-30} cm^2 sr^{-1} under non-resonant conditions, (*331*) and therefore too small to ensure sufficient Raman scattering efficiency), (*321, 331*) or the choice of an inappropriate excitation laser wavelength. In the case of low Raman cross sections, it is difficult to determine whether or not there is a Raman enhancement effect for these molecules on graphene. In this work, we focus on molecules with large Raman cross sections and we study the effects of the molecular energy level and of the molecular symmetry on the GERS signal.

In the GERS system, the interaction strength between graphene and the molecule mainly depends on the degree of matching between the molecular energy levels and between the molecular symmetries with graphene. The Raman scattering intensity is strongly related to the energy band structure of the materials. (*310, 313, 320, 340*) Figure 5-2 shows the Raman spectra of three molecules, CuPc, ZnPc and F_{16}CuPc, on graphene which is supported by SiO_2/Si substrates. These three molecules have the same molecular structure (D_{4h} symmetry), with the only difference between them being in their metal ions (Cu^{2+} or Zn^{2+}) or the fluorine substituent (F^-) (Figure 5-2(a)). In addition, all of the

molecules have planar structures, which allow for strong interactions with graphene. According to our DFT calculations shown in Table 5-1, upon adsorption on graphene, these molecules share similar molecule-graphene separation distances (~ 3.2 Å) and adsorption energies (~ -0.06 eV per atom), largely due to the similarity of their planar structures. However, their HOMO/LUMO energies are different, which are -5.2/-3.5 eV, (*341*) -5.2/-3.8 eV (*342*) and -6.3/-4.8 eV, (*343*) respectively. Remarkable Raman enhancement has been observed for all of these three molecules on graphene using both 532 nm and 633 nm laser excitations, but the enhancement factors for them are very distinct, as seen in Figure 5-2(b-e). For example, at 633 nm laser excitation, the highest GERS EF of CuPc is 47.3 (at 1530 cm^{-1}), while the values are only 12.3 (at 1508 cm^{-1}) for ZnPc, and 6.2 (at 1540 cm^{-1}) for F_{16}CuPc. The EF at this vibrational mode of CuPc is 3.8 and 7.6 times larger than the EF of the same mode for ZnPc and F_{16}CuPc, respectively. These results indicate that despite their similar molecular structures, the presence of different molecular HOMO/LUMO levels plays an important role in GERS enhancement. E. Barros et al. (*333*) studied the relation between the GERS EF and other parameters, such as the graphene Fermi level, molecular HOMO/LUMO, phonon and laser energy. Using time-dependent perturbation theory for the Raman scattering process, they predicted that the energy levels of the molecule HOMO/LUMO are related to the GERS enhancement. (*333*) They found that strong GERS enhancement occurs when the phonon energy is close to the energy difference between the Fermi level of graphene and the HOMO/LUMO level of the molecules. Under such a condition, the GERS EF can be further increased if the laser energy is close to the HOMO-LUMO energy gap of the molecule. A previous work (*333*) clearly illustrates the enhancement conditions, which are due to the better matching to the Raman resonance condition. In detail, a large GERS EF can occur for the following four conditions: (*333*)

(i) $\hbar\omega_0 = \mathrm{LUMO} - \mathrm{HOMO}$ OR $\hbar\omega_0 = \mathrm{LUMO} - \mathrm{HOMO} + \hbar\omega_q$,

(ii) $E_F = \mathrm{HOMO} \pm \hbar\omega_q$ OR $E_F = \mathrm{LUMO} \pm \hbar\omega_q$,

(iii) $\hbar\omega_0 = E_F - \mathrm{HOMO}$ OR $\hbar\omega_0 = E_F - \mathrm{HOMO} + \hbar\omega_q$,

(iv) $\hbar\omega_0 = \mathrm{LUMO} - E_F$ OR $\hbar\omega_0 = \mathrm{LUMO} - E_F - \hbar\omega_q$,

in which $\hbar\omega_0$ is the incident photon energy, $\hbar\omega_q$ is the phonon energy, and E_F is the graphene Fermi level. According to the perturbation theory treatment of Raman scattering and the Fermi's Golden Rule, (*122*) the Raman scattering efficiency is inversely proportional to the energy difference between the graphene Fermi level and the electronic levels of the molecule. Therefore, energy level matching in the molecule-graphene systems plays an important role in achieving a high GERS EF. It is worth mentioning that from a chemistry perspective, the scattering mechanism of the asymmetric modes in porphyrin-like molecules, including CuPc, ZnPc, and F_{16}CuPc here, is the Herzberg-Teller mechanism. (*344–346*) The model mentioned previously by E. Barros et al. (*333*) describes the scattering process from the perspective of time-dependent perturbation theory, (*122*) but it is also sufficient to reproduce and explain the increasing GERS EF trend with increased phonon frequency.

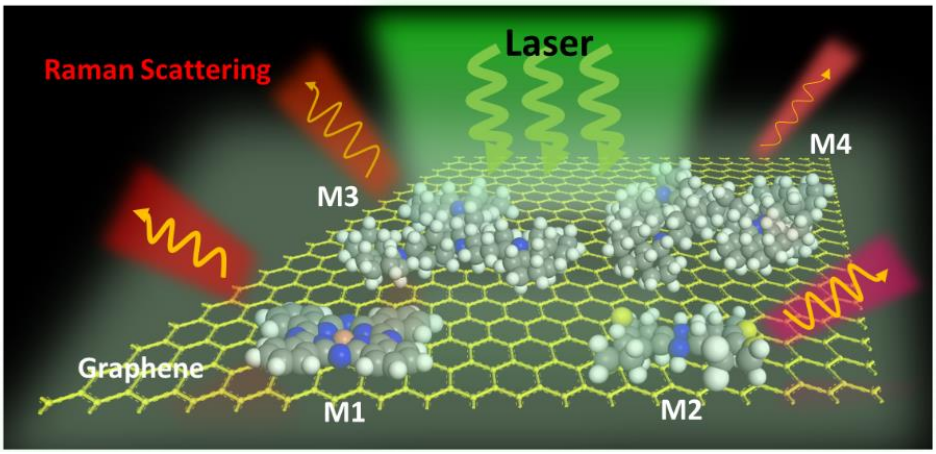

Figure 5-1. Schematic illustration of the molecular selectivity in GERS. Different types of molecules M1, M2, M3 and M4 are shown on graphene.

Our experimental results in Figure 5-2(d) show that the relation of EF vs. phonon frequency of the CuPc molecule at 633 nm laser excitation matches the theoretical predictions in Ref. (*333*) and the analyses above, as confirmed in the polynomial fitting (black dotted curve) shown in Figure 5-2 (d). With the phonon frequency increasing from 600 cm^{-1} (0.07 eV) to 1600 cm^{-1} (0.20 eV), EF increases because the system is closer to the

resonance condition: i.e., the phonon energy equals the energy difference between the graphene Fermi level and the molecular HOMO/LUMO levels (Eq. (ii) above), or the phonon energy equals the energy difference between the laser energy and the HOMO-LUMO gap (Eq. (i) above). For CuPc under 532 nm laser excitation, the EFs are weaker than under 633 nm laser excitation, and the behavior does not match the theoretical prediction, as shown for the case of the 633 nm laser excitation, possibly because the 532 nm laser excitation is not in the resonance window with the HOMO/LUMO energy gap of CuPc. The phenomenon that EF increases with phonon frequency was also observed in F_{16}CuPc under 633 nm laser excitation (stronger than the 532 nm excitation because of the resonance excitation (*347*, *348*)), shown in Figure 5-2(e). This mainly applies to the A_{1g} vibrational modes, and may be due to the mode selection of the GERS enhancement mechanism. (*321*) The "Energy Level Rule" is successful for explaining most of the observation in Figure 5-2, and for the molecules with similar structure. But it is not complete, since it does not consider other factors (such as the molecular structure and the variety of the vibration) besides the energy level, which may induce different coupling strengths between graphene and the molecules too.

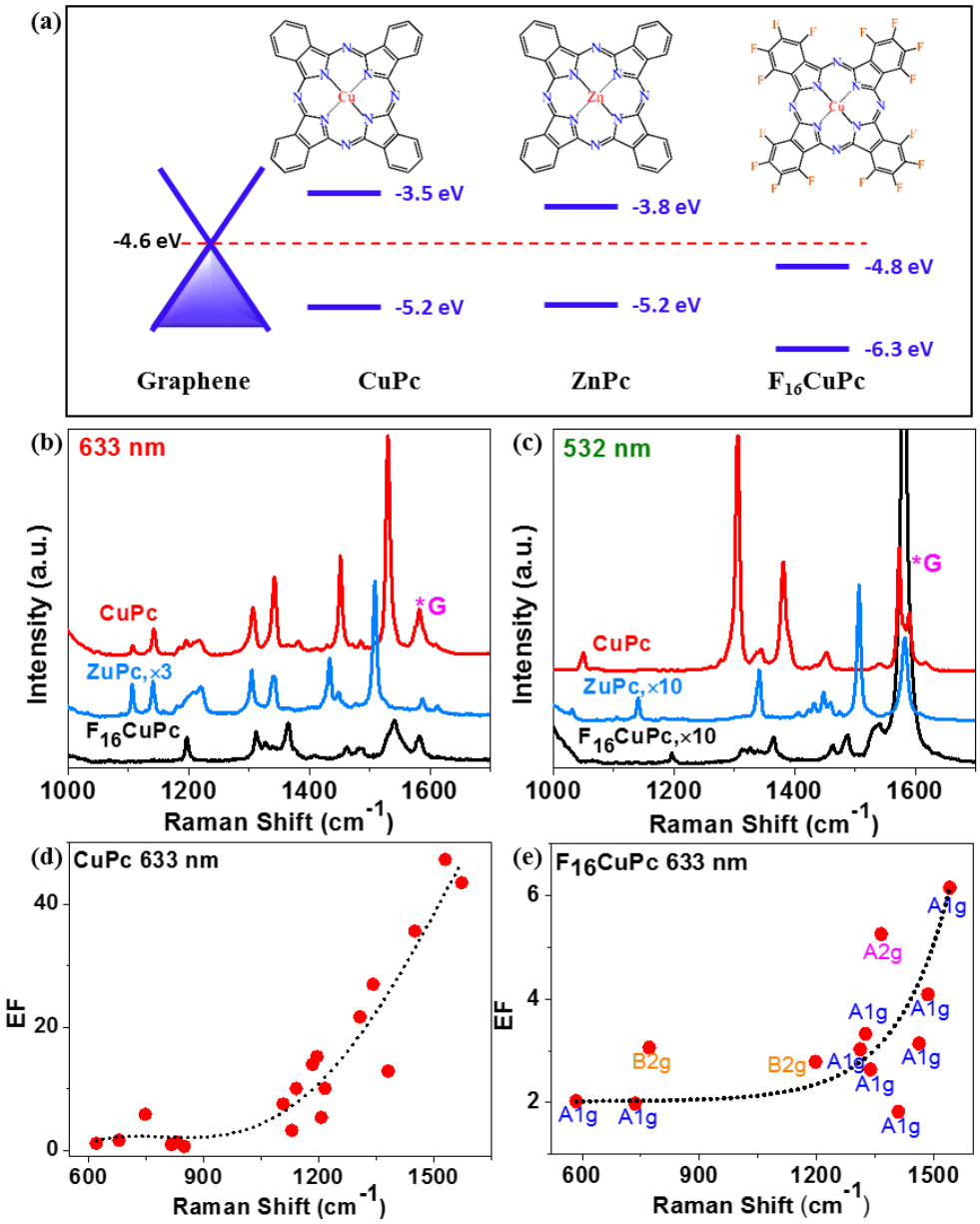

Figure 5-2. Influence of the molecular energy levels on GERS. (a) The first row shows the molecular structures of CuPc, ZnPc and F_{16}CuPc, from left to right. The second row shows the Dirac cone of graphene, the HOMO/LUMO energy levels of CuPc, ZnPc and F_{16}CuPc. (b-c) Raman spectra of 2 Å CuPc (red line), 5 Å ZnPc (blue line), and 5 Å F_{16}CuPc (black line) on graphene using the excitation laser wavelengths of 633 nm (b) and 532 nm (c). The spectra are normalized with the intensities of their corresponding 1450 cm^{-1} peaks on the Si/SiO_2 substrate. The "*" marked peaks in (b, c) are the G-band from graphene. (d-e) The

EF vs Raman shift for CuPc and F_{16}CuPc under 633 nm laser excitation. The red circles are experimental data and the black dotted curves are polynomial fits to the experimental data. (e) also shows the symmetry assignment of each mode, labeled beside the data points. Different symmetries are labeled with different colors.

To investigate the molecular selection rule of GERS in terms of the molecular structure and symmetry, the molecules with similar HOMO/LUMO energy levels but with different molecular symmetries are chosen as probe molecules. TTP, TCTA and sp2-NPB are three typical molecules with $D_{2h,}$ C_3, and S_4 symmetry structures, respectively. They have similar HOMO/LUMO energy levels, as shown in Figure 5-3(a). Their HOMO energy levels are at -5.5, -5.7, -5.6 eV, (*349–351*) respectively, and their LUMO energy levels are at -2.4, -2.4, -2.3 eV, respectively. Therefore, the difference between the HOMO and LUMO energy levels does not contribute to the GERS EF and can be excluded as a distinguishing feature. Figure 5-3 (b,c,d) show the Raman spectra of these three molecules: TTP, TCTA and sp2-NPB, including both the Raman spectra of the molecules on graphene (red line) and on SiO_2/Si substrates (black line) under the 633 nm laser excitation. It can be seen that the GERS EFs are different among these three molecules, which can be attributed to the influence of the molecular symmetry. Focusing on the 1450 cm^{-1} phonon mode, the distortion vibration of the 16-membered macrocycle and benzene ring, (*347*) the EFs of TTP, TCTA and sp2-NPB under 633 nm excitation are about 23.3, 6.9 and 4.3, respectively. The EF of TTP is 3.4 and 5.4 times that for TCTA and sp2-NPB, respectively, indicating that the contribution of the molecular symmetry to the GERS effect follows the order: D_{2h}>C_3>S_4. TPP has a symmetry (D_{2h}) that matches best that of graphene (D_{6h}). The importance of this matching is built on the perturbation theory of Raman scattering, (*122*) which dictates that the Raman scattering intensity is positively correlated to the molecule-graphene coupling. (*333*)

To confirm the positive correlation between the GERS effect and molecule-graphene coupling, we carried out DFT calculations on the TTP, TCTA and sp2-NPB molecules adsorbed on graphene. Contrary to TTP that has a planar structure, TCTA and sp2-NPB molecules prefer non-planar geometries. Consequently, for TCTA and sp2-NPB, the

average molecule-graphene distance is more than 4.3 Å and the energy release upon adsorption is around 0.04 eV per atom, as shown in Table 5-1. However, TTP is much closer to the graphene substrate (~3.24 Å) and presents a noticeably larger energy release upon adsorption (0.07 eV per atom). Clearly, the molecule-graphene coupling is strongest for TTP, and thus it has the highest GERS EFs among these three molecules. From a chemistry perspective, it is likely that these molecules are scattered through the Franck-Condon mechanism. (*352*) In this regard, we can also learn that the GERS mechanisms of molecules in Figure 5-2 (CuPc, ZnPc and F_{16}CuPc) and in Figure 5-3 (TTP, TCTA, sp2-NPB) are not the same. This is consistent with our analyses in this work: the GERS of molecules in Figure 5-2 can be attributed to the "Energy Level Rule", and that in Figure 5-3 can be attributed to the "Structure Rule". The usage of the "Energy Level Rule" and the "Structure Rule" can better and more straightforwardly reflect the relation between the molecule and graphene through a GERS process.

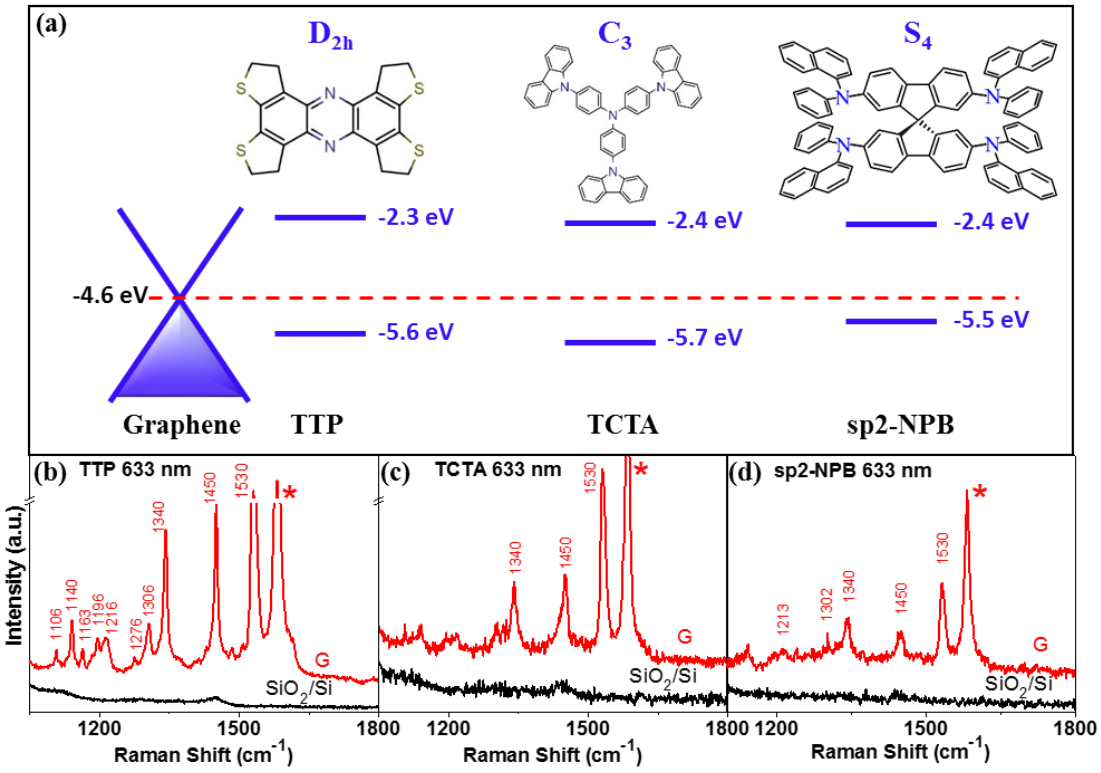

Figure 5-3. Influence of the molecular structure on GERS. (a) The first row shows the molecular structures of TCTA, TTP and sp2-NPB molecules, from left to right with labels above their corresponding Raman spectra, with their symmetries labeled above. The second

row shows the Dirac cone of graphene, the HOMO/LUMO energy levels of TCTA, TTP and sp2-NPB. (b-d) Raman spectra of 5 Å (b) TTP, (c) TCTA, and (d) sp2-NPB, on graphene (red line) and on a blank SiO_2/Si substrate (black line) with the excitation laser wavelengths of 633 nm. The "*" marked peaks in (b, c, d) are the G-band from graphene. Other peaks marked by the numbers come from the corresponding molecules.

From the above discussion of the influence of the molecular symmetry, we conclude that the molecular symmetry influencing the GERS intensity operates mostly through the molecule-graphene coupling. Figure 5-4 provides an example in support of the importance of the coupling between the molecule and graphene. We selected the N,N'-bis(3-methylphenyl)-N,N'-diphenyl-9,9-spirobifluorene-2,7-diamine (sp2-TPD) molecule, to compare with sp2-NPB. The GERS enhancement and energy levels of sp2-TPD are shown in Figure 5-4(a, d), respectively. The HOMO/LUMO energies of sp2-TPD (Figure 5-4(d)) and sp2-NPB (Figure 5-3(a)) are almost identical, with a difference of less than 0.1 eV.(*353*) In addition, these two molecules have the same structures, except for the substituents of $-CH_3$ in sp2-TPD and the parallel-connected conjugated benzene rings in sp2-NPB, shown in Figure 5-4(d) and Figure 5-3(a), respectively. The slight structural difference leads to different GERS enhancement effects, as seen in Figure 5-4(a) and Figure 5-3(d). Sp2-TPD does not have GERS enhancement under 633 nm laser excitation, but this enhancement is observable under 532 nm laser excitation. Sp2-NPB has GERS enhancement under both 633 nm and 532 nm excitations. In contrast, the 633 nm excitation yields stronger effects, including more molecular Raman peaks being resolved with observable intensities. Comparing these two molecules, sp2-NPB has a stronger GERS enhancement effect than sp2-TPD, where under 532 nm excitation, the phonon mode at 1450 cm^{-1} has an EF of 1.7 for sp2-NPB but only 0.9 for sp2-TPD, which is a factor of 2 lower.

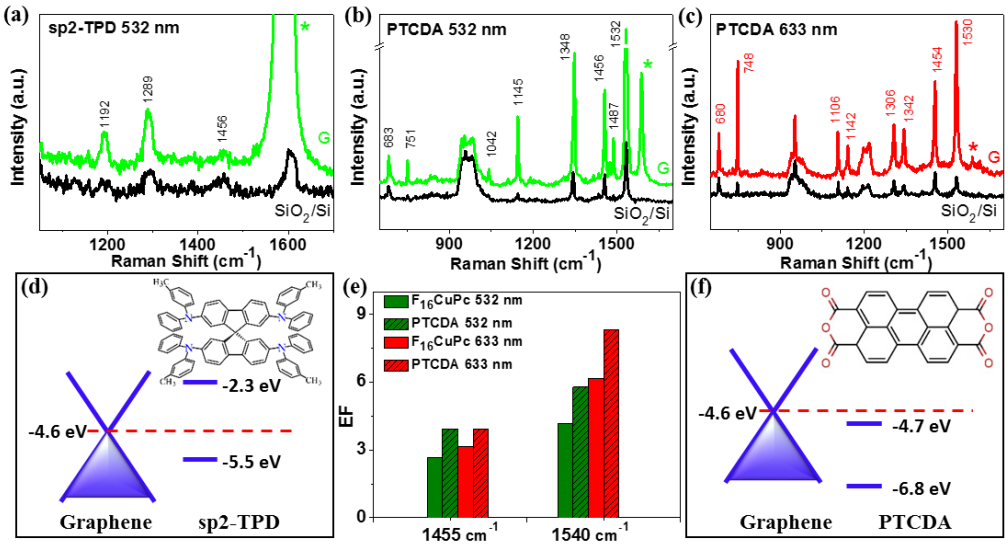

Figure 5-4. (a) Raman spectra of 5 Å sp2-TPD on graphene (colored line) and on a blank SiO_2/Si substrate (black line) taken with the excitation laser wavelengths of 532 nm. (b, c) Raman spectra of 5 Å PTCDA on graphene (colored line) and on a blank SiO_2/Si substrate (black line), with the excitation laser wavelengths of 532 nm (a) and 633 nm (b), respectively. (d) The Dirac cone of graphene, and the HOMO/LUMO energy levels of sp2-TPD. The inset of (d) shows the molecular structure of sp2-TPD. (e) EF of two vibrational modes, 1455 cm^{-1} and 1540 cm^{-1}, of $F_{16}CuPc$ and PTCDA (dashed) under 532 nm (green) and 633 nm (red) laser excitations. (f) The Dirac cone of graphene, and the HOMO/LUMO energy levels of PTCDA. The inset of (f) shows the molecular structure of PTCDA. The "*" marked peaks in (a, b, c) are the G-band from graphene.

This observation of different GERS EFs between sp2-TPD and sp2-NPB might be explained by the relatively weak coupling between sp2-TPD and graphene. For sp2-NPB, the parallel-connected conjugated benzene rings could strengthen the coupling between the molecule and graphene, because of the similarities between graphene's hexagonal carbon lattice and the benzene rings. Such an enhanced molecular-graphene coupling does not exist for sp2-TPD, where no parallel-connected conjugated benzene ring, but $-CH_3$ substituents make up the molecular structure. Our DFT calculations also indicate that sp2-

NPB has a slightly higher energy release upon adsorption (0.04 eV per atom) than sp2-TPD (0.03 eV per atom), as shown in Table 5-1. So the relatively weaker coupling possibly gives the overall smaller GERS enhancement in sp2-TPD than in sp2-NPB.

The effect of the molecule-graphene coupling can be strong in the GERS enhancement effect. In particular, the existence of connected benzene rings helps to strengthen the coupling and thus helps to enhance the GERS enhancement effect. To further confirm this hypothesis, we selected the molecule 3,4,9,10-perylene-tetracarboxylicacid-dianhydride (PTCDA) for GERS measurement, as shown in Figure 5-4(b,c,e,f). In terms of the HOMO/LUMO levels, F_{16}CuPc and PTCDA have similar LUMO energies that are only 0.1 eV different from each other, and PTCDA has a HOMO energy 0.5 eV lower than that of F_{16}CuPc. (*342*) The HOMO/LUMO gaps are therefore 2.1 eV for PTCDA and 1.5 eV for F_{16}CuPc. PTCDA is not resonant under 633 nm laser excitation, (*354*) but its GERS EFs are mostly larger for 633 nm laser excitation than for 532 nm laser excitation. This could be possibly attributed to the strong PTCDA-graphene coupling. The small energy difference of graphene's Fermi energy and the LUMO of PTCDA results in an effective charge transfer between graphene and PTCDA, and therefore results in the shifts of these energy levels. In addition, the seven parallel-connected conjugated rings of PTCDA, also with D_{2h} symmetry, make the molecule-graphene distance small (3.17 Å in Table 5-1) and the coupling between graphene and PTCDA strong (E^{ads} around -0.07 eV per atom).

Table 5-1. List of molecules with strong and weak GERS effect, including their structures (related references in superscript), symmetries (Symm.), HOMO/LUMO levels, the energy differences between HOMO (or LUMO) (*355*) and graphene's Fermi level (ΔE_{HF} / ΔE_{LF}), the typical phonon frequencies (ω_{ph}) and the corresponding EFs under both 532 nm (green shaded) and 633 nm (pink shaded) laser excitation. The red horizontal line divides the molecules showing larger and smaller GERS EFs. For a molecule above the red line, DFT-calculated average molecule-graphene distance d_z, and the adsorption energy E^{ads} per atom of the molecule are listed as well (negative sign means energy release upon adsorption).

[a] Excitation wavelength in the units of nm.

Molecule[Ref.]	Structure	Symm.	HOMO/LUMO (eV)	$\Delta E_{HF}/\Delta E_{LF}$ (eV)	d_z (Å)	E^{ads} (eV/atom)	ω_{ph} (cm^{-1})	EF
CuPc[29]	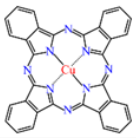	D_{4h}	-5.2/-3.5	-0.6/1.1	3.24	-0.06	1048 (532)[a] 1538 1451	37.5 11.6 24.3
							1530 (633) 1451	47.3 35.6
ZnPc[30]	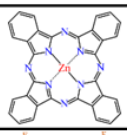	D_{4h}	-5.2/-3.8	-0.6/0.8	3.22	-0.06	1448 (532) 1508	4.1 11.9
							1508 (633) 1448	12.3 2.2
F_{16}CuPc[31]	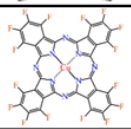	D_{4h}	-6.3/-4.8	-1.7/-0.2	3.19	-0.07	1540 (532) 1461	4.2 2.7
							1540 (633) 1461	6.2 3.1
PTCDA[30]	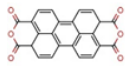	D_{2h}	-6.8/-4.7	-2.2/-0.1	3.17	-0.07	1532 (532) 1455	5.8 3.9
							1531 (633) 1454	8.3 3.9
TTP[38]	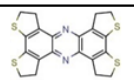	D_{2h}	-5.6/-2.3	-1.0/2.3	3.24	-0.07	1450 (633)	23.3
TCTA[39]	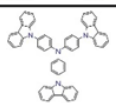	C_3	-5.7/-2.4	-1.1/2.2	4.34	-0.04	1340 (532) 1455	1.3 0.9
							1449 (633)	6.9
Sp2-NPB[40]	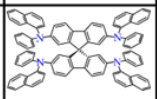	S_4	-5.5/-2.4	-0.9/2.2	4.36	-0.04	1503 (532) 1450	5.3 1.7
							1447 (633)	4.3
Sp2-TPD[42]	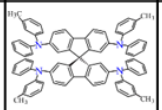	S_4	-5.5/-2.3	-0.9/2.3	4.27	-0.03	1450 (532) 1290	0.9 2.3
							1446 (633) 1290	0.9 1.0
TPBi[48]	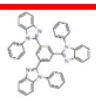	C_3	-6.7/-2.7	-2.1/1.9			1450 (532) 1280	1 1.5
							1449 (633)	2.9
$Ir(ppy)_3$[47]	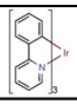	C_3	-5.6/-3.0	-1.0/1.6			none	
BCP[49]	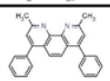	C_2	-7.0/-3.5	-2.4/1.1			1446 (633) (532 none)	1
Alq_3[49]		C_3	-5.8/-3.1	-1.2/1.5			none	

Compared to PTCDA, F_{16}CuPc has a similar HOMO level and a smaller HOMO/LUMO energy gap which makes it easier for the 633 nm laser to yield strong Raman scattering. The GERS EFs of F_{16}CuPc and PTCDA are similar, with slightly higher

EF values for PTCDA. Take the 1540 cm^{-1} phonon mode (the C-C stretching vibration on the benzene and pyrolle ring (*356*)) as an example. Under 532 nm laser excitation, the EFs of F_{16}CuPc and PTCDA are 4.2 and 5.8, respectively. Under 633 nm laser excitation, the EFs of F_{16}CuPc and PTCDA are 6.2 and 8.3, respectively. For the 1450 cm^{-1} phonon mode, under 532 nm laser excitation, the EFs of F_{16}CuPc and PTCDA are 2.7 and 3.9, respectively; under 633 nm laser excitation, the EFs of F_{16}CuPc and PTCDA are 3.1 and 3.9, respectively. For both these vibrational modes, the GERS EFs for PTCDA are about 1.4 times that for F_{16}CuPc under both 532 nm and 633 nm laser excitations, shown in Figure 5-4(e). Compared to the large GERS EF differences between CuPc, ZnPc and F_{16}CuPc, or between TTP, TCTA and sp2-NPB, the EF difference between F_{16}CuPc and PTCDA is relatively small, which can be attributed to their similar molecule-graphene distance and coupling. The slightly stronger GERS enhancement of PTCDA could be partly due to the parallel-connected conjugated ring structure of PTCDA and thus the relatively smaller PTCDA-graphene distance (see Table 5-1), (*357*) which is important to strengthen the coupling between the molecule and its graphene substrate. This strengthened coupling with graphene due to conjugated-rings, which has been reported before, (*358*) might result in a shift of the molecular HOMO/LUMO energy levels. Overall, these experimental observations suggest that the GERS EF is increased with the smaller distance and stronger coupling between the molecules and graphene.

We can now summarize our findings with the establishment of a set of rules for the molecular selectivity of the GERS enhancement process. Table 5-1 summarizes results obtained for 12 molecules. The table includes their structures, symmetries, HOMO/LUMO energies, (*355*) the energy differences between the HOMO/LUMO and the graphene Fermi energy (ΔE_{HF}, ΔE_{LF}), molecule-graphene distance (d_z), adsorption energy, typical phonon modes (ω_{ph}) and the corresponding EFs. In this table, TPBi, iridium, tris(2-phenylpyidine) ($Ir(ppy)_3$), BCP and Tris-(8-hydroxyquinoline) aluminum (Alq_3) all show very small or no GERS enhancement under 532 nm or 633 nm laser excitations. From the other molecules, it is clear to see that the GERS effect follows the molecular selectivity rules as below: (1) Energy Level Rule: GERS enhancement requires the appropriate HOMO/LUMO energy levels of the molecules with a certain energy laser excitation (Eqs. (i-iv)). Briefly, strong

enhancement occurs when the HOMO/LUMO differs from the graphene Fermi Level by the phonon energy. Further enhancement can occur when the excitation laser energy is close to the molecular HOMO/LUMO energy separation. The different GERS EF values of CuPc, ZnPc and F_{16}CuPc support this rule, because these molecules have similar molecule-graphene coupling but different HOMO/LUMO values. As another example, TPBi and BCP have HOMO/LUMO gaps of 4 eV (*359*) and 3.5 eV, (*360*) which are too large to be resonant with the 532 nm or 633 nm laser. Their HOMO/LUMO energies are also too far away from the graphene Fermi energy, possibly leading to a weak charge transfer between the molecule and graphene. This may be part of the reason why no GERS effects were observed for these molecules under 532 nm or 633 nm excitation. (2) Structure Rule: molecular structure with D_{nh} symmetry is favorable for GERS enhancement. A strong molecule-graphene coupling, which helps GERS enhancement, requires a small molecule-graphene distance and a structural match of the molecules and graphene. D_{nh} symmetry of the molecule is a good condition for structural compatibility. Symmetry matching leads to the stronger GERS effect for Pc derivatives, PTCDA and TTP molecules, which have the symmetry of D_{4h}, D_{2h}, and D_{2h}, respectively, and a weaker GERS effect is seen for sp2-NPB and sp2-TPD with S_4 symmetry. Molecules TPBi, $Ir(ppy)_3$, BCP and Alq_3, each of which has the symmetry of C_3, C_3, C_2 and C_3, respectively, have non-planar structures. (*359–361*) Such low symmetries and non-planar structures could also lead to their weak molecule-graphene couplings, and contribute to the weak GERS enhancement effects of these four molecules. Additionally, parallel-connected conjugated rings in the molecular structure are favorable in obtaining strong GERS enhancement, since the connected rings increase the structural similarity between the molecule and graphene, and therefore generally reduce the molecule-graphene distance and strengthen the coupling. The stronger enhancements of TTP (compared to TCTA) and sp2-NPB (compared to sp2-TPD) support this rule of ring-connection and molecule-graphene coupling. Due to the different molecule-graphene interactions, the same vibrational mode shows different GERS EFs in different molecules. For example, the 1450 cm^{-1} vibrational mode under 633 nm laser excitation has a GERS EF ranging from 0.9 (in sp2-TPD) to 35.6 (in CuPc); for the 1530 cm^{-1} mode under 633 nm laser excitation, the GERS EF can range from 6.2 (in F_{16}CuPc) to 47.3 (in CuPc). This broad variation of the GERS EF for the same vibrational mode

demonstrates the strong effect of the molecular selectivity in GERS. From Table 5-1, we conclude that a strong GERS EF requires the appropriate HOMO/LUMO levels for the molecule, and the molecular symmetry and structure to be well matched with graphene to maximize the molecule-graphene coupling.

To further support the finding that the molecules with a strong GERS effect are strongly coupled with graphene, we performed a set of UV-visible absorption measurements for different molecules with and without contacting the graphene substrates (Figure 5-5). The molecules chosen here include F_{16}CuPc and PTCDA (Figure 5-5(a)), which have large GERS EFs, and sp2-TPD, sp2-NPB and BCP (Figure 5-5(b)), which have small or no GERS EFs. As seen in Figure 5-5(a), the absorption of graphene's π-band at 269 nm is obvious, indicating the good crystal quality of graphene. For all the molecules in Figure 5-5, the light absorptions are stronger when the molecules are deposited on graphene, suggesting the role of graphene in absorbing light. For F_{16}CuPc and PTCDA, molecular absorption peaks are also frequency shifted when molecules contact graphene. Upon contact to graphene, F_{16}CuPc presents absorption peaks at 631 nm and 645 nm that split into three peaks: 612 nm, 652 nm and 683 nm, and the absorption peak at 762 nm that red shifts to 766 nm. For PTCDA, the absorption peak at 612 nm does not show an observable frequency shift when PTCDA is on graphene, but the peak at 683 nm is red shifted by almost 20 nm. Graphene's π-band at 269 nm is also blue shifted to 266 nm when graphene contacts F_{16}CuPc or PTCDA. These phenomena suggest that the interaction between molecules and graphene, and the different UV-visible absorption changes between F_{16}CuPc and PTCDA demonstrate the different levels of the molecule-graphene interactions of these two molecules. Besides F_{16}CuPc and PTCDA, CuPc also shows its coupling with graphene and this conclusion is supported by the UV-visible absorption change before and after contacting graphene, (*362*) which shows an additional strong absorption peak at 706 nm when CuPc is on graphene. Compared to F_{16}CuPc and PTCDA, the molecules with a small GERS EF, i.e., sp2-TPD, sp2-NPB and BCP, do not show frequency shifts in their absorption peaks near 601 nm and 646 nm for all three molecules, and at approximately 380 nm for sp2-TPD and sp2-NPB. For the absorption peaks near 220 nm for sp2-TPD and sp2-NPB, slight frequency shifts appear when these molecules

are on graphene: a red shift of 3 nm for the 223 nm peak (without graphene) of sp2-NPB, and a red shift of 3 nm for the 221 nm peak of sp2-TPD. These slight frequency shifts suggest the weak coupling between graphene and these molecules, and this weak coupling is also reflected in the small GERS EF (less than 5). In contrast, no frequency shift in the absorption peak near 220 nm can be observed for the case of the BCP molecule, suggesting that graphene has an even weaker interaction with BCP than with sp2-NPB and sp2-TPD. This weaker interaction can also be demonstrated in the GERS EF, in which BCP's GERS EF is nearly 1, which is smaller than the values of sp2-TPD and sp2-NPB. TPBi, which has a low GERS EF, is similar to the situation of sp2-TPD and sp2-NPB in terms of UV-vis absorption. Moreover, sp2-NPB has larger light absorption than sp2-TPD in the visible range. The absorption differences between these two molecules ($\Delta\alpha_M = \alpha_{M1} - \alpha_{M2}$, where α_{M1} and α_{M2} are the absorptions of the two molecules, respectively) are not the same at wavelengths of 532 nm and 633 nm, and the difference of $\Delta\alpha_M$ between 532 nm and 633 nm light, $\Delta\alpha_{M,wl} = \left|\Delta\alpha_{M,532\,nm} - \Delta\alpha_{M,633\,nm}\right|$, becomes larger after the molecules come into contact with the graphene surface. As shown in Figure 5-5, before being placed in contact with graphene, their light absorption differences ($\Delta\alpha_M$) are 0.42% at 532 nm and 0.44% at 633 nm, resulting in $\Delta\alpha_{M,wl}$ of 0.02%. After contacting the graphene surface, the absorption differences ($\Delta\alpha_{M,on\,G}$) become 0.41% at 532 nm and 0.51% at 633 nm, resulting in $\Delta\alpha_{M,on\,G,wl}$ of 0.10%. The fact that $\Delta\alpha_{M,wl} \neq \Delta\alpha_{M,on\,G,wl}$ also shows the different strengths of the molecule-graphene coupling for sp2-NPB and sp2-TPD. Besides the difference in their adsorption energies E_{ads} shown in Table 5-1, the difference in light absorbance at different wavelengths may be another factor that contributes to their different Raman intensities with different excitation laser wavelengths.

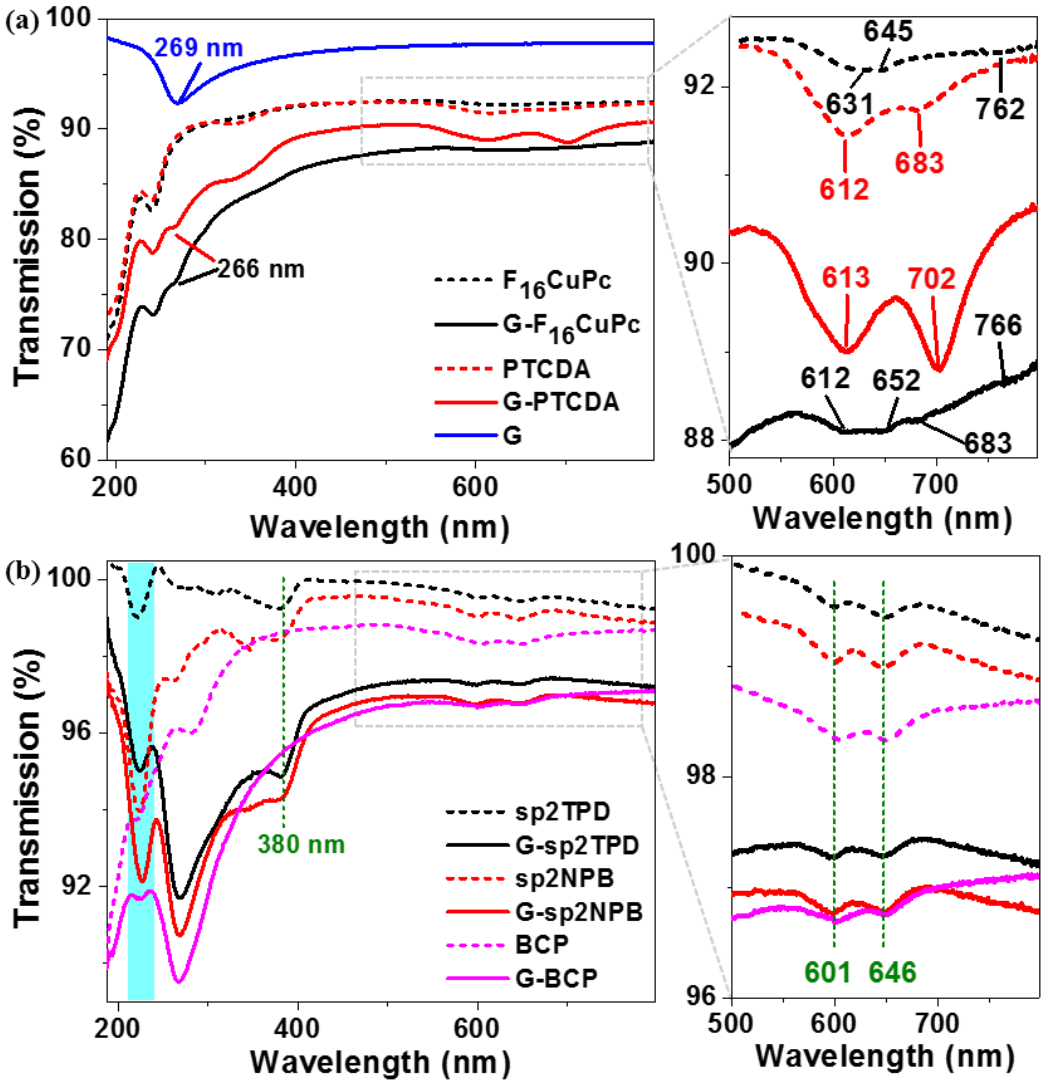

Figure 5-5. (a) The UV−vis transmission spectra of pristine graphene (blue solid line), $F_{16}CuPc$ (black dashed line), $F_{16}CuPc$ on graphene (black solid line), PTCDA (red dashed line) and PTCDA on graphene (red solid line). The enlarged spectra of (a) in the wavelength range of 500 nm to 800 nm are shown on the right. The wavelengths of the transmission valleys (absorption peaks) are labeled, including the graphene π-band at approximately 270 nm. (b) The UV−vis transmission spectra of sp2-TPD (black dashed line) and sp2-TPD on graphene (black solid line), sp2-NPB (red dashed line) and sp2-NPB on graphene (red solid line), BCP (magenta dashed line) and BCP on graphene (magenta solid line). The wavelengths of the transmission valleys (absorption peaks) are labeled with

a green dotted line and a cyan box. The enlarged spectra of (b) in the wavelength range of 500 nm to 800 nm are shown on the right of (b).

In conclusion, we have studied the molecular selectivity of GERS through systematic experimental measurements on a number of representative molecules. The experimental data were complemented with first-principles calculations to extract two general basic rules for strong GERS enhancement. First, we established that molecules should have the appropriate HOMO/LUMO energy level alignments. This rule is theoretically analyzed using third order perturbation theory in the application of Raman scattering, and is demonstrated by the GERS enhancement of the CuPc molecule. Second, the molecule's structure must display an appropriate point group symmetry, including D_{nh} symmetry, and parallel-connected conjugated rings in their structures. The former condition is a basic requirement for a strong molecule-graphene structural compatibility and interaction that yields a stronger charge-transfer and a larger GERS EF. The latter is an additional requirement for the molecule-graphene structural compatibility that has to be fulfilled in addition to the D_{nh} symmetry. Such parallel-connected rings, which are similar to graphene's hexagonal lattice structure, are important for both molecule-graphene coupling and charge transfer, and both factors can enhance the GERS EF. Both selection rules of the molecular energy levels and of the molecular structure cooperate to achieve a strong molecular-graphene interaction, and therefore an effective charge-transfer between the molecules and graphene. This requirement of molecule-graphene interaction was also supported by the UV-visible absorption spectra measurements before and after contact with the graphene substrate. Considerable frequency shifts are observed for molecules with large GERS EF, and negligible frequency shifts are observed for those molecules showing a small GERS EF. This work is important for the study of the chemical mechanism for the SERS effect, and more generally for the study of molecule-graphene coupling. Moreover, GERS has many applications in the areas of chemical or biological sensing, and our work points out how to choose the right molecules in GERS measurements for different applications. Therefore, this work offers useful guidelines for the applications of the GERS

effect in chemical detection, as well as for the potential GERS effect application in medical and biological technologies.

5.2 Interaction of 2D Material with Plasmonic Nanocavity

Optical nanocavities are essential elements for photonic devices in diverse applications, including cavity quantum electrodynamics, (*363–367*) enhancement and suppression of spontaneous emission, (*368–371*) single molecule sensing, (*372*) photonic devices in optical communications such as sources (*366*, *373–375*) and filters. (*376*, *377*) Two key parameters, the mode volume V_{eff} and quality factor Q, can be used to characterize optical nanocavities. The mode volume is an equivalent volume if the modes are distributed homogeneously at the peak intensity value, (*378*) and is defined as $V_{eff} = \frac{\int \epsilon(\vec{r})|\vec{E}(\vec{r})|^2 d^3\vec{r}}{max\left(\epsilon(\vec{r})|\vec{E}(\vec{r})|^2\right)}$, where $\epsilon(\vec{r})$ and $\vec{E}(\vec{r})$ are the dielectric permittivity and electric field at the spatial location $\vec{r}$. The quality factor Q is proportional to the confinement time in the optical period, and is defined as $Q = \omega_r/\Delta\omega$, where ω_r and $\Delta\omega$ are the resonance frequency and full-width at half maximum, respectively. These parameters, V_{eff} and Q, represent the degrees of the spatial and spectral light confinement in the optical cavity, respectively. Enhancement of the spatial confinement has been achieved by the development of microresonators of various geometries, (*378*) while enhancement of the spectral confinement has been realized by making use of low-loss materials (such as silica) and low-leakage configurations. (*379–383*) The combination of V_{eff} and Q, the Purcell factor, $F_P = \frac{3}{4\pi^2}\left(\frac{\lambda}{n}\right)^3\left(\frac{Q}{V_{eff}}\right)$, is proportional to the ratio between the quality factor and effective volume and is proportional to the spontaneous emission rate. Therefore, the Purcell factor offers a guideline to control the light emission efficiency and other processes such as surface enhanced Raman scattering (SERS).

Moreover, in order to achieve high efficiency of spontaneous emission or SERS, another parameter, the scattering efficiency η_{scat}, needs to be optimized. η_{scat} can characterize the capability of a plasmonic structure to scatter light, and is defined as

$\eta_{scat} = \sigma_{scat}/\sigma_{phys}$, where σ_{scat} and σ_{phys} are the scattering cross-section and physical cross-section, respectively. It should be mentioned that η_{scat} can be either <1, =1 or >1. In particular, if $\eta_{scat} > 1$, the scattering cross section is larger than the physical cross section, which means that light can scatter stronger on a plasmonic structure. Obviously, the optimization of the nanocavity parameters V_{eff}, Q, F_P and η_{scat} will help in guiding the design of cavities for more efficient photonic devices, such as nanoscale light sources, switches and detectors for sensing purposes, photonic circuits and telecommunications.

There are various types of optical cavities and they have different performances regarding optical confinement. Dielectric optical cavities work well in spectrally confining the optical field, (*381*) with quality factors Q up to 10^9. However, they can hardly achieve deep sub-wavelength spatial confinement due to the diffraction limit and they only offer V_{eff} of around $10^{-2}(\lambda/2n)^3$. (*384*) In contrast, plasmonic cavites can achieve better spatial confinement with V_{eff} below $10^{-3}(\lambda/2n)^3$. (*385–387*) Therefore, despite the poor spectral confinement (low Q value typically below 100) resulting from using lossy metals and leaking cavities at optical frequencies, (*388, 389*) plasmonic cavities exhibit extraordinarily large enhancement over spontaneous emission rates, nonlinear optical responses, and strong coupling. (*390–396*) However, present plasmonic cavities suffer from sophisticated nanofabrication procedures. (*397–399*) Therefore they are costly in time and expense, which hinders their wider applications. Another type of optical cavities, nanoparticle-on-mirror (NPoM) cavity, (*391, 392, 400–406*) which was first proposed by Metiu, et al., (*400, 401*) has been found to have strong SERS enhancement (*392, 402, 403*) and plasmon tunability. (*391, 404, 406*) Moreover, the ease of NPoM cavity fabrication and flexibility in its usage make it more desirable than other plasmonic cavities, triggering the exploration of its optical properties and potential applications using NPoM cavity structures.

In this work, we show that plasmonic cavities based on the NPoM architecture overcome the disadvantages of conventional plasmonic cavities. (*407*) Using finite-difference time-domain (FDTD) simulations, we systematically study three types of NPoM structures, nanosphere-, nanorod- and nanocube-on-mirror in terms of various optical cavity parameters: scattering efficiency, field enhancement, effective mode volume, quality factor and Purcell factor. We show through FDTD simulation that by carefully

designing the NPoM plasmonic nanocavity, including tuning the gap distance between the nanoparticle and mirror, as well as the size of the nanoparticle, such NPoM structures can exhibit deep sub-diffraction mode volumes, reaching below $10^{-7}(\lambda/n)^3$. Despite the small quality factor of ~20, the Purcell factor can reach beyond 10^7, similar to the state-of-the-art microsphere cavity. (*393*) Such a strong Purcell effect can facilitate the enhancement of spontaneous emission in these NPoM nanocavities. Moreover, we experimentally study the nanosphere-on-mirror structure using dark field (DF) scattering spectroscopy and second-harmonic generation (SHG), which confirm the simulation results. Our study is important in guiding the design of optical nanocavities based on the NPoM structure for various applications. We envision NPoM cavities as promising candidates for nanoscale light sources, switches and detectors in photonic circuits and telecommunications. In fact, we also observed that this NPoM cavity can be effective in tuning and enhancing the optical response of monolayer MoS_2.

The NPoM structures studied in this work include nanosphere-, nanorod-, and nanocube-on-mirror, as schematically shown in Figure 5-6(a-c), respectively. All the three types of Au nanoparticles can be synthesized with controllable shapes and dimensions. (*408–411*) The mirrors that are thin film layers and the nanoparticles are both made of metal. For each of the structures in Figure 5-6, there is a layer of dielectric material between the mirror and the nanoparticle. In our study, we choose the mirrors to be a 50 nm thick Au film prepared using e-beam evaporation, and the nanoparticles are also made of Au. The dielectric material in the gap is Al_2O_3, which is grown using atomic layer deposition (ALD). In Figure 5-6, both the side and top views of the three structures are shown. The nanoparticles in the sphere, rod and cube shapes represent point contact, line contact and plane contact with the mirror, respectively. Therefore, these three structures constitute a relatively complete sample set for the study of the optical properties of the NPoM nanocavity.

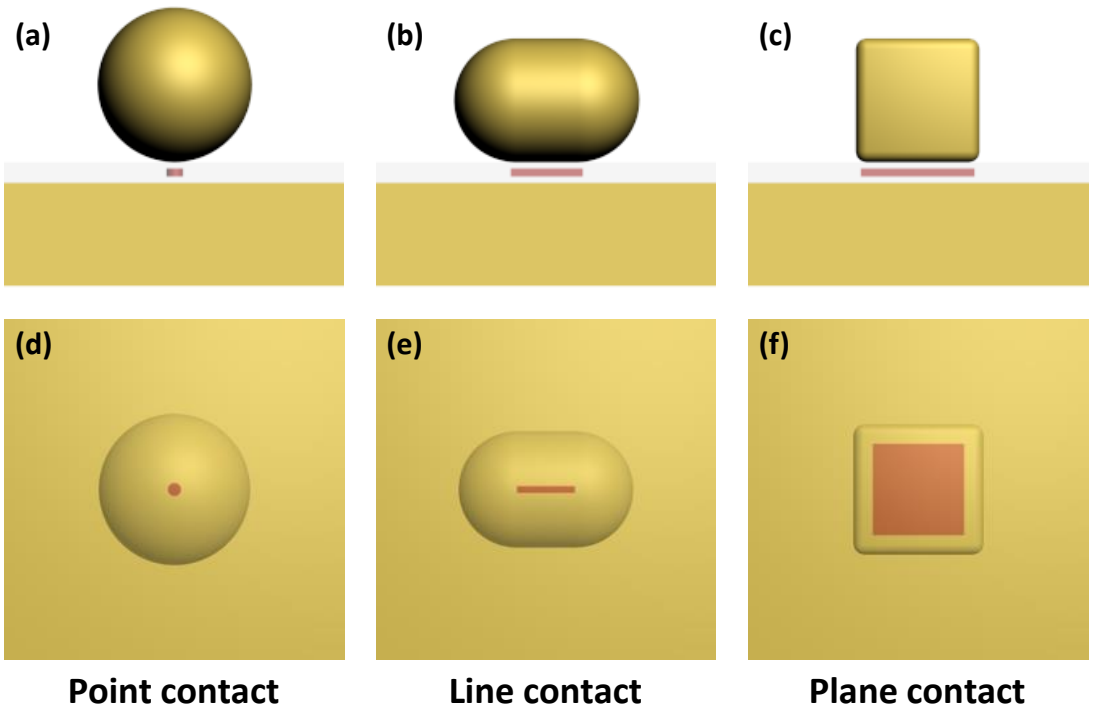

Figure 5-6. Schematic of three NPoM structures: sphere- (a,d), rod- (b,e) and cube- (c,f) on-mirror, which shows point contact, line contact and plane contact, respectively. A dielectric layer separates the nanoparticle and the mirror. (a-c) shows side views, and (d-f) shows top views.

For the NPoM structures studied here, the shape effects on their optical properties are first investigated. The parameters to merit such shape effects include the scattering efficiency, field enhancement, mode volume V_{eff} and quality factor Q, all of which are plotted as a function of both the incident light wavelength (480 to 980 nm) and the gap distance (2 to 10 nm), as shown in Figure 5-7. The sizes of the nanoparticles are chosen so that their surface areas exposed to the environment medium (in our case, air) are similar, which enables the comparison of nanoparticle shapes without the influence of nanoparticle sizes. For nanosphere-on-mirror, we choose the nanosphere diameter of 74 nm. The simulation results show that the scattering efficiency η_{scat} (plotted as $\log_{10}(\eta_{scat})$) is overall low, as seen in Figure 5-7(a). η_{scat} reaches the maximum value of around 1.6 at the

wavelength around 550 nm ~ 600 nm, and shows broad spectral peaks for all gap distances from 2 nm to 10 nm. For wavelengths below 500 nm and above 700 nm, the scattering is negligibly weak (η_{scat} smaller than 0.1). The field enhancement values $|E_{max}|^2/|E_0|^2$ (plotted as $\log_{10}\frac{|E_{max}|^2}{|E_0|^2}$, $|E_{max}|^2$ is the maximum field intensity among all the positions) are low as well, with the maximum value of about 3000, for a gap distance of 2 nm and wavelength of around 585 nm (Figure 5-7(b)). The field enhancement decreases with increasing gap distances or the change of wavelength. As a result, the effective mode volume V_{eff} (plotted as $\log_{10}\frac{V_{eff}}{(\lambda/n)^3}$) exhibits a minimum value around $10^{-5}(\lambda/n)^3$ at the same condition of the maximum field enhancement, shown in Figure 5-7(c). For the NPoM structure nanorod-on-mirror, the properties are very different from nanosphere-on-mirror. Here in Figure 5-7(d-f), we plot the optical properties for the nanorod with a diameter of 60 nm and a total length of 90 nm (therefore a cylinder with a diameter of 60 nm and a length of 30 nm is sandwiched between two hemispheres with a diameter of 60 nm). We use the notation 60-90 nm to indicate the size and shape of the nanorod. As can be seen, the scattering efficiency η_{scat} reaches the maximum value of ~7 for a gap distance 10 nm at a wavelength around 630 nm (Figure 5-7(d)). Such a maximum η_{scat} is much larger than the nanosphere-on-mirror structure, indicating that nanorods are more effective in scattering light at the wavelength and gap distance ranges studied here. With the decrease of the gap distance, the maximum scattering efficiency decreases and is redshifted. A secondary maximum value of the scattering efficiency is reached at a shorter wavelength for each gap distance, and for a gap distance of about 10 nm, for example, the secondary maximum 0.6 occurs at around 540 nm. With the gap distance decreasing, the major maximum of scattering efficiency decreases and its wavelength redshifts, while the secondary maximum scattering efficiency is almost unchanged and its wavelength redshifts only slightly compared to the major maximum. For the field enhancement effect shown in Figure 5-7(e), the nanorod structure also yields much higher enhancement values than the nanosphere. The maximum value of $|E_{max}|^2/|E_0|^2$ can reach ~4×10^4, which is an order of magnitude higher than that of the nanosphere, at a gap distance of 2 nm and wavelength around 780 nm. The mode volume (Figure 5-7(e)) roughly follows the opposite trend of the field enhancement, and the minimum value is around $10^{-7}(\lambda/n)^3$, 100 times smaller

than the nanosphere. The nanocube structure in Figure 5-7(g-i) is 60 nm in side length but each corner is rounded with a diameter of 5 nm (the contact area between nanocube and mirror is 55 nm × 55 nm). The major maximum η_{scat} can also reach 7 at wavelength 715 nm, and there is also a secondary maximum at around 530 nm. The evolution of the major and secondary maxima η_{scat} in nanocube-on-mirror as a function of gap distance is similar to nanorod-on-mirror, but for each gap distance, the major maximum η_{scat} is redshifted compared to the nanorod (Figure 5-7(g)). This is because the sharper corners of the nanocube can separate electrons more efficiently than the nanorod, and thus reduce the restoring force and collective oscillation frequency. (*412*) The same phenomenon occurs for the field enhancement. Besides, the maximum field enhancement for the nanocube is only around $|E_{max}|^2/|E_0|^2 \sim 6 \times 10^3$ (Figure 5-7(h)), about one tenth of the maximum field enhancement achieved in the nanorod structure, but the minimum mode volume for the nanocube (Figure 5-7(i)) can reach as small as $10^{-8}(\lambda/n)^3$ within the wavelength range 480 to 980 nm. Compared to the nanosphere, the stronger scattering efficiency, larger field enhancement and smaller mode volume of the nanorod and nanocube are due to their lower symmetries and sharper features than the nanosphere, which have been shown to be more effective in concentrating the near field close to the nanoparticle surface. (*413–416*)

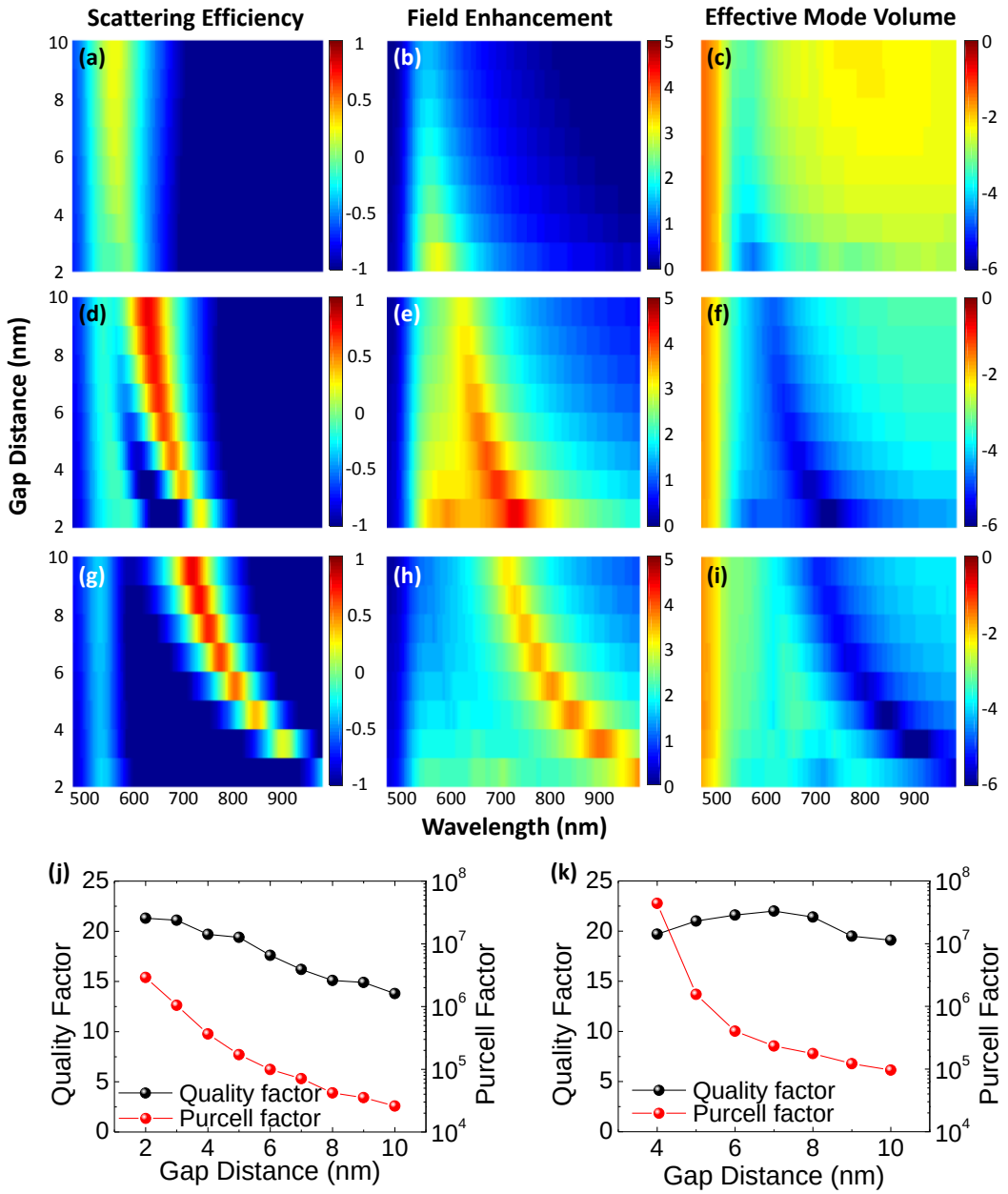

Figure 5-7. FDTD simulation results of scattering efficiency (a,d,f), field enhancement (b,e,h) and effective mode volume (c,f,i), all in log scale, as functions of gap distance and wavelength for three NPoM structures: Au sphere- (a-c), Au rod- (d-f) and Au cube- (g-i) on-mirror. The Au sphere is 74 nm in diameter. The Au rod is 60nm in diameter and 90 nm in length. The Au cube is 60 nm in length with rounded corners of 5 nm in diameter. (j-k) Quality factor and Purcell factor of Au rod- (j) and Au cube- (k) on-mirror.

Notice that the maximum scattering efficiency for all of these three NPoM structures show a decreasing trend when the gap distance decreases from 10 nm to 2 nm. This occurs because a decrease in the gap distance causes an increase in the absorption efficiency and more light field to be coupled in the gap. The local plasmon modes of the two systems, nanoparticle and nanofilm, couple stronger as the gap shrinks. (*417*) In fact, the smaller resonance wavelengths in scattering (Figure 5-7(a,d,g)) correspond to the resonance of the nanoparticle itself (nanoparticle mode), so they are almost unchanged with changes in the gap distance. The redshifted wavelengths (Figure 5-7(a,d,g)) correspond to the coupled mode between the nanoparticle and nanofilm. Therefore, as the gap shrinks, a redshift can be observed. (*391*) For the nanosphere in Figure 5-7(a), the separation between the coupled mode and nanoparticle mode is almost negligible, and as the size of the nanosphere increases, the separation will be more observable. The fundamental mode for NPoM is the dipole mode, which strongly radiates. (*418, 419*) There may be other modes, such as a quadrupole mode or modes with other orders, which radiate much weaker than dipole modes. (*419*) As will be discussed later, our simulations in Figure 5-8 show that the coupled mode has a dipolar nature. Therefore, it has stronger scattering than the other mode. Actually, for the dipole mode, the maximum field intensity extends beyond the interface between the nanoparticle and the dielectric film, and penetrates into the dielectric layer. This phenomenon was also reported in the literature, (*420*) and is similar to the case of nanoparticle dimers, (*421*) since the NPoM structure shows a mirror image of the nanoparticle. (*418*) In contrast, the field penetration for the higher-order mode is relatively small, which supports the interpretation that this mode is inherent to the nanoparticle itself. This observation is consistent with the results reported in other works. (*417*, *422*, *423*) Moreover, the wavelength for maximum scattering also corresponds to the maximum field enhancement and minimum mode volume, which can be viewed as the resonance condition for the NPoM system.

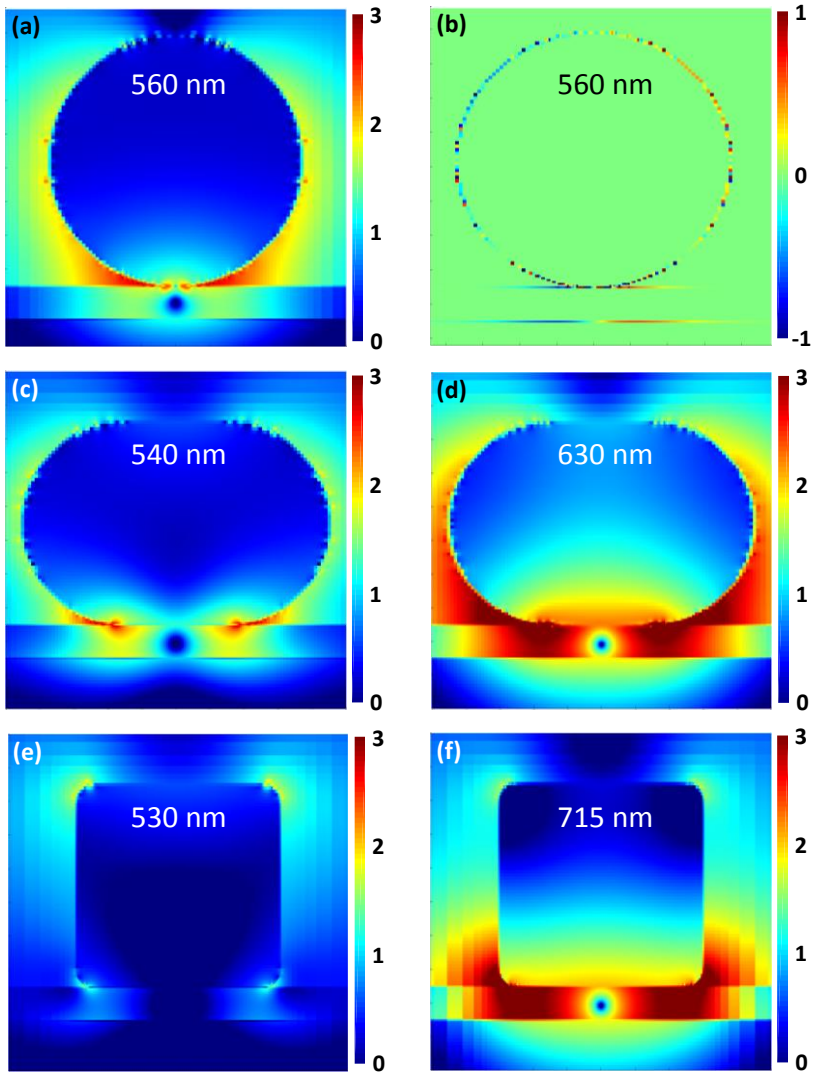

Figure 5-8. Maps of field enhancement $|E|^2$ in xz plane (a,c-f) for Au nanosphere- (a), nanorod- (c-d) and nanocube- (e-f) on-mirror. The charge distribution contours in xz plane of Au nanosphere-on-mirror is shown in (b). The wavelengths are chosen at the major and secondary maxima of scattering efficiency, and are labeled in each panel. The sizes of the nanoparticle are the same as in Figure 5-7: the nanosphere (a-b) is 74 nm in diameter, the nanorod (c-d) dimension is 60-90nm, and the nanocube (e-f) is 60 nm in side length. The dielectric gap distance is 10 nm.

For both the nanorod and nanocube, the quality factors and Purcell factors at different gap distances are shown in Figure 5-7(j-k), respectively. Both structures give quality factors of around 20. The nanosphere-on-mirror structure only gives relatively small quality factors, generally smaller than 10, and are not plotted here. Compared to the structures previously studied, (*381*) the quality factors for these NPoM structures are not high, but the mode volume is much decreased. With the quality factor and mode volume, we can calculate the Purcell factor F_P, which can reach 10^7. Such a high Purcell factor value is similar to the state-of-the-art microsphere cavity, (*393*) indicating the potential of nanophotonic light sources, light emission enhancement and high-density optical information processing using these NPoM structures.

For each structure shown in Figure 5-7, we perform careful analyses of their field and charge distributions. We choose the gap distance and wavelength with the maximum scattering efficiency, and plot the cross sections of their field intensity $|E|^2$ and charge distribution in both side (xz plane) and top (xy plane) views, as seen in Figure 5-8. Figure 5-8(a-b) and S1 show the nanosphere (diameter 74 nm) with a gap distance of 10 nm and wavelength of 560 nm. As can be seen in Figure 5-8(a), the strongest field enhancement occurs near the contact point of the nanosphere and the dielectric plane, and minimum field intensity occurs in the middle of the dielectric material, below the center point of the nanosphere. The lateral field confinement for the nanosphere-on-mirror is not strong, which can span for around 60 nm (Figure 5-8(a)), matching the results shown in Figure 5-7(c) where the mode volume for the nanosphere-on-mirror is not very small. The charge distribution in Figure 5-8(b) shows that the maximum scattering of the 74 nm-diameter nanosphere arises from a dipole mode. Figure 5-8(c-d) shows the nanorod with a gap distance of 10 nm and wavelength of 630 nm (major maximum) and 540 nm (secondary maximum). It is clear from Figure 5-8(c,d) that the maximum field enhancement for the nanorod occurs at the edge of the contact line between the nanorod and the film. A similar phenomenon can be observed for the nanocube-on-mirror, in which the maximum field is at the edges of the contact plane between the nanocube and film (Figure 5-8(e-f)). Moreover, it is seen from Figure 5-8(c-d) that the field intensity is much stronger for the 630 nm wavelength than for 540 nm. The charge distribution shows that the dipole mode

is reached at 630 nm, which is the wavelength for the major maximum scattering efficiency. On the other hand, a higher-order mode is reached at wavelength 540 nm, which is the wavelength for the secondary maximum scattering efficiency. This observation confirms that the dipole mode radiates stronger than the other modes. It is clear that for the dipole mode at wavelength 630 nm (Figure 5-8(d)), the maximum field intensity extends beyond the interface between the nanoparticle and dielectric film, and penetrates into the dielectric layer. In contrast, the field penetration for the 540 nm mode is relatively small (Figure 5-8(c)). This is a clear indication of the splitting of the scattering spectra, which shows that the 30 nm mode is the coupled mode between the nanoparticle and the film, while the 540 nm mode is from the nanoparticle itself. This result corresponds well with Figure 5-7(d) and is consistent with other works. (*417*, *422*, *423*) The similar observations exist for the nanocube, which is shown in Figure 5-8(e-f). The gap distance is 10 nm, and the major peak (wavelength 715 nm, Figure 5-8(f)) and secondary peak (wavelength 530 nm, Figure 5-8(e)) of the scattering efficiency are shown. Note that the major maxima of scattering efficiency for the nanorod and nanocube are redshifted compared to the nanosphere, which is because the lowered symmetries and shaper features separate electrons more than the nanosphere, and therefore reduce the restoring forces and slow the collective oscillation. (*412*)

The size of the nanoparticles in the NPoM structure can also vary the optical properties. In Figure 5-9, the size effects on the scattering efficiency, field enhancement and mode volume are shown. NPoMs with nanospheres of diameters from 50 nm to 200 nm and a gap distance of 5 nm are studied. As shown in Figure 5-9(a), with the increase of the nanosphere diameter, the scattering efficiency generally increases, and the maximum value redshifts. The redshifts are due to the increase of the electron separation and thus the decreased frequency of the collective electron oscillation with larger nanospheres. (*424*, *425*) When the nanosphere diameter is over 100 nm, a secondary maximum of the scattering efficiency appears at a shorter wavelength than the major maximum, and such a secondary maximum, similar to the cases in nanorod- and nanocube-on-mirror, becomes more obvious with the increase of the nanosphere diameter. This phenomenon is ascribed to the fact that large nanospheres can support higher-order modes. (*426*) Similar to the

scattering efficiency, the field enhancement also increases with the increase of the nanosphere diameter, and the maximum value redshifts. When the diameter is over ~100 nm, the peak in the field enhancement becomes broad, and a shoulder at a slightly shorter wavelength shows up (Figure 5-9(b)), which is due to the proliferation of multiple modes in larger nanospheres. (*427*, *428*) Finally, the mode volume decreases with the increasing diameter of the nanosphere, but such a decreasing trend levels off when the diameter is 125 nm or more, shown in Figure 5-9(c). This observation shows that the field confinement is not effective for nanospheres with small diameters (< ~100 nm). In fact, for small nanoparticles, the absorption becomes comparable to the scattering. (*429*) The wavelength for the minimum mode volume is increased as the nanosphere diameter increases, indicating the increase of the resonance wavelength, which is also suggested in the scattering efficiency shown in Figure 5-9(a).

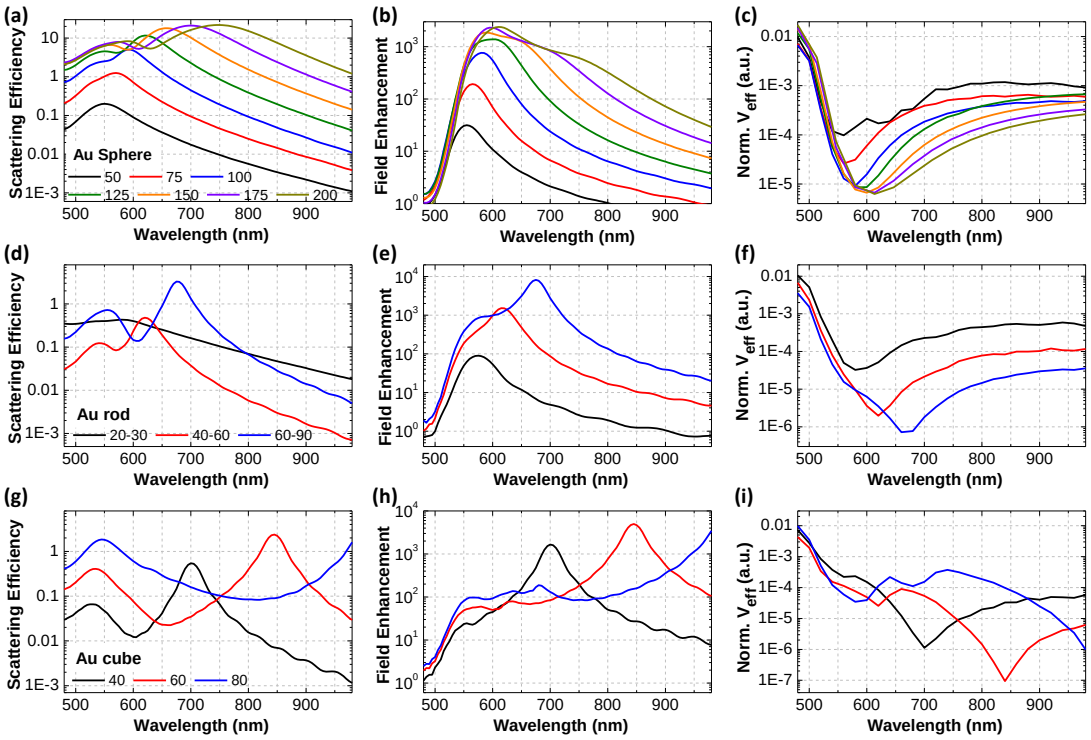

Figure 5-9. Size effect of NPoM structures. (a-c) Scattering efficiency (a), field enhancement (b) and normalized mode volume (c) of Au sphere-on-mirror with sphere diameter from 50 nm to 200 nm. (d-f) and (g-i) show the same plots of Au rod-on-mirror with rod sizes 20-30 nm to 60-90 nm, and Au cube-on-mirror with cube sizes 40 nm to 80

nm, respectively. All the Au cubes have rounded corners with diameter 5 nm. The gap distance is 5 nm for all cases. The values of scattering efficiency, field enhancement and normalized mode volume are calculated the same way as in Figure 5-7.

Similar size effects can also be observed in the nanorod and nanocube cases, as shown in Figure 5-9(d-f,g-i), respectively. For example, In Figure 5-9(d-i), an increase of the nanorod and nanocube sizes shows a redshift of the peak positions in the scattering efficiency and field enhancement, and valley position in the mode volume. For the 80 nm nanocube, the wavelength of the major maximum in the scattering efficiency and field enhancement (and a major minimum of the mode volume) is longer than the wavelength range we studied and are thus not shown in Figure 5-9. The mode splitting effect also becomes clearer as the nanoparticle size increases, which supports our conclusion that the splitting is due to the decoupling of the nanoparticle and film. As the nanoparticle size shrinks, the coupling between the two plasmonic systems becomes easier. As can be seen in Figure 5-9(f,i), the minimum mode volume can reach $10^{-7}(\lambda/n)^3$ for a 60 nm Au cube, and below $10^{-6}(\lambda/n)^3$ for a 60-90 nm Au rod. Moreover, it can be observed from Figure 5-7 and Figure 5-9 that generally, the nanorod and nanocube easily induce more peaks in scattering than the nanosphere. This effect originates from the lowered symmetry, which provides additional configurations for electron distribution and polarization. In fact, the elongated structures such as nanorods and nanobars usually have at least two modes: transverse and longitudinal, along the short and long axes, respectively. (*430*) For the nanocube, the sharpened corners also enable multiple resonances other than dipole modes. (*431*)

Finally, the gap distance effect is studied experimentally. We measure the SHG intensity for 200 nm-diameter Au nanospheres with gap distances from 2 nm to 30 nm, as shown in Figure 5-10. Scanning electron microscopy (SEM) and SHG images are presented in Figure 5-10(a,b), respectively. The SEM image indicates the good quality and shape of the 200 nm Au nanospheres. In the SHG image in Figure 5-10(b), the bright dots are SHG signals from the Au nanospheres. Except for a few outliers (outlined by the red circles) which might be due to the nanosphere clustering, most of the dots have similar brightness,

indicating the uniformity of the nanospheres. The SHG intensity as a function of the gap distance is shown in Figure 5-10(c). The intensity first increases with the increase of the gap distance, then peaks at around 9 nm, followed by the decrease of the SHG intensity as the gap distance further increases. SHG is caused by the strong electric field in the structure: $E(2\omega) \sim \chi^{(2)} E(\omega) E(\omega)$, where $E(2\omega)$ and $E(\omega)$ are the field at the doubled frequency and original frequency (which is 800 nm in wavelength in our experiment), respectively, and $\chi^{(2)}$ is the nonlinear susceptibility tensor and sensitive to the bulk and surface properties. (*432–434*) The experimentally observed SHG signal is a spatial integration of the field, so it combines the information of the linear field enhancement, field distribution and geometric properties in the nanosphere-on-mirror cavity. In the classical regime, (*435–438*) a smaller gap distance gives a stronger linear field enhancement in non-resonant case, as suggested by our FDTD simulation in Figure 5-7(b) for 74 nm-diameter nanosphere, and for 200 nm-diameter nanosphere-on-mirror, which also suggest a smaller mode volume as gap distance decreases at wavelength 800 nm. (*439*, *440*) Since the maximum field enhancement is much stronger than the field enhancement at other locations, the changing trend of the SHG intensity as a function of gap distance can be approximated as the changing trend of the product of mode volume and the maximum field enhancement, and the results are shown as the pink curve in Figure 5-10(c). The dependence on gap distance agrees with the experiment. Therefore, it is clear that SHG signal may not monotonically change with the linear field enhancement, gap distance or mode volume, but it is a parameter incorporating multiple factors. Practically, SHG may not be a good probe to measure the linear field enhancement in NPoM structure, as was also pointed out by Lombardi, *et al*. (*441*) However, our calculation is a rough approximation, and the detailed modeling of SHG signal and geometrical factors of NPoM cavity is rather complicated (*434*, *441–443*) and is beyond the scope of this manuscript, and will be included in future work. Moreover, this NPoM cavity we fabricated, the 200 nm-diameter Au nanosphere-on-mirror, can reach the effective mode volume on the order of $10^{-7}(\lambda/n)^3$ for the wavelength of 680 nm and gap distance of 2 nm according to the FDTD simulation, which suggests the experimental realization of ultra-small mode volume in NPoM cavity.

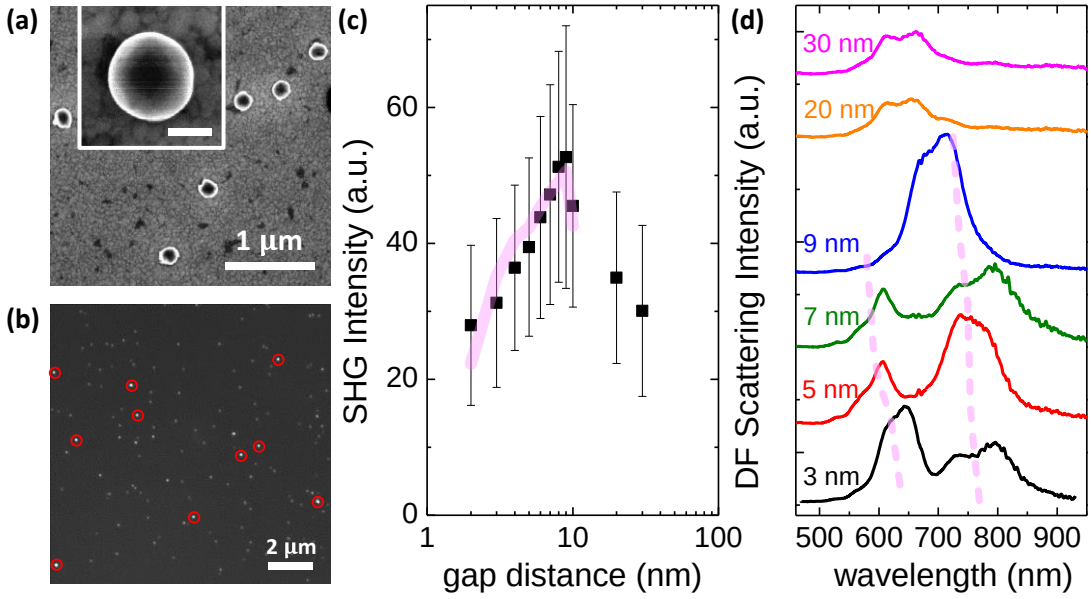

Figure 5-10. Experimental field enhancement and scattering efficiency of Au nanosphere-on-mirror structures with various gap sizes. The sphere diameter is 200 nm and gap material is Al_2O_3. (a) SEM of Au sphere-on-mirror structures. Inset: enlargement of one Au sphere. Scale bar: 100 nm. The background is the Al_2O_3 dielectric layer and Au nanofilm. (b) SHG image with gap distance 6 nm. The red circles show the outliers which are nanosphere clusters and have much brighter SHG than single Au nanosphere. (c) SHG intensity vs. gap distance. The black squares are experimental data and the pink curve is the calculated result. (d) Dark field (DF) scattering intensity spectra with various gap distances from 3 nm to 30 nm. The pink curves show the FDTD simulated peak positions of scattering efficiency for corresponding gap distances.

On the other hand, the DF scattering measurement can more directly reflect the optical properties of the nanocavity of 200 nm-diameter nanosphere-on-mirror. The result is shown in Figure 5-10(d). It can be found that for small gap distances like 3, 5 and 7 nm, there are two scattering peaks at wavelengths around 600 nm and 780 nm, which agrees well with the FDTD simulation shown in Figure 5-9(a). The pink curves in Figure 5-10(d) show the

peak positions of scattering efficiency obtained from FDTD simulation for corresponding gap distances. It can be seen the experimental results match well with the simulation. As the gap distance increases, the two peaks merge to one, as can be seen as the 714 nm peak for the 9 nm gap distance, and the scattering efficiency increases, in line with Figure 5-7(a). As the gap distance further increases to 20 or 30 nm, the scattering efficiency is lowered and blueshifted, and does not change much with gap distance. This confirms our simulation results in Figure 5-7: for large gap distances, the nanosphere and film decouples, and the scattering is mainly due to the nanoparticle mode; however, when the gap distance decreases, the scattering resonance wavelength is redshifted; with further decrease in the gap distance, the nanosphere couples with the film, which generates two scattering peaks which are identified as the nanoparticle mode and the coupled mode.

In conclusion, we systematically study the optical cavity properties of the NPoM structure, including Au nanospheres, nanorods and nanocubes on a Au-film supported dielectric material layer Al_2O_3. These three structures represent the point, line and plane contacts of the NP and mirror, and they show different optical performances regarding their scattering efficiency, field enhancement, effective mode volume and quality factor, as the function of wavelength, nanoparticle size and gap distance. Compared to the nanosphere, the nanorod and nanocube can easily generate multiple modes and show more effective scattering and spatial confinement of the fields, but their resonance frequencies are redshifted. In particular, ultra-small mode volumes below $10^{-7}(\lambda/n)^3$ can be reached in FDTD simulation for the nanorod- and nanocube-on-mirror. Despite the low quality factor on the order of 20, a Purcell factor as high as ~10^7 can be achieved from the simulation. This performance is comparable to the state-of-the-art photonic devices. Moreover, our DF scattering measurement confirms the effect of gap distance on the coupling between the nanosphere and film revealed by the FDTD simulation. This work reveals the optical properties of the NPoM nanocavities with various geometries and dimensions systematically. Moreover, the FDTD simulation results presented here demonstrate the achievement of the ultra-small mode volume and a high Purcell factor. These studies can provide important guidance for the design of optical and photonic information processing devices towards higher speed and larger information density. Moreover, such a NPoM

structure has also been experimentally demonstrated to effectively enhance and tune the optical response of 2D materials.

Chapter 6
Conclusion and Outlook

6.1 From the Materials perspective

It is predicted that about 500 types of 2D materials exist. The current study only covers a small portions of it, yet many new are emerging. 2D materials cover a plethora of properties, and can thus be used to build 2D systems. With the emergence of tens of new 2D materials each year, the challenges remains for effective synthesis and universal characterization methods. The understanding of material properties are also essential. Here we focus on two major types of 2D materials, BP and TMD.

6.1.1 Outlook for BP

Looking forward, BP is very promising for a number of optoelectronic and photonic applications. It has a highly tunable bandgap with thickness ranging all the way from 0.3 to 2.0 eV, and the strong anisotropy provides another dimension of tunability for BP as photonic devices. To achieve effective application of BP, there are still several issues that need to be solved.

Regarding the basic properties of BP, many works have been performed to explore optical absorption, Raman, PL spectroscopies and plasmonics of BP, including their thickness and polarization dependences. There are still several ongoing debates that need to be settled, including the optical effect of degradation in BP, how the protective coating layers affect the optical properties of BP, the exact bandgap and exciton binding energy, the PL yield, further exploration of BP plasmonics and its hybridization with other materials. In addition, the role of defects on the BP optical performance still needs further explorations.

Regarding the optoelectronic devices based on BP, many works have been mainly focusing on enhancing the BP photoresponsivity in different spectral ranges. From the opinions of the authors, in the future, additional works can focus on the improvement of response speed of BP, exploring BP for photodetectors in various spectral range, especially in mid-IR range which is hardly accessible using TMD, as well as the heterostructure of BP with other 2D materials to achieve higher performance photodetectors. Moreover, other types of photonic devices, such as photonic modulator, light emitting devices, photonic devices integrating with other photonic structures such as waveguide and optical cavities, should be explored.

Besides, BP ignited the study of 2D materials with in-plane anisotropy and that are easily degraded. In fact, most of the 2D materials newly emerged have in-plane anisotropy, including $ReSe_2$, 1T'-$MoTe_2$, GaTe, SnSe, etc,(*68–71*) and many are also subjective to easy-degradation in air, such as 1T'-$MoTe_2$. The studies of BP also offer important guidelines for these new 2D materials. Many characterization and analyzing methods developed for BP, such as optical transition selection rule mentioned in this review, can also be broadly applied to many other 2D materials, accelerating the research on 2D materials as well as their applications in practical devices.

6.1.2 Outlook for TMD

With the wide variety of structures and phases presently available for TMD materials, the research community can already see that TMD materials can obtain various electronic and optical properties enabling their applications in different areas of fundamental scientific research and for new applications capabilities at the nanoscale. From the viewpoint of fundamental research, Raman spectroscopy is becoming a common and standard tool for probing the properties of layered materials. Pure TMDs are becoming a class of standard reference materials for well-defined 2D layered materials with a bandgap. Thus combining TMD materials into a new artificial material will provide new possibilities for electronic applications.

We can expect this TMD material MoS_2 to be followed by a whole family of new materials and their hetero structured systems with different levels of complexity as they are

combined. After TMDs, more complex systems are expected. Such materials systems are now under investigation and include low-symmetry systems with only one or two symmetry operations. Such systems are also found in nature and may become more important once we know more about them and their unique advantages for different types of applications.

We have provided a systematic discussion of the Raman spectra of TMDs, (*309*) giving particular attention to the control of TMD properties as classical layered materials. Here control of the properties of the whole class of materials comes, as in all cases, from the control of the properties of the individual fundamental building block layer. Additional control comes through the change in properties coming from increasing the number of layers, one by one at first, and then use of possible stable phases of the fundamental materials. Further control comes from use of different excitation energy wavelengths, looking for resonance behaviors from a quantum mechanical standpoint, and then when assembling multilayer structures of more than one material. Many variations are possible through exploitation of materials parameters such as layer thickness, structural phases and phase transitions, excitation laser wavelengths, including very long wavelength or low frequency excitation and polarization-dependent characteristics. In addition, use can be made of variations coming from commonly used parameters of temperature, pressure, stress, and materials processing characteristics. This large number of variables can be further increased by using more than one building block, thereby giving us a large phase space for operation and the exploration of new environments for nanomaterial heterostructures. This research landscape offers great complexity because the appropriate variables for each of the constituents in the heterostructures that is somewhat independent, though they need to be assembled in a way as to be mutually compatible.

Some future goals include both to find new scientific phenomena occurring at the nanoscale through these heterostructures not found in natural nanostructured materials, and to identify the structures and environments of particular promise and interest for science and for applications. The next step is to pursue the new science and to develop optoelectronic devices in two dimensions. At this point, new variables enter, such as safety in production and use, cost of materials and their processing, long term stability, materials

availability, and possible commercial interest. At the research and applications level, nano heterostructures are likely to become more complex with time. Studies of fundamental scientific interest going beyond the model systems will have to be carried out and we will be excited whenever new scientific ideas are identified through these studies and also when sensitive methods are found to control more effectively the research directions that have already been identified.

6.2 From Application Perspective

6.2.1 Sensing Applications: Raman Enhancement

We introduced a newly developed technique for Raman enhancement, named "graphene-enhanced Raman scattering (GERS)". It is a novel branch of surface-enhanced Raman scattering (SERS), which uses graphene, as well as other 2D materials as an active substrate. Different from the conventional SERS substrate, which is based on the rough surface of a metal and is dominated by EM (electromagnetic mechanism), GERS shows its superiority in lighting up molecules uniformly, repeatably and quantifiably, due to the flat and chemically inert surface of 2D materials. In particular, it is an available model and substrate to study CM (chemical mechanism), since GERS has no disturbance from EM, which opens a window to study CM in more detail and offers possibilities to realize the additional picture for the SERS mechanism. In addition, great progress has been made to extend this effect to other graphene derivatives, and to enhance the effect of more diverse molecules with particular functions. It offers potential stages to study this effect more deeply and to reveal new applications for CM. In the future, from the fundamental study side, more detailed theoretical models are expected based on this system to understand the principles of CM. From the application side, more promising applications are expected in the process monitoring of chemical and biological systems, utilizing the ability of graphene in "lighting up" the molecule as it is excited.

6.2.2 Photonic Applications

2D materials have many properties that make them ideal for photonic applications. There are several ongoing challenges for their photonic applications.

First, the frequency coverage for mid-IR applications. The renaissance of BP partly solved the problem, due to its direct bandgap and large tuning range from 0.3 to 1.5 eV with thickness. Below 0.3 eV, there is still a gap, and several candidates, like bilayer graphene, or As-BP alloy can potentially be used to fill the gap. There should be efforts in experimental demonstration of such devices.

Second, the tunability. There has been many efforts towards the tunability of 2D materials for photonic properties, like the frequency coverage. While many, like photonic cavity, strain, chemical adsorbance, can work, there are still some issues to be solved, like the larger tuning range and dynamic range, reversible tuning, preservation of high performance, etc.

Third, the further enhancement of material performance. 2D materials have good photonic performance, if considering their thickness. For example, monolayer MoS_2 absorbs 10% of the light in resonance. However, as a device, 10% absorption is not sufficient, and further enhancement is required. Methods of enhancement include coupling with cavities or other photonic structures, (*444*) chemical adsorbance, constructing heterostructures. Ongoing work is required for 2D materials to outperform many of the current mature technologies.

Furthermore, the new properties and devices with new functionalities. 2D and layered materials possess many extraordinary properties, including the valleytronics, (*444*) spin Hall effect, (*445*) Weyl semimetal, (*446*) single-photon source, (*447*) etc. Gaining a further understanding of these properties, and to transform the properties into real devices and systems, remains to be promising yet challenging.

Appendix: Calculation Methods for BP Anisotropy

DFT Calculations. Plane-wave DFT calculations were performed using the VASP package equipped with projector augmented wave (PAW) pseudopotentials for electron-ion interactions. (*448*)

The exchange-correlation interactions were considered in the generalized gradient approximation (GGA) using Perdew-Burke-Ernzerhof (PBE) functional. The interlayer interactions were included using the van der Waals (vdW) density functional method optB88-vdW. For bulk BP, both atoms and cell volume were allowed to relax until the residual forces were below 0.001 eV/Å, with a cutoff energy set at 500 eV and a 9×4×12 k-point sampling in the Monkhorst-Pack scheme. By taking the in-plane armchair direction as the *x*-axis, the out-of-plane direction as the *y*-axis, and in-plane zigzag direction as the *z*-axis, the optimized lattice parameters in our DFT calculations for bulk BP are $a_1 = 4.45$ Å, $a_2 = 10.67$ Å, and $a_3 = 3.35$ Å. Monolayer, bilayer, trilayer, and 10-layer BP systems were then modeled by a periodic slab geometry using the optimized in-plane lattice constants of the bulk. A vacuum region of at least 18 Å in the out-of-plane direction was used to avoid spurious interactions with replicas. For the 2D slab calculations, all atoms were relaxed until the residual forces were below 0.001 eV/Å and 9×1×12 k-point samplings were used. As GGA-PBE xc functional tends to underestimate energy separations between valence and conduction bands, electronic bands were then updated by the hybrid functional (HSE06) method. (*285*) By extracting the important outputs from the DFT-HSE06 calculations including the electronic energy dispersion, electronic wave function coefficients, and symmetry information of the wave functions, we can determine whether an electronic transition is preferable to armchair-polarized or zigzag-polarized incident light, based on Eq. 4-2 and Eq. 4-3. It allows us to calculate the optical transition probability between two specific electronic states at a particular *k*-point via the electronic energy dispersions and wave function coefficients, while the symmetry information was used to analyze the selection rule for optical absorption and the phonon mode, as shown in Figure 4-3.

To compute the absorption coefficient $\alpha(E_L)$ considering the contributions from all electronic states across the Brillouin zone, the energy dependent complex dielectric function ϵ was then calculated by summation over all valence/conduction bands at every *k*-point in the Brillouin zone. The number of empty conduction bands was set to be triple of the number of occupied valence bands. Using the armchair-direction and zigzag-direction components of the dielectric function ϵ, we can compute the optical absorption coefficient $\alpha(E_L)$ along the armchair and zigzag directions (shown in Figure 4-2(a)), respectively, based on the formula (*285*) $\alpha(E_L) = \frac{E_L \mathrm{Im}(\mathcal{E})}{\hbar c n}$. E_L is the energy, $n = \sqrt{\frac{\sqrt{\mathrm{Re}(\epsilon)^2+\mathrm{Im}(\epsilon)^2}+\mathrm{Re}(\epsilon)}{2}}$ is the real part of the complex refractive index, $\mathrm{Re}(\epsilon)$ and $\mathrm{Im}(\epsilon)$ are the real and imaginary parts of the dielectric function ϵ, $\hbar$ is the reduced Planck constant, and c is the speed of light. Such method yields consistent results with the approach discussed in Eq. 4-2 and Eq. 4-3, particularly regarding the optical absorption anisotropy that the absorption along armchair direction is larger than that along zigzag direction in the visible spectral range.

For BP, the complex refractive index is expressed as $n^* = \sqrt{\epsilon} = n + ik$, where the real part n is the usual refractive index and the imaginary part k is the extinction coefficient. Based on these quantities, we have absorption α=$\frac{4\pi k}{\lambda}$, and reflection R=$\frac{(n-1)^2+k^2}{(n+1)^2+k^2}$ for the BP/air interface under normal incidence. According to our calculations and a previous experimental work,[26] n is notably larger than κ and then R $\approx \frac{(n-1)^2}{(n+1)^2}$. Compared to κ, n shows much weaker dependence on the crystalline orientation. This leads to weaker anisotropy of reflection than that of the absorption in BP.

Enhancement Factor by Classical Interference Effect Calculation. When the thickness of BP flakes and the substrate are comparable with the wavelength of light, we expect a classical interference effect due to multiple reflections in BP/substrates layers as reported before. (*286*, *294*) This interference effect depends on the polarization of light due to the different refractive indices in the armchair and zigzag direction of BP. The net enhancement of incident light F_{ex} caused by multiple reflections at a position x measured from the BP surface is given by[27]

$$F_{\mathrm{ex}}(x) = t_{01}\frac{\left(1 + r_{12}r_{23}e^{-2i\beta_2^{\mathrm{ex}}}\right)e^{-i\beta_x^{\mathrm{ex}}} + \left(r_{12} + r_{23}e^{-2i\beta_2^{\mathrm{ex}}}\right)e^{-i(2\beta_1^{\mathrm{ex}} - \beta_x^{\mathrm{ex}})}}{1 + r_{12}r_{23}e^{-2i\beta_2^{\mathrm{ex}}} + \left(r_{12} + r_{23}e^{-2i\beta_2^{\mathrm{ex}}}\right)r_{01}e^{-2i\beta_1^{\mathrm{ex}}}}$$

where $t_{ij} = 2n_i/(n_i + n_j)$ and $r_{ij} = (n_i - n_j)/(n_i + n_j)$ are the Fresnel transmittance and reflectance coefficients, respectively, at the interfaces of the *i*-th and *j*-th layer with *i*,*j* indices are given by air (0), BP (1), 0.5 mm thick quartz (2), and air (3). n_i is the complex refractive index of the *i*-th layer. $\beta_x^{\mathrm{ex}} = 2\pi x n_1/\lambda_{ex}$ and $\beta_i^{\mathrm{ex}} = 2\pi d_i n_i/\lambda_{ex}$ are the phase factors with d_i is the thickness of the *i*-th layer and λ_{ex} is the excitation wavelength.

The net enhancement of scattered light $F_{\mathrm{sc}}(x)$ due to multiple reflections at a position x measured from the BP surface is given by

$$F_{\mathrm{sc}}(x) = t_{10}\frac{\left(1 + r_{12}r_{23}e^{-2i\beta_2^{\mathrm{sc}}}\right)e^{-i\beta_x^{\mathrm{sc}}} + \left(r_{12} + r_{23}e^{-2i\beta_2^{\mathrm{sc}}}\right)e^{-i(2\beta_1^{\mathrm{sc}} - \beta_x^{\mathrm{sc}})}}{1 + r_{12}r_{23}e^{-2i\beta_2^{\mathrm{sc}}} + \left(r_{12} + r_{23}e^{-2i\beta_2^{\mathrm{sc}}}\right)r_{01}e^{-2i\beta_1^{\mathrm{sc}}}}$$

where $\beta_x^{\mathrm{sc}} = 2\pi x n_1/\lambda_{sc}$ and $\beta_i^{\mathrm{sc}} = 2\pi d_i n_i/\lambda_{sc}$ are the phase factors for scattered light with a wavelength λ_{sc} related to the Raman shift of a particular spectrum. The total enhancement factors are then given by

$$F = N\int_0^{d_1} |F_{\mathrm{ex}}(x)F_{\mathrm{sc}}(x)|^2 dx$$

where *N* is the normalization constant. The observed Raman intensity is $R = I \cdot F$, where *I* is the intrinsic Raman intensity considering only electron-photon and electron-phonon interactions. We use the refractive index of BP reported before. (*286*)

Bibliography

1. X. Ling, H. Wang, S. Huang, F. Xia, M. S. Dresselhaus, The renaissance of black phosphorus. *Proc. Natl. Acad. Sci.* **112**, 4523–4530 (2015).
2. S. Huang, J. E. Weis, S. Costa, M. Kalbac, M. S. Dresselhaus, in *Electrochemistry of Carbon Electrodes* (Wiley - VCH Verlag GmbH & Co. KGaA, 2016; http://doi.wiley.com/10.1002/9783527697489.ch1), pp. 1–30.
3. A. K. Geim, K. S. Novoselov, The rise of graphene. *Nat. Mater.* **6**, 183–191 (2007).
4. D. Nezich, T. Palacios, Graphene Frequency Multipliers. *IEEE Electron Device Lett.* **30**, 547–549 (2009).
5. H. Wang, A. Hsu, J. Wu, J. Kong, T. Palacios, Graphene-Based Ambipolar RF Mixers. *IEEE Electron Device Lett.* **31**, 906–908 (2010).
6. L. Ci *et al.*, Atomic layers of hybridized boron nitride and graphene domains. *Nat. Mater.* **9**, 430–5 (2010).
7. A. L. M. Reddy *et al.*, Synthesis of nitrogen-doped graphene films for lithium battery application. *ACS Nano*. **4**, 6337–42 (2010).
8. J. J. Yoo *et al.*, Ultrathin planar graphene supercapacitors. *Nano Lett.* **11**, 1423–7 (2011).
9. X. Luo, T. Qiu, W. Lu, Z. Ni, Plasmons in graphene: Recent progress and applications. *Mater. Sci. Eng. R Reports*. **74**, 351–376 (2013).
10. A. N. Grigorenko, M. Polini, K. S. Novoselov, Graphene plasmonics. *Nat. Photonics*. **6**, 749–758 (2012).
11. S. H. Abedinpour *et al.*, Drude weight, plasmon dispersion, and ac conductivity in doped graphene sheets. *Phys. Rev. B.* **84**, 45429 (2011).
12. M. Polini *et al.*, Plasmons and the spectral function of graphene. *Phys. Rev. B.* **77**, 81411 (2008).
13. E. H. Hwang, S. Das Sarma, Dielectric function, screening, and plasmons in two-

dimensional graphene. *Phys. Rev. B.* **75**, 205418 (2007).

14. B. Wunsch, T. Stauber, F. Sols, F. Guinea, Dynamical polarization of graphene at finite doping. *New J. Phys.* **8**, 318–318 (2006).
15. A. Kuzmenko, E. van Heumen, F. Carbone, D. van der Marel, Universal Optical Conductance of Graphite. *Phys. Rev. Lett.* **100**, 117401 (2008).
16. R. R. Nair *et al.*, Fine structure constant defines visual transparency of graphene. *Science*. **320**, 1308 (2008).
17. N. W. Ashcroft, N. D. Mermin, *Solid State Physics* (Cengage Learning, 1976; http://zh.scribd.com/doc/207078972/Solid-State-Physics-Neil-W-Ashcroft-N-David-Mermin-Brooks-Cole-1976).
18. Z. Fei *et al.*, Gate-tuning of graphene plasmons revealed by infrared nano-imaging. *Nature*. **487**, 82–5 (2012).
19. L. Ju *et al.*, Graphene plasmonics for tunable terahertz metamaterials. *Nat. Nanotechnol.* **6**, 630–4 (2011).
20. Q. Bao, K. P. Loh, Graphene photonics, plasmonics, and broadband optoelectronic devices. *ACS Nano*. **6**, 3677–94 (2012).
21. K. F. Mak *et al.*, Measurement of the Optical Conductivity of Graphene. *Phys. Rev. Lett.* **101**, 196405 (2008).
22. K. F. Mak, L. Ju, F. Wang, T. F. Heinz, Optical Spectroscopy of Graphene: From the far infrared to the ultraviolet. *Solid State Commun.* **152**, 1341–1349 (2012).
23. T. Eberlein *et al.*, Plasmon spectroscopy of free-standing graphene films. *Phys. Rev. B.* **77**, 233406 (2008).
24. J. Chen *et al.*, Optical nano-imaging of gate-tunable graphene plasmons. *Nature*. **487**, 77–81 (2012).
25. H. Yan *et al.*, Tunable infrared plasmonic devices using graphene/insulator stacks. *Nat. Nanotechnol.* **7**, 330–4 (2012).
26. N. Jung *et al.*, Charge transfer chemical doping of few layer graphenes: charge

distribution and band gap formation. *Nano Lett.* **9**, 4133–7 (2009).

27. W. Zhang *et al.*, Opening an electrical band gap of bilayer graphene with molecular doping. *ACS Nano*. **5**, 7517–24 (2011).

28. A. Das *et al.*, Monitoring dopants by Raman scattering in an electrochemically top-gated graphene transistor. *Nat. Nanotechnol.* **3**, 210–5 (2008).

29. M. Kalbac *et al.*, Raman spectroscopy and in situ Raman spectroelectrochemistry of bilayer $^{12}C/^{13}C$ graphene. *Nano Lett.* **11**, 1957–63 (2011).

30. M. Kalbac, J. Kong, M. S. Dresselhaus, Raman Spectroscopy as a Tool to Address Individual Graphene Layers in Few-Layer Graphene. *J. Phys. Chem. C*. **116**, 19046–19050 (2012).

31. M. Kalbac *et al.*, The influence of strong electron and hole doping on the Raman intensity of chemical vapor-deposition graphene. *ACS Nano*. **4**, 6055–63 (2010).

32. M. Freitag *et al.*, Energy dissipation in graphene field-effect transistors. *Nano Lett.* **9**, 1883–8 (2009).

33. L. M. Malard, M. A. Pimenta, G. Dresselhaus, M. S. Dresselhaus, Raman spectroscopy in graphene. *Phys. Rep.* **473**, 51–87 (2009).

34. J. Yan, Y. Zhang, P. Kim, A. Pinczuk, Electric Field Effect Tuning of Electron-Phonon Coupling in Graphene. *Phys. Rev. Lett.* **98**, 166802 (2007).

35. J. C. Meyer *et al.*, Experimental analysis of charge redistribution due to chemical bonding by high-resolution transmission electron microscopy. *Nat. Mater.* **10**, 209–15 (2011).

36. Z. Kominkova, M. Kalbac, Extreme electrochemical doping of a graphene–polyelectrolyte heterostructure. *RSC Adv.* **4**, 11311 (2014).

37. M. Kalbac, J. Kong, M. S. Dresselhaus, Doping of bi-layer graphene by gradually polarizing a ferroelectric polymer. *Phys. Status Solidi*. **250**, 2649–2652 (2013).

38. M. Bruna *et al.*, Doping dependence of the Raman spectrum of defected graphene. *ACS Nano*. **8**, 7432–41 (2014).

39. S. Piscanec, M. Lazzeri, F. Mauri, A. Ferrari, J. Robertson, Kohn Anomalies and Electron-Phonon Interactions in Graphite. *Phys. Rev. Lett.* **93**, 185503 (2004).

40. J. E. Lee, G. Ahn, J. Shim, Y. S. Lee, S. Ryu, Optical separation of mechanical strain from charge doping in graphene. *Nat. Commun.* **3**, 1024 (2012).

41. Z. Yin *et al.*, Single-layer MoS2 phototransistors. *ACS Nano*. **6**, 74–80 (2012).

42. K. Mak, C. Lee, J. Hone, J. Shan, T. Heinz, Atomically Thin MoS2: A New Direct-Gap Semiconductor. *Phys. Rev. Lett.* **105** (2010), pp. 2–5.

43. A. K. Geim, I. V Grigorieva, Van der Waals heterostructures. *Nature*. **499**, 419–425 (2013).

44. Q. H. Wang, K. Kalantar-Zadeh, A. Kis, J. N. Coleman, M. S. Strano, Electronics and optoelectronics of two-dimensional transition metal dichalcogenides. *Nat. Nanotechnol.* **7**, 699–712 (2012).

45. R. S. Sundaram *et al.*, Electroluminescence in single layer MoS2. *Nano Lett.* **13**, 1416–21 (2013).

46. H. S. Lee *et al.*, MoS2 nanosheet phototransistors with thickness-modulated optical energy gap. *Nano Lett.* **12**, 3695–700 (2012).

47. X. Ling *et al.*, Parallel Stitching of 2D Materials. *Adv. Mater.* **28**, 2322–2329 (2016).

48. M. Fontana *et al.*, Electron-hole transport and photovoltaic effect in gated MoS2 Schottky junctions. *Sci. Rep.* **3**, 1634 (2013).

49. A. Splendiani *et al.*, Emerging photoluminescence in monolayer MoS2. *Nano Lett.* **10**, 1271–5 (2010).

50. N. Scheuschner *et al.*, Photoluminescence of freestanding single- and few-layer MoS2. *Phys. Rev. B.* **89**, 125406 (2014).

51. G. Eda *et al.*, Photoluminescence from chemically exfoliated MoS2. *Nano Lett.* **11**, 5111–6 (2011).

52. S. Huang *et al.*, Probing the interlayer coupling of twisted bilayer MoS2 using photoluminescence spectroscopy. *Nano Lett.* **14**, 5500–8 (2014).

53. Y. Lin *et al.*, Dielectric screening of excitons and trions in single-layer MoS2. *Nano Lett.* **14**, 5569–76 (2014).

54. O. Lopez-Sanchez, D. Lembke, M. Kayci, A. Radenovic, A. Kis, Ultrasensitive photodetectors based on monolayer MoS2. *Nat. Nanotechnol.* **8**, 497–501 (2013).

55. C. Mai *et al.*, Many-body effects in valleytronics: direct measurement of valley lifetimes in single-layer MoS2. *Nano Lett.* **14**, 202–6 (2014).

56. H. Zeng, J. Dai, W. Yao, D. Xiao, X. Cui, Valley polarization in MoS2 monolayers by optical pumping. *Nat. Nanotechnol.* **7**, 490–3 (2012).

57. D. Xiao, G.-B. Liu, W. Feng, X. Xu, W. Yao, Coupled Spin and Valley Physics in Monolayers of MoS_{2} and Other Group-VI Dichalcogenides. *Phys. Rev. Lett.* **108**, 196802 (2012).

58. W. Jin *et al.*, Direct Measurement of the Thickness-Dependent Electronic Band Structure of MoS_{2} Using Angle-Resolved Photoemission Spectroscopy. *Phys. Rev. Lett.* **111**, 106801 (2013).

59. T. Cheiwchanchamnangij, W. R. L. Lambrecht, Quasiparticle band structure calculation of monolayer, bilayer, and bulk MoS_{2}. *Phys. Rev. B.* **85**, 205302 (2012).

60. A. Kormányos *et al.*, Monolayer MoS_{2}: Trigonal warping, the Γ valley, and spin-orbit coupling effects. *Phys. Rev. B.* **88**, 45416 (2013).

61. T. Jiang *et al.*, Valley and band structure engineering of folded MoS2 bilayers. *Nat. Nanotechnol.* **9**, 825–9 (2014).

62. H. Wang *et al.*, Integrated circuits based on bilayer MoS_2 transistors. *Nano Lett.* **12**, 4674–80 (2012).

63. K. F. Mak, K. L. McGill, J. Park, P. L. McEuen, Valleytronics. The valley Hall effect in MoS_2 transistors. *Science.* **344**, 1489–92 (2014).

64. S. Wu *et al.*, Electrical tuning of valley magnetic moment through symmetry control in bilayer MoS2. *Nat. Phys.* **9**, 149–153 (2013).

65. A. M. van der Zande *et al.*, Tailoring the Electronic Structure in Bilayer Molybdenum Disulfide via Interlayer Twist. *Nano Lett.* **14**, 3869–75 (2014).

66. K. Liu *et al.*, Evolution of interlayer coupling in twisted molybdenum disulfide bilayers. *Nat. Commun.* **5**, 4966 (2014).

67. X. Wang, S. Lan, Optical properties of black phosphorus. *Adv. Opt. Photonics*. **8**, 618 (2016).

68. S. Huang *et al.*, In-Plane Optical Anisotropy of Layered Gallium Telluride. *ACS Nano*. **10**, 8964–8972 (2016).

69. L.-D. Zhao *et al.*, Ultrahigh power factor and thermoelectric performance in hole-doped single-crystal SnSe. *Science*. **351**, 141–4 (2016).

70. D. Wolverson, S. Crampin, A. S. Kazemi, A. Ilie, S. J. Bending, Raman Spectra of Monolayer, Few-Layer, and Bulk ReSe2: An Anisotropic Layered Semiconductor. *ACS Nano*. **8**, 11154–11164 (2014).

71. D. A. Chenet *et al.*, In-Plane Anisotropy in Mono- and Few-Layer ReS2 Probed by Raman Spectroscopy and Scanning Transmission Electron Microscopy. *Nano Lett.* **15**, 5667–5672 (2015).

72. V. Tran, R. Soklaski, Y. Liang, L. Yang, Layer-controlled band gap and anisotropic excitons in few-layer black phosphorus. *Phys. Rev. B.* **89**, 235319 (2014).

73. L. Liang *et al.*, Electronic Bandgap and Edge Reconstruction in Phosphorene Materials. *Nano Lett.* **14**, 6400–6406 (2014).

74. B. Radisavljevic, A. Radenovic, J. Brivio, V. Giacometti, A. Kis, Single-layer MoS2 transistors. *Nat. Nanotechnol.* **6**, 147–150 (2011).

75. S. Huang *et al.*, Low-Frequency Interlayer Raman Modes to Probe Interface of Twisted Bilayer MoS 2. *Nano Lett.* **16**, 1435–1444 (2016).

76. A. Favron *et al.*, Photooxidation and quantum confinement effects in exfoliated black phosphorus. *Nat. Mater.* **14**, 826–32 (2015).

77. J. D. Wood *et al.*, Effective Passivation of Exfoliated Black Phosphorus Transistors

against Ambient Degradation. *Nano Lett.*, 141112095629008 (2014).

78. S. Endo, Y. Akahama, S. Terada, S. Narita, Growth of Large Single Crystals of Black Phosphorus under High Pressure. *Jpn. J. Appl. Phys.* **21**, L482–L484 (1982).

79. S. Lange, P. Schmidt, T. Nilges, Au_3SnP_7@Black Phosphorus: An Easy Access to Black Phosphorus. *Inorg. Chem.* **46**, 4028–4035 (2007).

80. X. Li *et al.*, Synthesis of thin-film black phosphorus on a flexible substrate. *2D Mater.* **2**, 31002 (2015).

81. P. Masih Das *et al.*, Controlled Sculpture of Black Phosphorus Nanoribbons. *ACS Nano*. **10**, 5687–5695 (2016).

82. A. Autere *et al., J. Phys. Chem. Lett.*, in press, doi:10.1021/acs.jpclett.7b00140.

83. L. Li *et al.*, Quantum oscillations in a two-dimensional electron gas in black phosphorus thin films. *Nat. Nanotechnol.* **10**, 608–613 (2015).

84. X. Zheng *et al.*, Characterization of nonlinear properties of black phosphorus nanoplatelets with femtosecond pulsed Z-scan measurements. *Opt. Lett.* **40**, 3480 (2015).

85. A. Castellanos-Gomez *et al.*, Isolation and characterization of few-layer black phosphorus. *2D Mater.* **1**, 25001 (2014).

86. X. Ling *et al.*, Low-Frequency Interlayer Breathing Modes in Few-Layer Black Phosphorus. *Nano Lett.* **15**, 4080–8 (2015).

87. X. Ling *et al.*, Anisotropic Electron-Photon and Electron-Phonon Interactions in Black Phosphorus. *Nano Lett.* **16**, 2260–2267 (2016).

88. Y. Takao, A. Morita, Electronic structure of black phosphorus: Tight binding approach. *Phys. B+C.* **105**, 93–98 (1981).

89. M. Fox, *Optical properties of solids* (Oxford University Press, Oxford ; New York, 2nd ed., 2010), *Oxford master series in condensed matter physics*.

90. H.-L. Liu *et al.*, Anomalous lattice vibrations of monolayer MoS2 probed by ultraviolet Raman scattering. *Phys. Chem. Chem. Phys.* **17**, 14561–8 (2015).

91. J. F. Sánchez-Royo, A. Segura, V. Muñoz, Anisotropy of the refractive index and absorption coefficient in the layer plane of gallium telluride single crystals. *Phys. Status Solidi*. **151**, 257–265 (1995).

92. G. Lucovsky, R. M. White, Optical-phonon anisotropies in layered crystals. *Nuovo Cim. B Ser. 11*. **38**, 290–300 (1977).

93. A. Taube, A. Łapińska, J. Judek, M. Zdrojek, Temperature dependence of Raman shifts in layered ReSe2 and SnSe2 semiconductor nanosheets. *Appl. Phys. Lett.* **107**, 13105 (2015).

94. H. Wang *et al.*, Black Phosphorus Radio-Frequency Transistors. *Nano Lett.* **14**, 6424–6429 (2014).

95. T. Low *et al.*, Tunable optical properties of multilayer black phosphorus thin films. *Phys. Rev. B*. **90**, 75434 (2014).

96. X. Wang *et al.*, Highly anisotropic and robust excitons in monolayer black phosphorus. *Nat. Nanotechnol.* **10**, 517–521 (2015).

97. C. H. Ho, Y. S. Huang, K. K. Tiong, P. C. Liao, Absorption-edge anisotropy in ReS 2 and ReSe 2 layered semiconductors. *Phys. Rev. B*. **58**, 16130–16135 (1998).

98. C. H. Ho, Y. S. Huang, K. K. Tiong, In-plane anisotropy of the optical and electrical properties of ReS2 and ReSe2 layered crystals. *J. Alloys Compd.* **317**–**318**, 222–226 (2001).

99. R. Guo, X. Wang, Y. Kuang, B. Huang, First-principles study of anisotropic thermoelectric transport properties of IV-VI semiconductor compounds SnSe and SnS. *Phys. Rev. B*. **92**, 115202 (2015).

100. F. Xia, H. Wang, Y. Jia, Rediscovering black phosphorus as an anisotropic layered material for optoelectronics and electronics. *Nat. Commun.* **5**, 4458 (2014).

101. Z. Luo *et al.*, Anisotropic in-plane thermal conductivity observed in few-layer black phosphorus. *Nat. Commun.* **6**, 8572 (2015).

102. S. Lee *et al.*, Anisotropic in-plane thermal conductivity of black phosphorus

nanoribbons at temperatures higher than 100 K. *Nat. Commun.* **6**, 8573 (2015).

103. F. Xia, H. Wang, D. Xiao, M. Dubey, A. Ramasubramaniam, Two-dimensional material nanophotonics. *Nat. Photonics*. **8**, 899–907 (2014).

104. E. Liu *et al.*, Integrated digital inverters based on two-dimensional anisotropic ReS2 field-effect transistors. *Nat. Commun.* **6**, 6991 (2015).

105. V. Zólyomi, N. D. Drummond, V. I. Fal'ko, Band structure and optical transitions in atomic layers of hexagonal gallium chalcogenides. *Phys. Rev. B.* **87**, 195403 (2013).

106. P. Hu *et al.*, Highly sensitive phototransistors based on two-dimensional GaTe nanosheets with direct bandgap. *Nano Res.* **7**, 694–703 (2014).

107. F. Liu *et al.*, High-Sensitivity Photodetectors Based on Multilayer GaTe Flakes. *ACS Nano*. **8**, 752–760 (2014).

108. O. A. Balitskii, B. Jaeckel, W. Jaegermann, Surface properties of GaTe single crystals. *Phys. Lett. A.* **372**, 3303–3306 (2008).

109. D. N. Bose, S. Pal, Photoconductivity, low-temperature conductivity, and magnetoresistance studies on the layered semiconductor GaTe. *Phys. Rev. B.* **63**, 235321 (2001).

110. J. F. Sánchez-Royo *et al.*, Angle-resolved photoemission study and first-principles calculation of the electronic structure of GaTe. *Phys. Rev. B.* **65**, 115201 (2002).

111. A. Yamamoto *et al.*, Excitons and band structure of highly anisotropic GaTe single crystals. *Phys. Rev. B.* **64**, 35210 (2001).

112. J. J. Fonseca *et al.*, Bandgap Restructuring of the Layered Semiconductor Gallium Telluride in Air. *Adv. Mater.* (2016), doi:10.1002/adma.201601151.

113. U. S. Shenoy *et al.*, Electronic structure and properties of layered gallium telluride. *Chem. Phys. Lett.* **651**, 148–154 (2016).

114. J. Susoma *et al.*, Second and third harmonic generation in few-layer gallium telluride characterized by multiphoton microscopy. *Appl. Phys. Lett.* **108**, 73103 (2016).

115. Q. Zhao *et al.*, Thickness-induced structural phase transformation of layered gallium telluride. *Phys. Chem. Chem. Phys.* **18**, 18719–18726 (2016).

116. K. C. Mandal *et al.*, in *IEEE Nuclear Science Symposuim & Medical Imaging Conference* (IEEE, 2010; http://ieeexplore.ieee.org/lpdocs/epic03/wrapper.htm?arnumber=5874507), pp. 3719–3724.

117. T. D. Rahmlow *et al.*, in *AIP Conference Proceedings* (AIP, 2007; http://scitation.aip.org/content/aip/proceeding/aipcp/10.1063/1.2711720), vol. 890, pp. 59–67.

118. S. Pal, D. Bose, Growth, characterisation and electrical anisotropy in layered chalcogenides GaTe and InTe. *Solid State Commun.* **97**, 725–729 (1996).

119. L. Gouskov, A. Gouskov, Resistivity anisotropy in the layer plane of GaTe. *Phys. Status Solidi*. **51**, K213–K215 (1979).

120. L. Zhou *et al.*, A Sensitive Phonon-Based Probe for Structure Identification of 1T' MoTe2. *J. Am. Chem. Soc.* **under revi** (2017).

121. R. Saito, M. Hofmann, G. Dresselhaus, A. Jorio, M. S. Dresselhaus, Raman spectroscopy of graphene and carbon nanotubes. *Adv. Phys.* **60**, 413–550 (2011).

122. A. Jorio, R. Saito, G. Dresselhaus, M. S. Dresselhaus, *Raman Spectroscopy in Graphene Related Systems* (Wiley-VCH, 2011).

123. M. S. Dresselhaus, A. Jorio, R. Saito, Characterizing Graphene, Graphite, and Carbon Nanotubes by Raman Spectroscopy. *Annu. Rev. Condens. Matter Phys.* **1**, 89–108 (2010).

124. M. S. Dresselhaus, A. Jorio, M. Hofmann, G. Dresselhaus, R. Saito, Perspectives on Carbon Nanotubes and Graphene Raman Spectroscopy. *Nano Lett.* **10**, 751–758 (2010).

125. X. Zhang *et al.*, Phonon and Raman scattering of two-dimensional transition metal dichalcogenides from monolayer, multilayer to bulk material. *Chem. Soc. Rev.* **44**, 2757–2785 (2015).

126. A. Molina-Sánchez, K. Hummer, L. Wirtz, Vibrational and optical properties of MoS2: From monolayer to bulk. *Surf. Sci. Rep.* **70**, 554–586 (2015).

127. A. G. Souza Filho *et al.*, Stokes and anti-Stokes Raman spectra of small-diameter isolated carbon nanotubes. *Phys. Rev. B.* **69**, 115428 (2004).

128. R. Roldán, A. Castellanos-Gomez, E. Cappelluti, F. Guinea, Strain engineering in semiconducting two-dimensional crystals. *J. Phys. Condens. Matter*. **27**, 313201 (2015).

129. C. Cong *et al.*, Raman Characterization of ABA- and ABC-Stacked Trilayer Graphene. *ACS Nano*. **5**, 8760–8768 (2011).

130. M. A. Pimenta *et al.*, Studying disorder in graphite-based systems by Raman spectroscopy. *Phys. Chem. Chem. Phys.* **9**, 1276–1290 (2007).

131. K. F. Mak *et al.*, Tightly bound trions in monolayer MoS2. *Nat. Mater.* **12**, 207–11 (2013).

132. F. Crowne *et al.*, Blueshift of the A-exciton peak in folded monolayer 1H-MoS2. *Phys. Rev. B.* **88**, 235302 (2013).

133. A. Ramasubramaniam, Large excitonic effects in monolayers of molybdenum and tungsten dichalcogenides. *Phys. Rev. B.* **86**, 115409 (2012).

134. T. Li, G. Galli, Electronic Properties of MoS2 Nanoparticles. *J. Phys. Chem. C*. **111**, 16192–16196 (2007).

135. A. J. Shields, M. Pepper, M. Y. Simmons, D. A. Ritchie, Spin-triplet negatively charged excitons in GaAs quantum wells. *Phys. Rev. B.* **52**, 7841–7844 (1995).

136. G. Finkelstein, H. Shtrikman, I. Bar-Joseph, Optical Spectroscopy of a Two-Dimensional Electron Gas near the Metal-Insulator Transition. *Phys. Rev. Lett.* **74**, 976–979 (1995).

137. B. Stébé, A. Ainane, Ground state energy and optical absorption of excitonic trions in two dimensional semiconductors. *Superlattices Microstruct.* **5**, 545–548 (1989).

138. S. Tongay *et al.*, Broad-range modulation of light emission in two-dimensional

semiconductors by molecular physisorption gating. *Nano Lett.* **13**, 2831–6 (2013).

139. J. S. Ross *et al.*, Electrical control of neutral and charged excitons in a monolayer semiconductor. *Nat. Commun.* **4**, 1474 (2013).

140. S. Mouri, Y. Miyauchi, K. Matsuda, Tunable Photoluminescence of Monolayer MoS 2 via Chemical Doping. *Nano Lett.* **13**, 5944–5948 (2013).

141. J. R. Schaibley *et al.*, Valleytronics in 2D materials. *Nat. Rev. Mater.* **1**, 16055 (2016).

142. G. Plechinger *et al.*, Low-temperature photoluminescence of oxide-covered single-layer MoS2. *Phys. status solidi - Rapid Res. Lett.* **6**, 126–128 (2012).

143. T. Korn, S. Heydrich, M. Hirmer, J. Schmutzler, C. Schüller, Low-temperature photocarrier dynamics in monolayer MoS2. *Appl. Phys. Lett.* **99**, 102109 (2011).

144. A. Castellanos-Gomez *et al.*, Local strain engineering in atomically thin MoS2. *Nano Lett.* **13**, 5361–6 (2013).

145. Y. Chen *et al.*, Tunable band gap photoluminescence from atomically thin transition-metal dichalcogenide alloys. *ACS Nano*. **7**, 4610–6 (2013).

146. V. Carozo *et al.*, Resonance effects on the Raman spectra of graphene superlattices. *Phys. Rev. B.* **88**, 85401 (2013).

147. K. Kim *et al.*, Raman Spectroscopy Study of Rotated Double-Layer Graphene: Misorientation-Angle Dependence of Electronic Structure. *Phys. Rev. Lett.* **108**, 246103 (2012).

148. V. Carozo *et al.*, Raman signature of graphene superlattices. *Nano Lett.* **11**, 4527–34 (2011).

149. K. Sato, R. Saito, C. Cong, T. Yu, M. S. Dresselhaus, Zone folding effect in Raman G-band intensity of twisted bilayer graphene. *Phys. Rev. B.* **86**, 125414 (2012).

150. P. Moon, M. Koshino, Optical absorption in twisted bilayer graphene. *Phys. Rev. B.* **87**, 205404 (2013).

151. D. S. Lee *et al.*, Quantum Hall Effect in Twisted Bilayer Graphene. *Phys. Rev. Lett.*

107, 216602 (2011).

152. B. Hunt *et al.*, Massive Dirac fermions and Hofstadter butterfly in a van der Waals heterostructure. *Science*. **340**, 1427–30 (2013).

153. A. M. van der Zande *et al.*, Grains and grain boundaries in highly crystalline monolayer molybdenum disulphide. *Nat. Mater.* **12**, 554–61 (2013).

154. C. Lee *et al.*, Anomalous lattice vibrations of single- and few-layer MoS2. *ACS Nano*. **4**, 2695–700 (2010).

155. A. Molina-Sánchez, L. Wirtz, Phonons in single-layer and few-layer MoS <math display="“inline”> <msub> <mrow/> <mn>2</mn> </msub> </math> and WS <math display="“inline”> <msub> <mrow/> <mn>2</mn> </msub> </math>. *Phys. Rev. B.* **84**, 155413 (2011).

156. Y. Wang, C. Cong, C. Qiu, T. Yu, Raman spectroscopy study of lattice vibration and crystallographic orientation of monolayer MoS2 under uniaxial strain. *Small*. **9**, 2857–61 (2013).

157. L. Liang, V. Meunier, First-principles Raman spectra of MoS2, WS2 and their heterostructures. *Nanoscale*. **6**, 5394 (2014).

158. H. Terrones *et al.*, New First Order Raman-active Modes in Few Layered Transition Metal Dichalcogenides. *Sci. Rep.* **4**, 4215 (2014).

159. Y.-H. Lee *et al.*, Synthesis and Transfer of Single-Layer Transition Metal Disulfides on Diverse Surfaces. *Nano Lett.* **13**, 1852–1857 (2013).

160. N. Scheuschner *et al.*, Photoluminescence of freestanding single- and few-layer <math> <msub> <mtext>MoS</mtext> <mn>2</mn> </msub> </math>. *Phys. Rev. B.* **89**, 125406 (2014).

161. D. Sercombe *et al.*, Optical investigation of the natural electron doping in thin MoS2 films deposited on dielectric substrates. *Sci. Rep.* **3**, 3489 (2013).

162. M. Chhowalla *et al.*, The chemistry of two-dimensional layered transition metal dichalcogenide nanosheets. *Nat. Chem.* **5**, 263–75 (2013).

163. A. Molina-Sánchez, D. Sangalli, K. Hummer, A. Marini, L. Wirtz, Effect of spin-orbit interaction on the optical spectra of single-layer, double-layer, and bulk MoS <math display="“inline”> <msub> <mrow/> <mn>2</mn> </msub> </math>. *Phys. Rev. B.* **88**, 45412 (2013).

164. J. He, K. Hummer, C. Franchini, Stacking effects on the electronic and optical properties of bilayer transition metal dichalcogenides MoS 2 , MoSe 2 , WS 2 , and WSe 2. *Phys. Rev. B.* **89**, 75409 (2014).

165. H.-P. Komsa, A. V. Krasheninnikov, Effects of confinement and environment on the electronic structure and exciton binding energy of MoS <math display="“inline”> <msub> <mrow/> <mn>2</mn> </msub> </math> from first principles. *Phys. Rev. B.* **86**, 241201 (2012).

166. L. Liang, E. C. Girão, V. Meunier, Quasiparticle band gaps of graphene nanowiggles and their magnetism on Au(111). *Phys. Rev. B.* **88**, 35420 (2013).

167. H.-P. Komsa *et al.*, Two-Dimensional Transition Metal Dichalcogenides under Electron Irradiation: Defect Production and Doping. *Phys. Rev. Lett.* **109**, 35503 (2012).

168. L. Tao, X. Duan, C. Wang, X. Duan, S. Wang, Plasma-engineered MoS 2 thin-film as an efficient electrocatalyst for hydrogen evolution reaction. *Chem. Commun.* **51**, 7470–7473 (2015).

169. H. Li *et al.*, Activating and optimizing MoS2 basal planes for hydrogen evolution through the formation of strained sulphur vacancies. *Nat. Mater.* **15**, 48–53 (2015).

170. W. Zhou *et al.*, Intrinsic Structural Defects in Monolayer Molybdenum Disulfide. *Nano Lett.* **13**, 2615–2622 (2013).

171. S. W. Han *et al.*, Controlling Ferromagnetic Easy Axis in a Layered MoS2 Single Crystal. *Phys. Rev. Lett.* **110**, 247201 (2013).

172. S. Tongay *et al.*, Defects activated photoluminescence in two-dimensional semiconductors: interplay between bound, charged, and free excitons. *Sci. Rep.* **3** (2013), doi:10.1038/srep02657.

173. D. Le, T. B. Rawal, T. S. Rahman, Single-Layer MoS 2 with Sulfur Vacancies: Structure and Catalytic Application. *J. Phys. Chem. C*. **118**, 5346–5351 (2014).

174. S. McDonnell, R. Addou, C. Buie, R. M. Wallace, C. L. Hinkle, Defect-Dominated Doping and Contact Resistance in MoS 2. *ACS Nano*. **8**, 2880–2888 (2014).

175. H. Qiu *et al.*, Hopping transport through defect-induced localized states in molybdenum disulphide. *Nat. Commun.* **4** (2013), doi:10.1038/ncomms3642.

176. M. M. Ugeda *et al.*, Giant bandgap renormalization and excitonic effects in a monolayer transition metal dichalcogenide semiconductor. *Nat. Mater.* **13**, 1091–1095 (2014).

177. H.-P. Komsa, A. V. Krasheninnikov, Native defects in bulk and monolayer <math> <msub> <mi>MoS</mi> <mn>2</mn> </msub> </math> from first principles. *Phys. Rev. B*. **91**, 125304 (2015).

178. Z. G. Yu, Y.-W. Zhang, B. I. Yakobson, An Anomalous Formation Pathway for Dislocation-Sulfur Vacancy Complexes in Polycrystalline Monolayer MoS 2. *Nano Lett.* **15**, 6855–6861 (2015).

179. X. Ling *et al.*, Role of the seeding promoter in MoS2 growth by chemical vapor deposition. *Nano Lett.* **14**, 464–72 (2014).

180. M. Donarelli, F. Bisti, F. Perrozzi, L. Ottaviano, Tunable sulfur desorption in exfoliated MoS2 by means of thermal annealing in ultra-high vacuum. *Chem. Phys. Lett.* **588**, 198–202 (2013).

181. Q. Ma *et al.*, Postgrowth Tuning of the Bandgap of Single-Layer Molybdenum Disulfide Films by Sulfur/Selenium Exchange. *ACS Nano*. **8**, 4672–4677 (2014).

182. D. S. Fox *et al.*, Nanopatterning and Electrical Tuning of MoS 2 Layers with a Subnanometer Helium Ion Beam. *Nano Lett.* **15**, 5307–5313 (2015).

183. Q. Ma *et al.*, Controlled argon beam-induced desulfurization of monolayer molybdenum disulfide. *J. Phys. Condens. Matter*. **25**, 252201 (2013).

184. S. Mathew *et al.*, Magnetism in MoS2 induced by proton irradiation. *Appl. Phys.*

Lett. **101**, 102103 (2012).

185. A. Inoue, T. Komori, K. Shudo, Atomic-scale structures and electronic states of defects on Ar+-ion irradiated MoS2. *J. Electron Spectros. Relat. Phenomena*. **189**, 11–18 (2013).

186. S. Mignuzzi *et al.*, Effect of disorder on Raman scattering of single-layer Mo S 2. *Phys. Rev. B.* **91**, 195411 (2015).

187. M. . Baker, R. Gilmore, C. Lenardi, W. Gissler, XPS investigation of preferential sputtering of S from MoS2 and determination of MoSx stoichiometry from Mo and S peak positions. *Appl. Surf. Sci.* **150**, 255–262 (1999).

188. S. Bertolazzi *et al.*, Engineering Chemically Active Defects in Monolayer MoS $_2$ Transistors via Ion-Beam Irradiation and Their Healing via Vapor Deposition of Alkanethiols. *Adv. Mater.*, 1606760 (2017).

189. S. Huang *et al.*, Tuning Electronic Structure of Single Layer MoS2 through Defect Engineering. *Prep.*

190. A. Pfau, K. D. Schierbaum, The electronic structure of stoichiometric and reduced CeO2 surfaces: an XPS, UPS and HREELS study. *Surf. Sci.* **321**, 71–80 (1994).

191. J. Cumings, A. Zettl, Field emission and current-voltage properties of boron nitride nanotubes. *Solid State Commun.* **129**, 661–664 (2004).

192. G.-H. Lee *et al.*, Electron tunneling through atomically flat and ultrathin hexagonal boron nitride. *Appl. Phys. Lett.* **99**, 243114 (2011).

193. C. Gong, L. Colombo, R. M. Wallace, K. Cho, The Unusual Mechanism of Partial Fermi Level Pinning at Metal–MoS 2 Interfaces. *Nano Lett.* **14**, 1714–1720 (2014).

194. S. Tongay *et al.*, Tuning Interlayer Coupling in Large-Area Heterostructures with CVD-Grown MoS 2 and WS 2 Monolayers. *Nano Lett.* **14**, 3185–3190 (2014).

195. H. Terrones, F. López-Urías, M. Terrones, Novel hetero-layered materials with tunable direct band gaps by sandwiching different metal disulfides and diselenides. *Sci. Rep.* **3**, 1549 (2013).

196. B. Chakraborty *et al.*, Symmetry-dependent phonon renormalization in monolayer MoS${}_{2}$ transistor. *Phys. Rev. B.* **85**, 161403 (2012).

197. H. J. Conley *et al.*, Bandgap Engineering of Strained Monolayer and Bilayer MoS 2. *Nano Lett.* **13**, 3626–3630 (2013).

198. H. L. Tuller, S. R. Bishop, Point Defects in Oxides: Tailoring Materials Through Defect Engineering. *Annu. Rev. Mater. Res.* **41**, 369–398 (2011).

199. T. Zacherle, A. Schriever, R. A. De Souza, M. Martin, Ab initio analysis of the defect structure of ceria. *Phys. Rev. B.* **87**, 134104 (2013).

200. Z. A. Feng *et al.*, Origin of Overpotential-Dependent Surface Dipole at CeO 2– x /Gas Interface During Electrochemical Oxygen Insertion Reactions. *Chem. Mater.* **28**, 6233–6242 (2016).

201. D. . Mullins, S. . Overbury, D. . Huntley, Electron spectroscopy of single crystal and polycrystalline cerium oxide surfaces. *Surf. Sci.* **409**, 307–319 (1998).

202. W. C. Chueh *et al.*, Highly Enhanced Concentration and Stability of Reactive Ce^{3+} on Doped CeO_2 Surface Revealed In Operando. *Chem. Mater.* **24**, 1876–1882 (2012).

203. E. Shoko, M. F. Smith, R. H. McKenzie, A Consistent Picture of Charge Distribution in Reduced Ceria Phases (2009) (available at http://arxiv.org/abs/0910.0669).

204. K. He, C. Poole, K. F. Mak, J. Shan, Experimental demonstration of continuous electronic structure tuning via strain in atomically thin MoS2. *Nano Lett.* **13**, 2931–6 (2013).

205. J. Ryou, Y.-S. Kim, S. KC, K. Cho, Monolayer MoS2 Bandgap Modulation by Dielectric Environments and Tunable Bandgap Transistors. *Sci. Rep.* **6**, 29184 (2016).

206. Y. L. Huang *et al.*, Bandgap tunability at single-layer molybdenum disulphide grain boundaries. *Nat. Commun.* **6**, 6298 (2015).

207. H. Li *et al.*, Optoelectronic crystal of artificial atoms in strain-textured molybdenum

disulphide. *Nat. Commun.* **6**, 7381 (2015).

208. C. Zhang, A. Johnson, C.-L. Hsu, L.-J. Li, C.-K. Shih, Direct Imaging of Band Profile in Single Layer MoS 2 on Graphite: Quasiparticle Energy Gap, Metallic Edge States, and Edge Band Bending. *Nano Lett.* **14**, 2443–2447 (2014).

209. C.-P. Lu, G. Li, J. Mao, L.-M. Wang, E. Y. Andrei, Bandgap, Mid-Gap States, and Gating Effects in MoS 2. *Nano Lett.* **14**, 4628–4633 (2014).

210. G. Li *et al.*, All The Catalytic Active Sites of MoS 2 for Hydrogen Evolution. *J. Am. Chem. Soc.* **138**, 16632–16638 (2016).

211. H. Li *et al.*, From Bulk to Monolayer MoS2: Evolution of Raman Scattering. *Adv. Funct. Mater.* **22**, 1385–1390 (2012).

212. A. Castellanos-Gomez *et al.*, Local strain engineering in atomically thin MoS2. *Nano Lett.* **13**, 5361–6 (2013).

213. H. J. Conley *et al.*, Bandgap engineering of strained monolayer and bilayer MoS2. *Nano Lett.* **13**, 3626–30 (2013).

214. Y. Shi *et al.*, Selective decoration of Au nanoparticles on monolayer MoS2 single crystals. *Sci. Rep.* **3**, 1839 (2013).

215. Y. Zhao *et al.*, Interlayer Breathing and Shear Modes in Few-Trilayer MoS2 and WSe2. *Nano Lett.* **13**, 1007–1015 (2013).

216. X. Zhang *et al.*, Raman spectroscopy of shear and layer breathing modes in multilayer MoS 2. *Phys. Rev. B.* **87**, 115413 (2013).

217. P. H. Tan *et al.*, The shear mode of multilayer graphene. *Nat. Mater.* **11**, 294–300 (2012).

218. C. H. Lui, T. F. Heinz, Measurement of layer breathing mode vibrations in few-layer graphene. *Phys. Rev. B.* **87**, 121404 (2013).

219. X. Luo *et al.*, Large Frequency Change with Thickness in Interlayer Breathing Mode-Significant Interlayer Interactions in Few Layer Black Phosphorus. *Nano Lett.* **15**, 3931–8 (2015).

220. J.-B. Wu *et al.*, Resonant Raman spectroscopy of twisted multilayer graphene. *Nat. Commun.* **5**, 5309 (2014).

221. C. Cong, T. Yu, Enhanced ultra-low-frequency interlayer shear modes in folded graphene layers. *Nat. Commun.* **5**, 4709 (2014).

222. J.-B. Wu *et al.*, Interface Coupling in Twisted Multilayer Graphene by Resonant Raman Spectroscopy of Layer Breathing Modes. *ACS Nano*. **9**, 7440–7449 (2015).

223. A. A. Puretzky *et al.*, Low-Frequency Raman Fingerprints of Two-Dimensional Metal Dichalcogenide Layer Stacking Configurations. *ACS Nano*. **9**, 6333–6342 (2015).

224. X. Lu *et al.*, Rapid and Nondestructive Identification of Polytypism and Stacking Sequences in Few-Layer Molybdenum Diselenide by Raman Spectroscopy. *Adv. Mater.* **27**, 4502–4508 (2015).

225. X. Luo *et al.*, Stacking sequence determines Raman intensities of observed interlayer shear modes in 2D layered materials - A general bond polarizability model. *Sci. Rep.* **5**, 14565 (2015).

226. C. H. Lui *et al.*, Observation of interlayer phonon modes in van der Waals heterostructures. *Phys. Rev. B.* **91**, 165403 (2015).

227. X. Hong *et al.*, Ultrafast charge transfer in atomically thin MoS2/WS2 heterostructures. *Nat. Nanotechnol.* **9**, 682–686 (2014).

228. C.-H. Lee *et al.*, Atomically thin p–n junctions with van der Waals heterointerfaces. *Nat. Nanotechnol.* **9**, 676–681 (2014).

229. F. Ceballos, M. Z. Bellus, H.-Y. Chiu, H. Zhao, Ultrafast charge separation and indirect exciton formation in a MoS2-MoSe2 van der Waals heterostructure. *ACS Nano*. **8**, 12717–24 (2014).

230. S. Memaran *et al.*, Pronounced Photovoltaic Response from Multilayered Transition-Metal Dichalcogenides PN-Junctions. *Nano Lett.* **15**, 7532–7538 (2015).

231. G. R. Bhimanapati *et al.*, Recent Advances in Two-Dimensional Materials beyond

Graphene. *ACS Nano*. **9**, 11509–11539 (2015).

232. C. Rice *et al.*, Raman-scattering measurements and first-principles calculations of strain-induced phonon shifts in monolayer MoS<math><msub><mrow></mrow><mn>2</mn></msub></math>. *Phys. Rev. B.* **87**, 81307 (2013).

233. Y. Y. Hui *et al.*, Exceptional Tunability of Band Energy in a Compressively Strained Trilayer MoS 2 Sheet. *ACS Nano*. **7**, 7126–7131 (2013).

234. J. He, K. Hummer, C. Franchini, Stacking effects on the electronic and optical properties of bilayer transition metal dichalcogenides MoS 2 , MoSe 2 , WS 2 , and WSe 2. *Phys. Rev. B.* **89**, 75409 (2014).

235. B. Cao, T. Li, Interlayer Electronic Coupling in Arbitrarily Stacked MoS 2 Bilayers Controlled by Interlayer S–S Interaction. *J. Phys. Chem. C*. **119**, 1247–1252 (2015).

236. L. Liang, V. Meunier, First-principles Raman spectra of MoS2, WS2 and their heterostructures. *Nanoscale*. **6**, 5394–401 (2014).

237. C. Kittel, *Introduction to Solid State Physics* (Wiley, ed. 8, 2004; http://www.wiley.com/WileyCDA/WileyTitle/productCd-EHEP000803.html).

238. H. Zabel, Phonons in layered compounds. *J. Phys. Condens. Matter*. **13**, 7679 (2001).

239. J.-H. Chen, C. Jang, S. Xiao, M. Ishigami, M. S. Fuhrer, Intrinsic and extrinsic performance limits of graphene devices on SiO2. *Nat. Nanotechnol.* **3**, 206–209 (2008).

240. E. H. Hwang, S. Das Sarma, Acoustic phonon scattering limited carrier mobility in two-dimensional extrinsic graphene. *Phys. Rev. B.* **77**, 115449 (2008).

241. D. K. Efetov, P. Kim, Controlling Electron-Phonon Interactions in Graphene at Ultrahigh Carrier Densities. *Phys. Rev. Lett.* **105**, 256805 (2010).

242. N. Bonini, M. Lazzeri, N. Marzari, F. Mauri, Phonon Anharmonicities in Graphite and Graphene. *Phys. Rev. Lett.* **99**, 176802 (2007).

243. C. H. Lui *et al.*, Observation of Layer-Breathing Mode Vibrations in Few-Layer Graphene through Combination Raman Scattering. *Nano Lett.* **12**, 5539–5544 (2012).

244. S. Uchida, S. Tanaka, Optical Phonon Modes and Localized Effective Charges of Transition-Metal Dichalcogenides. *J. Phys. Soc. Japan*. **45**, 153–161 (1978).

245. W. G. Stirling, B. Dorner, J. D. N. Cheeke, J. Revelli, Acoustic phonons in the transition-metal dichalcogenide layer compound, TiSe2. *Solid State Commun.* **18**, 931–933 (1976).

246. H. Li *et al.*, From Bulk to Monolayer MoS2: Evolution of Raman Scattering. *Adv. Funct. Mater.* **22**, 1385–1390 (2012).

247. A. C. Ferrari, Raman spectroscopy of graphene and graphite: Disorder, electron-phonon coupling, doping and nonadiabatic effects. *Solid State Commun.* **143**, 47–57 (2007).

248. B. Chakraborty *et al.*, Symmetry-dependent phonon renormalization in monolayer MoS2 transistor. *Phys. Rev. B.* **85**, 161403 (2012).

249. A. C. Ferrari, D. M. Basko, Raman spectroscopy as a versatile tool for studying the properties of graphene. *Nat. Nanotechnol.* **8**, 235–246 (2013).

250. C. H. Lui, T. F. Heinz, Measurement of layer breathing mode vibrations in few-layer graphene. *Phys. Rev. B.* **87**, 121404 (2013).

251. S. Sugai, I. Shirotani, Raman and infrared reflection spectroscopy in black phosphorus. *Solid State Commun.* **53**, 753–755 (1985).

252. J. Wu, N. Mao, L. Xie, H. Xu, J. Zhang, Identifying the Crystalline Orientation of Black Phosphorus Using Angle-Resolved Polarized Raman Spectroscopy. *Angew. Chemie*. **127**, 2396–2399 (2015).

253. A. Castellanos-Gomez *et al.*, Isolation and characterization of few-layer black phosphorus. *2D Mater.* **1**, 25001 (2014).

254. S. Zhang *et al.*, Extraordinary Photoluminescence and Strong Temperature/Angle-

Dependent Raman Responses in Few-Layer Phosphorene. *ACS Nano*. **8**, 9590–9596 (2014).

255. Y. Fujii *et al.*, Inelastic neutron scattering study of acoustic phonons of black phosphorus. *Solid State Commun.* **44**, 579–582 (1982).

256. Y. Yamada *et al.*, Lattice-dynamical properties of black phosphorus under pressure studied by inelastic neutron scattering. *Phys. Rev. B.* **30**, 2410–2413 (1984).

257. J.-W. Jiang, B.-S. Wang, H. S. Park, Interlayer Breathing and Shear Modes in Few-Layer Black Phosphorus (2014) (available at http://arxiv.org/abs/1412.7587).

258. Y. Cai *et al.*, Giant Phononic Anisotropy and Unusual Anharmonicity of Phosphorene: Interlayer Coupling and Strain Engineering (2015) (available at http://arxiv.org/abs/1502.00375).

259. A. Togo, F. Oba, I. Tanaka, First-principles calculations of the ferroelastic transition between rutile-type and CaCl2-type SiO2 at high pressures. *Phys. Rev. B.* **78**, 134106 (2008).

260. M. I. Aroyo *et al.*, Crystallography online: Bilbao Crystallographic Server. *Bulg Chem Commun*. **43**, 183–197 (2011).

261. C. Kaneta, H. Katayama-Yoshida, A. Morita, Lattice Dynamics of Black Phosphorus. I. Valence Force Field Model. *J. Phys. Soc. Japan*. **55**, 1213–1223 (1986).

262. S. Sugai, T. Ueda, K. Murase, Pressure Dependence of the Lattice Vibration in the Orthorhombic and Rhombohedral Structures of Black Phosphorus. *J. Phys. Soc. Japan*. **50**, 3356–3361 (1981).

263. J. Ribeiro-Soares, R. M. Almeida, L. G. Cançado, M. S. Dresselhaus, A. Jorio, Group theory for structural analysis and lattice vibrations in phosphorene systems. *Phys. Rev. B.* **91**, 205421 (2015).

264. Z.-Y. Ong, Y. Cai, G. Zhang, Y.-W. Zhang, Strong Thermal Transport Anisotropy and Strain Modulation in Single-Layer Phosphorene. *J. Phys. Chem. C*. **118**, 25272–25277 (2014).

265. Z. H. Ni *et al.*, Graphene Thickness Determination Using Reflection and Contrast Spectroscopy. *Nano Lett.* **7**, 2758–2763 (2007).

266. L. Li *et al.*, Black phosphorus field-effect transistors. *Nat. Nanotechnol.* **9**, 372–377 (2014).

267. H. B. Ribeiro *et al.*, Unusual Angular Dependence of the Raman Response in Black Phosphorus. *ACS Nano*. **9**, 4270–4276 (2015).

268. W. Lu *et al.*, Plasma-assisted fabrication of monolayer phosphorene and its Raman characterization. *Nano Res.* **7**, 853–859 (2014).

269. M. Yamamoto *et al.*, Strong Enhancement of Raman Scattering from a Bulk-Inactive Vibrational Mode in Few-Layer MoTe 2. *ACS Nano*. **8**, 3895–3903 (2014).

270. D. Teweldebrhan, V. Goyal, A. A. Balandin, Exfoliation and Characterization of Bismuth Telluride Atomic Quintuples and Quasi-Two-Dimensional Crystals. *Nano Lett.* **10**, 1209–1218 (2010).

271. M. Boukhicha, M. Calandra, M.-A. Measson, O. Lancry, A. Shukla, Anharmonic phonons in few-layer MoS2: Raman spectroscopy of ultralow energy compression and shear modes. *Phys. Rev. B (Condensed Matter Mater. Physics)*. **87**, 195316 (2013).

272. P. G. Klemens, Anharmonic Decay of Optical Phonons. *Phys. Rev.* **148**, 845–848 (1966).

273. J. Lin *et al.*, Anharmonic phonon effects in Raman spectra of unsupported vertical graphene sheets. *Phys. Rev. B.* **83**, 125430 (2011).

274. I. Calizo, A. A. Balandin, W. Bao, F. Miao, C. N. Lau, Temperature Dependence of the Raman Spectra of Graphene and Graphene Multilayers. *Nano Lett.* **7**, 2645–2649 (2007).

275. S. Sahoo, A. P. S. Gaur, M. Ahmadi, M. J.-F. Guinel, R. S. Katiyar, Temperature-Dependent Raman Studies and Thermal Conductivity of Few-Layer MoS2. *J. Phys. Chem. C*. **117**, 9042–9047 (2013).

276. N. A. Lanzillo *et al.*, Temperature-dependent phonon shifts in monolayer MoS2. *Appl. Phys. Lett.* **103**, 93102 (2013).

277. R. J. Riedner *et al.*, (ASCE, 1974), pp. 8–20.

278. N. Raravikar *et al.*, Temperature dependence of radial breathing mode Raman frequency of single-walled carbon nanotubes. *Phys. Rev. B.* **66** (2002), p. 235424.

279. E. Liu *et al.*, Integrated digital inverters based on two-dimensional anisotropic ReS_2 field-effect transistors. *Nat. Commun.* **6**, 6991 (2015).

280. L.-D. Zhao *et al.*, Ultralow thermal conductivity and high thermoelectric figure of merit in SnSe crystals. *Nature*. **508**, 373–7 (2014).

281. H. Yuan *et al.*, Polarization-sensitive broadband photodetector using a black phosphorus vertical p-n junction. *Nat. Nanotechnol.* (2015), doi:10.1038/nnano.2015.112.

282. R. Fei *et al.*, Enhanced Thermoelectric Efficiency via Orthogonal Electrical and Thermal Conductances in Phosphorene. *Nano Lett.* **14**, 6393–6399 (2014).

283. M. Ikezawa, Y. Kondo, I. Shirotani, Infrared Optical Absorption Due to One and Two Phonon Processes in Black Phosphorus. *J. Phys. Soc. Japan*. **52**, 1518–1520 (1983).

284. W. Lu *et al.*, Probing the anisotropic behaviors of black phosphorus by transmission electron microscopy, angular-dependent Raman spectra, and electronic transport measurements. *Appl. Phys. Lett.* **107**, 21906 (2015).

285. J. Qiao, X. Kong, Z.-X. Hu, F. Yang, W. Ji, High-mobility transport anisotropy and linear dichroism in few-layer black phosphorus. *Nat. Commun.* **5**, 4475 (2014).

286. J. Kim *et al.*, Anomalous polarization dependence of Raman scattering and crystallographic orientation of black phosphorus. *Nanoscale*. **7**, 18708–18715 (2015).

287. *<i>We found that in the literature, different coordinate notations have been used. For example, some use x as armchair, y as zigzag, z as out-of-plane directions, such*

as refs 7, 9 and 21); some use x as armchair, z as zigzag, y as out-of-plane (ref. 12);

288. J. J. Sakurai, J. J. Napolitano, *Modern Quantum Mechanics* (Addison-Wesley, ed. 2, 2011; http://www.pearsonhighered.com/educator/product/Modern-Quantum-Mechanics/9780805382914.page).

289. H. Asahina, A. Morita, Band structure and optical properties of black phosphorus. *J. Phys. C Solid State Phys.* **17**, 1839–1852 (1984).

290. B. Liao, J. Zhou, B. Qiu, M. S. Dresselhaus, G. Chen, Ab initio study of electron-phonon interaction in phosphorene. *Phys. Rev. B.* **91**, 235419 (2015).

291. A.-M. Zhang, Q.-M. Zhang, Electron—phonon coupling in cuprate and iron-based superconductors revealed by Raman scattering. *Chinese Phys. B.* **22**, 87103 (2013).

292. Y. Ma, J. S. Tse, D. D. Klug, R. Ahuja, Electron-phonon coupling of α−Ga boron. *Phys. Rev. B.* **70** (2004), doi:10.1103/PhysRevB.70.214107.

293. X. Ling *et al.*, Low-Frequency Interlayer Breathing Modes in Few-Layer Black Phosphorus. *Nano Lett.* **15**, 4080–4088 (2015).

294. D. Yoon *et al.*, Interference effect on Raman spectrum of graphene on SiO2/Si. *Phys. Rev. B.* **80**, 125422 (2009).

295. L. Gao *et al.*, Surface and Interference Coenhanced Raman Scattering of Graphene. *ACS Nano*. **3**, 933–939 (2009).

296. W. B. Pearson, The crystal structures of semiconductors and a general valence rule. *Acta Crystallogr.* **17**, 1–15 (1964).

297. J. Camassel, P. Merle, H. Mathieu, Excitonic absorption edge of GaTe. *Phys. B+C.* **99**, 309–313 (1980).

298. M. Lazzeri, F. Mauri, First-principles calculation of vibrational Raman spectra in large systems: signature of small rings in crystalline SiO2. *Phys. Rev. Lett.* **90**, 36401 (2003).

299. H. Guo *et al.*, Double resonance Raman modes in monolayer and few-layer MoTe2. *Phys. Rev. B.* **91**, 205415 (2015).

300. P. Venezuela, M. Lazzeri, F. Mauri, Theory of double-resonant Raman spectra in graphene: Intensity and line shape of defect-induced and two-phonon bands. *Phys. Rev. B.* **84**, 35433 (2011).

301. J. C. Irwin, B. P. Clayman, D. G. Mead, Long-wavelength phonons in GaTe. *Phys. Rev. B.* **19**, 2099–2105 (1979).

302. N. Mao *et al.*, Birefringence-Directed Raman Selection Rules in 2D Black Phosphorus Crystals. *Small*. **12**, 2627–2633 (2016).

303. C. Kranert, C. Sturm, R. Schmidt-Grund, M. Grundmann, Raman Tensor Formalism for Optically Anisotropic Crystals. *Phys. Rev. Lett.* **116**, 127401 (2016).

304. R. Saito, Y. Tatsumi, S. Huang, X. Ling, M. S. Dresselhaus, Raman spectroscopy of transition metal dichalcogenides. *J. Phys. Condens. Matter*. **28**, 353002 (2016).

305. S.-L. Li *et al.*, Quantitative Raman Spectrum and Reliable Thickness Identification for Atomic Layers on Insulating Substrates. *ACS Nano*. **6**, 7381–7388 (2012).

306. Y. Y. Wang, Z. H. Ni, Z. X. Shen, H. M. Wang, Y. H. Wu, Interference enhancement of Raman signal of graphene. *Appl. Phys. Lett.* **92**, 43121 (2008).

307. H. Zhao *et al.*, Interlayer interactions in anisotropic atomically thin rhenium diselenide. *Nano Res.* **8**, 3651–3661 (2015).

308. R. He *et al.*, Coupling and Stacking Order of ReS2 Atomic Layers Revealed by Ultralow-Frequency Raman Spectroscopy. *Nano Lett.* **ASAP** (2016), doi:10.1021/acs.nanolett.5b04925.

309. R. Saito, Y. Tatsumi, S. Huang, X. Ling, M. S. Dresselhaus, Raman spectroscopy of transition metal dichalcogenides. *J. Phys. Condens. Matter*. **28**, 353002 (2016).

310. A. Campion, P. Kambhampati, Surface-enhanced Raman scattering. *Chem. Soceity Rev.* **27**, 241–250 (1998).

311. M. G. Albrecht, J. A. Creighton, Anomalously intense Raman spectra of pyridine at a silver electrode. *J. Am. Chem. Soc.* **99**, 5215–5217 (1977).

312. D. L. Jeanmaire, R. P. Van Duyne, Surface raman spectroelectrochemistry. *J.*

Electroanal. Chem. Interfacial Electrochem. **84**, 1–20 (1977).

313. K. Kneipp, M. Moskovits, H. Kneipp, *Surface-enhanced Raman scattering: physics and applications* (Springer-Verlag: Berlin Heidelberg, 2006; http://www.springer.com/physics/).

314. Z.-Q. Tian, B. Ren, D.-Y. Wu, Surface-Enhanced Raman Scattering: From Noble to Transition Metals and from Rough Surfaces to Ordered Nanostructures. *J. Phys. Chem. B.* **106**, 9463–9483 (2002).

315. B. Ren *et al.*, Surface raman spectra of pyridine and hydrogen on bare platinum and nickel electrodes. *J. Electroanal. Chem.* **415**, 175–178 (1996).

316. G. Schatz, M. Young, R. P. Van Duyne, Electromagnetic mechanism of SERS. *Surface-enhanced Raman Scatt.* **103**, 19–45 (2006).

317. A. Otto, M. Futamata, Electronic mechanisms of SERS. *Top. Appl. Phys.* **103**, 147–182 (2006).

318. E. C. Le Ru, E. Blackie, M. Meyer, P. G. Etchegoin, Surface Enhanced Raman Scattering Enhancement Factors: A Comprehensive Study. *J. Phys. Chem. C.* **111**, 13794–13803 (2007).

319. S. M. Morton, L. Jensen, Understanding the molecule-surface chemical coupling in SERS. *J. Am. Chem. Soc.* **131**, 4090–8 (2009).

320. A. Campion, J. E. Ivanecky, C. M. Child, M. Foster, On the Mechanism of Chemical Enhancement in Surface-Enhanced Raman Scattering. *J. Am. Chem. Soc.* **117**, 11807–11808 (1995).

321. X. Ling *et al.*, Can graphene be used as a substrate for Raman enhancement? *Nano Lett.* **10**, 553–61 (2010).

322. X. Ling, S. Huang, J. Kong, M. Dresselhaus, in *Recent Development of Surface-Enhanced Raman Scattering* (World Scientific Publishing Company, 2016).

323. X. Ling *et al.*, Lighting Up the Raman Signal of Molecules in the Vicinity of Graphene Related Materials. *Acc. Chem. Res.* **48**, 1862–1870 (2015).

324. X. Ling, L. G. Moura, M. A. Pimenta, J. Zhang, Charge-Transfer Mechanism in Graphene-Enhanced Raman Scattering. *J. Phys. Chem. C*. **116**, 25112–25118 (2012).

325. X. Ling, J. Wu, L. Xie, J. Zhang, Graphene-Thickness-Dependent Graphene-Enhanced Raman Scattering. *J. Phys. Chem. C*. **117**, 2369–2376 (2013).

326. X. Ling, J. Zhang, First-layer effect in graphene-enhanced Raman scattering. *Small*. **6**, 2020–5 (2010).

327. X. Ling, J. Wu, W. Xu, J. Zhang, Probing the effect of molecular orientation on the intensity of chemical enhancement using graphene-enhanced Raman spectroscopy. *Small*. **8**, 1365–72 (2012).

328. H. Xu, L. Xie, H. Zhang, J. Zhang, Effect of graphene Fermi level on the Raman scattering intensity of molecules on graphene. *ACS Nano*. **5**, 5338–44 (2011).

329. Y. Wang, Z. Li, J. Wang, J. Li, Y. Lin, Graphene and graphene oxide: biofunctionalization and applications in biotechnology. *Trends Biotechnol.* **29**, 205–12 (2011).

330. Y. Zhao *et al.*, Enhanced SERS Stability of R6G Molecules with Monolayer Graphene. *J. Phys. Chem. C*. **118**, 11827–11832 (2014).

331. E. C. Le Ru, P. G. Etchegoin, *Principles of Surface-Enhanced Raman Spectroscopy and related plasmonic effects* (Elsevier, 2008; http://www.elsevier.com/books/principles-of-surface-enhanced-raman-spectroscopy/le-ru/).

332. S. Huang *et al.*, Molecular Selectivity of Graphene-Enhanced Raman Scattering. *Nano Lett.* **15**, 2892–2901 (2015).

333. E. B. Barros, M. S. Dresselhaus, Theory for Raman Enhancement by 2D materials : Applications for GERS. *Phys. Rev. B*. **90**, 35443 (2014).

334. L. A. Austin, B. Kang, C.-W. Yen, M. A. El-Sayed, Nuclear targeted silver nanospheres perturb the cancer cell cycle differently than those of nanogold. *Bioconjug. Chem.* **22**, 2324–31 (2011).

335. Q. Liu, Q. Zhou, G. Jiang, Nanomaterials for analysis and monitoring of emerging chemical pollutants. *TrAC Trends Anal. Chem.* **58**, 10–22 (2014).

336. S. Jiao, Y. Wang, C. Chen, X. Wu, F. Bei, Graphene oxide mediated surface-enhanced Raman scattering substrate: Well-suspending and label-free detecting for protein. *J. Mol. Struct.* **1062**, 48–52 (2014).

337. D. Lin, T. Qin, Y. Wang, X. Sun, L. Chen, Graphene oxide wrapped SERS tags: multifunctional platforms toward optical labeling, photothermal ablation of bacteria, and the monitoring of killing effect. *ACS Appl. Mater. Interfaces*. **6**, 1320–9 (2014).

338. W. Xu *et al.*, Surface enhanced Raman spectroscopy on a flat graphene surface. *Proc. Natl. Acad. Sci. U. S. A.* **109**, 9281–6 (2012).

339. M. Manikandan, H. Nasser Abdelhamid, A. Talib, H.-F. Wu, Facile synthesis of gold nanohexagons on graphene templates in Raman spectroscopy for biosensing cancer and cancer stem cells. *Biosens. Bioelectron.* **55**, 180–6 (2014).

340. K. Kneipp, H. Kneipp, I. Itzkan, R. R. Dasari, M. S. Feld, Surface-enhanced Raman scattering and biophysics. *J. Phys. Condens. Matter*. **14**, R597–R624 (2002).

341. C.-W. Chu, V. Shrotriya, G. Li, Y. Yang, Tuning acceptor energy level for efficient charge collection in copper-phthalocyanine-based organic solar cells. *Appl. Phys. Lett.* **88**, 153504 (2006).

342. R. Schlaf, B. A. Parkinson, P. A. Lee, K. W. Nebesny, N. R. Armstrong, HOMO/LUMO Alignment at PTCDA/ZnPc and PTCDA/ClInPc Heterointerfaces Determined by Combined UPS and XPS Measurements. *J. Phys. Chem. B.* **103**, 2984–2992 (1999).

343. C. Shen, A. Kahn, J. Schwartz, Role of metal–molecule chemistry and interdiffusion on the electrical properties of an organic interface: The Al–F[sub 16]CuPc case. *J. Appl. Phys.* **90**, 6236 (2001).

344. P. Yang *et al.*, Influence of Duschinsky and Herzberg-Teller effects on $S_0 \rightarrow S_1$ vibrationally resolved absorption spectra of several porphyrin-like compounds. *J. Chem. Phys.* **141**, 124304 (2014).

345. F. Santoro, A. Lami, R. Improta, J. Bloino, V. Barone, Effective method for the computation of optical spectra of large molecules at finite temperature including the Duschinsky and Herzberg-Teller effect: the Qx band of porphyrin as a case study. *J. Chem. Phys.* **128**, 224311 (2008).

346. P. Corio, J. C. Rubim, R. Aroca, Contribution of the Herzberg−Teller Mechanism to the Surface-Enhanced Raman Scattering of Iron Phthalocyanine Adsorbed on a Silver Electrode. *Langmuir*. **14**, 4162–4168 (1998).

347. F. Cerdeira *et al.*, Raman spectroscopy as a probe of molecular order, orientation, and stacking of fluorinated copper-phthalocyanine (F 16 CuPc) thin films. *J. Raman Spectrosc.* **44**, 597–607 (2013).

348. F.-C. Wu *et al.*, Electron transport properties in fluorinated copper-phthalocyanine films: importance of vibrational reorganization energy and molecular microstructure. *Phys. Chem. Chem. Phys.* **12**, 2098–106 (2010).

349. Y. Xie *et al.*, Synthesis, optical properties and charge transport characteristics of a series of novel thiophene-fused phenazine derivatives. *J. Mater. Chem. C*. **1**, 3467 (2013).

350. W.-Y. Hung, G.-M. Tu, S.-W. Chen, Y. Chi, Phenylcarbazole-dipyridyl triazole hybrid as bipolar host material for phosphorescent OLEDs. *J. Mater. Chem.* **22**, 5410 (2012).

351. E. New, T. Howells, P. Sullivan, T. S. Jones, Small molecule tandem organic photovoltaic cells incorporating an α-NPD optical spacer layer. *Org. Electron.* **14**, 2353–2359 (2013).

352. M. Guo *et al.*, Franck-Condon simulation of vibrationally resolved optical spectra for zinc complexes of phthalocyanine and tetrabenzoporphyrin including the Duschinsky and Herzberg-Teller effects. *J. Chem. Phys.* **136**, 144313 (2012).

353. R. Scholz *et al.*, Asymmetry between absorption and photoluminescence line shapes of TPD: spectroscopic fingerprint of the twisted biphenyl core. *J. Phys. Chem. A.* **113**, 315–24 (2009).

354. A. Y. Kobitski *et al.*, Raman spectroscopy of the PTCDA–inorganic semiconductor interface: evidence for charge transfer. *Appl. Surf. Sci.* **190**, 386–389 (2002).

355. http://www.sigmaaldrich.com/materials-science/.

356. T. Basova, B. Kolesov, Raman Spectra of Copper Phthalocyanin: Experiment and Calculation. *J. Struct. Chem.* **41**, 770–777 (2000).

357. A. J. Martínez-Galera *et al.*, Imaging Molecular Orbitals of PTCDA on Graphene on Pt(111): Electronic Structure by STM and First-Principles Calculations. *J. Phys. Chem. C.* **118**, 12782–12788 (2014).

358. C. Huang *et al.*, Raman Enhancement of a Dipolar Molecule on Graphene. *J. Phys. Chem. C.* **118**, 2077–2084 (2014).

359. S. Takizawa, V. A. Montes, P. Anzenbacher, Phenylbenzimidazole-Based New Bipolar Host Materials for Efficient Phosphorescent Organic Light-Emitting Diodes. *Chem. Mater.* **21**, 2452–2458 (2009).

360. J.-A. Cheng, C. H. Chen, White organic electroluminescence from an exciplex based on the novel substituted aluminium quinolate complex. *J. Mater. Chem.* **15**, 1179 (2005).

361. H. Gao *et al.*, Theoretical characterization of a typical hole/exciton-blocking material bathocuproine and its analogues. *J. Phys. Chem. A.* **112**, 9097–103 (2008).

362. X. Ling *et al.*, Raman enhancement effect on two-dimensional layered materials: graphene, h-BN and MoS2. *Nano Lett.* **14**, 3033–40 (2014).

363. H. J. Kimble, Strong Interactions of Single Atoms and Photons in Cavity QED. *Phys. Scr.* **T76**, 127 (1998).

364. J. Vučković, M. Lončar, H. Mabuchi, A. Scherer, Design of photonic crystal microcavities for cavity QED. *Phys. Rev. E.* **65**, 16608 (2001).

365. C. J. Hood, The Atom-Cavity Microscope: Single Atoms Bound in Orbit by Single Photons. *Science (80-.).* **287**, 1447–1453 (2000).

366. V. Lefèvre-Seguin, S. Haroche, Towards cavity-QED experiments with silica

microspheres. *Mater. Sci. Eng. B.* **48**, 53–58 (1997).

367. P. W. H. Pinkse, T. Fischer, P. Maunz, G. Rempe, Trapping an atom with single photons. *Nature*. **404**, 365–368 (2000).

368. S. Noda, M. Fujita, T. Asano, Spontaneous-emission control by photonic crystals and nanocavities. *Nat. Photonics*. **1**, 449–458 (2007).

369. S. A. Maier, Plasmonic field enhancement and SERS in the effective mode volume picture. *Opt. Express*. **14**, 1957 (2006).

370. G. S. Solomon, M. Pelton, Y. Yamamoto, Modification of Spontaneous Emission of a Single Quantum Dot. *Phys. status solidi*. **178**, 341–344 (2000).

371. M. Bayer *et al.*, Inhibition and Enhancement of the Spontaneous Emission of Quantum Dots in Structured Microresonators. *Phys. Rev. Lett.* **86**, 3168–3171 (2001).

372. H.-G. Park *et al.*, Electrically driven single-cell photonic crystal laser. *Science*. **305**, 1444–7 (2004).

373. J. L. Jewell *et al.*, Lasing characteristics of GaAs microresonators. *Appl. Phys. Lett.* **54**, 1400 (1989).

374. S. L. McCall, A. F. J. Levi, R. E. Slusher, S. J. Pearton, R. A. Logan, Whispering-gallery mode microdisk lasers. *Appl. Phys. Lett.* **60**, 289 (1992).

375. M. Cai, O. Painter, K. J. Vahala, Observation of Critical Coupling in a Fiber Taper to a Silica-Microsphere Whispering-Gallery Mode System. *Phys. Rev. Lett.* **85**, 74–77 (2000).

376. K. Djordjev, Seung-June Choi, Sang-Jun Choi, R. D. Dapkus, Microdisk tunable resonant filters and switches. *IEEE Photonics Technol. Lett.* **14**, 828–830 (2002).

377. P. Rabiei, W. H. Steier, Cheng Zhang, L. R. Dalton, Polymer micro-ring filters and modulators. *J. Light. Technol.* **20**, 1968–1975 (2002).

378. K. J. Vahala, Optical microcavities. *Nature*. **424**, 839–846 (2003).

379. S. S. Verbridge, J. M. Parpia, R. B. Reichenbach, L. M. Bellan, H. G. Craighead,

High quality factor resonance at room temperature with nanostrings under high tensile stress. *J. Appl. Phys.* **99**, 124304 (2006).

380. P. B. Deotare, M. W. McCutcheon, I. W. Frank, M. Khan, M. Lončar, High quality factor photonic crystal nanobeam cavities. *Appl. Phys. Lett.* **94**, 121106 (2009).

381. T. Yoshie, L. Tang, S.-Y. Su, Optical Microcavity: Sensing down to Single Molecules and Atoms. *Sensors*. **11**, 1972–1991 (2011).

382. D. K. Armani, T. J. Kippenberg, S. M. Spillane, K. J. Vahala, Ultra-high-Q toroid microcavity on a chip. *Nature*. **421**, 925–928 (2003).

383. T. J. Kippenberg, S. M. Spillane, K. J. Vahala, Demonstration of ultra-high-Q small mode volume toroid microcavities on a chip. *Appl. Phys. Lett.* **85**, 6113 (2004).

384. J. T. Robinson, C. Manolatou, L. Chen, M. Lipson, Ultrasmall Mode Volumes in Dielectric Optical Microcavities. *Phys. Rev. Lett.* **95**, 143901 (2005).

385. S. A. Maier, Effective Mode Volume of Nanoscale Plasmon Cavities. *Opt. Quantum Electron.* **38**, 257–267 (2006).

386. E. Feigenbaum, M. Orenstein, Ultrasmall Volume Plasmons, yet with Complete Retardation Effects. *Phys. Rev. Lett.* **101**, 163902 (2008).

387. M. Kuttge, F. J. García de Abajo, A. Polman, Ultrasmall Mode Volume Plasmonic Nanodisk Resonators. *Nano Lett.* **10**, 1537–1541 (2010).

388. S. a Maier, Plasmonic field enhancement and SERS in the effective mode volume picture. *Opt. Express*. **14**, 1957–1964 (2006).

389. C. Sauvan, J. P. Hugonin, I. S. Maksymov, P. Lalanne, Theory of the Spontaneous Optical Emission of Nanosize Photonic and Plasmon Resonators. *Phys. Rev. Lett.* **110**, 237401 (2013).

390. T. Ding, L. O. Herrmann, B. de Nijs, F. Benz, J. J. Baumberg, Self-Aligned Colloidal Lithography for Controllable and Tuneable Plasmonic Nanogaps. *Small*. **11**, 2139–2143 (2015).

391. B. de Nijs *et al.*, Unfolding the contents of sub-nm plasmonic gaps using normalising

plasmon resonance spectroscopy. *Faraday Discuss.* **178**, 185–193 (2015).

392. R. W. Taylor *et al.*, Watching individual molecules flex within lipid membranes using SERS. *Sci. Rep.* **4** (2014), doi:10.1038/srep05940.

393. G. M. Akselrod *et al.*, Probing the mechanisms of large Purcell enhancement in plasmonic nanoantennas. *Nat. Photonics*. **8**, 835–840 (2014).

394. P. Genevet *et al.*, Large Enhancement of Nonlinear Optical Phenomena by Plasmonic Nanocavity Gratings. *Nano Lett.* **10**, 4880–4883 (2010).

395. W. Zhou *et al.*, Lasing action in strongly coupled plasmonic nanocavity arrays. *Nat. Nanotechnol.* **8**, 506–511 (2013).

396. K. J. Russell, T.-L. Liu, S. Cui, E. L. Hu, Large spontaneous emission enhancement in plasmonic nanocavities. *Nat. Photonics*. **6**, 459–462 (2012).

397. A. Tao, P. Sinsermsuksakul, P. Yang, Polyhedral Silver Nanocrystals with Distinct Scattering Signatures. *Angew. Chemie Int. Ed.* **45**, 4597–4601 (2006).

398. K. E. Korte, S. E. Skrabalak, Y. Xia, Rapid synthesis of silver nanowires through a CuCl- or CuCl 2 -mediated polyol process. *J. Mater. Chem.* **18**, 437–441 (2008).

399. D. J. Lipomi *et al.*, Fabrication and Replication of Arrays of Single- or Multicomponent Nanostructures by Replica Molding and Mechanical Sectioning. *ACS Nano*. **4**, 4017–4026 (2010).

400. P. K. Aravind, H. Metiu, Use of a perfectly conducting sphere to excite the plasmon of a flat surface. 1. Calculation of the local field with applications to surface-enhanced spectroscopy. *J. Phys. Chem.* **86**, 5076–5084 (1982).

401. P. K. Aravind, R. W. Rendell, H. Metiu, A new geometry for field enhancement in surface-enhanced spectroscopy. *Chem. Phys. Lett.* **85**, 396–403 (1982).

402. S. Mubeen *et al.*, Plasmonic Properties of Gold Nanoparticles Separated from a Gold Mirror by an Ultrathin Oxide. *Nano Lett.* **12**, 2088–2094 (2012).

403. L. Li, T. Hutter, U. Steiner, S. Mahajan, Single molecule SERS and detection of biomolecules with a single gold nanoparticle on a mirror junction. *Analyst*. **138**,

4574 (2013).

404. T. Ding, J. Mertens, D. O. Sigle, J. J. Baumberg, Capillary-Force-Assisted Optical Tuning of Coupled Plasmons. *Adv. Mater.* **27**, 6457–6461 (2015).

405. C. Tserkezis *et al.*, Hybridization of plasmonic antenna and cavity modes: Extreme optics of nanoparticle-on-mirror nanogaps. *Phys. Rev. A.* **92**, 53811 (2015).

406. C. Lumdee, B. Yun, P. G. Kik, Wide-Band Spectral Control of Au Nanoparticle Plasmon Resonances on a Thermally and Chemically Robust Sensing Platform. *J. Phys. Chem. C.* **117**, 19127–19133 (2013).

407. S. Huang *et al.*, Ultrasmall Mode Volumes in Plasmonic Cavities of Nanoparticle-On-Mirror Structures. *Small.* **12**, 5190–5199 (2016).

408. J. PEREZJUSTE, I. PASTORIZASANTOS, L. LIZMARZAN, P. MULVANEY, Gold nanorods: Synthesis, characterization and applications. *Coord. Chem. Rev.* **249**, 1870–1901 (2005).

409. M. Grzelczak, J. Pérez-Juste, P. Mulvaney, L. M. Liz-Marzán, Shape control in gold nanoparticle synthesis. *Chem. Soc. Rev.* **37**, 1783 (2008).

410. C.-J. Huang, Y.-H. Wang, P.-H. Chiu, M.-C. Shih, T.-H. Meen, Electrochemical synthesis of gold nanocubes. *Mater. Lett.* **60**, 1896–1900 (2006).

411. T. K. Sau, C. J. Murphy, Room Temperature, High-Yield Synthesis of Multiple Shapes of Gold Nanoparticles in Aqueous Solution. *J. Am. Chem. Soc.* **126**, 8648–8649 (2004).

412. J. Aizpurua *et al.*, Optical properties of coupled metallic nanorods for field-enhanced spectroscopy. *Phys. Rev. B.* **71**, 235420 (2005).

413. B. J. Wiley, D. J. Lipomi, J. Bao, F. Capasso, G. M. Whitesides, Fabrication of Surface Plasmon Resonators by Nanoskiving Single-Crystalline Gold Microplates. *Nano Lett.* **8**, 3023–3028 (2008).

414. E. Hao, G. C. Schatz, Electromagnetic fields around silver nanoparticles and dimers. *J. Chem. Phys.* **120**, 357 (2004).

415. M. Rang *et al.*, Optical Near-Field Mapping of Plasmonic Nanoprisms. *Nano Lett.* **8**, 3357–3363 (2008).

416. J. M. McLellan, A. Siekkinen, J. Chen, Y. Xia, Comparison of the surface-enhanced Raman scattering on sharp and truncated silver nanocubes. *Chem. Phys. Lett.* **427**, 122–126 (2006).

417. L. J. Sherry *et al.*, Localized Surface Plasmon Resonance Spectroscopy of Single Silver Nanocubes. *Nano Lett.* **5**, 2034–2038 (2005).

418. J. J. Mock *et al.*, Distance-dependent plasmon resonant coupling between a gold nanoparticle and gold film. *Nano Lett.* **8**, 2245–52 (2008).

419. B. J. Wiley *et al.*, Maneuvering the Surface Plasmon Resonance of Silver Nanostructures through Shape-Controlled Synthesis. *J. Phys. Chem. B.* **110**, 15666–15675 (2006).

420. Y. Wu, P. Nordlander, Finite-Difference Time-Domain Modeling of the Optical Properties of Nanoparticles near Dielectric Substrates †. *J. Phys. Chem. C.* **114**, 7302–7307 (2010).

421. L. Yang, H. Wang, B. Yan, B. M. Reinhard, Calibration of Silver Plasmon Rulers in the 1−25 nm Separation Range: Experimental Indications of Distinct Plasmon Coupling Regimes. *J. Phys. Chem. C.* **114**, 4901–4908 (2010).

422. M. W. Knight, Y. Wu, J. B. Lassiter, P. Nordlander, N. J. Halas, Substrates Matter: Influence of an Adjacent Dielectric on an Individual Plasmonic Nanoparticle. *Nano Lett.* **9**, 2188–2192 (2009).

423. J. M. McMahon *et al.*, Correlating the Structure, Optical Spectra, and Electrodynamics of Single Silver Nanocubes. *J. Phys. Chem. C.* **113**, 2731–2735 (2009).

424. C. M. Cobley, M. Rycenga, F. Zhou, Z.-Y. Li, Y. Xia, Controlled Etching as a Route to High Quality Silver Nanospheres for Optical Studies. *J. Phys. Chem. C.* **113**, 16975–16982 (2009).

425. S. Link, M. A. El-Sayed, Size and Temperature Dependence of the Plasmon

Absorption of Colloidal Gold Nanoparticles. *J. Phys. Chem. B.* **103**, 4212–4217 (1999).

426. K. L. Kelly, E. Coronado, L. L. Zhao, G. C. Schatz, The Optical Properties of Metal Nanoparticles: The Influence of Size, Shape, and Dielectric Environment. *J. Phys. Chem. B.* **107**, 668–677 (2003).

427. T. Klar *et al.*, Surface-Plasmon Resonances in Single Metallic Nanoparticles. *Phys. Rev. Lett.* **80**, 4249–4252 (1998).

428. T. V. Shahbazyan, I. E. Perakis, J.-Y. Bigot, Size-Dependent Surface Plasmon Dynamics in Metal Nanoparticles. *Phys. Rev. Lett.* **81**, 3120–3123 (1998).

429. M. Hu *et al.*, Dark-field microscopy studies of single metal nanoparticles: understanding the factors that influence the linewidth of the localized surface plasmon resonance. *J. Mater. Chem.* **18**, 1949 (2008).

430. B. J. Wiley *et al.*, Synthesis and Optical Properties of Silver Nanobars and Nanorice. *Nano Lett.* **7**, 1032–1036 (2007).

431. R. Fuchs, Theory of the optical properties of ionic crystal cubes. *Phys. Rev. B.* **11**, 1732–1740 (1975).

432. G. S. Agarwal, S. S. Jha, Theory of second harmonic generation at a metal surface with surface plasmon excitation. *Solid State Commun.* **41**, 499–501 (1982).

433. A. Wokaun *et al.*, Surface second-harmonic generation from metal island films and microlithographic structures. *Phys. Rev. B.* **24**, 849–856 (1981).

434. B. K. Canfield *et al.*, Local Field Asymmetry Drives Second-Harmonic Generation in Noncentrosymmetric Nanodimers. *Nano Lett.* **7**, 1251–1255 (2007).

435. R. Esteban, A. G. Borisov, P. Nordlander, J. Aizpurua, Bridging quantum and classical plasmonics with a quantum-corrected model. *Nat. Commun.* **3**, 825 (2012).

436. K. J. Savage *et al.*, Revealing the quantum regime in tunnelling plasmonics. *Nature*. **491**, 574–7 (2012).

437. W. Zhu, K. B. Crozier, Quantum mechanical limit to plasmonic enhancement as

observed by surface-enhanced Raman scattering. *Nat. Commun.* **5**, 5228 (2014).

438. C. Ciracì *et al.*, Probing the ultimate limits of plasmonic enhancement. *Science*. **337**, 1072–4 (2012).

439. E. M. Purcell, Spontaneous emission probabilities at radio frequencies. *Phys. Rev.* **69**, 674–674 (1946).

440. P. K. Jain, W. Huang, M. A. El-Sayed, On the Universal Scaling Behavior of the Distance Decay of Plasmon Coupling in Metal Nanoparticle Pairs: A Plasmon Ruler Equation. *Nano Lett.* **7**, 2080–2088 (2007).

441. A. Lombardi *et al.*, Anomalous Spectral Shift of Near- and Far-Field Plasmonic Resonances in Nanogaps. *ACS Photonics*. **3**, 471–477 (2016).

442. J. Butet, P.-F. Brevet, O. J. F. Martin, Optical Second Harmonic Generation in Plasmonic Nanostructures: From Fundamental Principles to Advanced Applications. *ACS Nano*. **9**, 10545–10562 (2015).

443. Y. R. Shen, Surface properties probed by second-harmonic and sum-frequency generation. *Nature*. **337**, 519–525 (1989).

444. D. Jariwala *et al.*, Near-Unity Absorption in van der Waals Semiconductors for Ultrathin Optoelectronics. *Nano Lett.* **16**, 5482–5487 (2016).

445. Xiaodong Xu, Wang Yao, Di Xiao, Tony F. Heinz, Spin and pseudospins in layered transition metal dichalcogenides. **10**, 343–350 (2014).

446. K. Deng *et al.*, Experimental observation of topological Fermi arcs in type-II Weyl semimetal MoTe2. *Nat. Phys.* **12**, 1105–1110 (2016).

447. I. Aharonovich, D. Englund, M. Toth, Solid-state single-photon emitters. *Nat. Photonics*. **10**, 631–641 (2016).

448. G. Kresse, J. Furthmüller, Efficiency of ab-initio total energy calculations for metals and semiconductors using a plane-wave basis set. *Comput. Mater. Sci.* **6**, 15–50 (1996).